



SMOS ESL for SMOS Level 1 and Level 2 over Land, Ocean and Ice



L2 OS 3rd Mission Reprocessing Report

Ref.: ARG-003-081

Date: 16th July 2021

Customer: ESA





SMOS ESL for SMOS Level 1 and Level 2 over Land, Ocean and Ice

Report created by

ARGANS LTD, United Kingdom



IFREMER



LOCEAN



Barcelona Expert Center



ACRI-ST



OceanDataLab





Signatures

	Name	Company or Institute	Signature
Prepared by	Nicolas Reul	IFREMER	
	Jacqueline Boutin	LOCEAN	
	Estrella Olmedo	BEC	
	Jean-Luc Vergely	ACRI-ST	
	Joseph Tenerelli	ODL	
	Manuel Arias Ballesteros	ARGANS Ltd	
Reviewed by	Roberto Sabia	ESA	
Authorized by	Klaus Scipal	ESA	



Table of Contents

1	INTRODUCTION	16
1.1	PURPOSE AND SCOPE	16
1.2	REFERENCE AND APPLICABLE DOCUMENTS	16
1.3	SUMMARY OF THE ASSESSMENT OF RESULTS	17
2	SALINITY GLOBAL BIASES AND UNCERTAINTIES	22
2.1	GLOBAL VALIDATION VS ISAS	22
2.1.1	Methods	22
2.1.2	Results	23
2.2	GLOBAL VALIDATION VS PUNCTUAL ARGO	31
2.2.1	Methods	31
2.2.2	Spatial distribution of the biases	32
2.2.3	Temporal evolution of the biases	35
2.2.4	Regional statistics	39
2.2.5	Standard deviation of the differences with respect to in situ	57
2.2.6	Estimated uncertainty by Correlated Triple Collocation	59
2.3	PI-MEP RESULTS: GLOBAL FEATURES AND GEOPHYSICAL DEPENDENCIES	65
2.3.1	Spatial Maps of the Temporal mean and Std of Argo and L2v700 SSS difference (Δ SSS)	65
2.3.2	Time series of the monthly median and Std of in situ and satellite SSS and of the difference (Δ SSS) at Global Scale	66
2.3.3	Time series of the monthly median and Std of in situ and satellite SSS and of the difference (Δ SSS) sorted by latitudinal bands	67
2.3.4	Δ SSS (L2v700 - Argo) sorted as function of geophysical parameters	67
3	ASSESSMENT AT TB LEVEL	70
3.1	GEOPHYSICAL MODEL FUNCTION VS SMOS TBs	70
3.2	HOVMÖLLER PLOTS	70
4	ASCENDING/DESCENDING DIFFERENCES	73
4.1	LATITUDINAL DRIFT	73
4.1.1	Results from ISAS	73
4.1.2	Results from Pi-MEP: L2OSv700/V662 biases versus Argo as a function of Latitude for Ascending + Descending	75
4.1.3	L2OSv700/V662 biases versus Argo as a function of Latitude for Ascending	77
4.1.4	L2OSv700/V662 biases versus Argo as a function of Latitude for Descending	78
4.1.5	L3 (from v700/V662) biases versus Argo as a function of Latitude for Ascending + Descending	79
5	LAND/SEA, ICE/SEA, AND FOREIGN SOURCES OF ERROR	80
5.1	LAND/SEA CONTAMINATION ASSESSMENT	80
5.1.1	Forward model vs SMOS Tbs intercomparison	80
5.1.1.1	LSC Uncorrected Ascending passes	80
5.1.1.2	LSC corrected Ascending passes	80
5.1.1.3	Impact of the reference SSS on Ascending passes	82
5.1.1.4	LSC uncorrected and corrected Descending passes	82
5.1.1.5	Impact of the reference SSS on Descending passes	84
5.1.1.6	Impact of the LSC on the Ascending-Descending passes differences	85
5.1.1.7	Summary of Forward model/SMOS Tbs comparison	86
5.1.2	Pi-Mep SMOS L2 vs in-situ matchup analyses	87
5.1.2.1	L2/Argo match-up Results at Global scale	87
5.1.2.2	L2/TSG match-up at global scale	88



**SMOS ESL for SMOS Level 1 and Level 2
over Land, Ocean, and Ice
- L2OS 3rd Mission Reprocessing Report -**

Ref.: ARG-003-081

Date: 16.07.2021

Page: 5

5.1.2.3	L2/Argo match-up Results in the mid-latitudes (45°S-45°N)	89
5.1.2.4	L2/TSG match-up Results in the mid-latitudes (45°S-45°N)	90
5.1.2.5	L2/Argo match-up Results in the tropics (23°S-23°N)	92
5.1.2.6	L2/Argo match-up Results North of 45°N	93
5.1.2.7	L2/Argo match-up Results South of 45°S	94
5.1.2.8	L2/Argo match-up Results for each PI-MEP region	95
5.1.3	Validation protocol analyses and L3 validation with Argo	104
5.1.3.1	Validation protocol for LSC corrected L2 SSS Ascending+Descending	104
5.1.3.2	Validation protocol for LSC uncorrected L2 SSS- Global Scale	106
5.1.3.3	Validation protocol for LSC corrected L2 SSS separating Ascending & Descending passes	106
5.1.3.4	Conclusions of the Validation protocol analyses in the coastal domain	108
5.1.3.5	L3 validation with ARGO	108
5.1.4	LSC assessment summary	109
5.2	ICE/SEA CONTAMINATION ASSESSMENT	112
5.3	SUN GLINT	113
6	OCEAN TARGET TRANSFORMATION TRENDS	116
7	DIELECTRIC CONSTANT AND CARDIROID MODELS	120
7.1	IMPACT OF NEW DIELECTRIC CONSTANT MODEL	120
7.2	CARDIROID MODEL	122
	REFERENCES	126



List of Figures

- Figure 1: Mean difference of SMOS SSS minus ISAS SSS (left) and standard deviation of the difference (right) **farther than 1000km from coast. Descending orbits. 45°N-45°S**. Only SMOS pixels with more than 50 measurements and only ISAS SSS with PCTVAR<80% have been retained. Blue: SMOS v662; Black: v700. ----- 23
- Figure 2: SMOS SSS minus ISAS SSS in December 2019, descending orbits (left) v662, (right) v700. ----- 23
- Figure 3: SMOS SSS minus ISAS SSS in October 2015, descending orbits (left) v662, (right) v700. ----- 24
- Figure 4: Mean difference of SMOS SSS minus ISAS SSS (left) and standard deviation of the difference (right) **farther than 1000km from coast. Descending orbits. Global Ocean**. Only SMOS pixels with more than 50 measurements and only ISAS SSS with PCTVAR<80% have been retained. Blue: SMOS v662; Black: v700. ----- 24
- Figure 5: Mean difference of SMOS SSS minus ISAS SSS (left) and standard deviation of the difference (right) **farther than 1000km from coast. Ascending orbits. 45°N-45°S**. Only SMOS pixels with more than 50 measurements and only ISAS SSS with PCTVAR<80% have been retained. Blue: SMOS v662; Black: v700. ----- 25
- Figure 6: SMOS SSS minus ISAS SSS in August 2015, ascending orbits (left) v662, (right) v700. ----- 25
- Figure 7: SMOS SSS minus ISAS SSS in May 2014, Ascending orbits (left) v662, (right) v700. ----- 25
- Figure 8: Mean difference of SMOS SSS minus ISAS SSS (left) and standard deviation of the difference (right) **farther than 1000km from coast. Ascending orbits. Global Ocean**. Only SMOS pixels with more than 50 measurements and only ISAS SSS with PCTVAR<80% have been retained. Blue: SMOS v662; Black: v700. ----- 26
- Figure 9: Standard deviation of SMOS SSS minus ISAS SSS **farther than 1000km from coast. Ascending orbits for 10°N-40°N (left) and 10°S-40°S (right)**. Only SMOS pixels with more than 50 measurements and only ISAS SSS with PCTVAR<80% have been retained. ----- 26
- Figure 10: Mean difference of SMOS SSS minus ISAS SSS (left) and standard deviation of the difference (right) at **less than 1000km from coast. Ascending orbits. 45°N-45°S**. Only SMOS pixels with more than 50 measurements and only ISAS SSS with PCTVAR<80% have been retained. Blue: SMOS v662; Green: v700. ----- 27
- Figure 11: Mean difference of SMOS SSS minus ISAS SSS (left) and standard deviation of the difference (right) at **less than 1000km from coast. Descending orbits. 45°N-45°S**. Only SMOS pixels with more than 50 measurements and only ISAS SSS with PCTVAR<80% have been retained. Blue: SMOS v662; Green: v700. ----- 27
- Figure 12: Time series of the monthly mean (left) and monthly std (right) of the differences between SMOS and ISAS, for **Global, Asc+Desc orbits**. Blue curves: v662, orange curves: v700. ----- 27
- Figure 13: Time series of the monthly MAD of the differences between SMOS and ISAS, for **Global, Asc+Desc orbits**. Blue curves: v662, orange curves: v700. ----- 28
- Figure 14: Time series of the monthly mean (upper left), monthly std (upper right), and monthly MAD (lower) of the differences between SMOS and ISAS, for **Global, Descending orbits** only. Blue - v662, green - v700. ----- 28
- Figure 15: Time series of the monthly median (left) and monthly MAD (right) of the differences between SMOS and ISAS, for **45°S-45°N, Asc+Desc orbits**. Blue - v662, orange - v700. ----- 29
- Figure 16: Time series of the monthly std(diff) for the 45°S-45°N band (left) and for the **30°S-30°N band (right) for Asc+Desc orbits**. Blue curves - v662, orange (left) and black (right) - v700. ----- 29



Figure 17: Time series of the monthly std(diff) for the **45°S-45°N band for Ascending (left) and Descending (right) orbits**. Blue curves - v662, orange (left) and green (right) - v700. ----- 29

Figure 18: Time series of the monthly mean(diff) (upper panels) and std(diff) (lower panels) for the **70-40°S band for Ascending (left) and Descending (right) orbits**. Blue curves - v662, black (right) - v700. - 30

Figure 19: Mean differences between SMOS and Argo SSS for ascending and descending satellite overpasses: Left: Differences correspond to SMOS SSS v662; Right: Differences correspond to SMOS SSS v700. ----- 32

Figure 20: Mean differences between SMOS and Argo SSS for ascending satellite overpasses: Left: Differences correspond to SMOS SSS v662; Right: Differences correspond to SMOS SSS v700.----- 33

Figure 21: Mean differences between SMOS and Argo SSS for descending satellite overpasses: Left: Differences correspond to SMOS SSS v662; Right: Differences correspond to SMOS SSS v700.----- 33

Figure 22: Left: Latitudinal averaged SMOS-Argo SSS differences for ascending and descending together. The plot only represents the biases in the range of 60°S-60°N of latitudes. Right: Averaged SMOS-Argo SSS differences as function of the distance to the coast.----- 34

Figure 23: Left: Latitudinal averaged SMOS-Argo SSS differences for ascending orbits. The plot only represents the biases in the range of 60°S-60°N of latitudes. Right: Averaged SMOS-Argo SSS differences as function of the distance to the coast.----- 34

Figure 24: Left: Latitudinal averaged SMOS-Argo SSS differences for descending orbits. The plot only represents the biases in the range of 60°S-60°N of latitudes. Right: Averaged SMOS-Argo SSS differences as function of the distance to the coast.----- 35

Figure 25: Hovmöller plots representing the temporal evolution (x-axis) of the averaged difference between SMOS and Argo in latitudinal bands of 5 degrees (y-axis) for ascending and descending satellite overpasses together. Top: Hovmöller diagram for v662. Bottom Hovmöller diagram for v700. ----- 36

Figure 26: Hovmöller plots representing the temporal evolution (x-axis) of the averaged difference between SMOS and Argo in latitudinal bands of 5 degrees (y-axis) for ascending satellite overpasses. Top: Hovmöller diagram for v662. Bottom Hovmöller diagram for v700.----- 36

Figure 27: Hovmöller plots representing the temporal evolution (x-axis) of the averaged difference between SMOS and Argo in latitudinal bands of 5 degrees (y-axis) for descending satellite overpasses. Top: Hovmöller diagram for v662. Bottom Hovmöller diagram for v700.----- 37

Figure 28: Temporal evolution of the latitudinal gradient. Top left: Ascending satellite overpasses. Top right: Descending satellite overpasses. Bottom: Ascending and descending together.----- 38

Figure 29: Latitudinal stability of the differences between SMOS and Argo. Top left: Ascending satellite overpasses. Top right: Descending satellite overpasses. Bottom: Ascending and descending together. - 38

Figure 30: Latitudinal trends of the differences between SMOS and Argo. Top left: Ascending satellite overpasses. Top right: Descending satellite overpasses. Bottom: Ascending and descending together. - 39

Figure 31: Region comprising 60°S-60°N and all longitudes. In the first three rows the temporal evolution of the daily averaged differences between SMOS and Argo SSS (left) and the corresponding standard deviation of the differences (right) for ascending and descending together (first row), ascending (second row) and descending satellite overpasses (third row). Dark blue line corresponds to v700, and the sky-blue line corresponds to v662. Bottom: Yearly Root Mean Squared differences between SMOS and Argo. -- 41

Figure 32: Region comprising 30°S-30°N and all longitudes. In the first three rows the temporal evolution of the daily averaged differences between SMOS and Argo SSS (left) and the corresponding standard deviation of the differences (right) for ascending and descending together (first row), ascending (second



row) and descending satellite overpasses (third row). Dark blue line corresponds to v700, and the sky-blue line corresponds to v662. Bottom: Yearly Root Mean Squared differences between SMOS and Argo. -- 42

Figure 33: Region comprising 10°S-10°N and all longitudes. In the first three rows the temporal evolution of the daily averaged differences between SMOS and Argo SSS (left) and the corresponding standard deviation of the differences (right) for ascending and descending together (first row), ascending (second row) and descending satellite overpasses (third row). Dark blue line corresponds to v700, and the sky-blue line corresponds to v662. Bottom: Yearly Root Mean Squared differences between SMOS and Argo. -- 43

Figure 34: Region comprising 30°N-0°N and 150°W-120°W. In the first three rows the temporal evolution of the daily averaged differences between SMOS and Argo SSS (left) and the corresponding standard deviation of the differences (right) for ascending and descending together (first row), ascending (second row) and descending satellite overpasses (third row). Dark blue line corresponds to v700, and the sky-blue line corresponds to v662. Bottom: Yearly Root Mean Squared differences between SMOS and Argo. -- 45

Figure 35: Region comprising 30°N-50°N and 50°W-0°W. In the first three rows the temporal evolution of the daily averaged differences between SMOS and Argo SSS (left) and the corresponding standard deviation of the differences (right) for ascending and descending together (first row), ascending (second row) and descending satellite overpasses (third row). Dark blue line corresponds to v700, and the sky-blue line corresponds to v662. Bottom: Yearly Root Mean Squared differences between SMOS and Argo. -- 46

Figure 36: Region comprising 0°N-20°N and 70°W-40°W. In the first three rows the temporal evolution of the daily averaged differences between SMOS and Argo SSS (left) and the corresponding standard deviation of the differences (right) for ascending and descending together (first row), ascending (second row) and descending satellite overpasses (third row). Dark blue line corresponds to v700, and the sky-blue line corresponds to v662. Bottom: Yearly Root Mean Squared differences between SMOS and Argo. -- 47

Figure 37: Region comprising 10°S-10°N and 180°W-80°W. In the first three rows the temporal evolution of the daily averaged differences between SMOS and Argo SSS (left) and the corresponding standard deviation of the differences (right) for ascending and descending together (first row), ascending (second row) and descending satellite overpasses (third row). Dark blue line corresponds to v700, and the sky-blue line corresponds to v662. Bottom: Yearly Root Mean Squared differences between SMOS and Argo. -- 49

Figure 38: Region comprising 30°N-50°N and 180°W-120°W. In the first three rows the temporal evolution of the daily averaged differences between SMOS and Argo SSS (left) and the corresponding standard deviation of the differences (right) for ascending and descending together (first row), ascending (second row) and descending satellite overpasses (third row). Dark blue line corresponds to v700, and the sky-blue line corresponds to v662. Bottom: Yearly Root Mean Squared differences between SMOS and Argo. ----- 50

Figure 39: Region comprising 40°S-0°N and 30°W-0°W. In the first three rows the temporal evolution of the daily averaged differences between SMOS and Argo SSS (left) and the corresponding standard deviation of the differences (right) for ascending and descending together (first row), ascending (second row) and descending satellite overpasses (third row). Dark blue line corresponds to v700, and the sky-blue line corresponds to v662. Bottom: Yearly Root Mean Squared differences between SMOS and Argo. -- 51

Figure 40: Region comprising 30°S-0°N and 60°E-120°E. In the first three rows the temporal evolution of the daily averaged differences between SMOS and Argo SSS (left) and the corresponding standard deviation of the differences (right) for ascending and descending together (first row), ascending (second row) and descending satellite overpasses (third row). Dark blue line corresponds to v700, and the sky-blue line corresponds to v662. Bottom: Yearly Root Mean Squared differences between SMOS and Argo. -- 53

Figure 41: Region comprising 50°N-90°N and all longitudes. In the first three rows the temporal evolution of the daily averaged differences between SMOS and Argo SSS (left) and the corresponding standard deviation of the differences (right) for ascending and descending together (first row), ascending (second



row) and descending satellite overpasses (third row). Dark blue line corresponds to v700, and the sky-blue line corresponds to v662. Bottom: Yearly Root Mean Squared differences between SMOS and Argo. -- 54

Figure 42: Region comprising 90°S-50°S and all longitudes. In the first three rows the temporal evolution of the daily averaged differences between SMOS and Argo SSS (left) and the corresponding standard deviation of the differences (right) for ascending and descending together (first row), ascending (second row) and descending satellite overpasses (third row). Dark blue line corresponds to v700, and the sky-blue line corresponds to v662. Bottom: Yearly Root Mean Squared differences between SMOS and Argo. -- 55

Figure 43: Standard deviation of the differences between SMOS and Argo SSS for ascending and descending orbits together. Top left: differences correspond to v662. Top right: differences correspond to v700. Bottom plot represents the differences between the two top maps, such that the pixels in blue (red) represent regions where the SD of v700 is larger (lower) than the one of v662. ----- 57

Figure 44: Standard deviation of the differences between SMOS and Argo SSS for ascending orbits. Top left: differences correspond to v662. Top right: differences correspond to v700. Bottom plot represents the differences between the two top maps, such that the pixels in blue (red) represent regions where the SD of v700 is larger (lower) than the one of v662.----- 58

Figure 45: Standard deviation of the differences between SMOS and Argo SSS for descending orbits. Top left: differences correspond to v662. Top right: differences correspond to v700. Bottom plot represents the differences between the two top maps, such that the pixels in blue (red) represent regions where the SD of v700 is larger (lower) than the one of v662.----- 59

Figure 46: Estimated standard deviation of the SMOS SSS errors as result of the TC analysis. Left plots correspond to v662 and right plots to v700. First row presents the results for ascending and descending orbits together, the second row presents the results for ascending orbits, and the third row represents the results for descending orbits.----- 61

Figure 47: Differences between the estimated standard deviation of v662 and v700 for ascending and descending orbits together, such that the pixels in blue (red) represent regions where the error of v700 is larger (lower) than the one of v662. ----- 62

Figure 48: Differences between the estimated standard deviation of v662 and v700 for ascending orbits together, such that the pixels in blue (red) represent regions where the error of v700 is larger (lower) than the one from v662. ----- 63

Figure 49: Differences between the estimated standard deviation of v662 and v700 for descending orbits together, such that the pixels in blue (red) represent regions where the error of v700 is larger (lower) than the one of v662.----- 64

Figure 50: Temporal mean (left) and Std (right) of Δ SSS (Satellite - Argo). Top plots are for LSC corrected SSS from SMOS L2 v662. Bottom plots are for LSC corrected SSS from SMOS L2 v700. Only match-up pairs are used to generate these maps.----- 65

Figure 51 : Temporal mean of the SSS difference (SMOS v662 – SMOS v700) in spatial bins of 1 degree over 2010-2021.----- 66

Figure 52: Time series of the monthly median SSS (top), median of Δ SSS (SMOS L2v700 - Argo) and Std of SSS (Satellite - Argo) over the Global Ocean Pi-MEP region considering all matchups collected by the Pi-MEP. ----- 66

Figure 53: Monthly median (red curves) of Δ SSS (Satellite - Argo) and ± 1 Std (black vertical thick bars) as function of time for all the collected Pi-MEP match-up pairs estimated over the Global Ocean Pi-MEP region and for the full satellite product period are shown for different latitude bands: (a) 80°S-80°N, (b) 20°S-20°N, (c) 40°S-20°S and 20°N-40°N and (d) 60°S-40°S and 40°N-60°N.----- 67



Figure 54: Δ SSS (Satellite - Argo) sorted as function of Argo SSS values a), Argo SST b), ASCAT Wind speed c), CMORPH rain rate d) and distance to coast e). In all plots the median and Std of Δ SSS for each bin is indicated by the red curves and black vertical thick bars (± 1 Std). Left column is for v662. Right column is for v700.----- 69

Figure 55: Definition of region of the unit circle used to produce the Hovmöller plots (in red). Left: AF-FoV; Right: EAF-FoV.----- 70

Figure 56: Hovmöller plots showing the time-latitude evolution of the bias in $(T_x+T_y)/2$ for the alias-free field of view (AF-FoV, top panels) and extended alias-free field of view (EAF-FoV, bottom panels) defined in the previous figure. Left: ascending passes; right: descending passes. No average bias has been removed in these plots. Units are kelvin.----- 71

Figure 57: Same as the previous figure except that in each plot the average has been removed to better reveal the seasonal and latitudinal variations.----- 71

Figure 58: Top row: Hovmöller plots showing the difference between ascending and descending pass bias in $(T_x+T_y)/2$. Bottom row: Celestial sky glint for descending passes for the alias-free (left) and extended alias-free (right) fields of view. Units are kelvin.----- 72

Figure 59: SMOS SSS minus ISAS SSS further than 1000km from coast. Ascending orbits. Only SMOS pixels with more than 50 measurements and only ISAS SSS with PCTVAR<80% have been retained. Left v662, right v700.----- 73

Figure 60: SMOS SSS minus ISAS SSS further than 1000km from coast. Descending orbits. Only SMOS pixels with more than 50 measurements and only ISAS SSS with PCTVAR<80% have been retained. Left v662, right v700.----- 73

Figure 61: Standard deviation of SMOS SSS minus ISAS SSS further than 1000km from coast. Ascending orbits. Only SMOS pixels with more than 50 measurements and only ISAS SSS with PCTVAR<80% have been retained. Left v662, right v700.----- 74

Figure 62: Standard deviation of SMOS SSS minus ISAS SSS further than 1000km from coast. Descending orbits. Only SMOS pixels with more than 50 measurements and only ISAS SSS with PCTVAR<80% have been retained. Left v662, right v700.----- 74

Figure 63 : Zonal mean of Δ SSS (SMOS - Argo) for all the collected Pi-MEP match-up pairs estimated 2010-2021. SMOS V662 is in red and v700 in Black using SSS corrected (left) and uncorrected (right).----- 75

Figure 64: Left panel: Zonal mean SSS from SMOS SSS L2 v662 LSC corrected (black) and from Argo (blue). Right panel: same but for L2 v700.----- 76

Figure 65: Left panel: Zonal mean of the difference Δ SSS between SMOS SSS L2 v662 LSC corrected and Argo (blue). Right panel: same but for L2 v700.----- 76

Figure 66 : Zonal mean of Δ SSS (SMOS - Argo) for all the collected Pi-MEP match-up pairs estimated 2010-2021. SMOS V662 is in red and v700 in Black using Ascending SSS corrected (left) and uncorrected (right).----- 77

Figure 67: Latitude-time Hovmöller diagram of the difference between SMOS and Argo SSS for Ascending passes v662 (Top) and v700 (Bottom)----- 77

Figure 68 : Zonal mean of Δ SSS (SMOS - Argo) for all the collected Pi-MEP match-up pairs estimated 2010-2021. SMOS V662 is in red and v700 in Black using Descending SSS corrected (left) and uncorrected (right).----- 78

Figure 69: Latitude-time Hovmöller diagram of the difference between SMOS and Argo SSS for Descending passes v662 (Top) and v700 (Bottom)----- 78

Figure 70: Latitudinal and seasonal biases: ASC+DES. Top is v662. Bottom is v700.----- 79



Figure 71: **LSC uncorrected ascending** passes, the Standard deviations of the differences in individual reconstructed brightness temperatures between forward model (forced **using RSS SMAP weekly SSS**) and SMOS Tbs over July 2016 as a function of dwell line location on earth. (top left) Std(dTx) (top right) Std(dTy). (Bottom Left) Corresponding biases in retrieved SSS (simple linearized method) and (bottom right) dwell line averaged brightness temperature first Stokes parameter divided by two.----- 81

Figure 72: **LSC corrected Ascending** passes, the Standard deviations of the differences in individual reconstructed brightness temperatures between forward model (forced **using RSS SMAP weekly SSS**) and SMOS Tbs over July 2016 as a function of dwell line location on earth. (top left) Std(dTx) (top right) Std(dTy). (Bottom Left) Corresponding biases in retrieved SSS (simple linearized method) and (bottom right) dwell line averaged brightness temperature first Stokes parameter divided by two.----- 81

Figure 73: **LSC corrected Ascending** passes, the Standard deviations of the differences in individual reconstructed brightness temperatures between forward model (forced **using ISAS weekly SSS**) and SMOS Tbs over July 2016 as a function of dwell line location on earth. (top left) Std(dTx) (top right) Std(dTy). (Bottom Left) Corresponding biases in retrieved SSS (simple linearized method) and (bottom right) dwell line averaged brightness temperature first Stokes parameter divided by two.----- 82

Figure 74: **LSC uncorrected descending** passes, the Standard deviations of the differences in individual reconstructed brightness temperatures between **forward model (forced using RSS SMAP weekly SSS) and SMOS Tbs** over July 2016 as a function of dwell line location on earth. (top left) Std(dTx) (top right) Std(dTy). (Bottom Left) Corresponding biases in retrieved SSS (simple linearized method) and (bottom right) dwell line averaged brightness temperature first Stokes parameter divided by two.----- 83

Figure 75 **LSC corrected descending** passes, the Standard deviations of the differences in individual reconstructed brightness temperatures between **forward model (forced using RSS SMAP weekly SSS) and SMOS Tbs** over July 2016 as a function of dwell line location on earth. (top left) Std(dTx) (top right) Std(dTy). (Bottom Left) Corresponding biases in retrieved SSS (simple linearized method) and (bottom right) dwell line averaged brightness temperature first Stokes parameter divided by two.----- 83

Figure 76: **LSC corrected Descending** passes, the Standard deviations of the differences in individual reconstructed brightness temperatures between forward model (forced **using ISAS monthly SSS**) and SMOS Tbs over July 2016 as a function of dwell line location on earth. (top left) Std(dTx) (top right) Std(dTy). (Bottom Left) Corresponding biases in retrieved SSS (simple linearized method) and (bottom right) dwell line averaged brightness temperature first Stokes parameter divided by two.----- 84

Figure 77 : **LSC corrected Descending** passes, the Standard deviations of the differences in individual reconstructed brightness temperatures between forward model (forced **using RSS SMAP weekly SSS**) and SMOS Tbs over July 2016 as a function of dwell line location on earth. (top left) Std(dTx) (top right) Std(dTy). (Bottom Left) Corresponding biases in retrieved SSS (simple linearized method) and (bottom right) dwell line averaged brightness temperature first Stokes parameter divided by two.----- 84

Figure 78: The **uncorrected difference** between ascending and descending pass biases (top left) and brightness temperature standard deviations (top right). Retrieved SSS difference between ascending and descending passes (bottom left) and First Stokes bias (bottom right). Forward model is using RSS SMAP.----- 85

Figure 79: The **LSC corrected difference** between ascending and descending pass biases (top left) and brightness temperature standard deviations (top right). Retrieved SSS difference between ascending and descending L2OS passes (bottom left) and First Stokes bias (bottom right). Forward model is using RSS SMAP.----- 86

Figure 80 : Temporal mean of the SSS difference (SMOS – Argo) in spatial bins of 1 degree over 2010-2021 for v662 (left) and v700 (right). ----- 87



- Figure 81: Mean (left) and STD (right) differences between SMOS L2 (v662 in red; v700 in black) and **Argo** as a function of the distance to coasts (x-axis) at global scale. Top and bottom plots are for SSS_uncor and SSS_corr, respectively. Statistics are derived at **global scale**.----- 88
- Figure 82: Mean (left) and STD (right) differences between SMOS L2 (v662 in red; v700 in black) and **TSG SSS** as a function of the distance to coasts (x-axis) at global scale. Top and bottom plots are for SSS_uncor and SSS_corr, respectively. Statistics are derived at **global scale**.----- 89
- Figure 83: Mean (left) and STD (right) differences between SMOS L2 (v662 in red; v700 in black) and Argo as a function of the distance to coasts (x-axis) at global scale. Top and bottom plots are for SSS_uncor and SSS_corr, respectively. Statistics are derived from matchups collected only in the **mid-latitude (45°S-45°N) band**.----- 90
- Figure 84: Mean (left) and STD (right) differences between SMOS L2 (v662 in red; v700 in black) and **TSG SSS** as a function of the distance to coasts (x-axis) at global scale. Top and bottom plots are for SSS_uncor and SSS_corr, respectively . Statistics are derived in the mid-latitudes (45°S-45°N).----- 91
- Figure 85: Mean (left) and RMS (right) differences between SMOS L2 (v662 in red; v700 in black) and Argo as a function of the distance to coasts (x-axis) at global scale. Top and bottom plots are for SSS_uncor and SSS_corr, respectively . Statistics are derived from matchups collected only **in the Tropics (23°S-23°N) band**.----- 92
- Figure 86: Mean (left) and RMS (right) differences between SMOS L2 (v662 in red; v700 in black) and Argo as a function of the distance to coasts (x-axis) at global scale. Top and bottom plots are for SSS_uncor and SSS_corr, respectively . Statistics are derived from matchups collected only **North of 45°N**.----- 93
- Figure 87: Mean (left) and RMS (right) differences between SMOS L2 (v662 in red; v700 in black) and Argo as a function of the distance to coasts (x-axis) at global scale. Top and bottom plots are for SSS_uncor and SSS_corr, respectively . Statistics are derived from matchups collected only **South of 45°S**. ----- 94
- Figure 88: The mask of the region (left panels) and (right panel) the median (top) and the std (bottom) of the SSS difference between SMOS LSC corrected data and Argo data as a function of distance to coasts are provided for each region and each processor version (L2v662 (red) versus L2V700 (black)).----- 103
- Figure 89: Monthly MEDIAN (left) and MAD (right) difference between SMOS L2-averaged v662 (blue) or v700 (orange) with ISAS. **Global Scale**. Asc+Desc.----- 104
- Figure 90: Monthly MEDIAN (left) and MAD (right) difference between SMOS L2-averaged v662 (blue) or v700 (orange) with ISAS. **Mid-latitudes**. Asc+Desc.----- 104
- Figure 91: Monthly MEDIAN (left) and MAD (right) difference between SMOS L2-averaged v662 (blue) or v700 (black) with ISAS. **Tropical-latitudes (30°S-30°N)**. Asc+Desc.----- 105
- Figure 92: Monthly MEDIAN (left) and MAD (right) difference between SMOS L2-averaged v662 (blue) or v700 (black) with ISAS. **Southern Ocean (80°S-60°S)**. Asc+Desc. ----- 105
- Figure 93: Monthly MEDIAN (left) and MAD (right) difference between SMOS L2-averaged v662 (blue) or v700 (black) with ISAS. **Northern Ocean (60°N-80°N)**. Asc+Desc. ----- 106
- Figure 94: Monthly MEDIAN (left) and MAD (right) difference between SMOS L2-averaged v662 (green) or v700 (yellow) with ISAS. **Mid-latitudes (45°S-45°N)**. Asc+Desc. SMOS L2 SSS is **LSC Uncorrected**----- 106
- Figure 95: Mean bias (left) and STD (right) between SMOS L3 9-days average and Argo as a function of distance to coasts (v662 pink; v700 purple).----- 109
- Figure 96: Mean bias (top) and Standard deviation (bottom) between SMOS L3 9-days average and Argo as a function of distance to coasts for ascending passes (left, v662 blue; v700 dark blue) and descending passes (right, v662 green; v700 dark green). ----- 109



- Figure 97: SMOS SSS minus ISAS SSS. Left: Ascending orbits, right: Descending orbits. Only SMOS pixels with more than 50 measurements have been retained. Top v700, bottom: v662. ----- 112
- Figure 98: SMOS SSS minus ISAS SSS as a function to the distance from the ice edge in the Southern Ocean. Each colour line corresponds to a different month. Left: Ascending orbits, right: Descending orbits. Top v662, bottom: L1 Sce 8c processed with KS dielectric constant model.----- 113
- Figure 99: Time series of daily unpolarized solar flux (units of 105 K) obtained by rescaling the SERCO daily reference solar flux by a factor of 0.9196.----- 114
- Figure 100: Extended alias-free field of view averaged sun glint $(T_x+T_y)/2$ as a function of time in 2016 and latitude. Units are dbK since the signal level is extremely small. Left: ascending passes; Right: descending passes. ----- 114
- Figure 101: Examples of the impact of sun glint on dwell-line averaged difference between MIRAS and forward model first Stokes parameter divided by two $(T_x+T_y)/2$ (using brightness temperatures in the extended alias-free field of view). Units are kelvin. Top panels: 29 January 2012 without (left) and with (right) sun glint included in the forward model. Sun glint is computed using the rescaled SERCO daily reference solar flux.----- 115
- Figure 102: Median of the OTT according to the time for the four polarizations (TX,TY,St3,St4) in black, blue, green, and red, respectively. Full lines correspond to v700, dashed lines to v662. Ascending orbits. ----- 116
- Figure 103: Median of the OTT according to the time for the four polarizations (TX,TY,St3,St4) in black, blue, green, and red, respectively. Full lines correspond to v700, dashed lines to v662. Descending orbits. ----- 117
- Figure 104: Standard deviation of the OTT according to the time for the four polarizations (TX,TY,St3,St4) in black, blue, green, and red, respectively. Full lines correspond to v700, dashed lines to v662. Ascending orbits.----- 117
- Figure 105: Standard deviation of the OTT according to the time for the four polarizations (TX,TY,St3,St4) in black, blue, green, and red, respectively. Full lines correspond to v700, dashed lines to v662. Descending orbits.----- 118
- Figure 106: OTT anomalies over 2011-2019, X polarization, ascending orbits. Left panel shows v662 OTTs, right panel, v700 OTTs.----- 118
- Figure 107: OTT anomalies over 2011-2019, Y polarization, ascending orbits. Left panel shows v662 OTTs, right panel, v700 OTTs.----- 119
- Figure 108: Expected change in SSS (red curve minus black curve) due to dielectric constant model change (see Boutin et al. 2020 for more details).----- 120
- Figure 109: Expected SSS difference due to the change in dielectric constant model (SSS BV – SSS KS) over moderate to warm SST (left), over full SST range (right)----- 120
- Figure 110: SMOS minus ISAS SSS in the Southern hemisphere in May 2018. Left v662, right: v700. Top: SST, middle: Descending orbits, bottom: ascending orbits.----- 121
- Figure 111: SMOS SSS minus ISAS SSS as a function to the distance from the ice edge in the Southern Ocean. Each colour line corresponds to a different month. Left: Ascending orbits, right: Descending orbits. Top: L1 Sce 8c processed with KS dielectric constant model; bottom: L1 Sce 8c processed with BV dielectric constant model.----- 122
- Figure 112: Monthly average of Acard and SSS from v662 and v700, ascending orbits. Top left: mean(SSS v700 – SSS v662); top right: mean(Acard v700 – Acard v662); bottom left: std(SSS v700 – SSS v662); bottom right: std(Acard v700 – Acard v662). May 2016. ----- 123



Figure 113: Monthly average of Acard and SSS from v662 and v700, ascending orbits. Top left: mean(SSS v700 – SSS v662); top right: mean(Acard v700 – Acard v662); bottom left: std(SSS v700 – SSS v662); bottom right: std(Acard v700 – Acard v662). July 2016. ----- 123

Figure 114: Monthly average of Acard and SSS from v662 and v700, ascending orbits. Top left: mean(SSS v700 – SSS v662); top right: mean(Acard v700 – Acard v662); bottom left: std(SSS v700 – SSS v662); bottom right: std(Acard v700 – Acard v662). September 2016. ----- 124

Figure 115: Monthly average of Acard and SSS from v662 and v700, descending orbits. Top left: mean(SSS v700 – SSS v662); top right: mean(Acard v700 – Acard v662); bottom left: std(SSS v700 – SSS v662); bottom right: std(Acard v700 – Acard v662). May 2016. ----- 124

Figure 116: Monthly average of Acard and SSS from v662 and v700, descending orbits. Top left: mean(SSS v700 – SSS v662); top right: mean(Acard v700 – Acard v662); bottom left: std(SSS v700 – SSS v662); bottom right: std(Acard v700 – Acard v662). July 2016. ----- 125

Figure 117: Monthly average of Acard and SSS from v662 and v700, descending orbits. Top left: mean(SSS v700 – SSS v662); top right: mean(Acard v700 – Acard v662); bottom left: std(SSS v700 – SSS v662); bottom right: std(Acard v700 – Acard v662). September 2016. ----- 125



List of Tables

Table 1: Filtering criteria applied to the L2 SSS product. We discard the SSS retrievals when they meet one or more of the following conditions.-----	31
Table 2: Global statistics for the region comprising 60°S-60°N and all longitudes. -----	44
Table 3: Global statistics for the region comprising 30°S-30°N and all longitudes. -----	44
Table 4: Global statistics for the region comprising 10°S-10°N and all longitudes. -----	44
Table 5: Global statistics for the region comprising 30°N-0°N and 150°W-120°W. -----	48
Table 6: Global statistics for the region comprising 30°N-50°N and 50°W-0°W. -----	48
Table 7: Global statistics for the region comprising 0°N-20°N and 70°W-40°W. -----	48
Table 8: Global statistics for the region comprising 10°S-10°N and 180°W-80°W. -----	52
Table 9: Global statistics for the region comprising 30°N-50°N and 180°W-120°W. . -----	52
Table 10: Global statistics for the region comprising 40°S-0°N and 30°W-0°W. -----	52
Table 11: Global statistics for the region comprising 30°S-0°N and 60°E-120°E. -----	56
Table 12: Global statistics for the region comprising 50°N-90°N and all longitudes. -----	56
Table 13: Global statistics for the region comprising 90°S-50°S and all longitudes. -----	56

1 Introduction

1.1 Purpose and Scope

This report is an analysis of results from the ESA 3rd mission reprocessing campaign performed at ESAC DPGS from December 2020 till February 2021, using the v700 L2OS processor and v700 OSCOTT post-processor, with formerly reprocessed v724 L1c input products.

The purpose of this report is to quantify the quality of salinity retrievals, and to identify potential issues which need to be addressed in subsequent reprocessing campaigns, as well as guide the ESL activities for the next stages of the SMOS mission.

The L2OS v700 Reprocessing campaign was performed at ESAC DPGS by running 3 instances in parallel. Each one started with an empty OTT. To cope with the resulting degraded quality, an overlap of 35 days took place between each of the instances, so that a valid OTT was used for the first period of each reprocessing line, to correct for the expected degraded quality.

In addition, ARGANS Ltd provided ESA with three OTTs computed in-house, to be used during the Commissioning Phase (12th January 2010 till 12th April 2010).

L2 Ocean Salinity Expert Support Laboratories (ESL) were tasked with the assessment of the full time series of the reprocessing dataset (12th January 2010 till 1st June 2021) with the subsequent objectives:

1. Certify that global results of the reprocessing are nominal, and no significant degradations are found in the data from the preliminary assessments.
2. Assess the overall quality of the new results found from the combination of the L1c SMOS MIRAS TBs v724 baseline and the L2OS OP v700 baseline, and compare those against the mission objectives.
3. Identify potential fall pits and limitations of the new dataset that shall be addressed in the next cycle of development.
4. Advise on the fitness of the new dataset for public release.

The metrics and assessment performed in each case will cover various aspects of the SMOS L2 SSS of interest for the ESLs and to better understand the behaviour of the novel v700 dataset. Details of the procedures followed are provided in their corresponding sections.

1.2 Reference and Applicable Documents

All documents referenced [R.D. n] or [A.D.n] in the tables hereunder are applicable to the L2 OS SSS v700 dataset.

Reference	Title	Code	Issue	Date
[R.D. 1]	SMOS L2 OS Algorithm Theoretical Baseline Document	SO-TN-ARG-GS-0007	4.1	12-02-2021
[R.D. 2]	SMOS L2 OS Operational Processor Computation Resources Requirements	SO-TN-ARG-GS-0011	2.14	12-02-2021
[R.D. 3]	SMOS L2 OS Detailed Processing Model	SO-TN-ARG-GS-0008	2.19	12-02-2021
[R.D. 4]	SMOS Level 2 and Auxiliary Data Product Specification	SO-TN-IDR-GS-0006	8.5	03-02-2017



Reference	Title	Code	Issue	Date
[R.D. 5]	SMOS L2 OS Detailed Design Document	SO-DD-ARG-GS-0012 ¹	2.33	12-02-2021
[R.D. 6]	SMOS L2 OS Software Verification and Validation Plan - Unit Test	SO-TP-ARG-GS-0013	2.19	12-02-2021
[R.D. 7]	SMOS L2 OS Table Generation Requirement Document	SO-TN-ARG-GS-0014	3.17	12-02-2021
[R.D. 8]	SMOS L2 OS Operational Processor Software Release Document	SO-RN-ARG-GS-0019	2.32	12-02-2021
[R.D. 9]	SMOS Level 1 and Auxiliary Data Product Specification	SO-TN-IDR-GS-0005	6.3	31-01-2017
[R.D. 10]	SMOS L2 OS Input / Output Data Definition	SO-TN-ARG-GS-0009	2.37	12-02-2021
[R.D. 11]	SMOS L2 OS Operational Processor Software User Manual	SO-MA-ARG-GS-0018	1.21	12-02-2021
[R.D. 12]	SMOS L2 OS Operational Processor Auxiliary Data Files Configuration Control	SO-CS-ARG-GS-0039	1.41	12-02-2021
[R.D. 13]	SMOS L2 OS Test Data Description - Test Data Procedures	SO-TN-ARG-GS-0057	1.19	12-02-2021
[R.D. 14]	SMOS L2 OS OTT Post-Processor Software User Manual	SO-TN-ARG-GS-0081	0.6	12-02-2021

1.3 Summary of the assessment of results

The major improvements introduced in the currently operational version 700 of the SMOS Level 2 sea surface salinity processor are detailed in the paragraphs below.

The **SSS anomaly field** has been substantially revisited. The fields present in the former version v662 of the products were obtained by simply subtracting the climatological SSS value contained in WOA2009 from the retrieved SMOS SSS values. Since v700, the SSS anomaly is computed against a self-consistent SMOS-derived SSS climatology using 7 years of SSS retrievals (2013-2019). To improve quality, the SMOS-derived climatology corrects also for part of the systematic biases found in the SMOS SSS retrievals (such as land contamination). A full description of the method to produce the SMOS-based climatology appears in the section 2.2.9 of the TGRD document (see references of this report).

The Somaraju and Trumpf (ST) seawater **dielectric constant model** with updated parametrization by Boutin et al. (2020) (BV) has been now introduced to replace Klein and Swift's dielectric constant model that was used in the previous versions of the algorithm to estimate the specular sea surface emissivity and thus retrieve salinity. The BV tuning has been adjusted to minimize SMOS limitations found in the SSS retrievals and to improve SSS retrieval quality in cold waters with respect the Klein and Swift's dielectric constant model. This was achieved with the support of the cardioid parameters provided along with the UDP products (so called, Acard field). Further information can be found in the section 4.1.4 of the ATBD as well as in Boutin et al, 2020 (see references of this report).

The procedure to **optimize the Ocean Target Transformation (OTT)** for systematic instrumental bias correction has now improved. A more stringent filtering is applied to reduce the level of noise in the OTT, especially in the upper part of the AF-FOV. The novel filtering stabilizes the OTT which becomes less impacted by Radio Frequency Interferences (RFI), or by errors due to TEC variations. Further details are provided in section 5.8.3 of the ATBD (see references of this report).

¹ Detailed Design Document is available in electronic version only. The DDD is a web site dedicated to the documentation of the Operational Processor.



The estimation of the **theoretical retrieval error** has also been improved and is now more representative of the true error. This change impacts the values of the UDP fields Sigma_SSS_corr, Sigma_SSS_uncorr, and Sigma_SSS_anom. For further details, the reader is invited to check section 4.11.2 of the ATBD (see references of this report).

An improved **correction for the Land/Sea Contamination (LSC)** has also now been introduced to reduce SSS retrievals biases in areas located at distances less than 1,000 km from the nearest coasts. The main differences with respect v662 are that the new method makes use of an improved reference SSS to derive the correction and a longer time series to estimate the mean LSC-induced biases. Specifically, the In Situ Analysis System (ISAS-15; Gaillard et al., 2016) derived fields are used instead of the World Ocean Atlas (WOA) Climatology fields used in previous versions. A stricter RFI filtering and a gap-filling method based on an empirical convolution kernel are also applied in this latest LSC correction. These changes are meant to reduce the impact of the limitations from previous version, where areas with high natural dynamics or impacted frequently by RFI were not well represented in the correction (particularly in the tropical Atlantic). Further information is found in the section 2.2.8 of the TGRD (see references of this report).

The flags defined to estimate the impact of **sea-state conditions** on SSS retrieval quality have been now revisited. Six flags called Fg_sc_sea_state_n, with n=1, ...,6, are present in the UDP files, which can be combined to filter SSS retrievals according to sea-state. These flags are based on threshold values of inverse wave age (Omega) and swell fraction which have been now better defined and corrected to represent more accurately the presence of young seas, old seas, and swell, correspondingly. The worst SSS quality is observed for Fg_sc_sea_state_1 (wind sea dominated old seas) and Fg_sc_sea_state_5 (wind sea dominated young sea state). Data acquired in these conditions are often close to coast and therefore less reliable.

SMOS SSS retrievals from version 662 were obtained including a novel sun glint correction. The sun glint is estimated as a combination of the sun L-band radiation reflection at the ocean's surface and the impact of the surface roughness in the scattering of the signal. The modelled brightness temperature associated to sun glint within the SMOS scenes is calculated and included as part of the geophysical model function for the retrieval. In the version 700, the source of **solar L-band radio fluxes** has been modified, replacing the previously used rescaled Penticton datasets with a SMOS-based estimation of the solar flux at L-band, derived from the SMOS instrumental information. This has proved to be a more accurate source of L-band solar fluxes for the purposes of the mission. For further details, readers are directed to section 2.4.6 and Annex A.3 from TGRD (see references of this report).

Configuration of switches and filters used in the data processing has been updated. For further information see the section 2.4.7 of the TGRD (see references of this report).

The L2OS version 700 data set has been generated using a newly recalibrated L1c dataset of SMOS MIRAS Brightness Temperatures (version 724). For further details on the L1c data sets see the read-me-first note for the release of SMOS Level 1 data products available here:

<https://earth.esa.int/eogateway/catalog/smos-science-products>

The main conclusions of the analysis are:

- Land-sea contamination corrected salinities (SSS_corr) almost cancel the global mean bias with respect to in situ observations in near-to-coast regions (> 40 km and < 800 km) as compared to SSS_uncorr for the mid-latitudes ($|\text{lat}| \leq 45^\circ$). Caveats found in previous version in the tropical Atlantic Ocean, tip of south Africa or around Australia have disappeared in this new version. In the high northern or southern latitudes, data are still affected by the moving sea-ice transition, which effects are not corrected in SSS_corr.
- For SSS_uncorr, land-sea contamination is still present, but with different across track signatures and it is less variable across swath.

- High latitudes of the southern hemisphere: the new dielectric constant model corrects for a large part of positive SSS biases in descending orbits. However, due to remaining contamination of other origins, positive biases remain for the rest of the year. On ascending orbits, negative biases ~ -2.5 pss are observed all the year round in a latitudinal band around the ice edge as an effect of ice-sea contamination.
- The new salinity anomaly product exhibit reduced systematic errors (such as land-sea contamination) compared with the previous anomaly fields which used WOA climatology as a reference. Nevertheless, systematic seasonal latitudinal errors are not corrected in this version and generate artefacts.
- Ascending-descending differences in retrieved SSS remain, but they are more homogeneous spatially than in the previous version. We noticed stronger ice-sea contamination in the Southern Ocean on ascending orbits than in previous version.

Some more detailed conclusions are provided in the paragraphs below.

In terms of biases at SSS level:

- Global performance in the "coastal" areas (distance to coast < 1000 km) for the land/sea contamination-corrected products (SSS_corr) is only slightly improved in the 700 version but is degraded in terms of random errors.
- For land/sea contamination-uncorrected products (SSS_uncor), the v662 shows considerably smaller bias and variability at distance from coast larger than 1000 km, compared to v700.
- The temporal evolution of the biases on the period 2010-2021 is significantly reduced in v700 for the mid-latitudes and the LSC corrected SSS product. The improvement is particularly clear in the tropics and in the bay of Mexico, Gulf stream region and in the bands along south America and Africa (South of Equator) as well as south of Australia.
- There is nevertheless significant degradation at high latitudes in v700: in the Southern Ocean (south of $\sim 50^\circ$ S) and in north of $\sim 60^\circ$ N. The strong bias and its variability is related to ice transition areas and zones of ice/water contrast. These increases are found mainly in the Ascending orbits, whereas the bias variability for Descending orbits tends to decrease in v700 in high latitudes. The change of dielectric constant model leads to slightly more negative biases on ascending orbits but also to biases closer to 0 on descending orbits.
- Latitudinal seasonal biases have changed between v662 and v700. For Ascending orbits, a lower contrast is found between biases at mid latitude South and North, but biases are more negative in boreal summer. Latitudinal biases in this semi-orbit type have increased mainly due to the above mentioned Ice contamination in the South. For Descending orbits, positive biases are smaller in the South but have increased in the North. These patterns result in partial cancellation of these bias when combining Ascending and Descending orbits at global scale.
- With respect to in-situ SSS (Argo upper measurements), L2OS v700 is unbiased for Argo SSS > 31 pss. This is not the case for fresher Argo SSS values, where a larger negative bias appears correlated with Argo SSS freshening. This was not observed with v662.
- In terms of correlations with sea surface temperature, L2OS v700 is unbiased with Argo SST for SST $> 15^\circ$ C. Below 15° C, an increasing fresh bias is observed as SST decreases, reaching -2 pss (SMOS fresher than Argo) at SST $= -2^\circ$ C. Part of this change is likely attributable to an increased sea-ice transition contamination associated with Gibbs-2 correction applied on the SMOS L1 data and the new dielectric constant model. There is a net change in the bias pattern with respect v662.



in the lowest SST. L2OS v700-Argo SSS bias as a function of wind speed is very similar than with L2OS v662-Argo SSS but a bit reduced in the highest winds (at 20 m/s, it was ~ -1 pss with v662 and it is now ~ -0.6 pss with v700).

- Biases as a function for rain-rate and with respect distance to coasts are almost unchanged from v662 to v700.

In terms of noise at SSS level:

- L2OS v700 standard deviation with respect to in situ data is significantly more stable and is lower than v662 in most of the areas, but with the caveat of high latitudes, associated to the previously mentioned errors that are now larger in the transition from ice to sea. There is a special improvement in the Euro-Asian coast (typically affected by RFI), Equatorial regions and Arctic Ocean. In descending orbits, we also observe a general improvement in the Northern Hemisphere. In the Southern Ocean (especially in ascending passes) we observe a dipole pattern that shows the degradation in v700 at high southern latitudes but an improvement close to the ice-edge of the Antarctica continent.

Comparison of SMOS TBs with the Geophysical Radiative Transfer forward Model Function:

- For SSS uncorrected and both passes, there are clear increase of the standard deviation of the differences between the model and SMOS TB data for both T_x and T_y in a band extending ~ 500 kms from coastlines ($> 2K$). Linearized SSS retrievals exhibit a strongly underestimated (by 1-4 pss) SSS near coasts with respect to SMAP data. The underestimation is significantly higher at high latitudes.
- Retrieved SSS in both ascending and descending passes exhibit biases and dwell-line averaged first Stokes parameter that are significantly reduced with LSC correction compared with the uncorrected results. Moreover, the standard deviations of the individual T_x and T_y brightness temperatures at any given position on Earth are significantly reduced in the vicinity of the coastlines. This is true except north of $60^\circ N$ with a significant over-freshening of linearized SMOS SSS vs SMAP SSS. In descending passes, there is a smaller amplitude but clearly detectable bias showing successive negative and positive oscillations from $30^\circ S$ to $60^\circ S$.
- Impact of the use of SMAP SSS as opposed to ISAS SSS as the reference to evaluate the forward model has been assessed: SMOS Tb biases and standard deviations are similar except near river plumes where biases with respect to ISAS tend to be larger than with SMAP used as the reference (as expected).
- The uncorrected difference between ascending and descending pass biases exhibits distinct coastal shadows in both the retrieved SSS and first Stokes parameter bias maps. By contrast, the difference maps for the standard deviations show only very weak shadows, indicating that the increased Tb standard deviations in coastal areas exhibit only weak dependence on pass direction.
- The LSC LUT-corrected maps of ascending minus descending dT_b and SSS show virtually no shadows, suggesting that the LSC correction effectively reduces both the biases and Tb standard deviations.
- Finally, the analysis of the Ocean Target Transformation confirms the improved stability of L1c v724 SMOS TBs vs the previous baseline. Some long-term trends appear in the OTT information that require further study to be properly understood, to discriminate between instrumental drift or geophysical behaviour.



***SMOS ESL for SMOS Level 1 and Level 2
over Land, Ocean, and Ice
- L2OS 3rd Mission Reprocessing Report -***

Ref.: ARG-003-081

Date: 16.07.2021

Page: 21

2 Salinity global biases and uncertainties

2.1 Global validation vs ISAS

2.1.1 Methods

The ESL-agreed validation protocol has been applied to generate SMOS maps and compare them with In Situ Analysis System Salinity (ISAS) maps. The validation protocol data processing and associated analysis have been performed using the LSAT software developed at LOCEAN.

We recall below the main principles of the validation protocol (see more on https://smos.argans.co.uk/docs/technotes/SO-TN-ARG-GS-0116_Validation_Protocol_v1.0_20170217.pdf):

ISAS consists of an optimal interpolation of global salinity measured in situ, most of them being the entire data set of ARGO (Gaillard et al. 2016). The ISAS15 fields are used up to year 2015 (<https://www.seanoe.org/data/00412/52367/>), followed by the near-real-time data (http://marine.copernicus.eu/services-portfolio/access-to-products/?option=com_csw&view=details&product_id=INSITU_GLO_TS_OA_NRT_OBSERVATIONS_013_002_a). In most analysis, the variability criterion of less than 80% (PCTVAR < 80%) has been applied to filter the ISAS pixels where very small number of in situ measurements exist to constrain SSS variability.

SMOS L3OS monthly maps are built on a regular 0.25-degree grid. For each grid point, the returned salinity <SSS> is computed by means of a weighted average of the N L2 salinity retrievals falling in a temporal (1 month) and spatial (100 km x 100 km) bin [Yin et al. 2012].

Before averaging, a filtering strategy is applied to the salinity retrievals to discard those SSS values most probably affected by several types of noise sources or returned after a bad convergence of the retrieval algorithm.

Only salinity retrievals associated to an auxiliary 10-m ECMWF wind speed ranging from 3 to 12 m/s are kept as biases with respect to in situ data is known to be minimum in moderate wind conditions.

Furthermore, only SSS retrievals obtained from at least 130 brightness temperatures (TBs) falling inside the AF-FOV are considered (Dg_af_fov should be greater than 130, in the User Data Product). With the latter criteria, only retrievals at the centre of the satellite swath (within an across-track distance within +/- 350 km) are kept, where the error on the retrieved salinity is less than at the border of the swath.

The weight applied in the salinity average is equal to the inverse of the square of the equivalent footprint diameter R multiplied by the theoretical error σ . Weighting by the variance of the error is intended to put less weight onto pixels at the edge of the swath associated with larger uncertainties; the weight by the pixel size is because SMOS SSS are delivered over the oversampled ISEA grid at 15-km resolution, whereas the resolution of MIRAS TBs ranges from 30 to 100 km depending on the location within the swath. Nevertheless, over the selected central part of the swath, this weight has a small effect in most cases.

In terms of statistics, the mean differences are used to characterize the average bias, while the standard deviations (std) are used to characterize the difference variability. We have also used metrics that are more robust with respect to outliers: median differences for the average bias and mean absolute deviation (mad, equal to $\text{std} \times 0.67$ in case the statistical distribution is gaussian) for the difference variability.

2.1.2 Results

We first validate SMOS SSS far from coast, further than 1000km from coast and considering SSS without Tb correction related to land-sea contamination (SSS_uncorr). We first look at metrics over 45°N-45°S to avoid regions affected by ice-sea contamination.

Over descending orbits, 45°N-45°S, (Figure 1), seasonal variation of the mean differences is similar for both versions from 2011 to 2015. During this period, and especially during 2014-2015, most SSS in the northern hemisphere are filtered out by the L2OS quality flags. When SSS are not filtered out in the northern hemisphere, mean differences in northern latitudes in boreal winter are positive (instead of negative in v662) leading to positive overall mean difference. An example for December 2019 is presented on Figure 2. On another hand, it is remarkable that the standard deviation of the differences (Figure 1, right) systematically decreases meaning that the monthly differences maps are more homogeneous spatially. This is illustrated on Figure 3 for the month of October 2015.

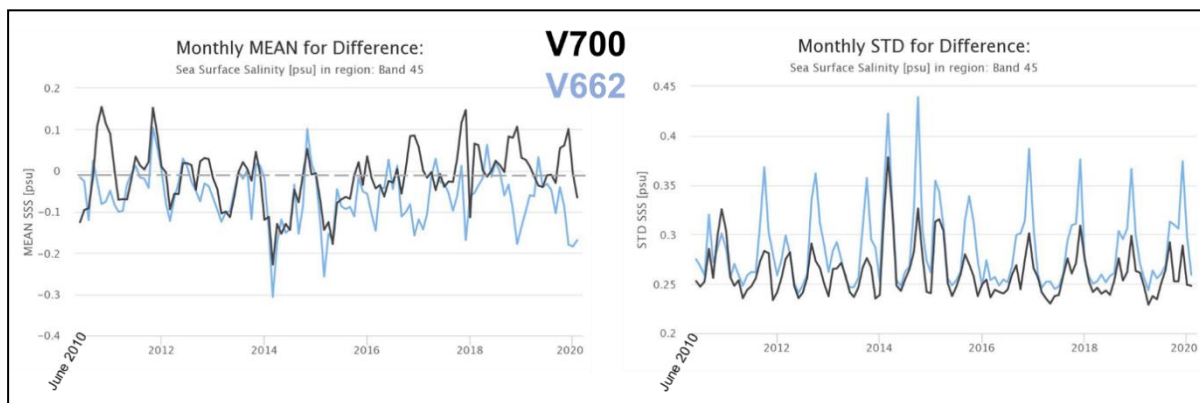


Figure 1: Mean difference of SMOS SSS minus ISAS SSS (left) and standard deviation of the difference (right) **farther than 1000km from coast. Descending orbits. 45°N-45°S. Only SMOS pixels with more than 50 measurements and only ISAS SSS with PCTVAR<80% have been retained. Blue: SMOS v662; Black: v700.**

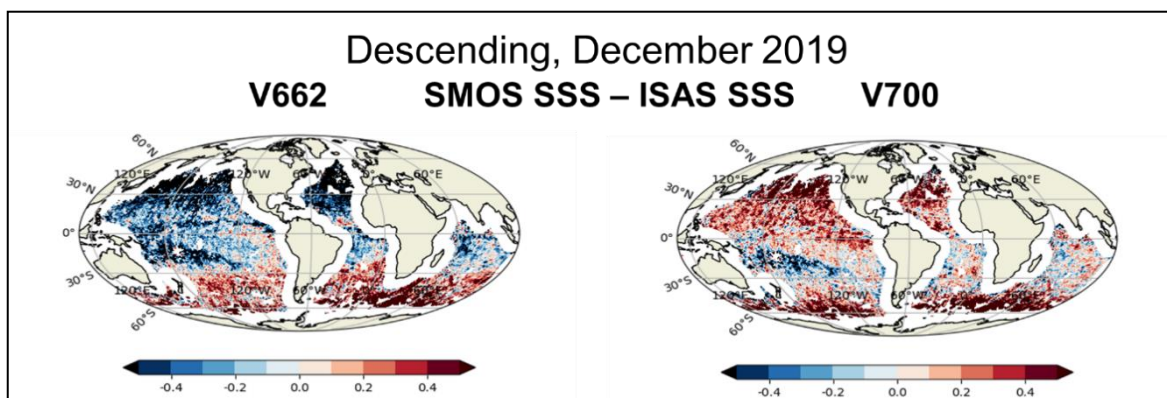


Figure 2: SMOS SSS minus ISAS SSS in December 2019, descending orbits (left) v662, (right) v700.

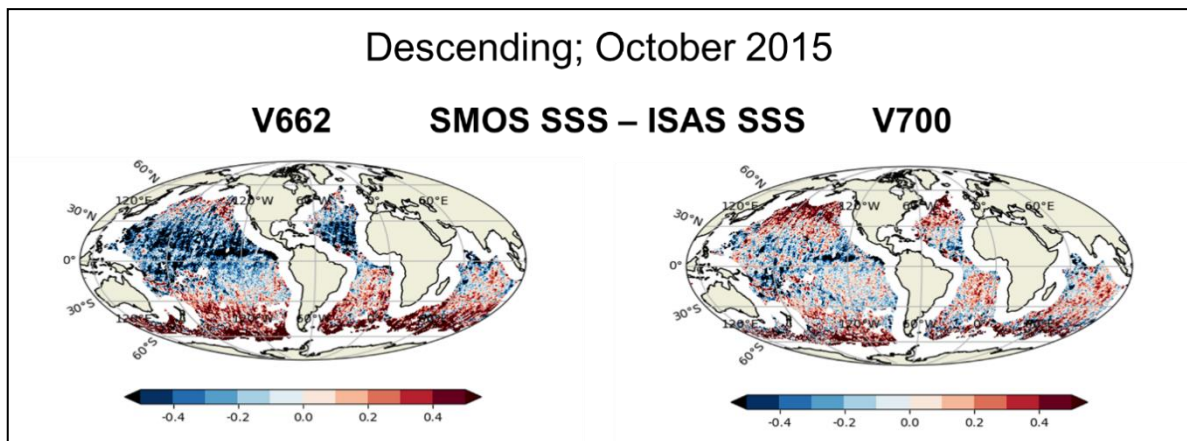


Figure 3: SMOS SSS minus ISAS SSS in October 2015, descending orbits (left) v662, (right) v700.

Over descending orbits, global ocean (Figure 4), the decrease of the std difference is even clearer due to the improvement in the modelling of the dielectric constant (see also section 7).

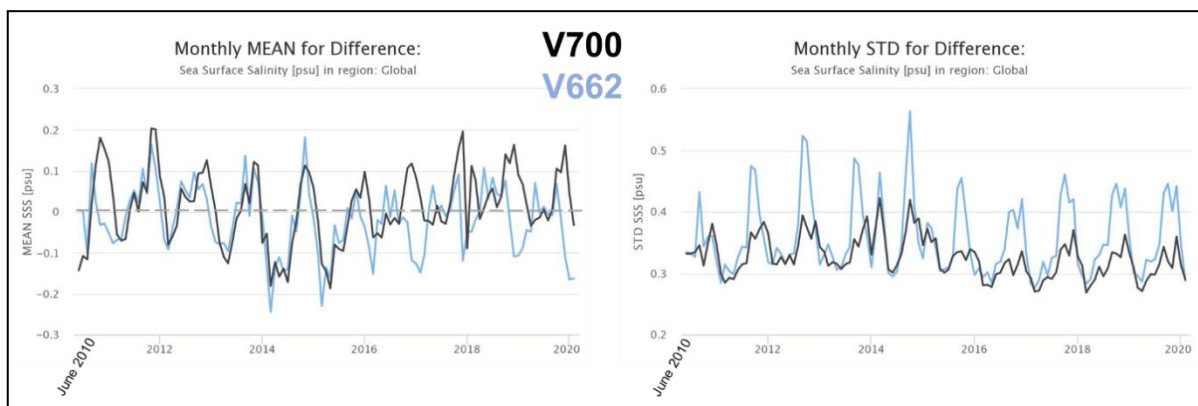


Figure 4: Mean difference of SMOS SSS minus ISAS SSS (left) and standard deviation of the difference (right) **farther than 1000km from coast. Descending orbits. Global Ocean.** Only SMOS pixels with more than 50 measurements and only ISAS SSS with PCTVAR<80% have been retained. Blue: SMOS v662; Black: v700.

Over ascending orbits, 45°N-45°S (Figure 5), overall negative difference in boreal summer (July-August) becomes slightly more negative, e.g. in August 2015 (Figure 6) due to more negative differences in the northern hemisphere. The standard deviation of the differences (Figure 5, right) decreases especially in April-May between 2012 and 2017. This is due to a decrease of the differences in the northern hemisphere as illustrated on Figure 7 for the month of May 2014.

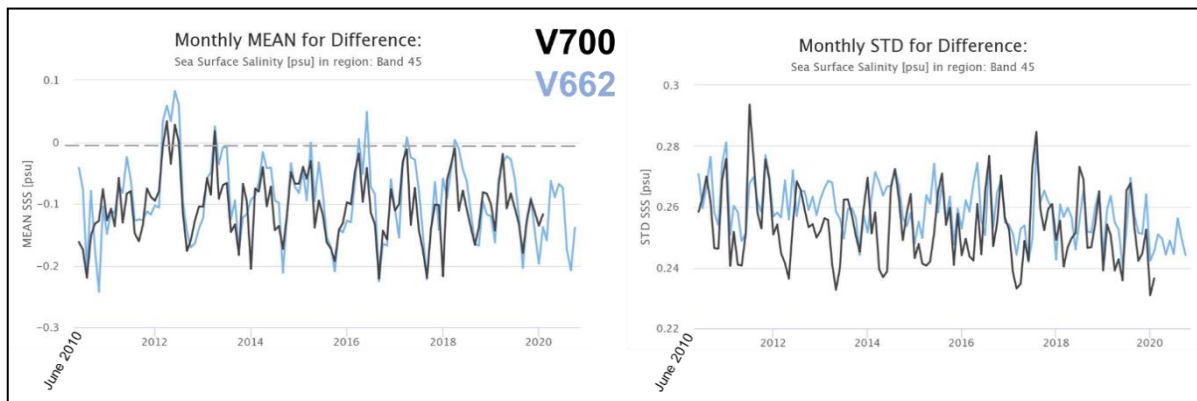


Figure 5: Mean difference of SMOS SSS minus ISAS SSS (left) and standard deviation of the difference (right) **farther than 1000km from coast. Ascending orbits. 45°N-45°S. Only SMOS pixels with more than 50 measurements and only ISAS SSS with PCTVAR<80% have been retained. Blue: SMOS v662; Black: v700.**

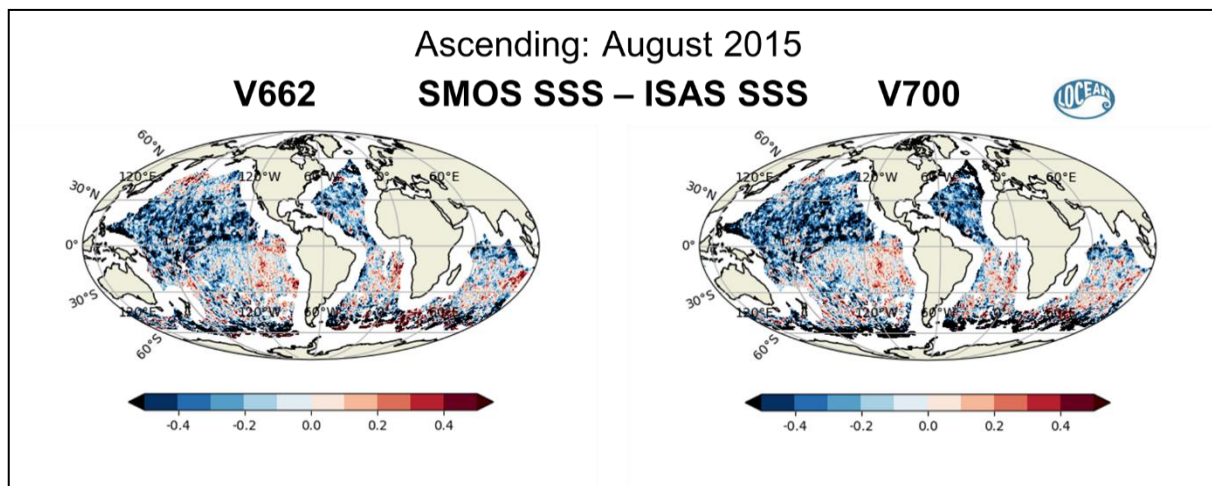


Figure 6: SMOS SSS minus ISAS SSS in August 2015, ascending orbits (left) v662, (right) v700.

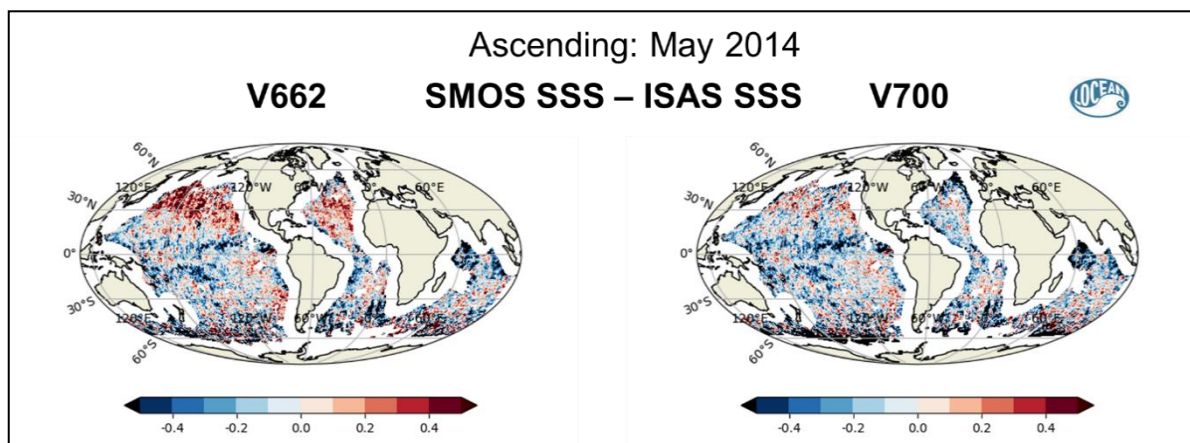


Figure 7: SMOS SSS minus ISAS SSS in May 2014, Ascending orbits (left) v662, (right) v700.

Over ascending orbits, global ocean (Figure 8), we observe a huge increase of the standard deviation of the difference due to the increase of ice-sea contamination.

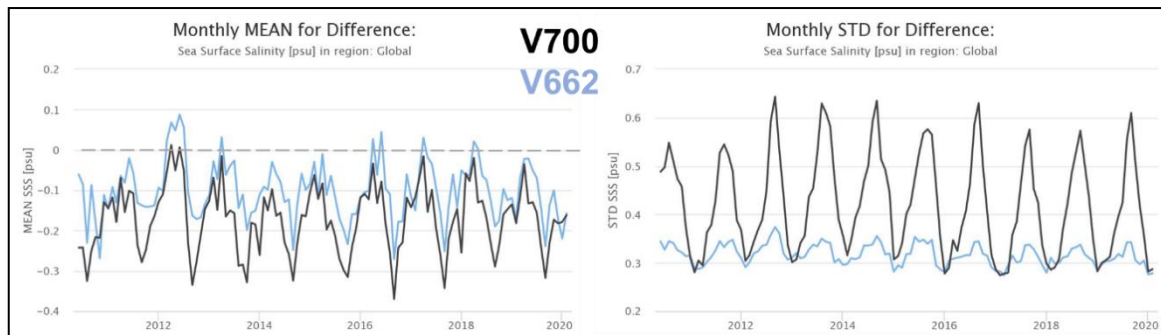


Figure 8: Mean difference of SMOS SSS minus ISAS SSS (left) and standard deviation of the difference (right) farther than 1000km from coast. Ascending orbits. Global Ocean. Only SMOS pixels with more than 50 measurements and only ISAS SSS with PCTVAR<80% have been retained. Blue: SMOS v662; Black: v700.

In summary, when combining ascending and descending orbits, at mid latitudes farther than 1000km from coasts (Figure 9), while SMOS minus ISAS SSS difference still shows some seasonal variations, especially before 2017, there is a clear reduction of the standard deviation of the differences with v700 showing that differences with v700 are more spatially homogeneous in mid latitudes (see also section 4.1).

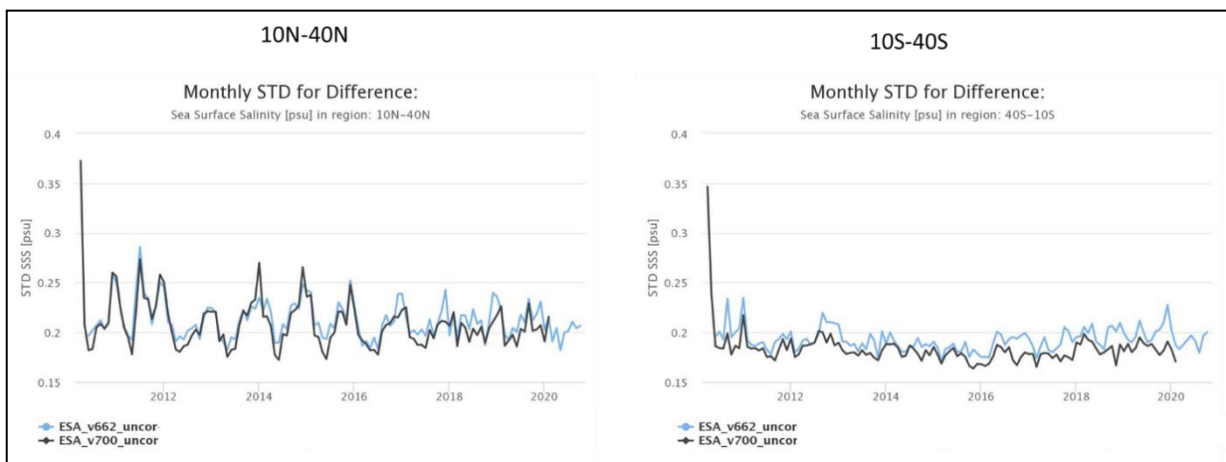


Figure 9: Standard deviation of SMOS SSS minus ISAS SSS farther than 1000km from coast. Ascending orbits for 10°N-40°N (left) and 10°S-40°S (right). Only SMOS pixels with more than 50 measurements and only ISAS SSS with PCTVAR<80% have been retained.

At less than 1000km from coast, before adding the empirical correction for land-sea contamination, the land-sea contamination creates more negative biases on SMOS minus ISAS SSS difference (Figure 10 & Figure 11). This indicates that even though these biases are better corrected with an empirical correction depending on the measurement geometry in V700 (because they are more stable for a given geometry as will be described later), when merging all geometries before the correction, as it is done when SSS monthly maps are created according to the validation protocol, these biases are larger in absolute value and more variable from one geometry to another. These larger land-sea contamination biases are of the same order of magnitude as the ice-sea contamination biases observed in the Southern Ocean in ascending orbits.

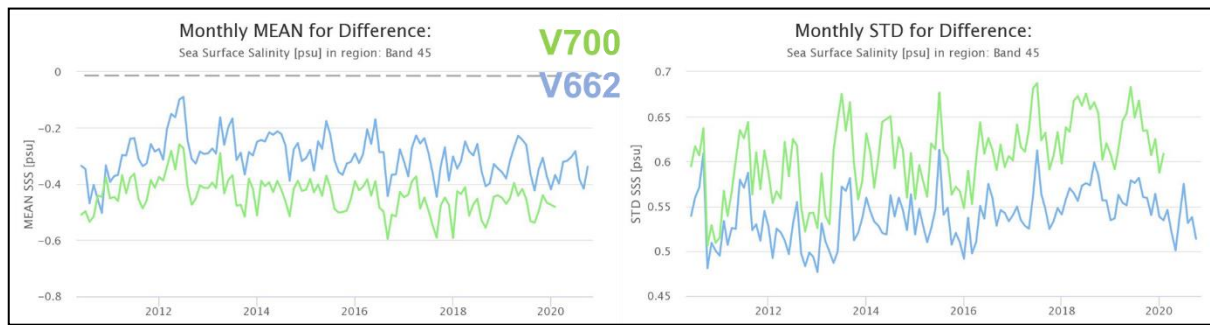


Figure 10: Mean difference of SMOS SSS minus ISAS SSS (left) and standard deviation of the difference (right) at less than 1000km from coast. Ascending orbits. 45°N-45°S. Only SMOS pixels with more than 50 measurements and only ISAS SSS with PCTVAR<80% have been retained. Blue: SMOS v662; Green: v700.



Figure 11: Mean difference of SMOS SSS minus ISAS SSS (left) and standard deviation of the difference (right) at less than 1000km from coast. Descending orbits. 45°N-45°S. Only SMOS pixels with more than 50 measurements and only ISAS SSS with PCTVAR<80% have been retained. Blue: SMOS v662; Green: v700.

Concerning SSS_{corr} (i.e., retrieved after correcting Tb from land-sea contamination), at a distance less than 1000km from coasts (Dcoast), global mean differences are larger in v700 (-0.14 vs 0 pss). The global std (difference) is slightly larger (0.55 vs 0.47 pss, on average) and manifests pronounced peaks, e.g., in the fall of 2017, 2018, 2020 (Figure 12).

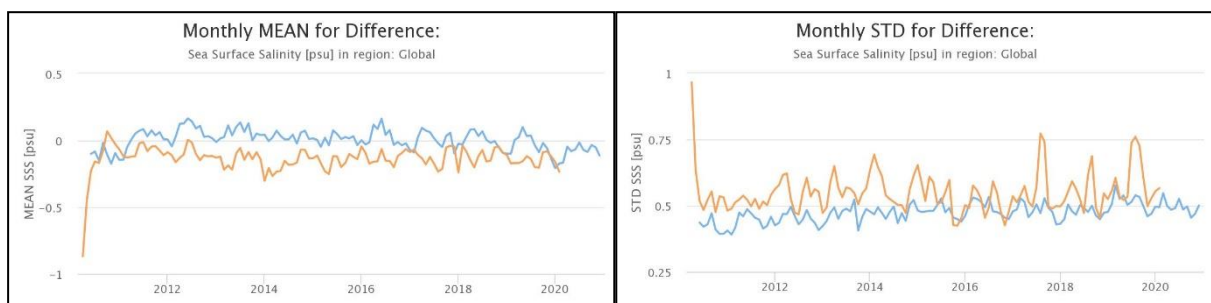


Figure 12: Time series of the monthly mean (left) and monthly std (right) of the differences between SMOS and ISAS, for Global, Asc+Desc orbits. Blue curves: v662, orange curves: v700.

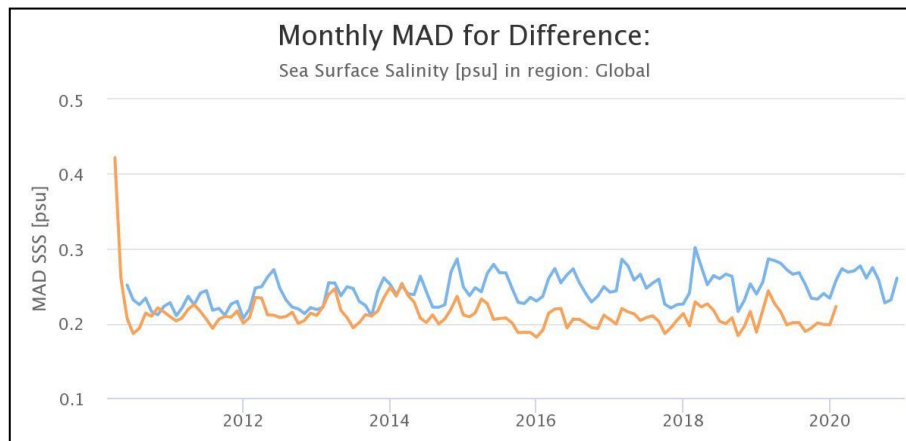


Figure 13: Time series of the monthly MAD of the differences between SMOS and ISAS, for **Global, Asc+Desc orbits**. Blue curves: v662, orange curves: v700.



Figure 14: Time series of the monthly mean (upper left), monthly std (upper right), and monthly MAD (lower) of the differences between SMOS and ISAS, for **Global, Descending orbits only**. Blue - v662, green - v700.

Considering the outlier-robust metrics, the global MAD (median absolute difference, equal to $\text{std} \cdot 0.67$ if the statistical distribution is gaussian) is smaller in v700, and the difference v700-v662 increases after 2015 (Figure 13). So, when considering the outlier-robust metrics for difference variability, the v700 does show a better performance (especially after 2015), while in terms of the usual $\text{std}(\text{diff})$ metrics the difference variability is larger in v700 when considering the whole (global) dataset.

When considering only Ascending orbits, the results are like those for both orbits (A+D), except that the MAD(Diff) time series show more stable behaviour, without a pronounced increase in the differences between the two versions after 2015.

When considering Descending orbits only (Figure 14), the mean biases are similar for the two versions, both in terms of the mean and median difference. However, the STD (diff) is larger for v700: 0.63 vs 0.53 for the means, but with pronounced seasonal peaks in v700 sometimes exceeding 0.9 psu. As for the MAD

series, the differences between the two versions become greater after 2015, with v700 showing smaller values.

When looking at the 45°S-45°N band, the mean biases are similar between the two versions (Figure 15). The time means are -0.06 pss for v700 and 0.00 (mean) and -0.03 (median) for v662. The biases are slightly negative in v700, while for v662 they are positive most of the time and become negative after 2018. In this regard v700 shows slightly more stable mean biases over time. The difference variability is reduced in v700 in terms of both std(diff) and also the outlier-robust MAD metrics. This reduction in v700 is more pronounced in terms of MAD and increases after 2015.

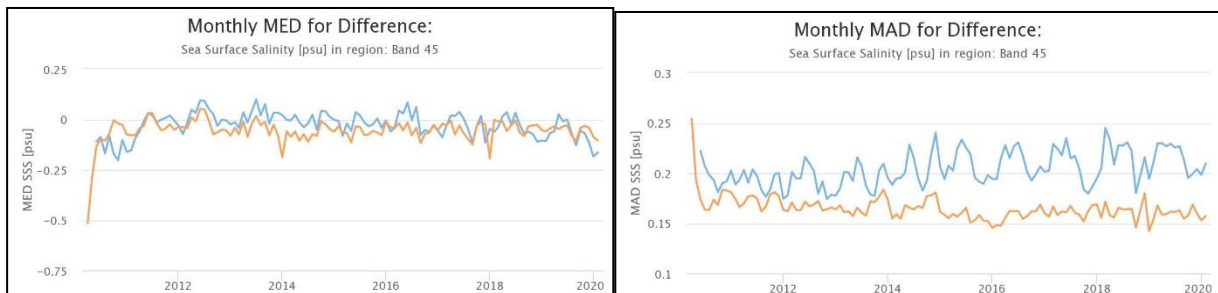


Figure 15: Time series of the monthly median (left) and monthly MAD (right) of the differences between SMOS and ISAS, for 45°S-45°N, Asc+Desc orbits. Blue - v662, orange - v700.

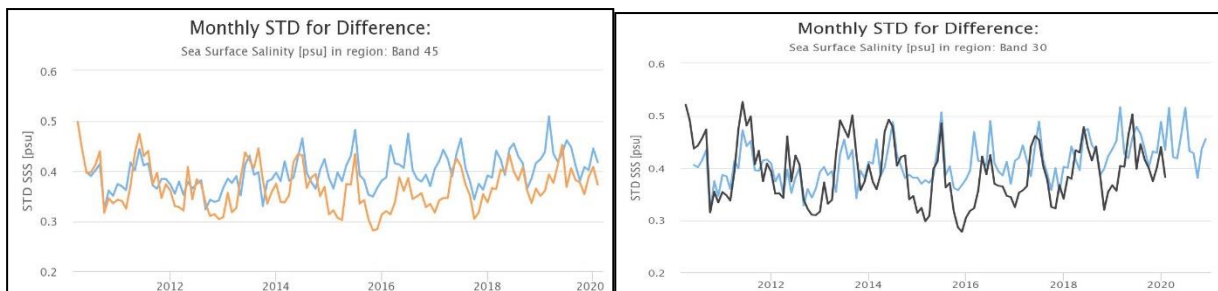


Figure 16: Time series of the monthly std(diff) for the 45°S-45°N band (left) and for the 30°S-30°N band (right) for Asc+Desc orbits. Blue curves - v662, orange (left) and black (right) - v700.

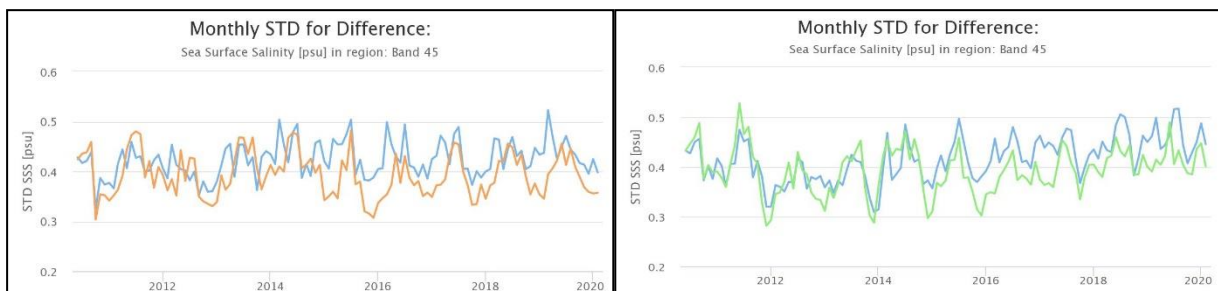


Figure 17: Time series of the monthly std(diff) for the 45°S-45°N band for Ascending (left) and Descending (right) orbits. Blue curves - v662, orange (left) and green (right) - v700.

Focusing still more on the tropical region (the 30°S-30°N band), the results reveal that the differences between the v662 and v700 products increase after 2015 also in terms of the std(diff). The time means of the std(diff) are close: 0.41 vs 0.39 psu, while strong minima corresponding to the std(diff) improvement occur for v700 after 2015 and are absent for v662 (Figure 16).

Looking at Ascending and Descending orbits separately shows similar behaviour as for both orbits (A+D) for the tropics (for both 30°S-30°N and 45°S-45°N bands, Figure 17).

In the high latitudes v700 shows much higher bias and variability, in terms of both mean(diff) and std(diff) and outlier-robust metrics median and MAD(diff). These large differences come from Ascending orbits (Figure 18, left panels), where the time-mean negative bias (mean(diff)) is more than the 3 times greater for v700 (-0.83 vs -0.27 psu), and the difference variability is 2 times larger for v700 in terms of std(diff): 1.23 vs 0.59 psu.

These are presumably related to ice areas and zones of ice/water contrast and come from the Ascending orbits only. For Descending orbits only (Figure 18, right panels), the mean biases are much closer between the two product versions (time-mean med(diff) is -0.04 psu for v662 vs 0.11 psu for v700 over the 70-40S band), while the std(diff) and MAD(diff) are smaller for v700 (time-mean std(diff) is 0.62 psu for v662 vs 0.56 psu for v700).

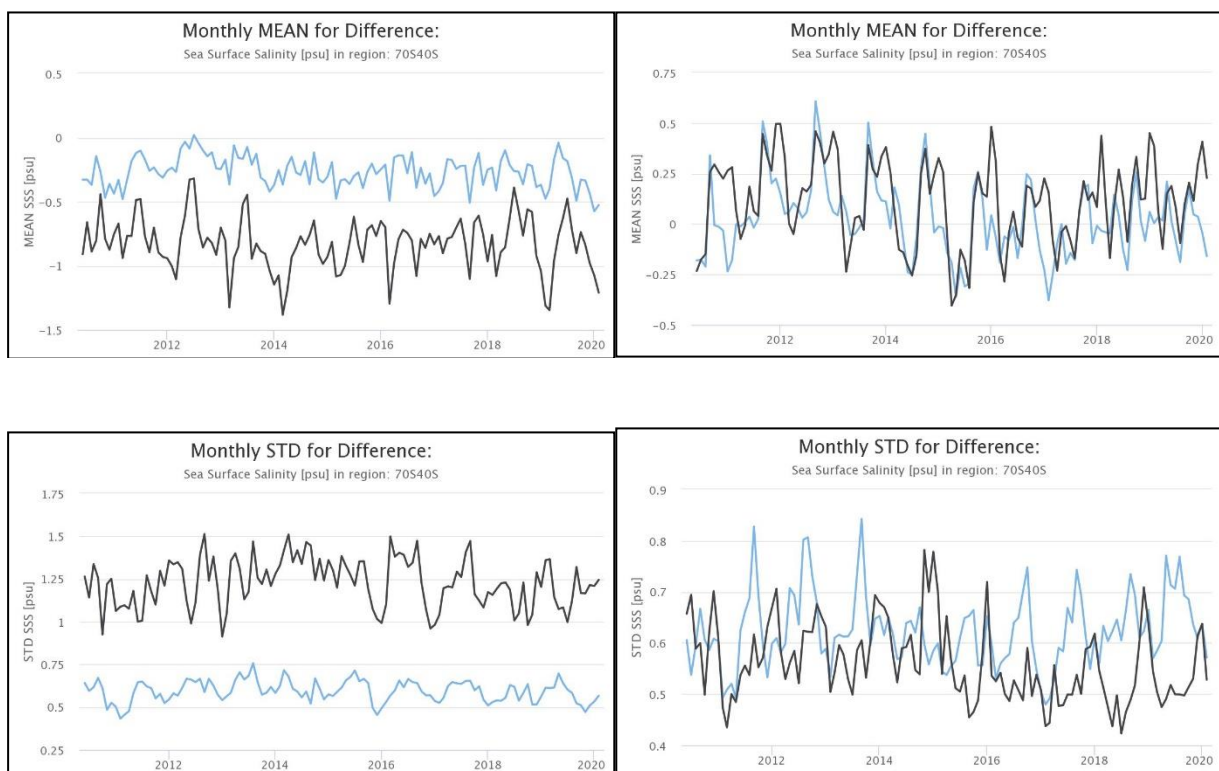


Figure 18: Time series of the monthly mean(diff) (upper panels) and std(diff) (lower panels) for the 70-40°S band for Ascending (left) and Descending (right) orbits. Blue curves - v662, black (right) - v700.

In summary, concerning SSS at less than 1000km from coast:

- Global performance in the "coastal" areas (Dcoast < 1000 km) for the coastal-corrected products (SSS_corr) is only slightly improved in terms of the MAD(Diff) metrics in the 700 version, but is degraded in terms of std (diff).
- Excluding the high latitudes, the bias becomes more stable, and the difference variability is smaller in v700.
- The strong bias and variability come from the high latitudes, probably due to ice areas and zones of ice/water contrast. These increases are related to the Ascending orbits, whereas the difference variability for Descending orbits tends to decrease in v700 at high latitudes.

- For coastal-uncorrected products, the v662 shows considerably smaller bias and variability at Dcoast < 1000 km, compared to v700.

2.2 Global validation vs punctual ARGO

2.2.1 Methods

In this section we analysed nine years (2011-2019) of the Land-Sea Corrected SSS salinity field (SSS1 in the UDP, i.e. SSS_corr). We compared the performance of both versions v662 and v700. Some considerations apply:

1. In this analysis, the first ten days in 2014 and 2018 for the v700 product are corrupted. This is not an issue of the final product.
2. The year 2017 for the product v662 is missing in the BEC repository, so it is not used in the analysis below.

Before collocating the SMOS SSS with the salinity provided by Argo (Argo SSS) we process the L2OS UDP as follows:

1. We filter the SSS retrievals according to the filtering criteria described in Table 1.
2. We re-grid the data into a regular latitude and longitude grid of 0.25°x0.25°.
3. We accumulate the retrievals in 9-day maps. For this we simply average the filtered L2 SSS retrieved in the 9 days in each cell of the regular grid.
4. With this, we compute 9-day maps for ascending, descending, and ascending and descending satellite overpasses together.

Table 1: Filtering criteria applied to the L2 SSS product. We discard the SSS retrievals when they meet one or more of the following conditions.

<i>Geophysical Filters</i>
<ul style="list-style-type: none"> • More than 50% of TB measurements used for the retrieval are contaminated by ice. • The rain rate at the retrieval grid point is greater than 0.01 mm/h. • More than 20% of the TB measurements used in the retrieval are outliers. • More than 10% of the TB measurements used in the retrieval are contaminated by sun glint or moon glint. • The retrieval is performed with less than 30 valid TB measurements. • The wind speed at the retrieval grid point is larger than 12 m/s. • More than 33% of the TB measurements used in the retrieval are flagged as RFI outliers.
<i>Retrieval Filters</i>
<ul style="list-style-type: none"> • Error in iterative scheme happens. • The resulting retrieved SSS is larger than 42 psu. • The resulting retrieved SSS is negative. • The resulting theoretical SSS uncertainty is larger than 5 psu. • The resulting Chi2_P parameter is larger than 95 % or lower than 5%. • The number of required iterations is larger or equal to 20. • The increment in iterative scheme is larger than 100.

- The number of measurements is lower than 16.

Geometrical Filters

- We discard systematically all the SSS retrievals farther than +/- 360 km to the satellite centre of the track.

We temporally and spatially collocate the Argo SSS [Argo] with the SMOS SSS 9-day maps as follows: every map is compared with the Argo SSS available during the same 9-day period used in the generation of that map. We compare the Argo SSS with the value of the SSS product corresponding to the cell where the Argo buoy is located. Before computing the matchups between Argo and SSS product, we apply the following quality control over the values of Argo SSS:

1. The cut-off depth for Argo profiles is between 5 and 10 m.
2. Profiles from BioArgo and those included in the grey list (i.e., floats which may have problems with one or more sensors) are discarded.
3. We use WOA2013 as an indicator: Argo float profiles with anomalies larger than 10°C in temperature or 5 psu in salinity when compared to WOA2013 are discarded.
4. Only profiles having temperature close to surface between -2.5 and 40°C and salinity between 2 and 41 psu are used.

Note: on the following plots, when referring to v699 it is intended the L2OS official v700.

2.2.2 Spatial distribution of the biases

In order to assess the spatial distributions of the biases we first accumulate all the SMOS and Argo SSS acquired during the years 2011-2016 and 2018-2019 in latitude x longitude cells of 5x5°. Figure 19 represents the mean differences between SMOS and Argo SSS at each 5x5° cell when the SMOS SSS maps are computed by using ascending and descending satellite overpasses together.

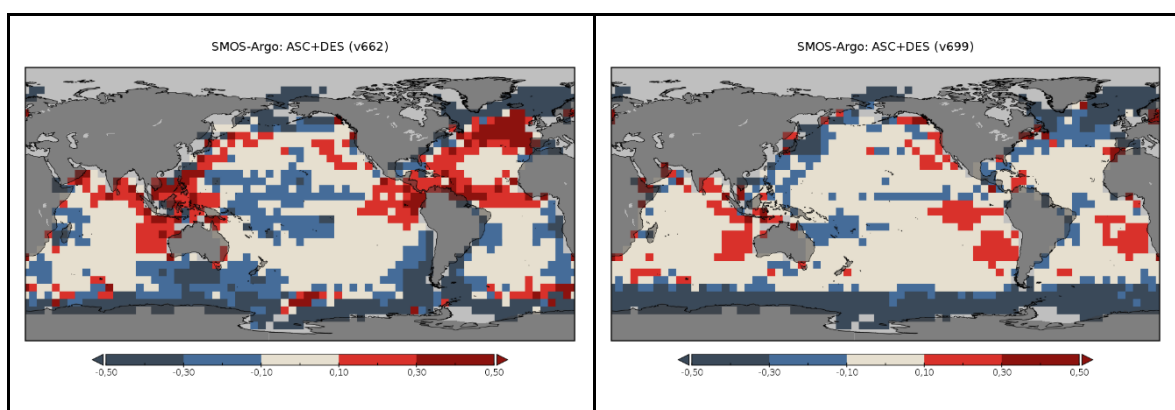


Figure 19: Mean differences between SMOS and Argo SSS for ascending and descending satellite overpasses: Left: Differences correspond to SMOS SSS v662; Right: Differences correspond to SMOS SSS v700.

We observe an improvement of the biases in the new V700 especially in the mid-latitudes. Equatorial and North west Atlantic where the v662 presented positive biases have been significantly reduced in v700. There is also an improvement in the south of the Australian coast where the negative bias present in v662 is significantly reduced in v700. There are some regions where we observe that biases in both versions

have opposite signs. This is the case of the Pacific coast of South America and the Coast of China. In the Southern Ocean and North Atlantic, the biases in v700 become more negative.

In the case of the performance for the ascending orbits, Figure 20 shows that in the Northern Hemisphere there is a change of the bias sign. While in v662 the predominant biases in the Northern Hemisphere are positive, the v700 present predominant negative biases in this region. We also observe a change in the bias sign in the Pacific coast of South America (that is also present when considering ascending and descending orbits together, Figure 19). Regarding Polar regions, while v662 presents changes in the bias sign, v700 presents significant negative biases in both Polar regions.

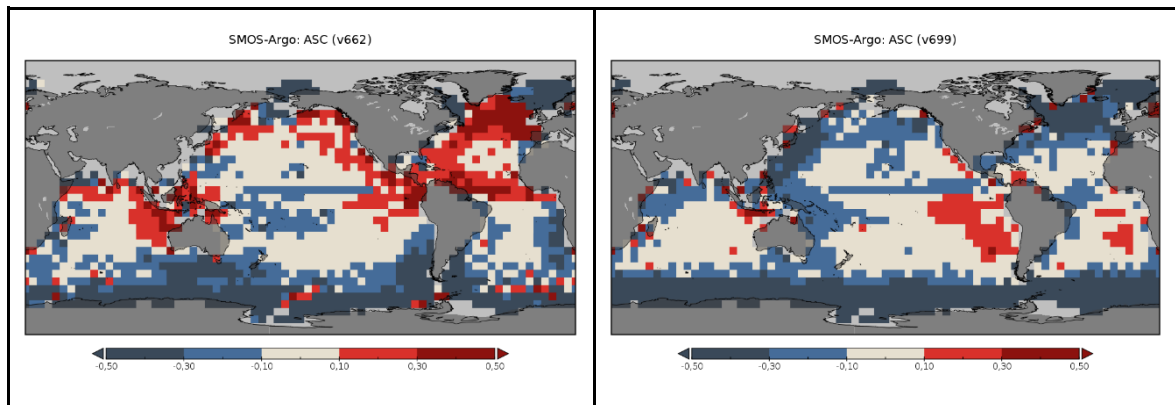


Figure 20: Mean differences between SMOS and Argo SSS for ascending satellite overpasses: Left: Differences correspond to SMOS SSS v662; Right: Differences correspond to SMOS SSS v700.

In the case of descending orbits, Figure 21 shows that while v662 presents different bias signs in different regions - negative biases in the North Pacific, Southern Australia and South America coasts, and positive biases in the North Atlantic and close to the whole Euro-Asian continent - v700 presents predominant positive biases almost everywhere except for the Arctic Ocean and very close to the ice edge of the Antarctica continent.

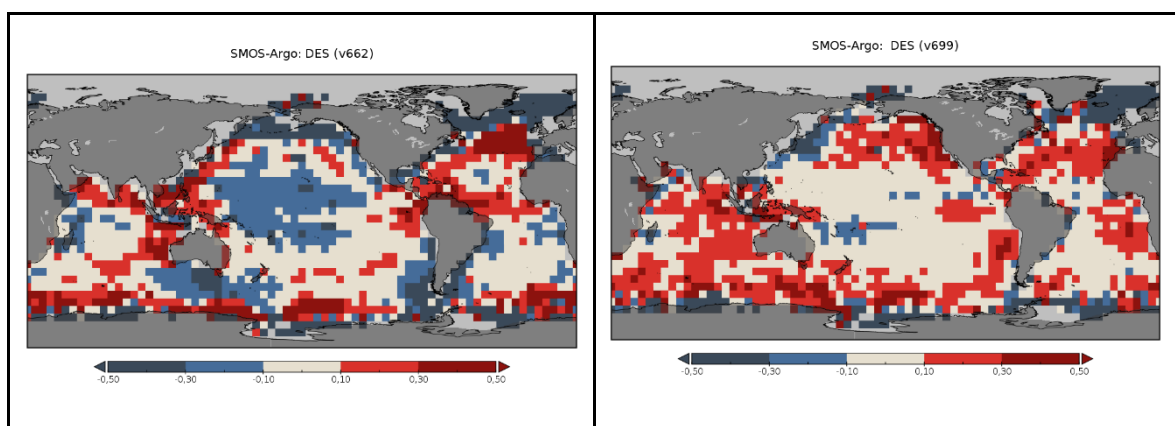


Figure 21: Mean differences between SMOS and Argo SSS for descending satellite overpasses: Left: Differences correspond to SMOS SSS v662; Right: Differences correspond to SMOS SSS v700.

Afterwards, we computed the averaged difference between SMOS and Argo SSS in latitudinal bands of 5 degrees in a range of 60°S-60°N latitudes (so polar regions excluded). Figure 22 (left) shows that the latitudinal biases in the case of considering together ascending and descending orbits are small for both

v662 (clear pink) and v700 (purple) and similar between them except for moderate southern latitudes where v662 performs worse than v700 (v662 has significant negative biases) and latitudes lower than 55° where v700 performs worse than v662 (v700 presents negative biases lower than -0.2 psu). Notice that Figure 19 shows that in the Northern Hemisphere v662 presents positive biases in the North Atlantic and negative biases in the North Pacific, therefore compensation between positive and negative biases could lead to spurious small biases in the Northern Hemisphere for v662.

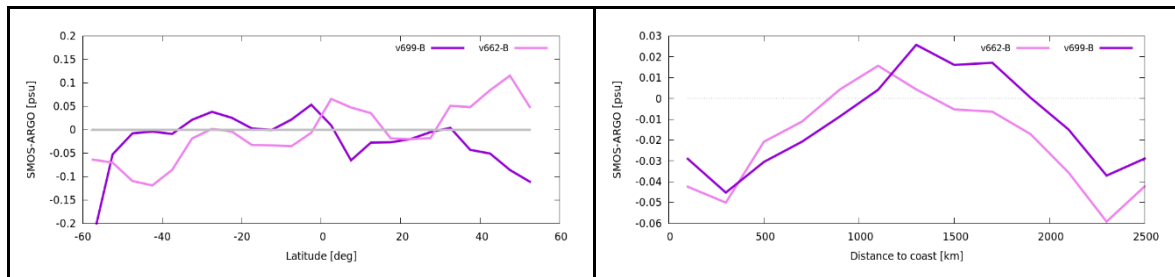


Figure 22: Left: Latitudinal averaged SMOS-Argo SSS differences for ascending and descending together. The plot only represents the biases in the range of 60°S-60°N of latitudes. Right: Averaged SMOS-Argo SSS differences as function of the distance to the coast.

Figure 23 (left) shows that the latitudinal gradient present in the ascending orbits of v662 (-sky blue line-negative biases in southern latitudes and positive biases in the northern latitudes) disappears in the ascending orbits of v700 (dark blue line) leading to a general negative bias. In the Southern Hemisphere the performance of the v700 is better (in absolute values, biases in v700 are lower than biases in v662). However, in latitudes lower than 55°S the performance of the v700 becomes worse than the one of v662. In the Northern Hemisphere the performance of v700 is worse than the one of v662.

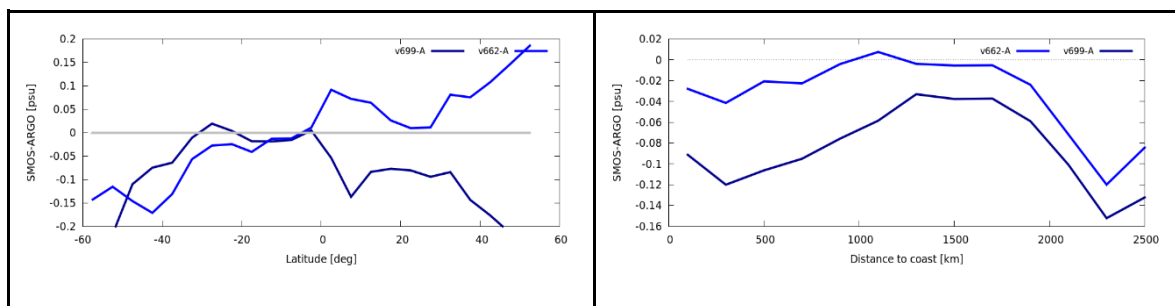


Figure 23: Left: Latitudinal averaged SMOS-Argo SSS differences for ascending orbits. The plot only represents the biases in the range of 60°S-60°N of latitudes. Right: Averaged SMOS-Argo SSS differences as function of the distance to the coast.

Regarding descending orbits, Figure 24 (left) shows that biases in v662 (sky green line) oscillate between positive and negative. Here, as for the case of ascending and descending together, we must consider that as shown in Figure 21, for a same latitudinal band, v662 presents negative and positive biases that in this computation compensate one with the others leading to spurious small biases. On the contrary descending orbits in v700 present a predominant positive bias. In terms of the comparison of performances, in this range of latitudes, the performance of both versions is similar, being better one of them for some latitudes and the other one for others.

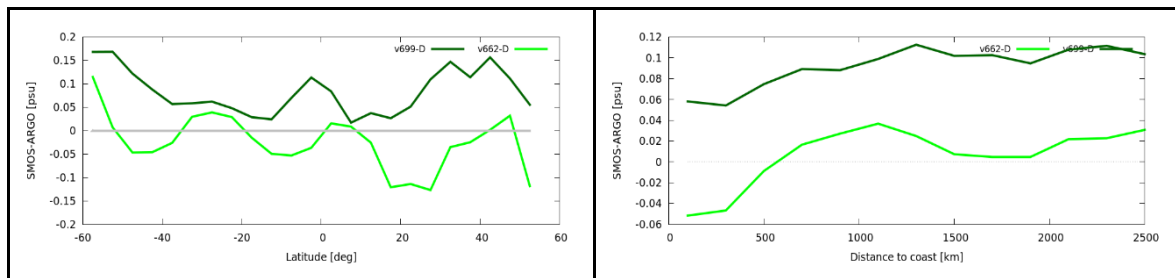
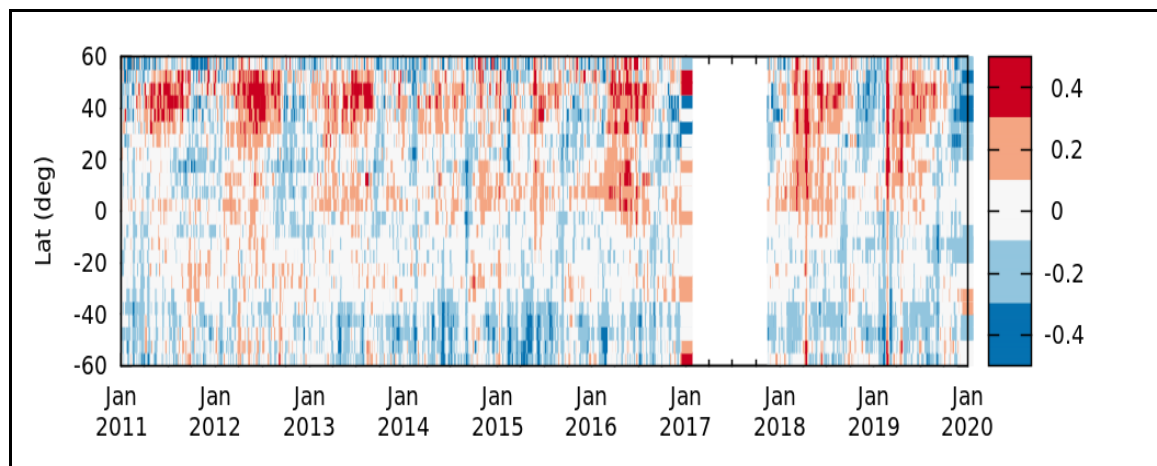


Figure 24: Left: Latitudinal averaged SMOS-Argo SSS differences for descending orbits. The plot only represents the biases in the range of 60°S-60°N of latitudes. Right: Averaged SMOS-Argo SSS differences as function of the distance to the coast.

We also analyse the averaged differences between SMOS and Argo SSS in bands of 200km distance to the coast. For this, we only consider the range of latitudes between 60°S and 60°N, so polar regions are excluded in this analysis. Figure 22 (right) shows that the averaged differences of v662 (light pink) and v700 (purple) are in both cases small and very similar between them. The performance of v700 is worse than the one of v662 when we consider ascending (Figure 23, right) and descending (Figure 24, right) separately. As above mentioned, this metric is favouring v662 that presents, for the same 200km-band positive and negative biases which leads to spurious averaged almost null bias.

2.2.3 Temporal evolution of the biases

The temporal evolution of the biases is analysed in this section by using Hovmöller diagrams as follows. For every SMOS SSS 9-day map, the differences of the available SMOS Argo collocations are averaged in latitudinal bands of 5 degrees. Figure 25 (below) shows the temporal evolution (x-axis) of the latitudinal biases for v662 (top plot) and v700 (bottom plots) in the case of considering ascending and descending satellite overpasses together. In the Northern Hemisphere the positive biases in v662 become negative biases in v700. In the southern latitudes v700 presents larger negative biases than v662. The same happens in ascending orbits (Figure 26). In this case positive biases of v662 in the Northern Hemisphere are more positive than when considering together ascending and descending, and the negative ones in the ascending orbits of v700 are more negative than those of v700 by considering together ascending and descending. Regarding descending orbits, Figure 27 shows that although there is still a clear seasonal behaviour of the biases (also present in ascending orbits), the biases in v700 are predominantly positive while in v662 there are more changes in the sign of the bias.



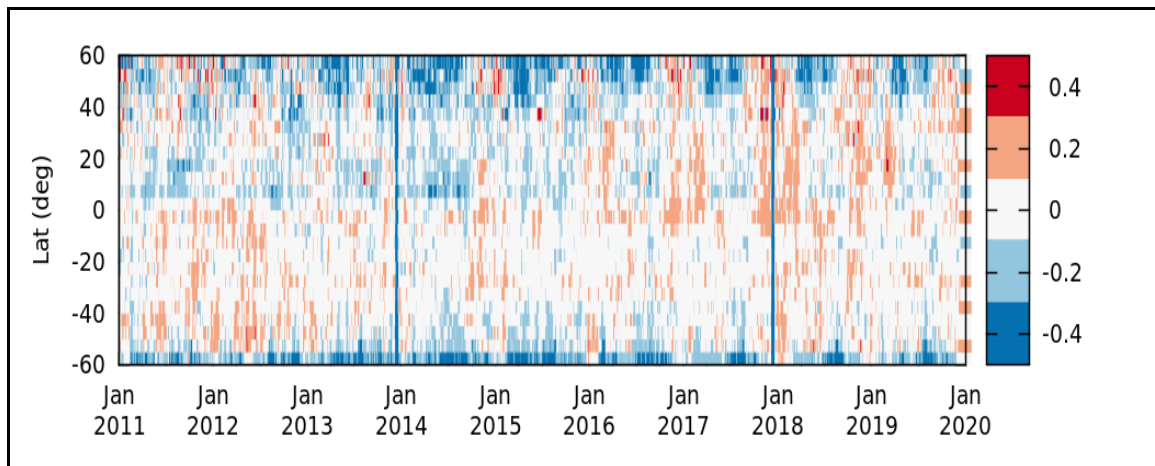


Figure 25: Hovmöller plots representing the temporal evolution (x-axis) of the averaged difference between SMOS and Argo in latitudinal bands of 5 degrees (y-axis) for ascending and descending satellite overpasses together. Top: Hovmöller diagram for v662. Bottom Hovmöller diagram for v700.

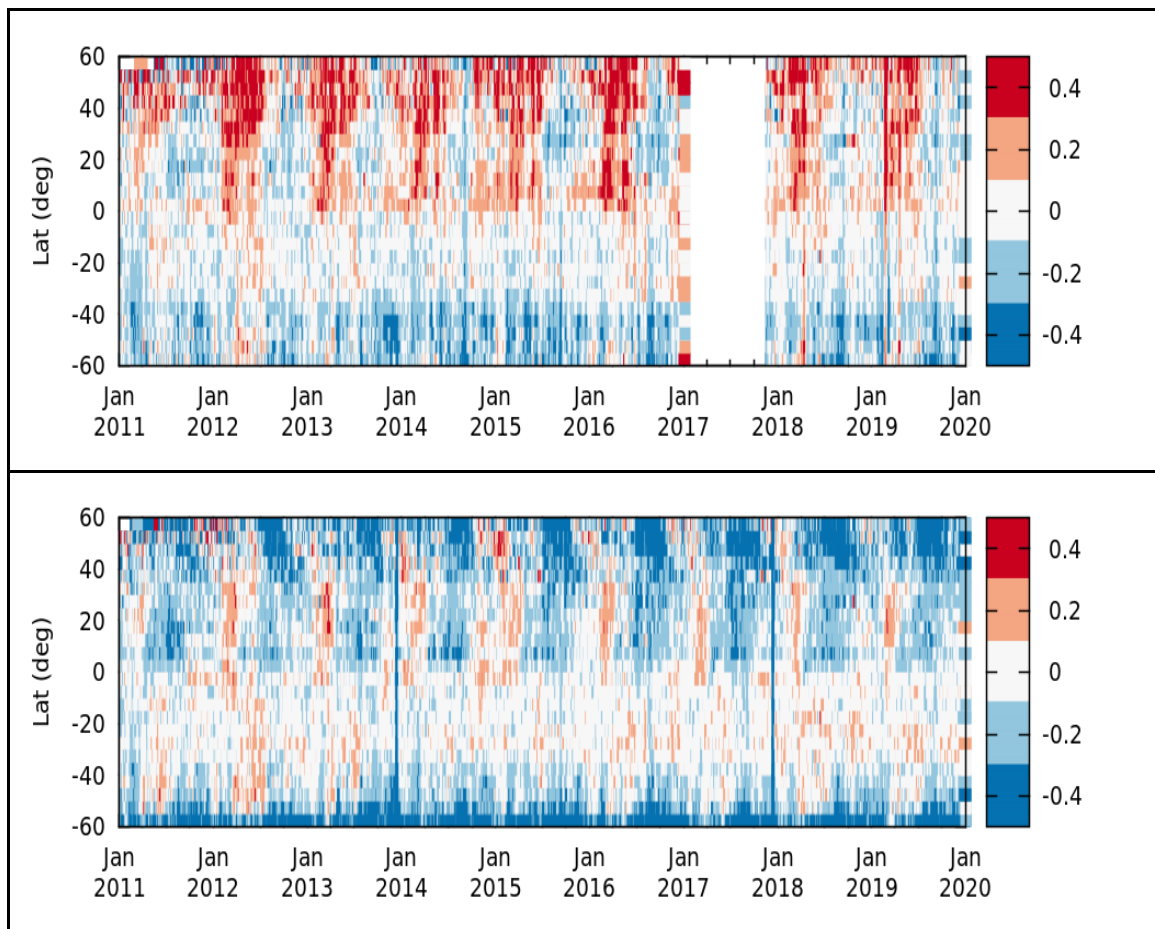


Figure 26: Hovmöller plots representing the temporal evolution (x-axis) of the averaged difference between SMOS and Argo in latitudinal bands of 5 degrees (y-axis) for ascending satellite overpasses. Top: Hovmöller diagram for v662. Bottom Hovmöller diagram for v700.

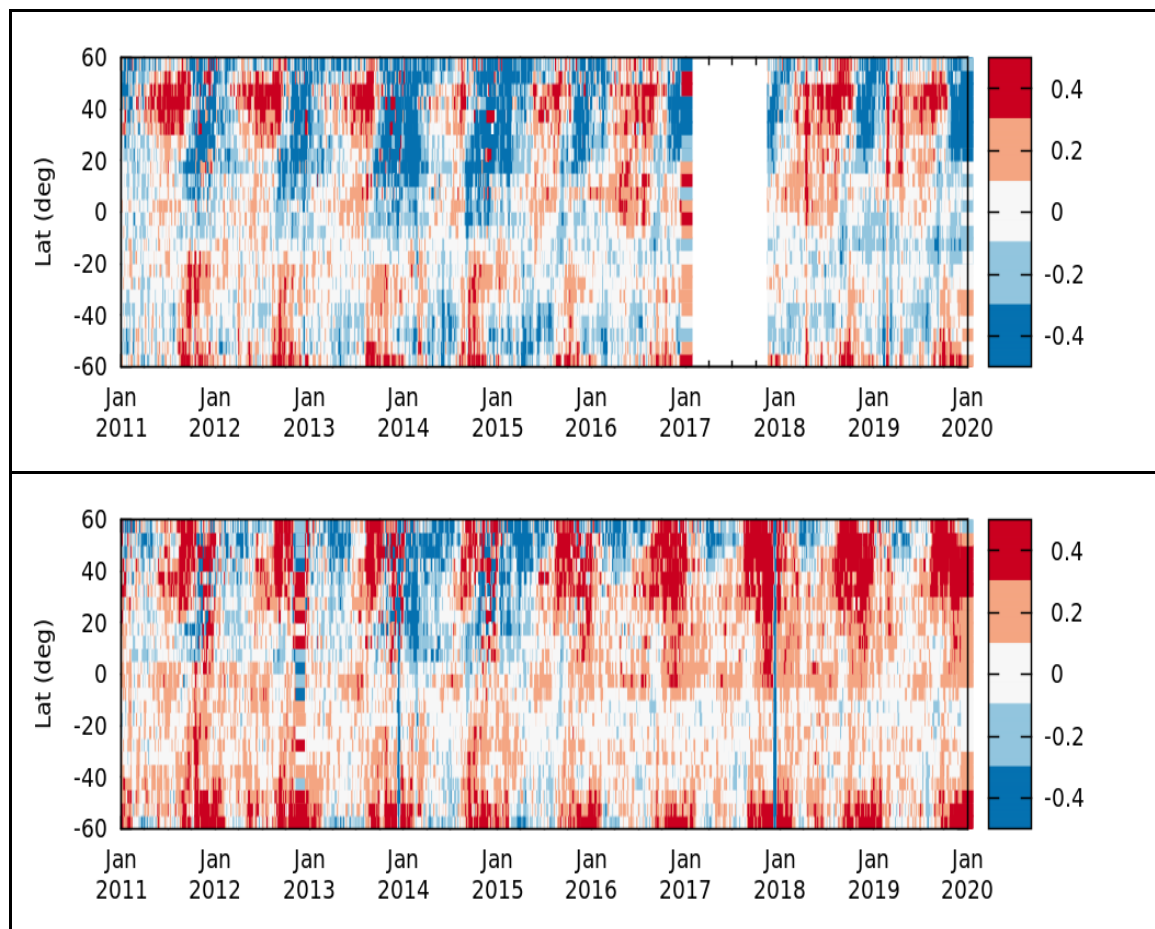


Figure 27: Hovmöller plots representing the temporal evolution (x-axis) of the averaged difference between SMOS and Argo in latitudinal bands of 5 degrees (y-axis) for descending satellite overpasses. Top: Hovmöller diagram for v662. Bottom Hovmöller diagram for v700.

We analysed as well the temporal evolution of the latitudinal gradient by computing per each 9-day period the linear regression coefficient of the differences between SMOS and Argo as function of the latitude (i.e., the linear regression coefficient per each vertical line of the Hovmöller plots in Figure 25 to Figure 27), such that positive linear regression coefficients mean that the biases in the northern hemisphere are more positive than the ones in the southern hemisphere. The latitude range in the computation is 60°S-60°N. The temporal evolution of the latitudinal gradient in v662 for ascending orbits (Figure 28, top left plot, sky blue) is predominantly positive while in v700 (dark blue) the latitudinal gradient changes seasonally. The amplitude of variation of the latitudinal gradient is similar in both versions. For descending orbits (Figure 28, top right plot) the range of variation of the latitude gradient in v662 (light green) is larger than in v700 (dark green). When we consider together ascending and descending orbits (Figure 28, bottom plot), although for some specific dates latitudinal gradient of v700 (purple) is larger than the one of the v662 (light pink), the range of variation in v662 is larger than in v700, and so, the performance of v700 is better with this metrics.

We analysed also the stability of the SMOS SSS products by computing per each latitudinal band considered in the Hovmöller diagrams of Figure 25 to Figure 27, the standard deviation of the differences between SMOS and Argo with respect to the time (i.e., the standard deviation of each horizontal line in the Hovmöller plots). The stability is very similar in latitudes between 50°S and 15°N. In northern moderate latitudes (between 20°N and 55°N) v700 is more stable than v662. On the contrary, at high latitudes v662 is more stable than v700. This is consistent in the three analyses: ascending, descending, and ascending and descending together.

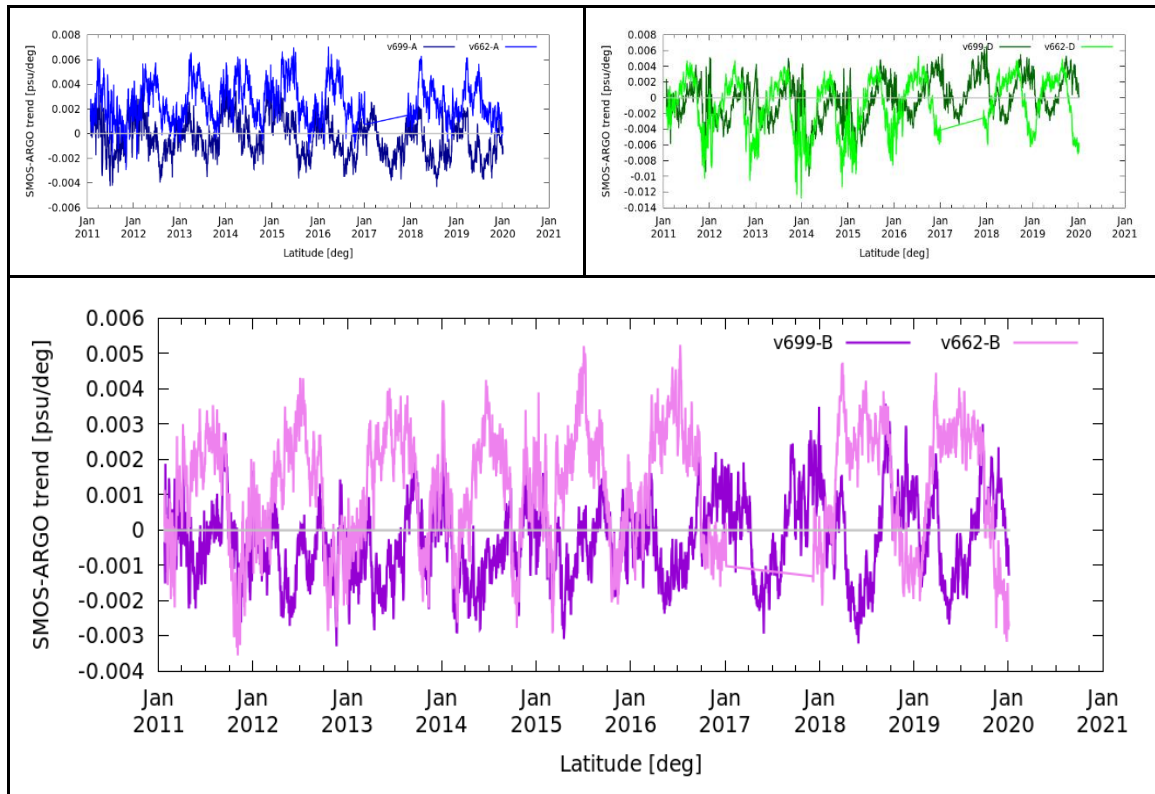


Figure 28: Temporal evolution of the latitudinal gradient. Top left: Ascending satellite overpasses. Top right: Descending satellite overpasses. Bottom: Ascending and descending together.

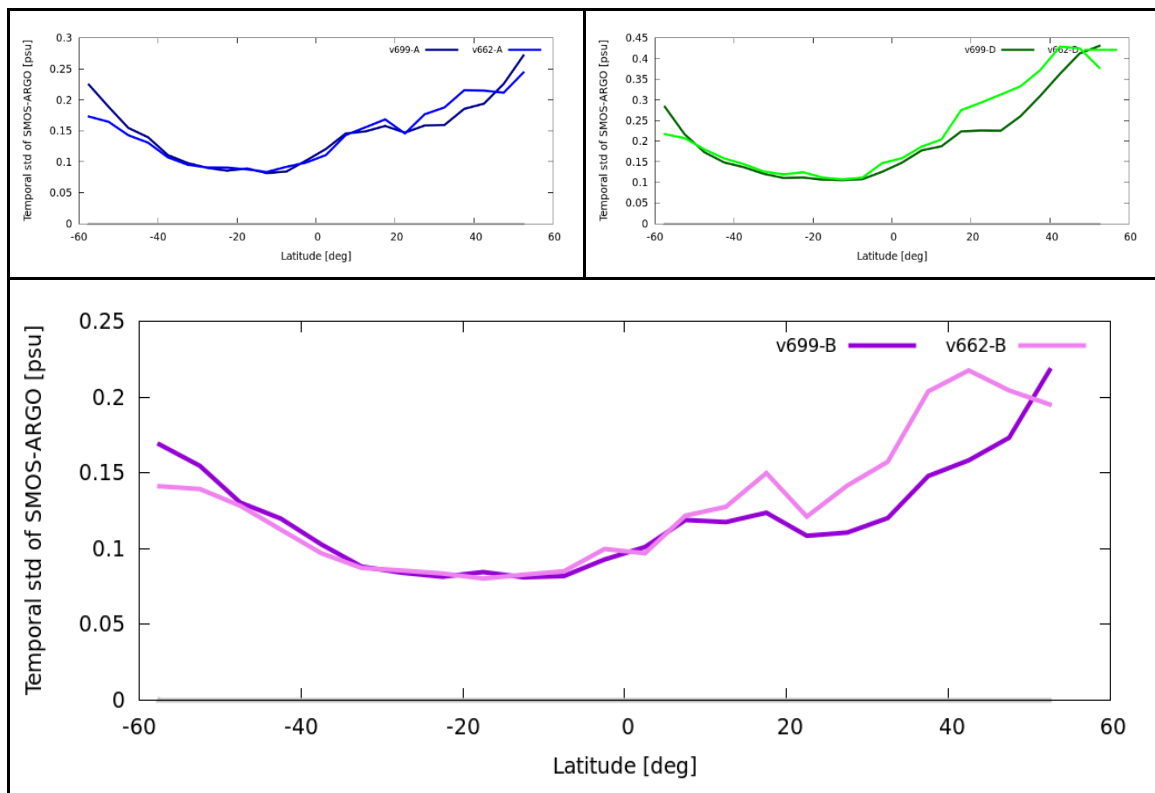


Figure 29: Latitudinal stability of the differences between SMOS and Argo. Top left: Ascending satellite overpasses. Top right: Descending satellite overpasses. Bottom: Ascending and descending together.

Finally, we computed the trend of the differences between SMOS and Argo per each latitude band of 5°, in a range of latitudes between [60°S: 60°N] (i.e., we compute the trend of each horizontal line in the Hovmöller plots of Figure 25 to Figure 27). The trends of v662 and v700 are different especially in Northern latitudes (see Figure 30). In ascending orbits (top left plot Figure 30), the positive trends observed in v662 (sky blue) reaching the 0.015psu/year disappear and become almost null trends in v700 (dark blue line). However, the trends at high northern latitudes in v700 become more negative than in v662 reaching the -0.025 psu/year. In this area, there is also a degradation in the trends of v700 for descending orbits (top right plot, dark green line): v662 presents almost null trends in this region and v700 presents positive trends larger than 0.03psu/year. Therefore, besides the increased trend in this region, we observed inconsistency between the trends observed in ascending with the ones observed in descending in v700. The patterns of the trends observed in v700 in the case of considering ascending and descending together (bottom plot, purple line) are like the ones of the descending orbits, i.e., negative (positive) trends in descending only and ascending and descending together are observed in the same range of latitudes. However, the magnitude of the trends in the case of ascending and descending together are lower than the ones observed in descending only.

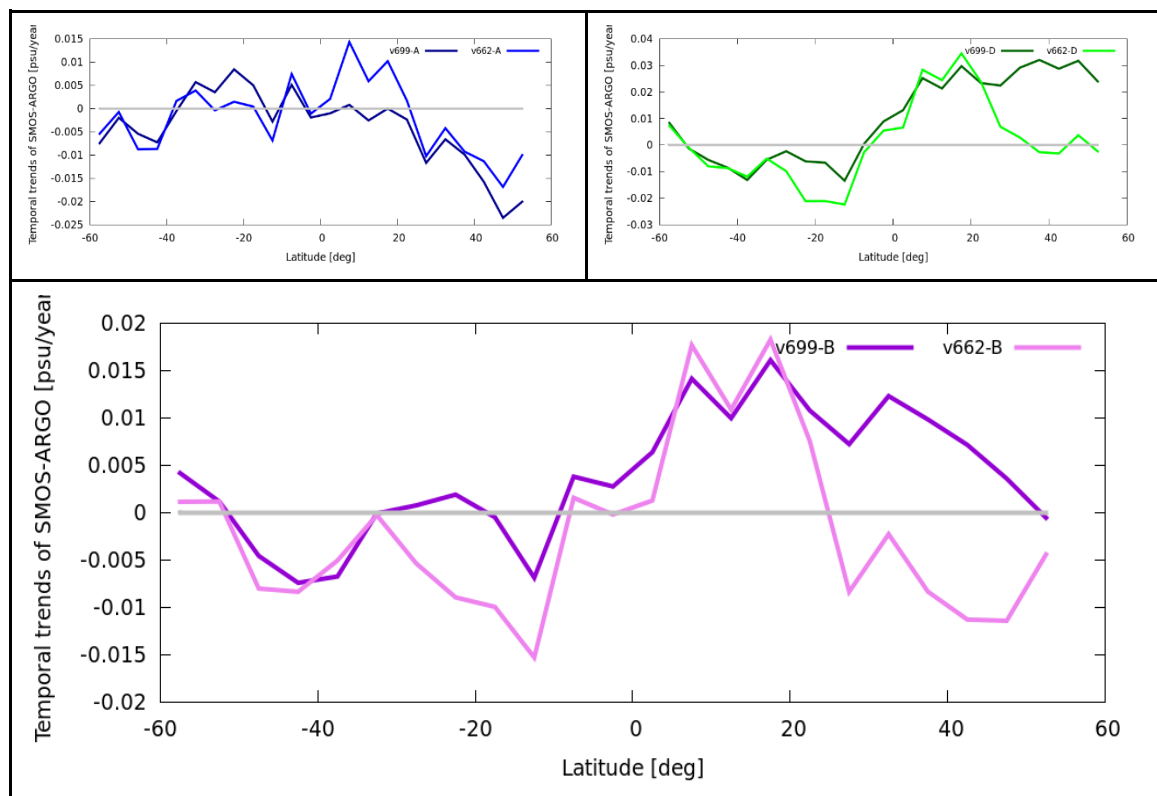


Figure 30: Latitudinal trends of the differences between SMOS and Argo. Top left: Ascending satellite overpasses. Top right: Descending satellite overpasses. Bottom: Ascending and descending together.

2.2.4 Regional statistics

We further analysed the differences between SMOS and Argo SSS in some specific regions. In each region we represent the temporal evolution of the daily averaged differences between SMOS and Argo SSS as well as the corresponding standard deviation. We also computed the yearly root mean squared of the SMOS and Argo SSS differences (RMSD) (see Figure 31 to Figure 42) and the corresponding tables (Table 2 to Table 13) with the global mean difference and standard deviation of the differences in the region. All these statistics are computed for ascending, descending and both types of orbits together.

The general situation is that the standard deviation of the differences between SMOS and Argo in v700 is lower than in v662. In the case of considering ascending and descending orbits together, the averaged differences between SMOS and Argo SSS are similar in both versions v700 and v662. In v700 biases are predominantly negative in ascending orbits and negative in descending ones. In absolute value, biases of v700 are slightly larger than in v662 (in general no larger than 0.05 psu). In terms of the RMSD, v700 performs similar (or slightly better) than v662.

However, there are some specific regions that deserve a separate comment:

- The Equatorial Atlantic (Figure 36 and Table 7): there is a clear improvement in v700 in all the metrics.
- The North Atlantic (Figure 35 and Table 6): there is an improvement of v700 with respect to v662 in the standard deviation of the differences SMOS and Argo, but still significant biases are present in ascending and descending orbits which leads to some years of larger RMSD in v700 than in v662.
- Arctic Ocean (Figure 41 and Table 12): v700 presents a lower standard deviation with respect to v662 when considering ascending and descending orbits together and ascending orbits only, but there is an increase when we consider descending orbits only. The biases in both ascending and descending orbits separately are negative, which leads to more negative biases in v700 than in v662. In general, the RMSD of v700 is lower than the one of v662, but not all the years.
- Southern Ocean (Figure 42 and Table 13): v700 presents lower standard deviation than v662 in ascending and descending together and descending only, but not in ascending orbits only. In v700 the biases in ascending orbits are significantly more negative than in v662, which leads to a significantly more negative bias in ASC+DES. The RMSD in v700 for ascending and descending together, but especially in ascending only, are significantly larger than in v662.

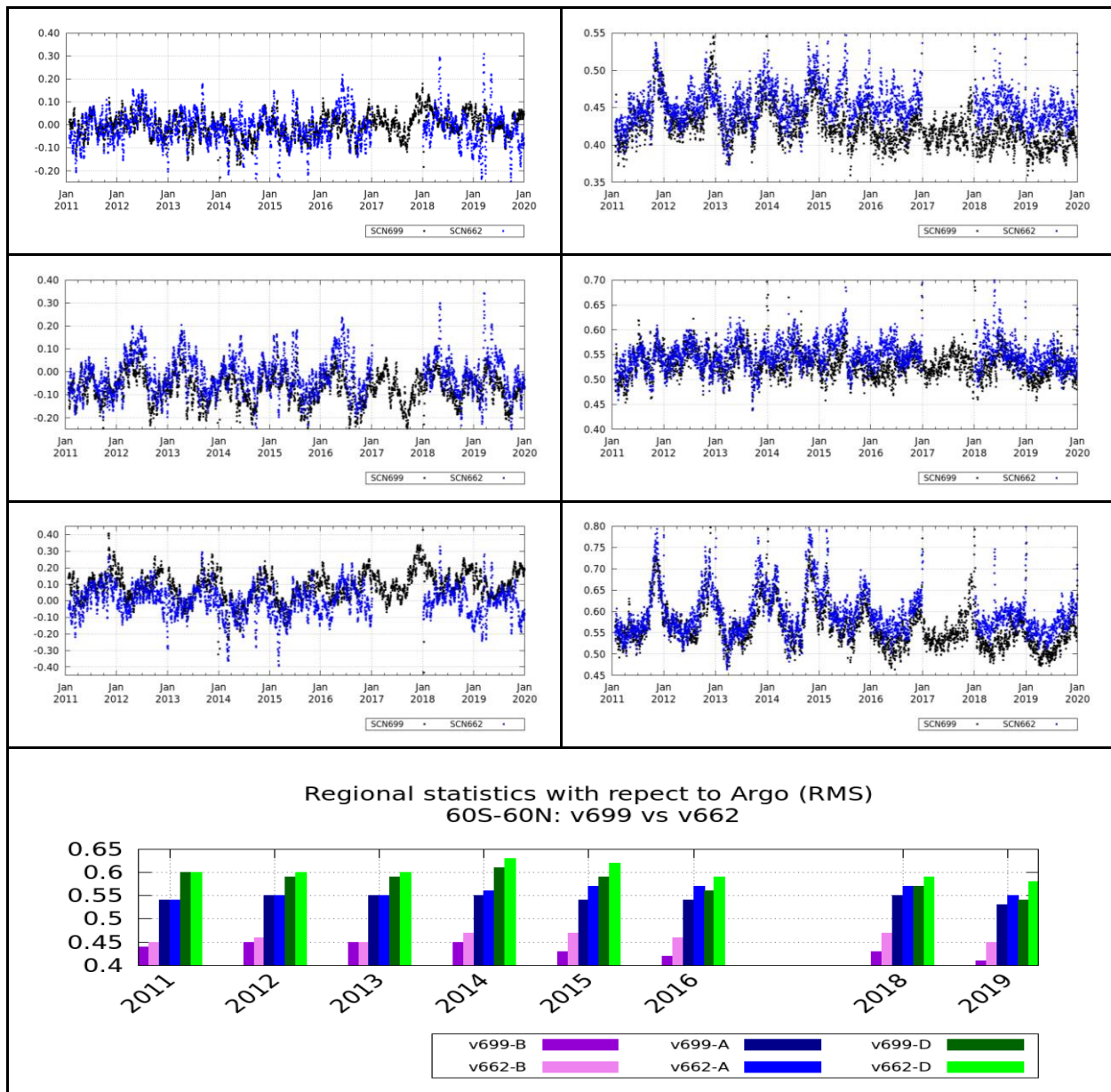


Figure 31: Region comprising 60°S-60°N and all longitudes. In the first three rows the temporal evolution of the daily averaged differences between SMOS and Argo SSS (left) and the corresponding standard deviation of the differences (right) for ascending and descending together (first row), ascending (second row) and descending satellite overpasses (third row). Dark blue line corresponds to v700, and the sky-blue line corresponds to v662. Bottom: Yearly Root Mean Squared differences between SMOS and Argo.

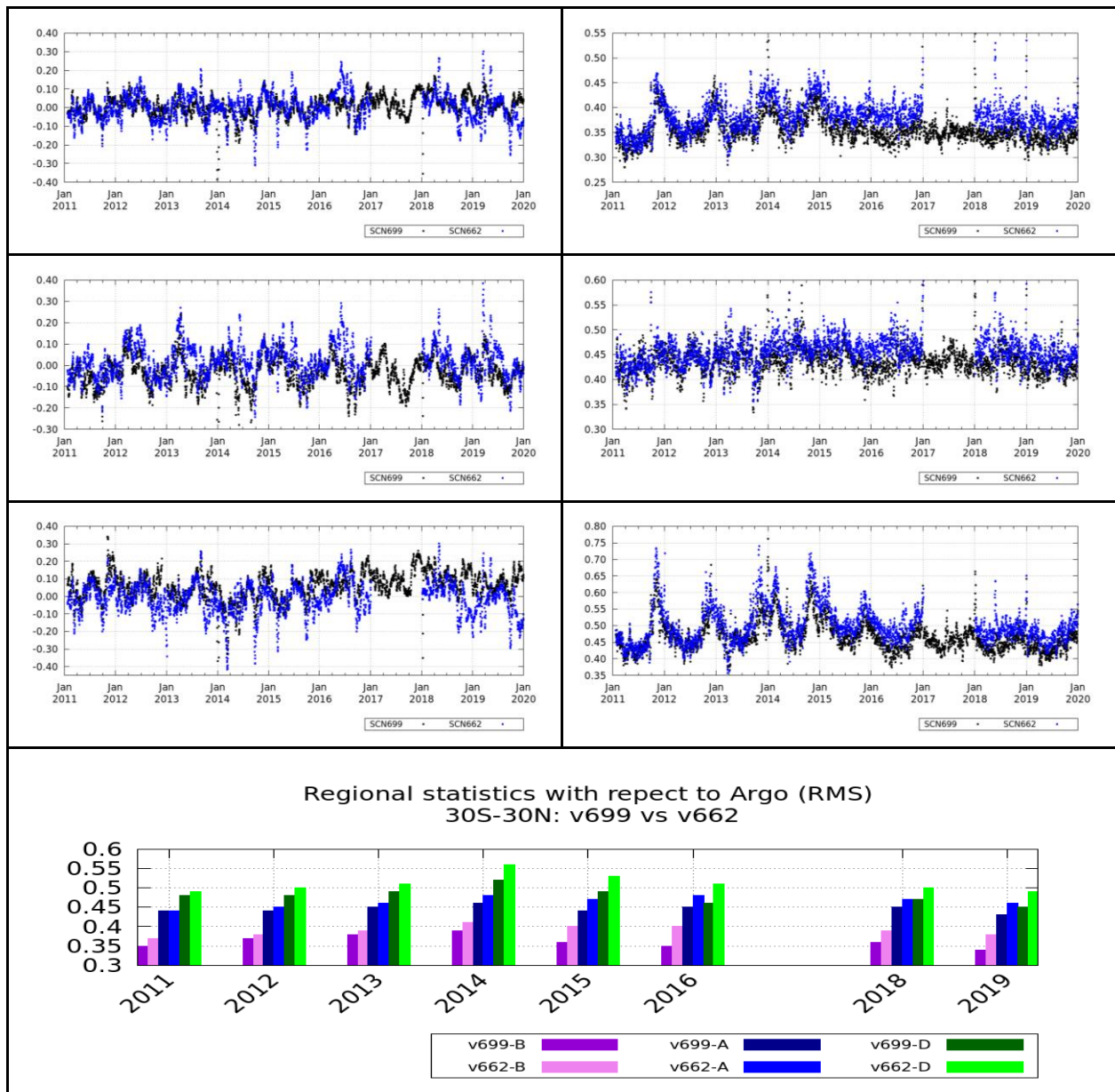


Figure 32: Region comprising 30°S-30°N and all longitudes. In the first three rows the temporal evolution of the daily averaged differences between SMOS and Argo SSS (left) and the corresponding standard deviation of the differences (right) for ascending and descending together (first row), ascending (second row) and descending satellite overpasses (third row). Dark blue line corresponds to v700, and the sky-blue line corresponds to v662. Bottom: Yearly Root Mean Squared differences between SMOS and Argo.

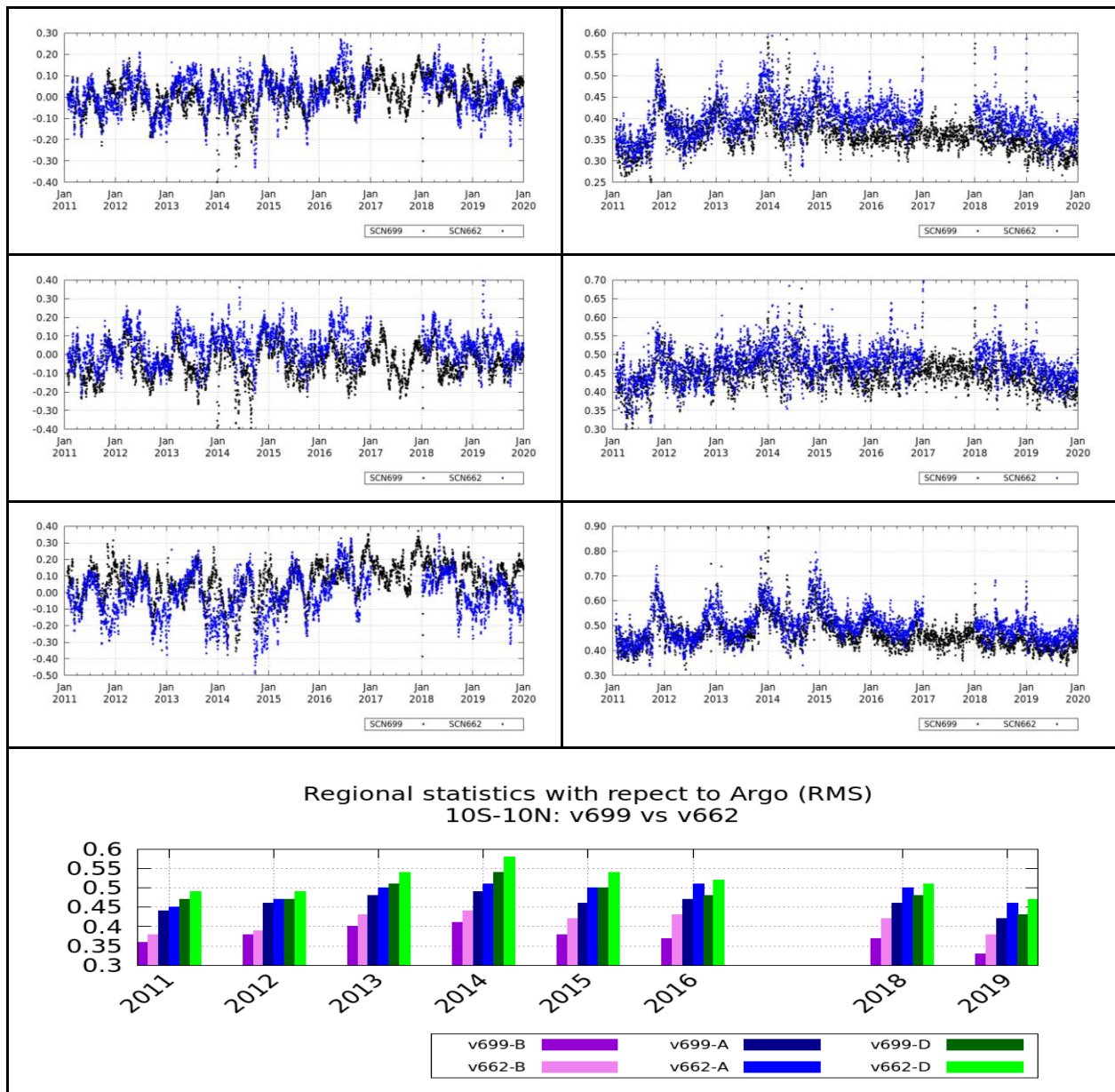


Figure 33: Region comprising 10°S-10°N and all longitudes. In the first three rows the temporal evolution of the daily averaged differences between SMOS and Argo SSS (left) and the corresponding standard deviation of the differences (right) for ascending and descending together (first row), ascending (second row) and descending satellite overpasses (third row). Dark blue line corresponds to v700, and the sky-blue line corresponds to v662. Bottom: Yearly Root Mean Squared differences between SMOS and Argo.

Table 2: Global statistics for the region comprising 60°S-60°N and all longitudes.

		ASC+DES	ASC	DES
MEAN (SMOS-ARGO)	V662	-0.01	-0.01	0.00
	V700	-0.01	-0.07	0.08
SD (SMOS-ARGO)	V662	0.46	0.55	0.60
	V700	0.43	0.53	0.57

Table 3: Global statistics for the region comprising 30°S-30°N and all longitudes.

		ASC+DES	ASC	DES
MEAN (SMOS-ARGO)	V662	0.00	0.02	-0.01
	V700	0.01	-0.03	0.06
SD (SMOS-ARGO)	V662	0.38	0.46	0.50
	V700	0.36	0.44	0.47

Table 4: Global statistics for the region comprising 10°S-10°N and all longitudes.

		ASC+DES	ASC	DES
MEAN (SMOS-ARGO)	V662	0.02	0.05	-0.02
	V700	0.01	-0.04	0.07
SD (SMOS-ARGO)	V662	0.40	0.48	0.50
	V700	0.37	0.45	0.47

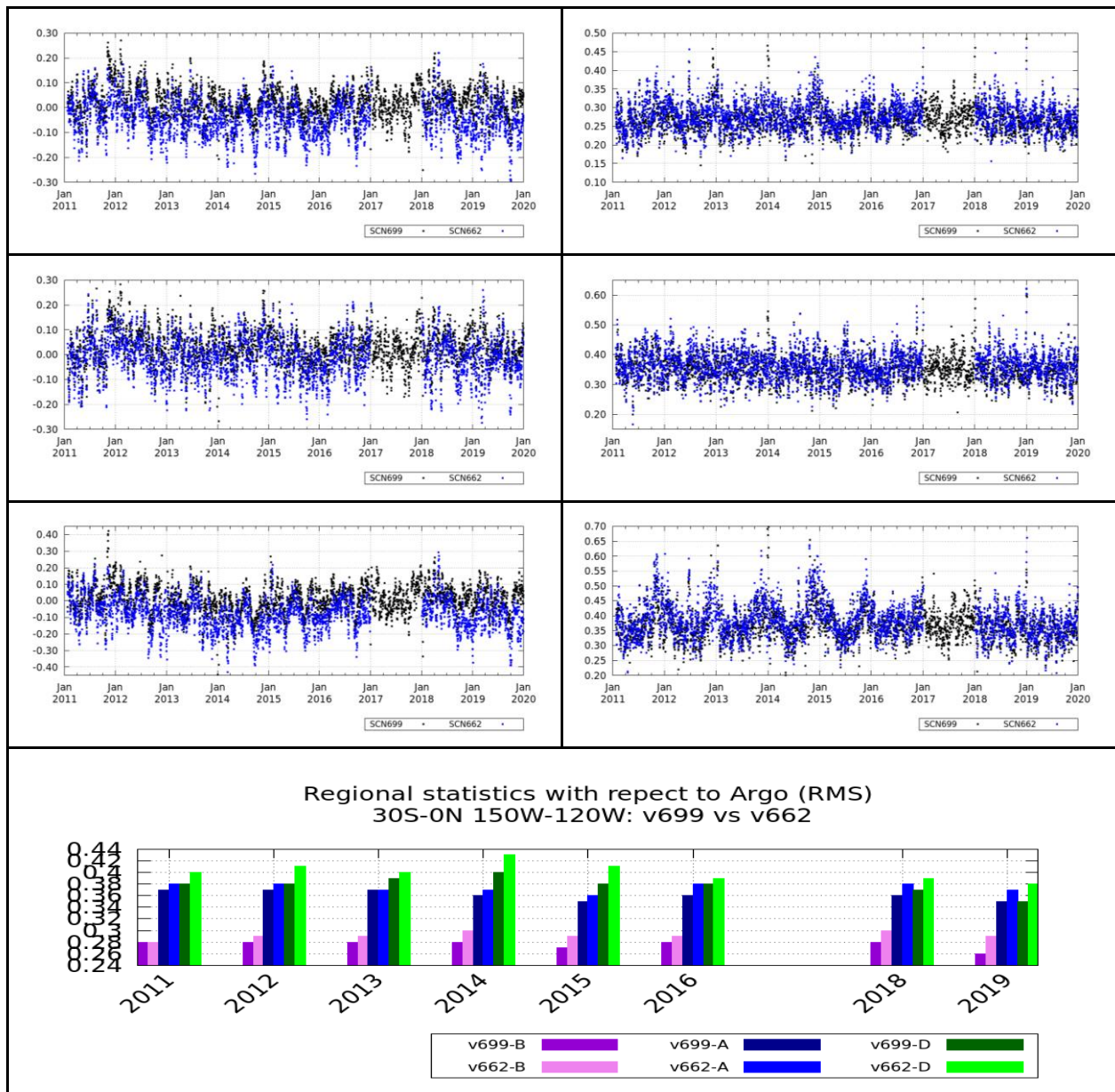


Figure 34: Region comprising 30°N-0°N and 150°W-120°W. In the first three rows the temporal evolution of the daily averaged differences between SMOS and Argo SSS (left) and the corresponding standard deviation of the differences (right) for ascending and descending together (first row), ascending (second row) and descending satellite overpasses (third row). Dark blue line corresponds to v700, and the sky-blue line corresponds to v662. Bottom: Yearly Root Mean Squared differences between SMOS and Argo.

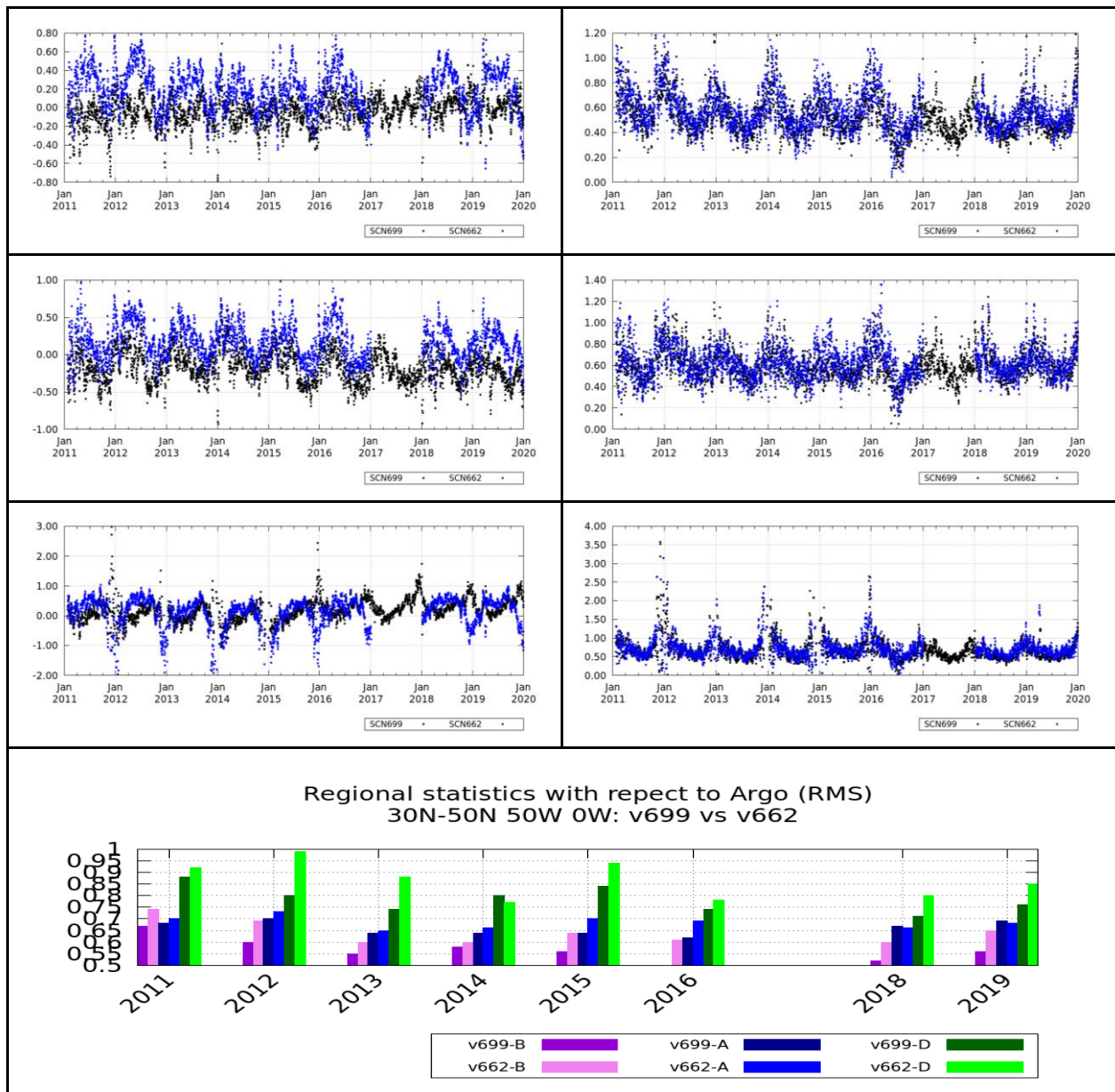


Figure 35: Region comprising 30°N-50°N and 50°W-0°W. In the first three rows the temporal evolution of the daily averaged differences between SMOS and Argo SSS (left) and the corresponding standard deviation of the differences (right) for ascending and descending together (first row), ascending (second row) and descending satellite overpasses (third row). Dark blue line corresponds to v700, and the sky-blue line corresponds to v662. Bottom: Yearly Root Mean Squared differences between SMOS and Argo.

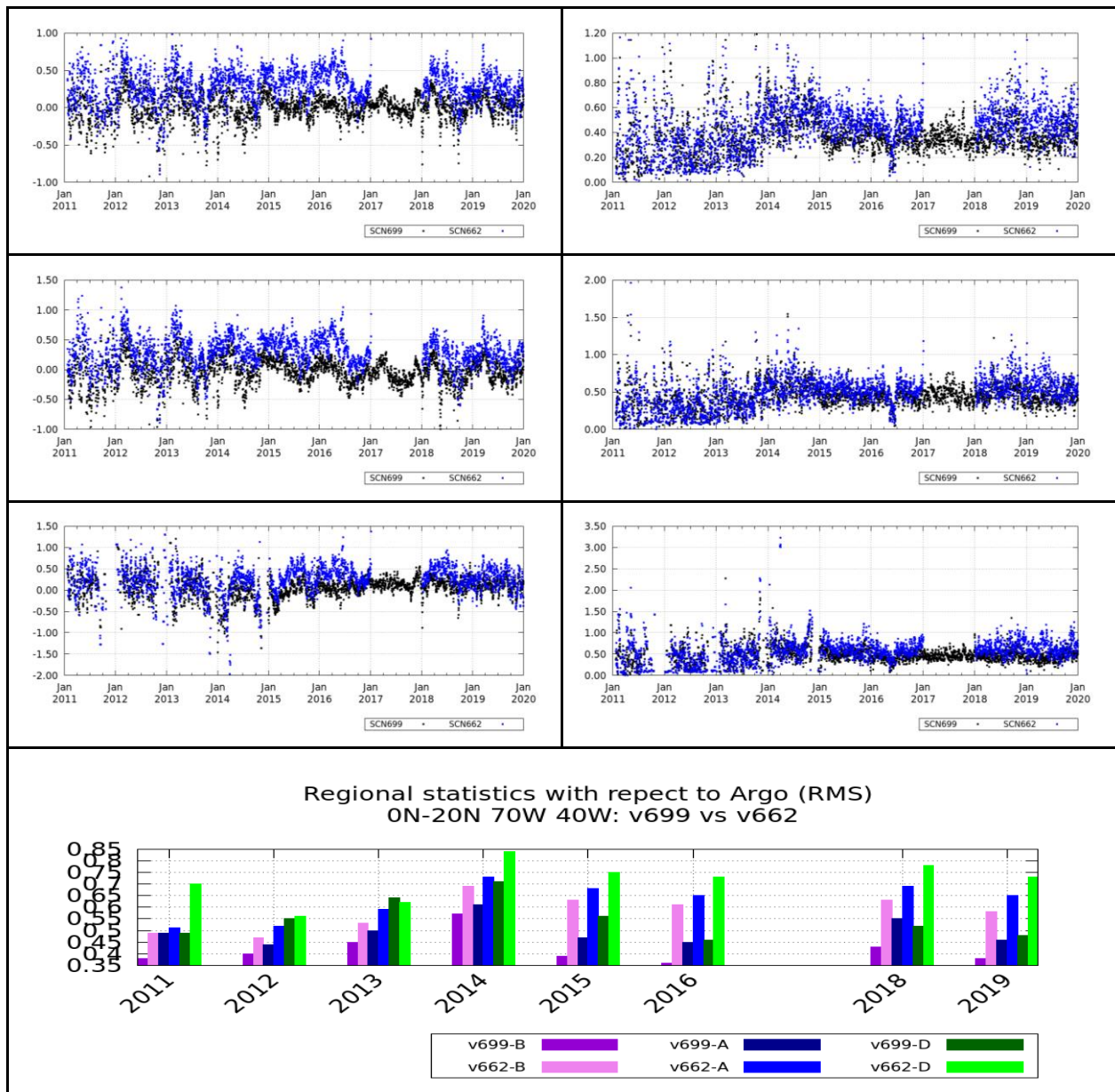


Figure 36: Region comprising 0°N-20°N and 70°W-40°W. In the first three rows the temporal evolution of the daily averaged differences between SMOS and Argo SSS (left) and the corresponding standard deviation of the differences (right) for ascending and descending together (first row), ascending (second row) and descending satellite overpasses (third row). Dark blue line corresponds to v700, and the sky-blue line corresponds to v662. Bottom: Yearly Root Mean Squared differences between SMOS and Argo.

Table 5: Global statistics for the region comprising 30°N-0°N and 150°W-120°W.

		ASC+DES	ASC	DES
MEAN (SMOS-ARGO)	V662	-0.04	-0.01	-0.08
	V700	0.02	0.03	0.01
SD (SMOS-ARGO)	V662	0.28	0.36	0.38
	V700	0.27	0.35	0.37

Table 6: Global statistics for the region comprising 30°N-50°N and 50°W-0°W.

		ASC+DES	ASC	DES
MEAN (SMOS-ARGO)	V662	0.19	0.17	0.11
	V700	-0.04	-0.17	0.17
SD (SMOS-ARGO)	V662	0.57	0.62	0.72
	V700	0.53	0.60	0.68

Table 7: Global statistics for the region comprising 0°N-20°N and 70°W-40°W.

		ASC+DES	ASC	DES
MEAN (SMOS-ARGO)	V662	0.29	0.30	0.25
	V700	0.01	-0.03	0.06
SD (SMOS-ARGO)	V662	0.45	0.50	0.58
	V700	0.37	0.43	0.47

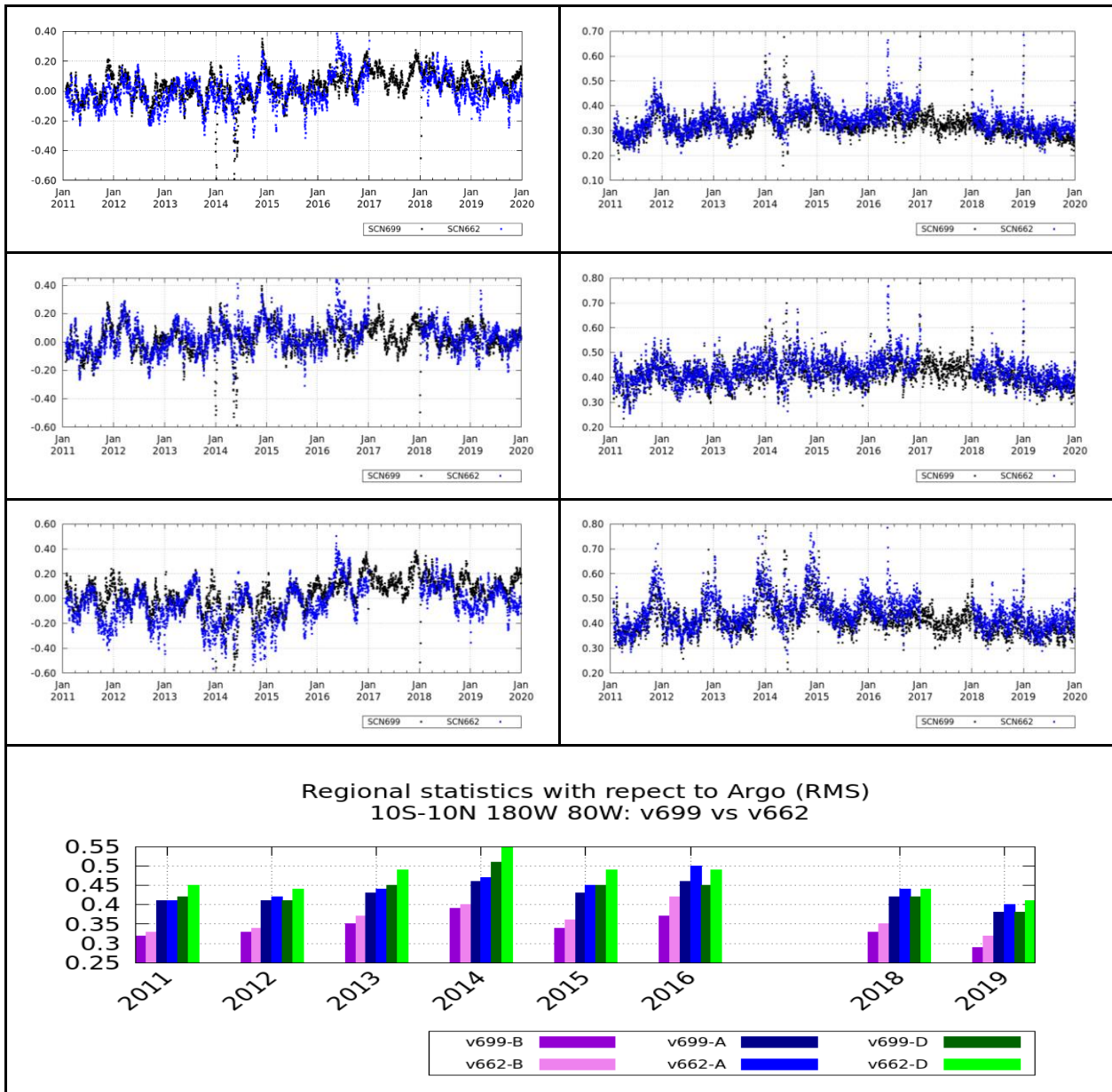


Figure 37: Region comprising 10°S-10°N and 180°W-80°W. In the first three rows the temporal evolution of the daily averaged differences between SMOS and Argo SSS (left) and the corresponding standard deviation of the differences (right) for ascending and descending together (first row), ascending (second row) and descending satellite overpasses (third row). Dark blue line corresponds to v700, and the sky-blue line corresponds to v662. Bottom: Yearly Root Mean Squared differences between SMOS and Argo.

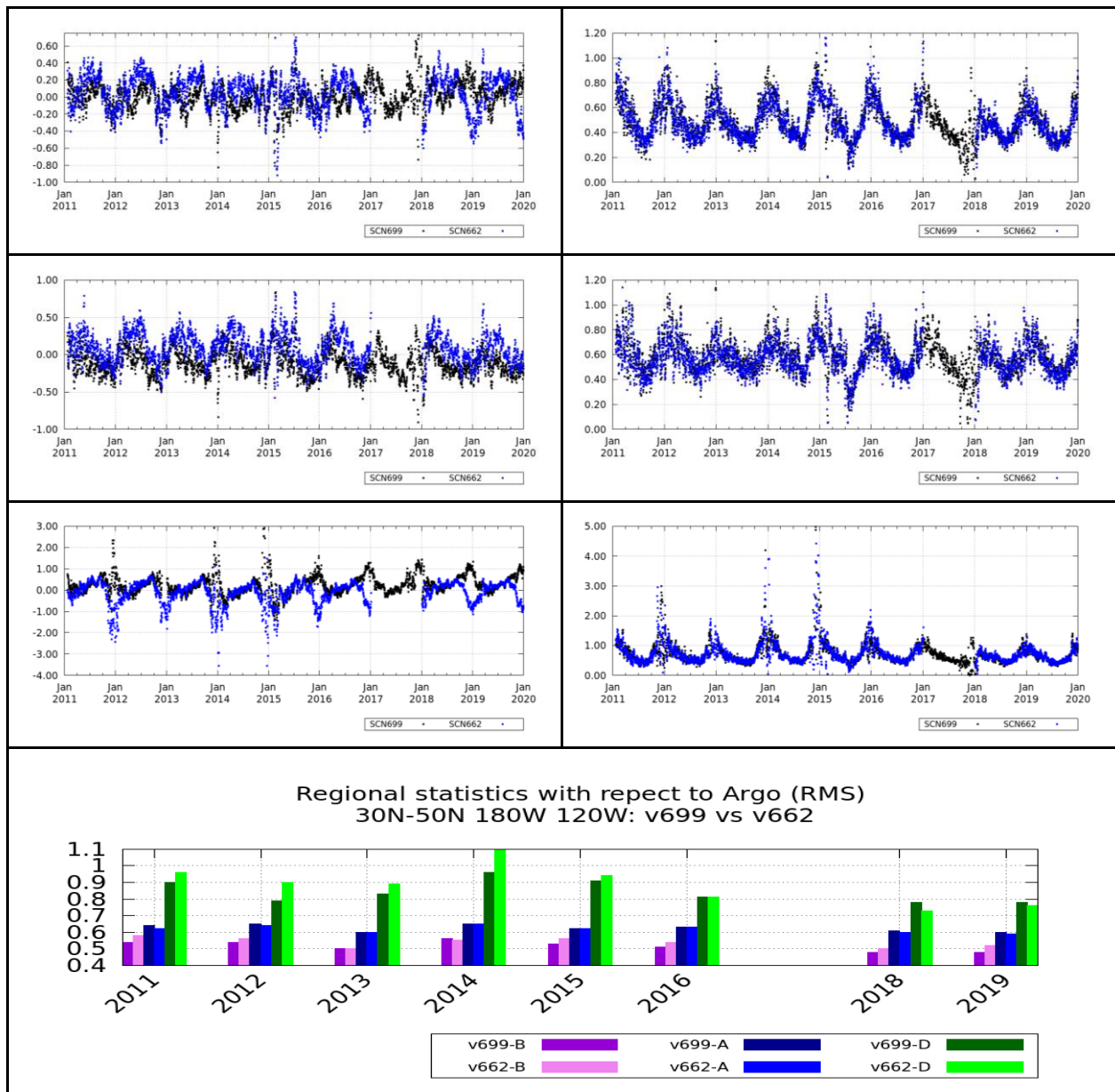


Figure 38: Region comprising 30°N-50°N and 180°W-120°W. In the first three rows the temporal evolution of the daily averaged differences between SMOS and Argo SSS (left) and the corresponding standard deviation of the differences (right) for ascending and descending together (first row), ascending (second row) and descending satellite overpasses (third row). Dark blue line corresponds to v700, and the sky-blue line corresponds to v662. Bottom: Yearly Root Mean Squared differences between SMOS and Argo.

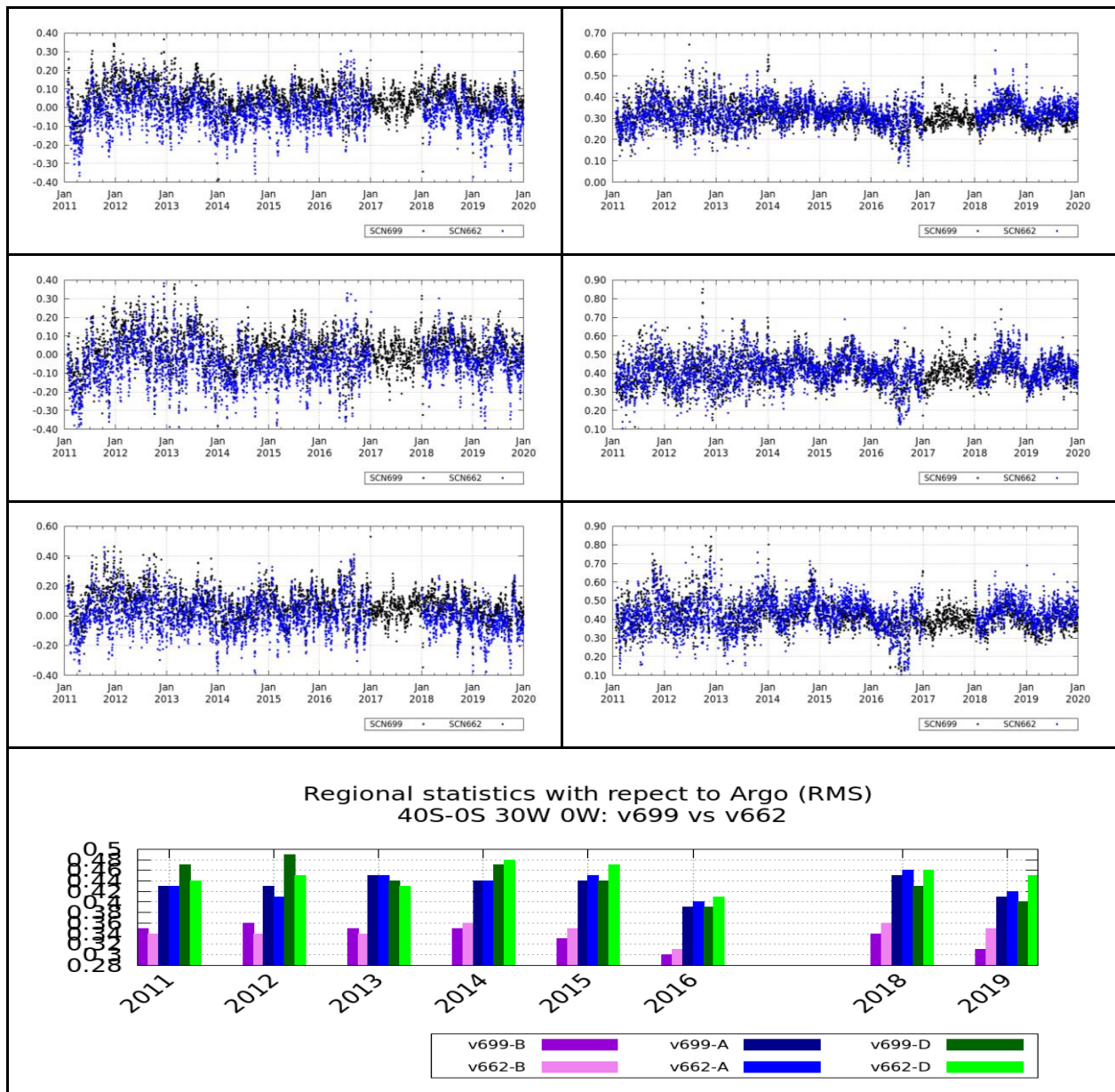


Figure 39: Region comprising 40°S-0°N and 30°W-0°W. In the first three rows the temporal evolution of the daily averaged differences between SMOS and Argo SSS (left) and the corresponding standard deviation of the differences (right) for ascending and descending together (first row), ascending (second row) and descending satellite overpasses (third row). Dark blue line corresponds to v700, and the sky-blue line corresponds to v662. Bottom: Yearly Root Mean Squared differences between SMOS and Argo.

Table 8: Global statistics for the region comprising 10°S-10°N and 180°W-80°W.

		ASC+DES	ASC	DES
MEAN (SMOS-ARGO)	V662	0.00	0.04	-0.05
	V700	0.03	0.02	0.04
SD (SMOS-ARGO)	V662	0.35	0.43	0.44
	V700	0.33	0.42	0.42

Table 9: Global statistics for the region comprising 30°N-50°N and 180°W-120°W. .

		ASC+DES	ASC	DES
MEAN (SMOS-ARGO)	V662	0.05	0.09	-0.13
	V700	0.01	-0.12	0.25
SD (SMOS-ARGO)	V662	0.49	0.58	0.74
	V700	0.49	0.58	0.71

Table 10: Global statistics for the region comprising 40°S-0°N and 30°W-0°W.

		ASC+DES	ASC	DES
MEAN (SMOS-ARGO)	V662	-0.03	-0.05	0.00
	V700	0.05	0.02	0.07
SD (SMOS-ARGO)	V662	0.33	0.42	0.43
	V700	0.32	0.41	0.42

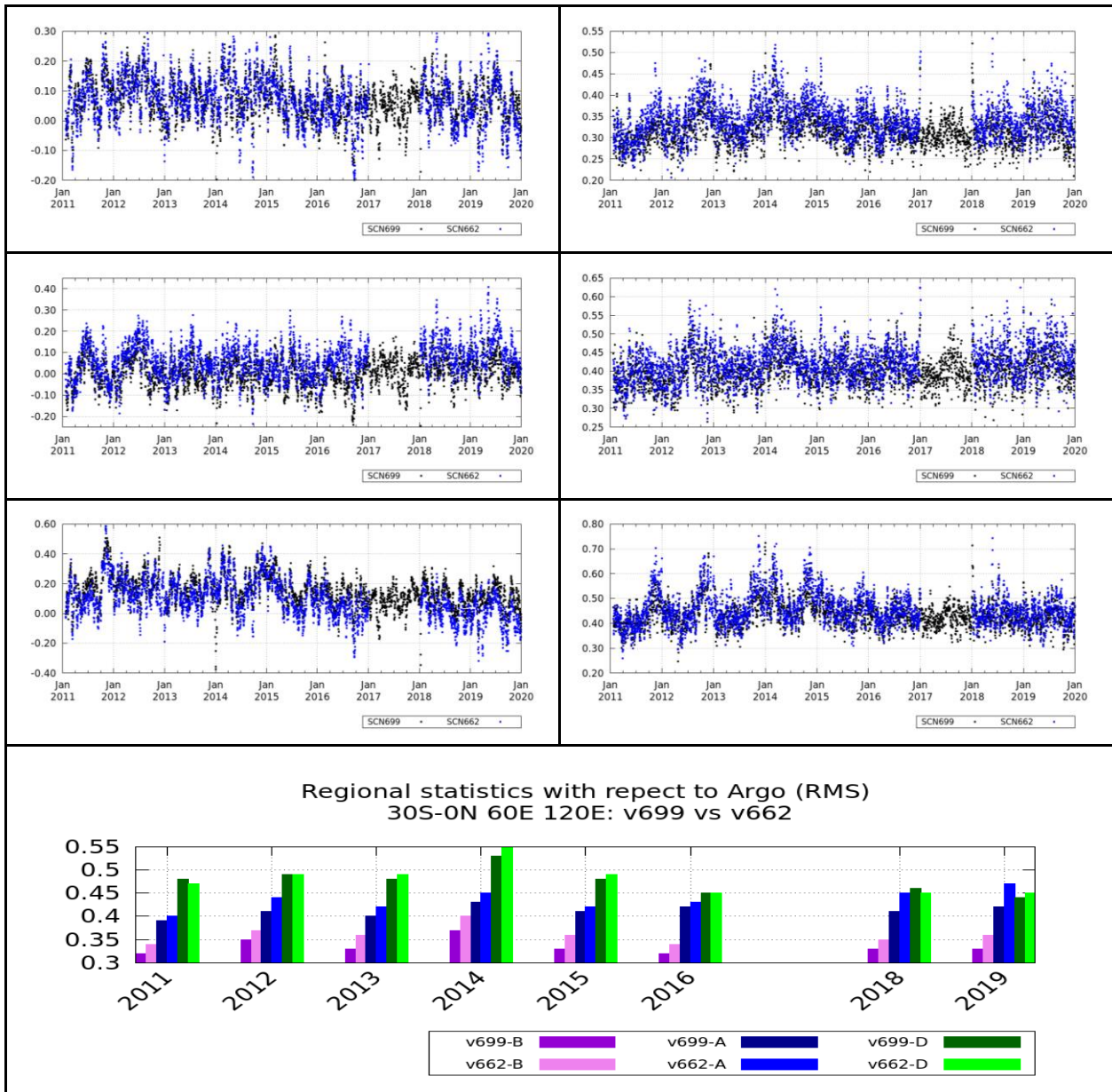


Figure 40: Region comprising 30°S-0°N and 60°E-120°E. In the first three rows the temporal evolution of the daily averaged differences between SMOS and Argo SSS (left) and the corresponding standard deviation of the differences (right) for ascending and descending together (first row), ascending (second row) and descending satellite overpasses (third row). Dark blue line corresponds to v700, and the sky-blue line corresponds to v662. Bottom: Yearly Root Mean Squared differences between SMOS and Argo.

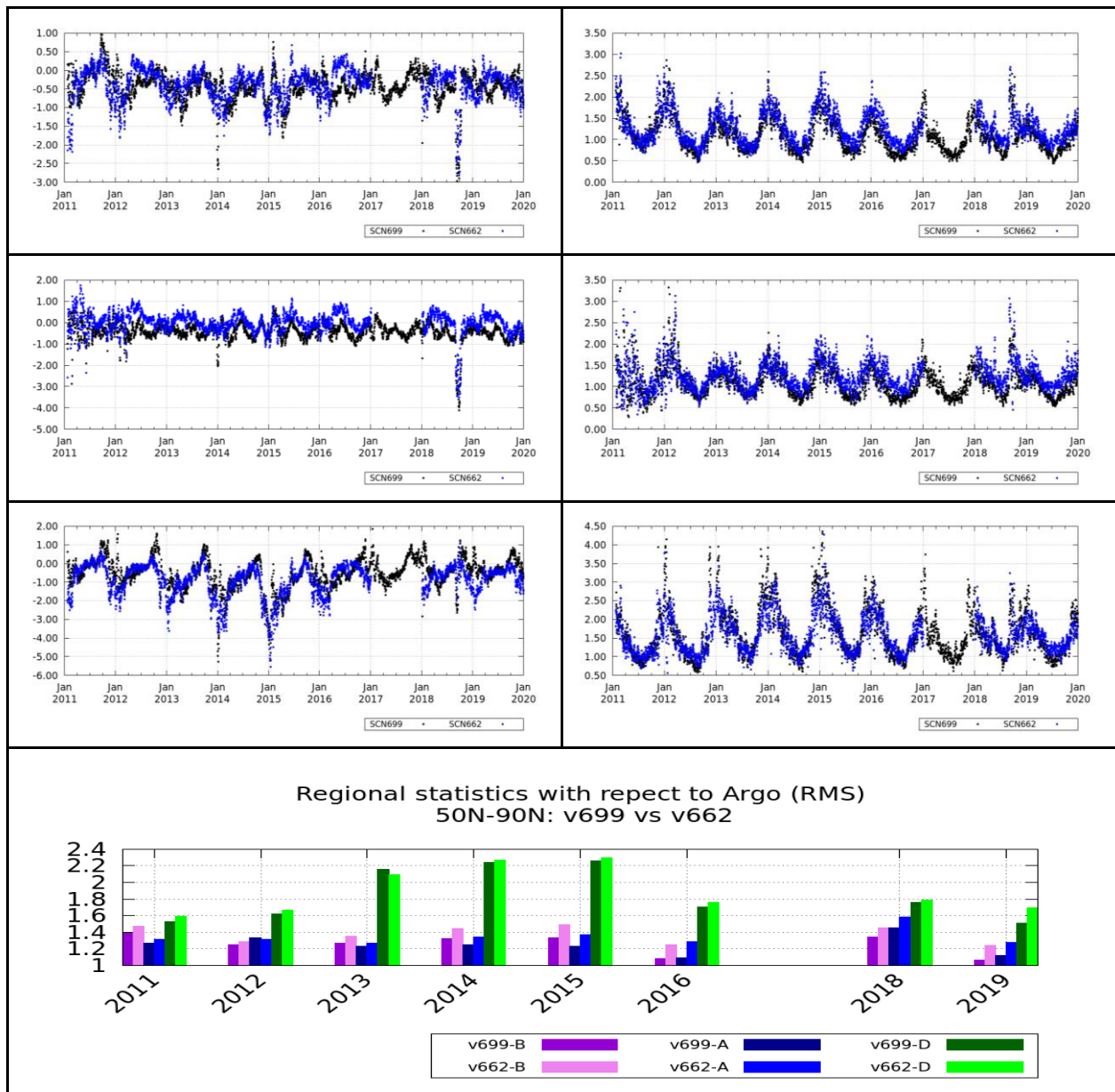


Figure 41: Region comprising 50°N-90°N and all longitudes. In the first three rows the temporal evolution of the daily averaged differences between SMOS and Argo SSS (left) and the corresponding standard deviation of the differences (right) for ascending and descending together (first row), ascending (second row) and descending satellite overpasses (third row). Dark blue line corresponds to v700, and the sky-blue line corresponds to v662. Bottom: Yearly Root Mean Squared differences between SMOS and Argo.

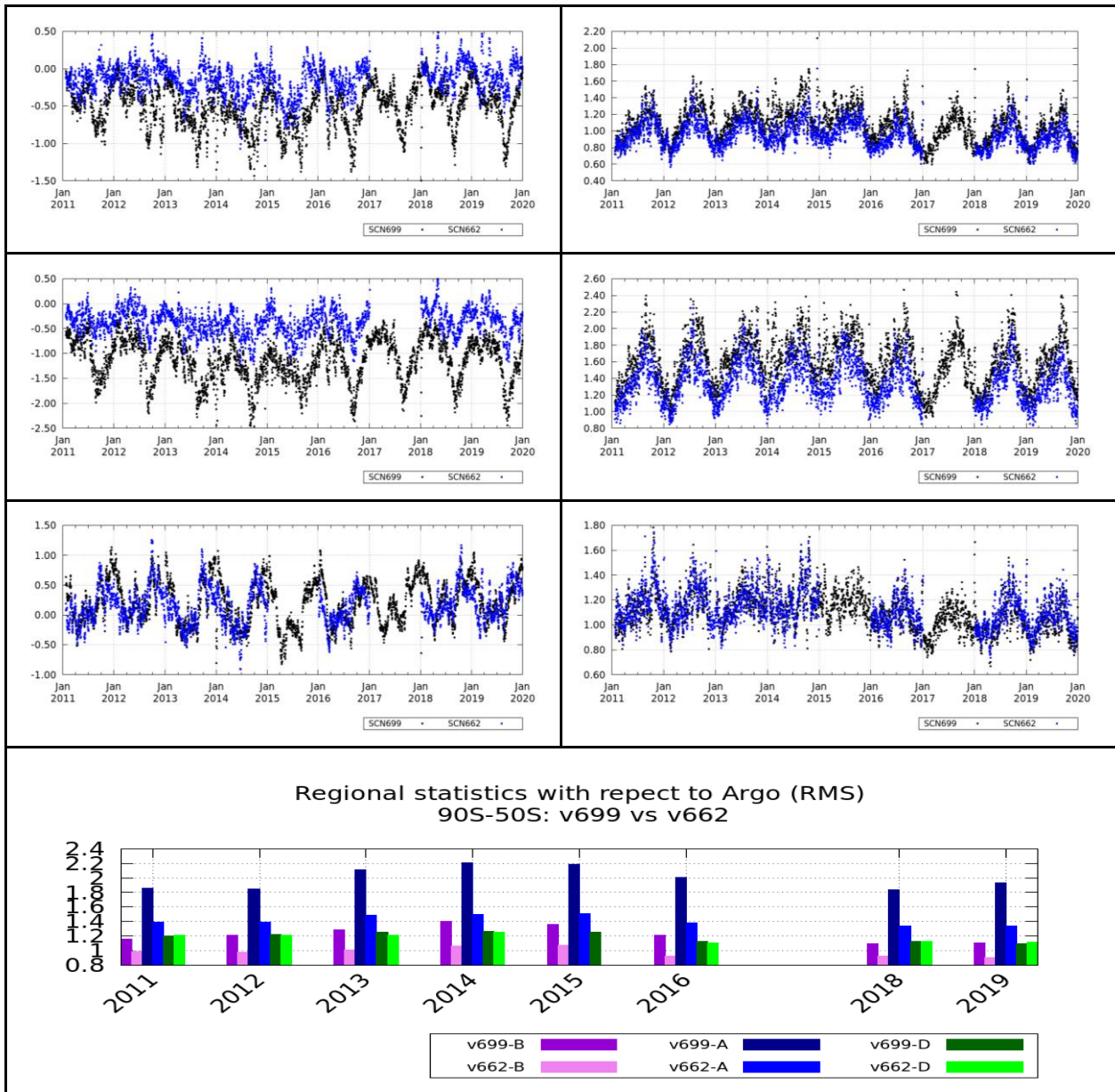


Figure 42: Region comprising 90°S-50°S and all longitudes. In the first three rows the temporal evolution of the daily averaged differences between SMOS and Argo SSS (left) and the corresponding standard deviation of the differences (right) for ascending and descending together (first row), ascending (second row) and descending satellite overpasses (third row). Dark blue line corresponds to v700, and the sky-blue line corresponds to v662. Bottom: Yearly Root Mean Squared differences between SMOS and Argo.

Table 11: Global statistics for the region comprising 30°S-0°N and 60°E-120°E.

		ASC+DES	ASC	DES
MEAN (SMOS-ARGO)	V662	0.07	0.06	0.09
	V700	0.07	0.00	0.14
SD (SMOS-ARGO)	V662	0.34	0.42	0.46
	V700	0.32	0.40	0.44

Table 12: Global statistics for the region comprising 50°N-90°N and all longitudes.

		ASC+DES	ASC	DES
MEAN (SMOS-ARGO)	V662	-0.39	0.01	-0.90
	V700	-0.44	-0.43	-0.55
SD (SMOS-ARGO)	V662	1.27	1.27	1.58
	V700	1.10	1.10	1.60

Table 13: Global statistics for the region comprising 90°S-50°S and all longitudes.

		ASC+DES	ASC	DES
MEAN (SMOS-ARGO)	V662	-0.14	-0.37	0.16
	V700	-0.51	-1.14	0.20
SD (SMOS-ARGO)	V662	0.95	1.35	1.13
	V700	1.08	1.60	1.10

2.2.5 Standard deviation of the differences with respect to in situ

In order to assess the spatial distributions of the standard deviation of the errors we first accumulated all the SMOS and Argo SSS acquired during the years 2011-2016 and 2018-2019 in latitude x longitude cells of 5x5°. Figure 43 to Figure 45 represent the temporal standard deviation of the accumulated differences between SMOS and Argo SSS (SD) at each 5x5° cell when the SMOS SSS maps are computed by using ascending and descending satellite overpasses together, ascending orbits only and descending orbits only (respectively). The top left plots in Figure 43 to Figure 45 represent the SD for v662 and the top right plots represent the SD for v700. The bottom plots show the differences between the previous two maps such that the pixels in blue (red) represent regions where the SD of v700 is larger (lower) than the one of v662. We can see that the predominant colour in the global ocean is red, meaning that in general the SD for v700 is lower than SD for v662. At high latitudes there is no clear colour predominant.

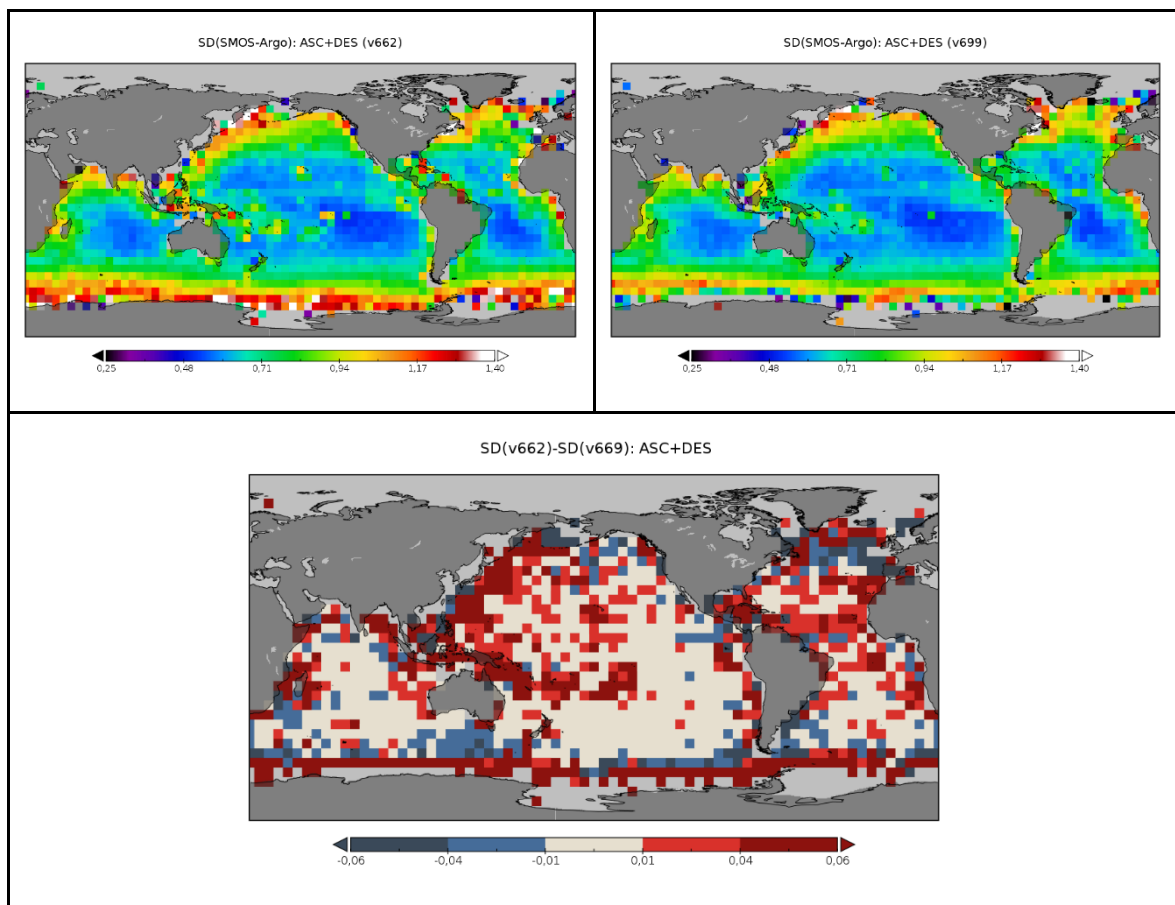


Figure 43: Standard deviation of the differences between SMOS and Argo SSS for ascending and descending orbits together. Top left: differences correspond to v662. Top right: differences correspond to v700. Bottom plot represents the differences between the two top maps, such that the pixels in blue (red) represent regions where the SD of v700 is larger (lower) than the one of v662.

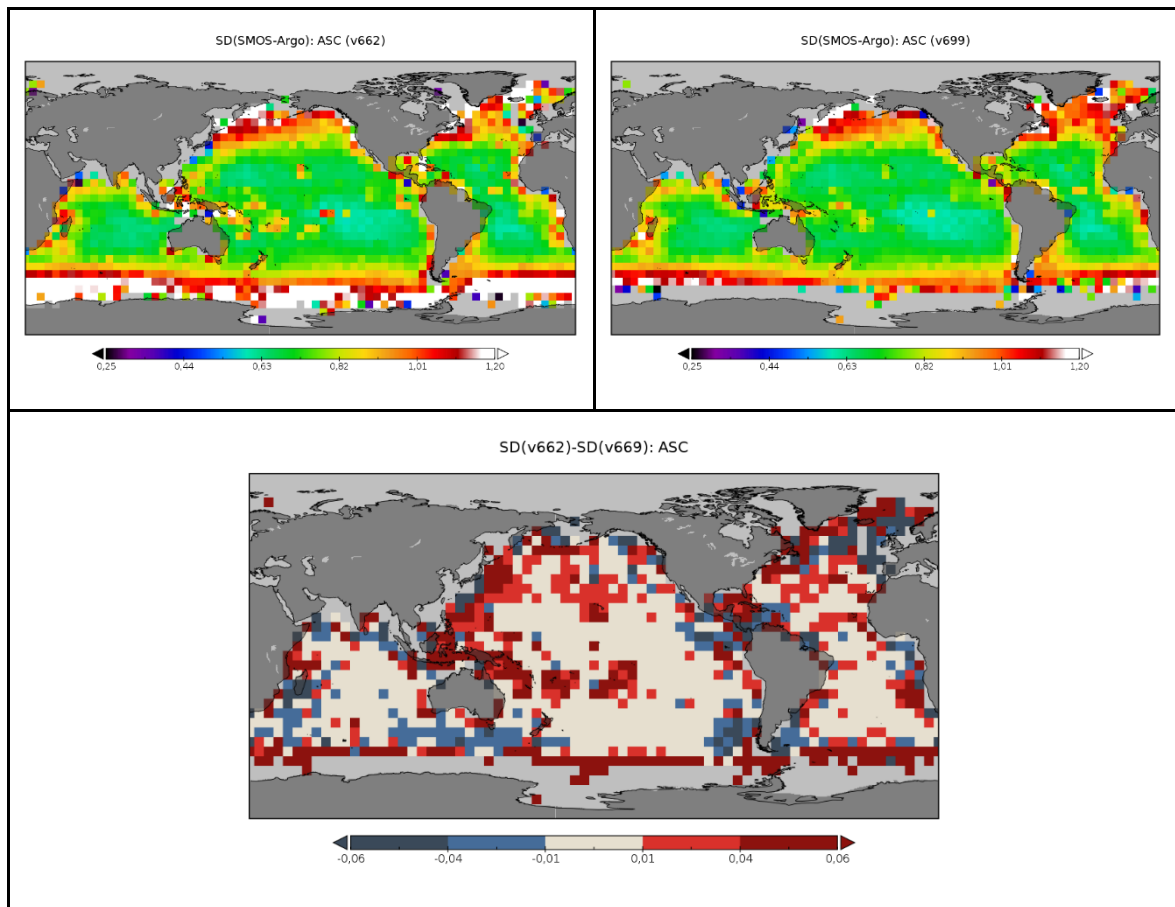


Figure 44: Standard deviation of the differences between SMOS and Argo SSS for ascending orbits. Top left: differences correspond to v662. Top right: differences correspond to v700. Bottom plot represents the differences between the two top maps, such that the pixels in blue (red) represent regions where the SD of v700 is larger (lower) than the one of v662.

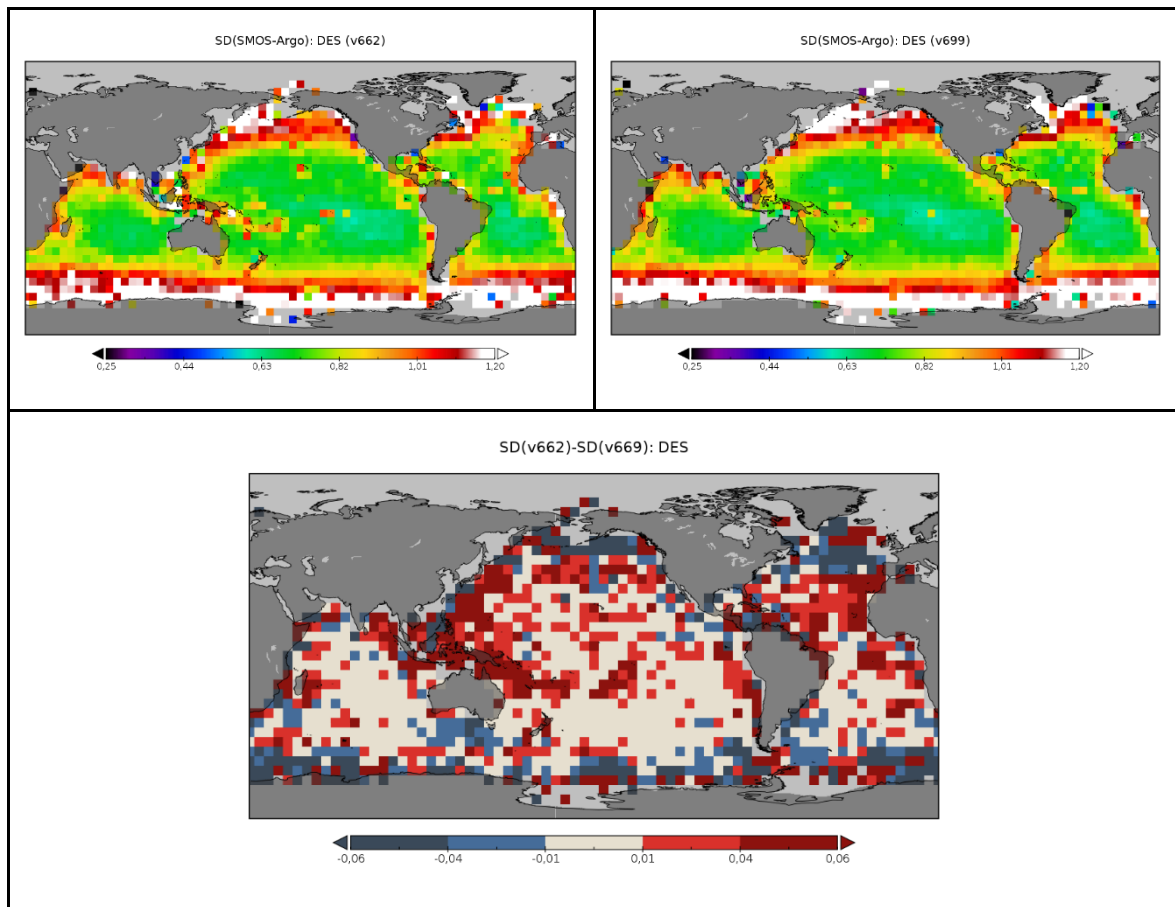


Figure 45: Standard deviation of the differences between SMOS and Argo SSS for descending orbits. Top left: differences correspond to v662. Top right: differences correspond to v700. Bottom plot represents the differences between the two top maps, such that the pixels in blue (red) represent regions where the SD of v700 is larger (lower) than the one of v662.

2.2.6 Estimated uncertainty by Correlated Triple Collocation

The triple collocation (TC) technique is a powerful tool to estimate the standard deviation of errors of three spatio-temporally collocated measurements of the same target. TC has been used to assess the quality of many remotely sensed variables, and SSS [Hoareau.2018]. The major assumptions of TC are that errors must be uncorrelated with the target variable and that the errors of the different data sets must be uncorrelated among them. Some refined formulations have been developed in recent years for considering the presence of cross-correlated errors between two of the data sets, but they require at least four data sets [Gruber.2016, Pierdicca.2017].

We have used a recently developed formulation of the triple collocation method, the Correlated Triple Collocation (CTC), for the case of three data sets that resolve similar spatial scales from which two of them present correlated errors [Gonzalez-Gambau.2020]. This TC can be particularly beneficial for the error characterization of variables for which getting measurement systems with uncorrelated errors is challenging or not feasible, and it is particularly well suited to work with limited samples of data because it has a fast convergence with the sampling size. This formulation has been proved for the characterization of radiometric errors in L-band brightness temperatures (TB). Using CTC, we have access to maps of errors, so we can characterize which places are less noisy, and we can ascertain which is the best suited product depending on the location. This technique has been already used for the comparison of different satellite SSS maps in [Olmedo.2021]

We used the year 2018 for doing the CTC analysis and the following SMAP SSS products:



- JPL SMAP products: 8-day SMAP SSS maps provided by Jet Propulsion Laboratory (JPL) [Fore.2016]. We use the Level 3 version 4.2 freely available at: <https://podaac-opendap.jpl.nasa.gov/opendap/allData/smap/L3/JPL/V4.2/>.
- REMSS SMAP products: 8-day running mean Remote Sensing Systems SMAP Level 3 Sea Surface Salinity Standard Mapped Image version v4 which is freely available at www.remss.com/missions/smap. We have used the field sss_smap, which is a smoothed measurement at approximately 70km resolution [Meissner.2018].

For each type of orbit (ascending, descending and both) we consider the following two triplets:

- SMOS v662, SMOS v700, SMAP JPL.
- SMOS v662, SMOS v700, SMAP REMSS.

The error associated with SMOS is computed as the mean average of the estimated error from the previous two triplets.

Figure 46 (next page) shows the estimated standard deviation of the errors as a result from TC analysis. In Figure 47 to Figure 49, the differences between the estimated errors for v662 and v700 are represented for ascending and descending orbits together, ascending only and descending only (respectively), such that the pixels in blue (red) represent regions where the error of v700 is larger (lower) than the one of v662.

In general, the estimated SSS error in v700 is lower than in v662 (reddish patterns). There is a special improvement in the Euro-Asian coast (typically affected by RFI), Equatorial regions and Arctic Ocean. In descending orbits, we also observe a general improvement in the Northern Hemisphere. In the Southern Ocean (especially in ascending and ascending with descending) we observe a dipole pattern that shows a degradation in v700 at high southern latitudes but an improvement close to the ice-edge of the Antarctica continent.

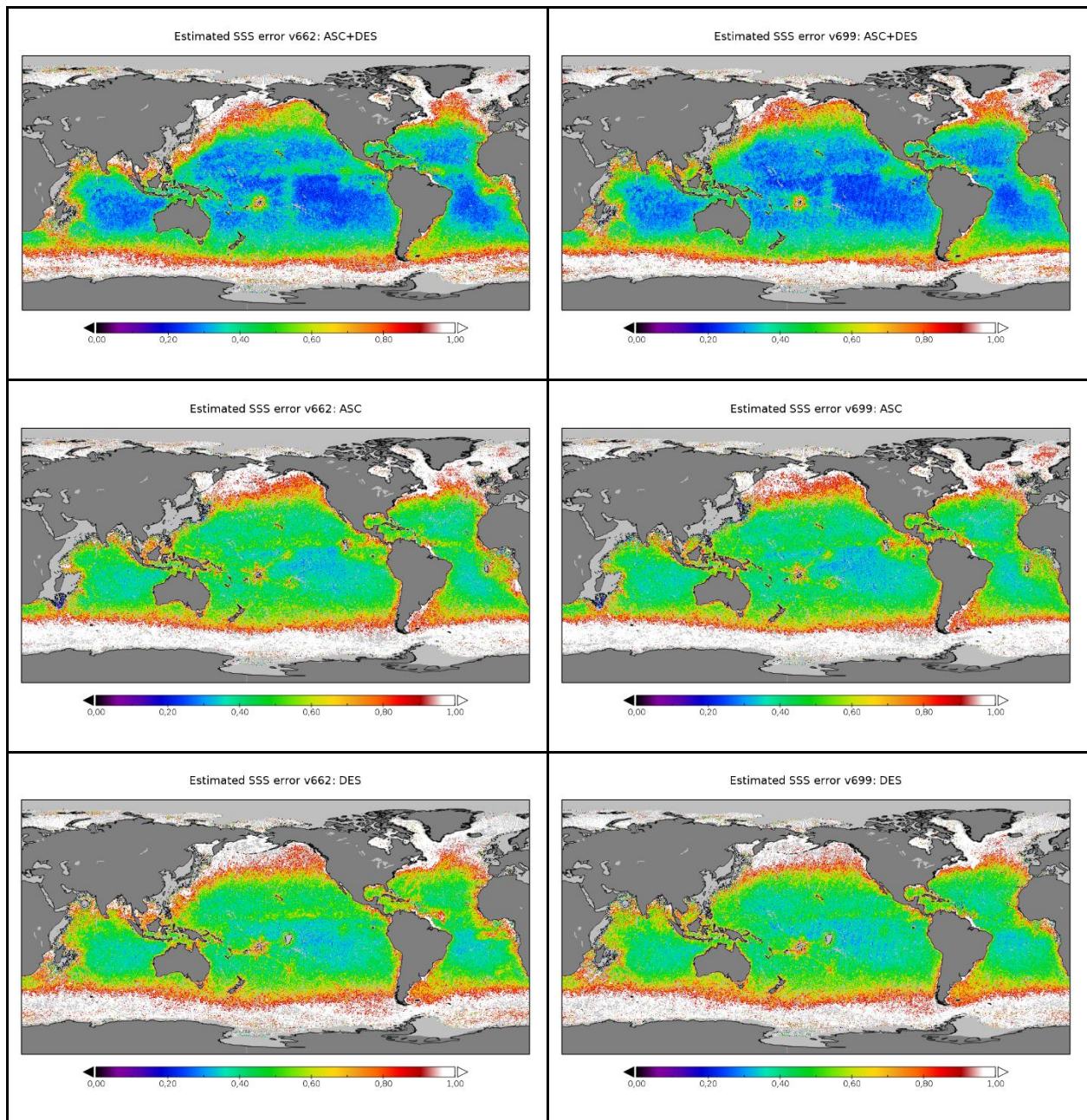


Figure 46: Estimated standard deviation of the SMOS SSS errors as result of the TC analysis. Left plots correspond to v662 and right plots to v700. First row presents the results for ascending and descending orbits together, the second row presents the results for ascending orbits, and the third row represents the results for descending orbits.

Estimated SSS v662 error - Estimated SSS v699 error: ASC+ DES

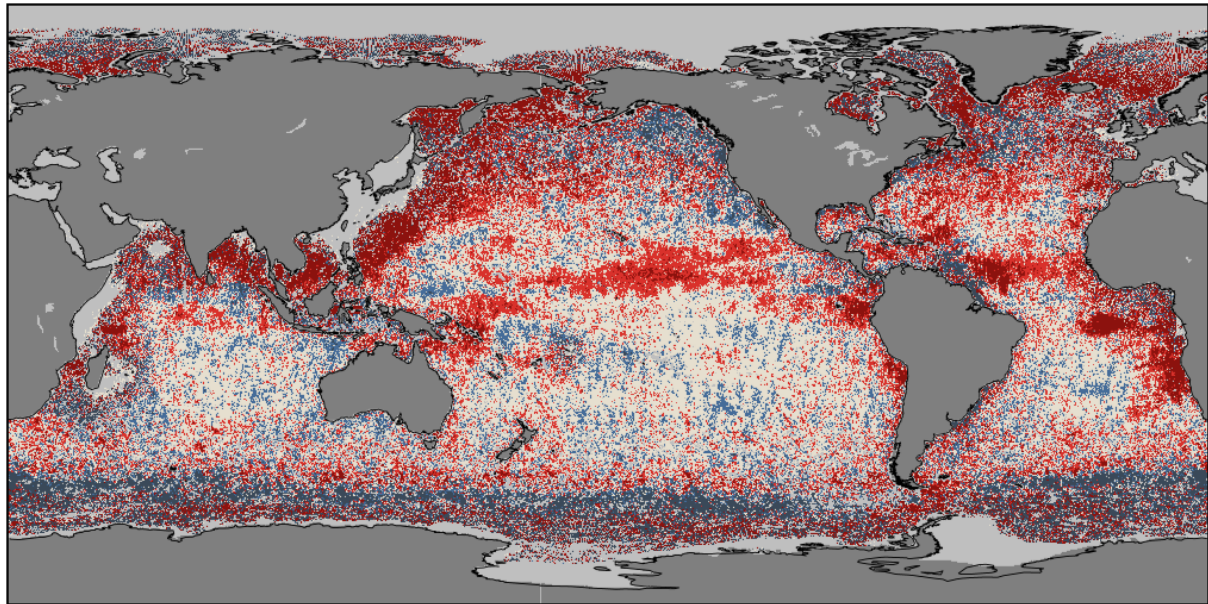


Figure 47: Differences between the estimated standard deviation of v662 and v700 for ascending and descending orbits together, such that the pixels in blue (red) represent regions where the error of v700 is larger (lower) than the one of v662.

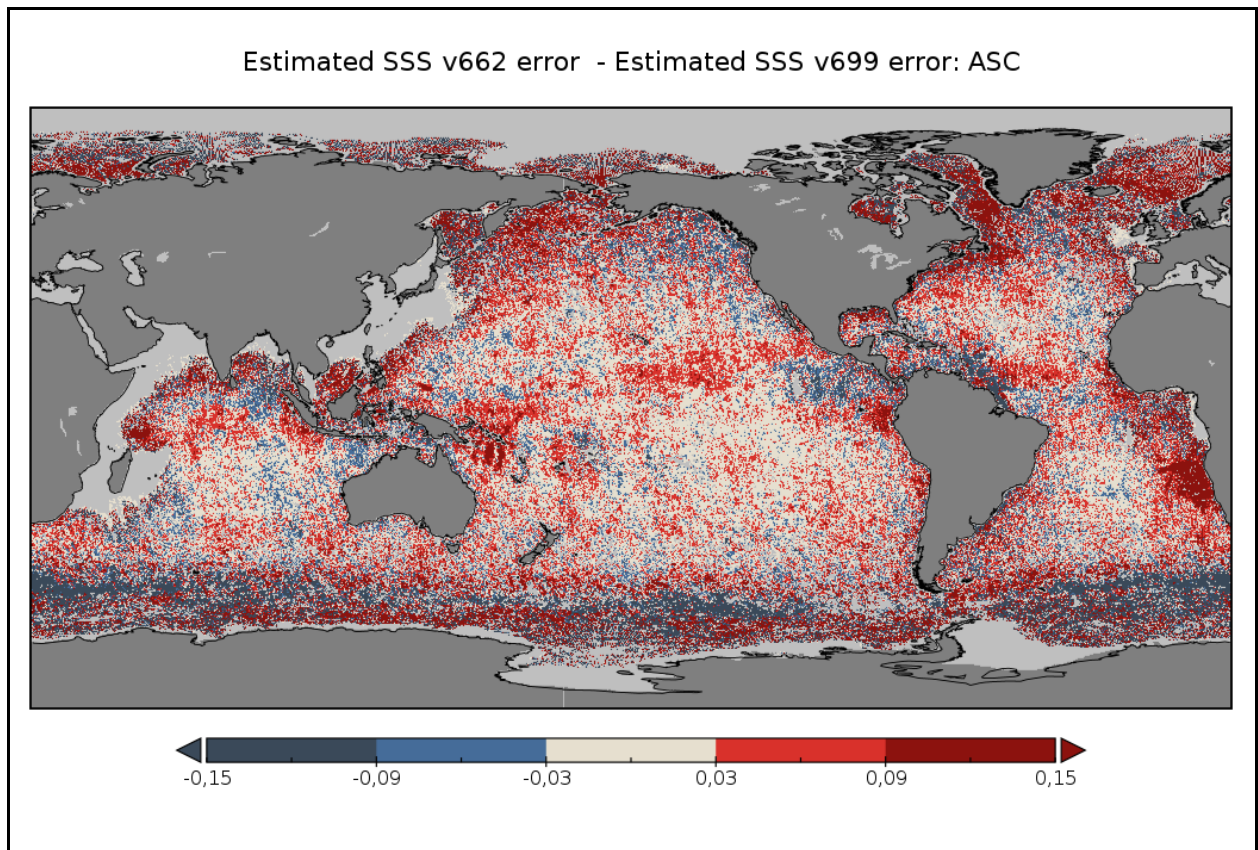


Figure 48: Differences between the estimated standard deviation of v662 and v700 for ascending orbits together, such that the pixels in blue (red) represent regions where the error of v700 is larger (lower) than the one from v662.

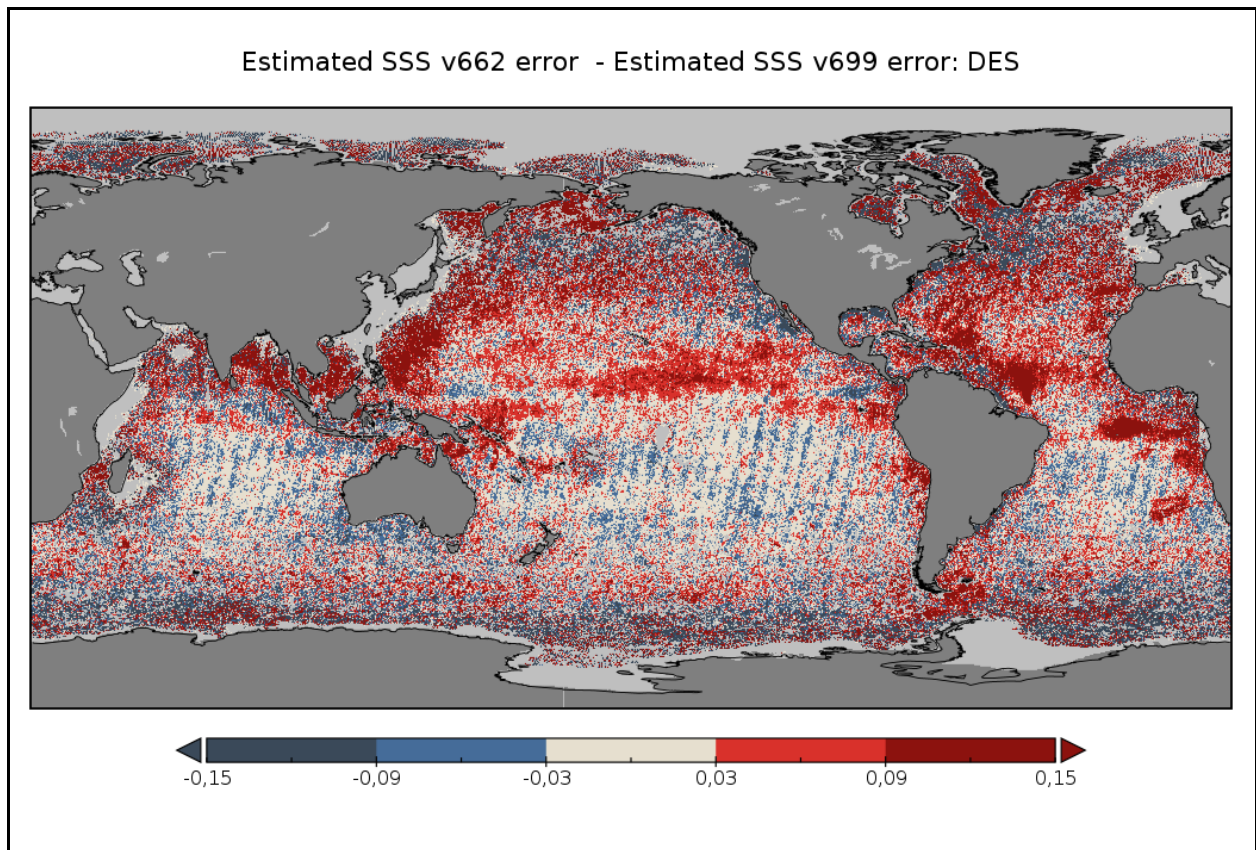


Figure 49: Differences between the estimated standard deviation of v662 and v700 for descending orbits together, such that the pixels in blue (red) represent regions where the error of v700 is larger (lower) than the one of v662.

2.3 Pi-MEP results: Global features and Geophysical dependencies

2.3.1 Spatial Maps of the Temporal mean and Std of Argo and L2v700 SSS difference (Δ SSS)

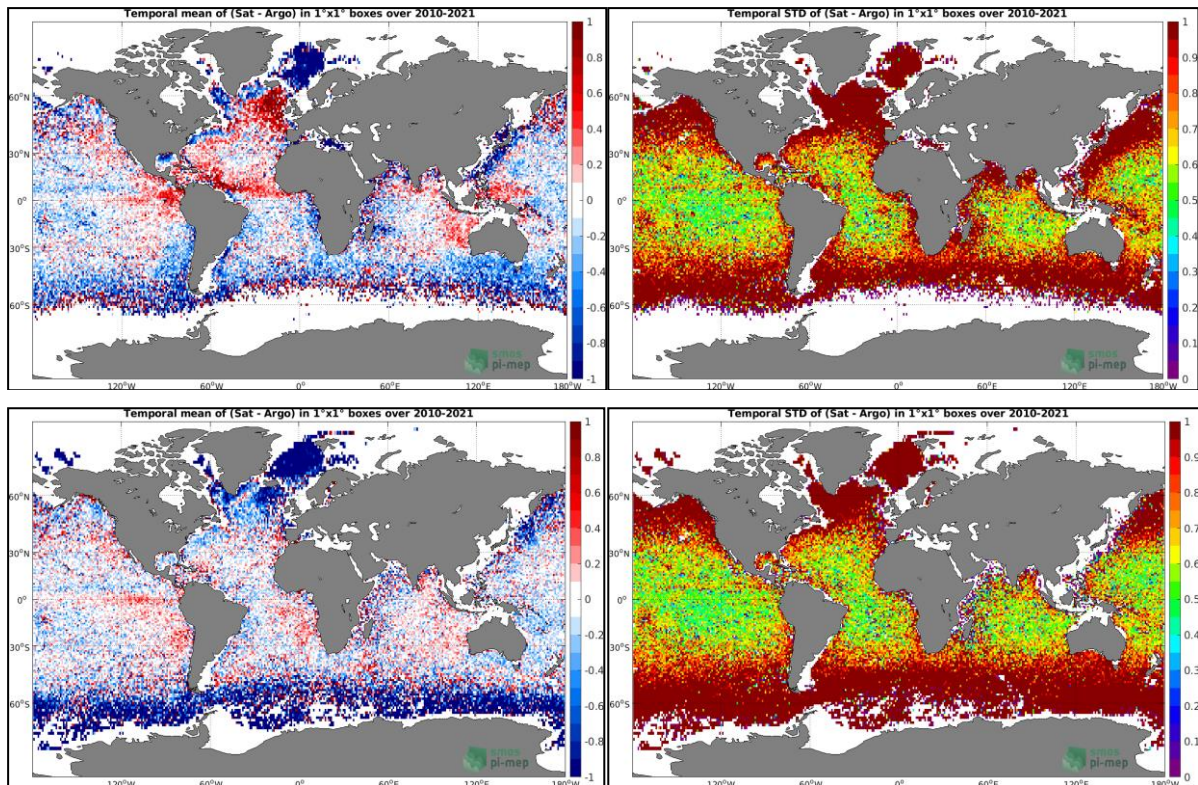


Figure 50: Temporal mean (left) and Std (right) of Δ SSS (Satellite - Argo). Top plots are for LSC corrected SSS from SMOS L2 v662. Bottom plots are for LSC corrected SSS from SMOS L2 v700. Only match-up pairs are used to generate these maps.

As illustrated in Figure 50, the temporal mean of the SSS difference (SMOS – Argo) in spatial bins of 1 degree over 2010-2021 exhibit more important biases for v662 (top) than for v700 (bottom) in the mid-latitudes for the LSC corrected SSS. The improvement is particularly clear in 1) the tropics where the L2 SSS v662 was too salty in the tropical and North Atlantic, tropical western Pacific, and in the Indian Ocean, Northwest of Australia’s coasts and 2) the too fresh L2v662 SSS in the bay of Mexico, Gulf stream region and in the bands along south America and Africa (South of Equator) as well as south of Australia, are now much closer to Argo data with v700. There is nevertheless significant degradation at high latitudes with v700: in the Southern Ocean (south of $\sim 50^\circ$) and north of $\sim 60^\circ\text{N}$, where the L2 SSS is now significantly fresher than Argo and fresher than v662.

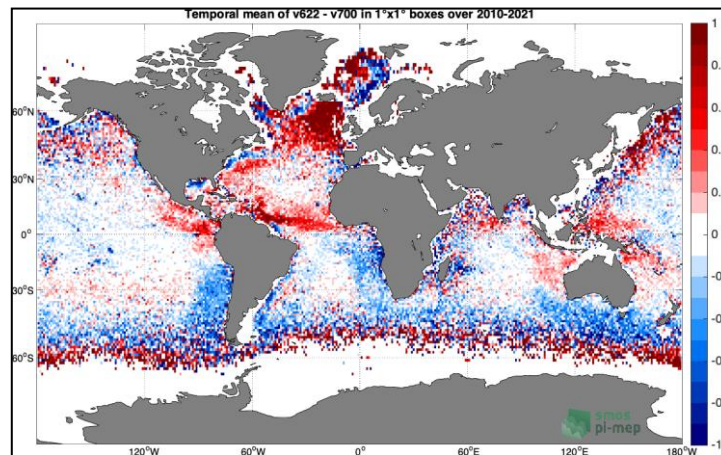


Figure 51 : Temporal mean of the SSS difference (SMOS v662 – SMOS v700) in spatial bins of 1 degree over 2010-2021.

As illustrated in Figure 51, the impact of the new L2 v700 with the new L1 v724 (3rd Mission reprocessing baseline) is to diminish the most important mid-latitude biases that were found along the continent.

2.3.2 Time series of the monthly median and Std of in situ and satellite SSS and of the difference (Δ SSS) at Global Scale

In the top panel of Figure 52, we show the time series of the monthly median SSS estimated over the full Global Ocean Pi-MEP region for both SMOS SSS L2 v700 (ESA) satellite SSS product (in black) and the Argo in situ dataset (in blue) at the collected Pi-MEP match-up pairs. In the middle panel, we show the time series of the monthly median of Δ SSS (Satellite - Argo) for the collected Pi-MEP match-up pairs and estimated over the full Global Ocean Pi-MEP region. In the bottom panel, we show the time series of the monthly standard deviation of Δ SSS (Satellite - Argo) for the collected Pi-MEP match-up pairs and estimated over the full Global Ocean Pi-MEP region.

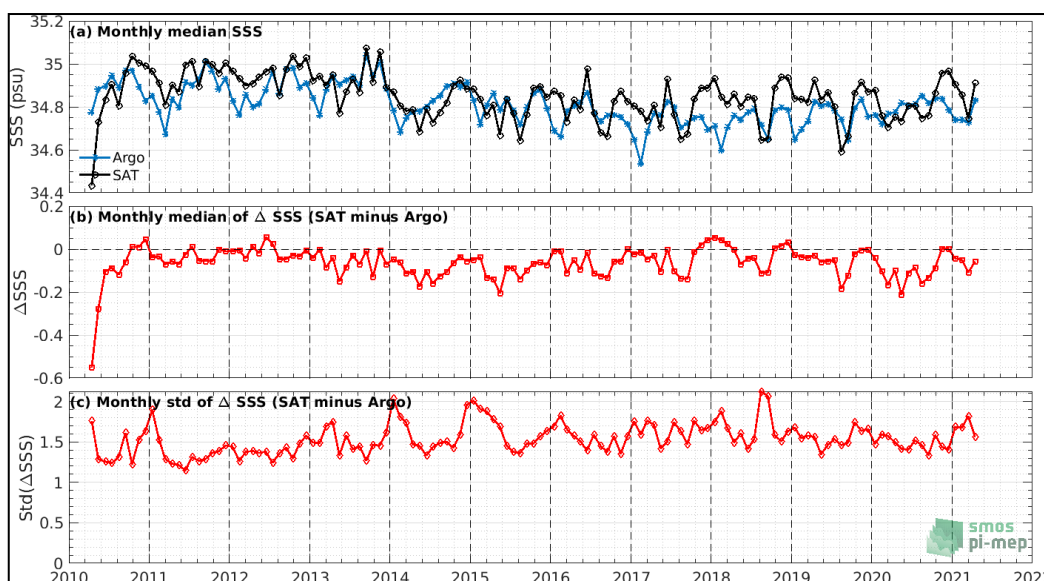


Figure 52: Time series of the monthly median SSS (top), median of Δ SSS (SMOS L2v700 - Argo) and Std of SSS (Satellite - Argo) over the Global Ocean Pi-MEP region considering all matchups collected by the Pi-MEP.

As found, the median and std L2v700 difference with Argo SSS at global scale are stable in time, if not considering the commissioning phase period.

2.3.3 Time series of the monthly median and Std of in situ and satellite SSS and of the difference (Δ SSS) sorted by latitudinal bands

In Figure 53, time series of the monthly median (red curves) of Δ SSS (L2v700 - Argo) and ± 1 Std (black vertical thick bars) as function of time for all the collected Pi-MEP match-up pairs estimated over the Global Ocean Pi-MEP region and for the full satellite product period are shown for different latitude bands: (a) 80°S-80°N, (b) 20°S-20°N, (c) 40°S-20°S and 20°N-40°N and (d) 60°S-40°S and 40°N-60°N.

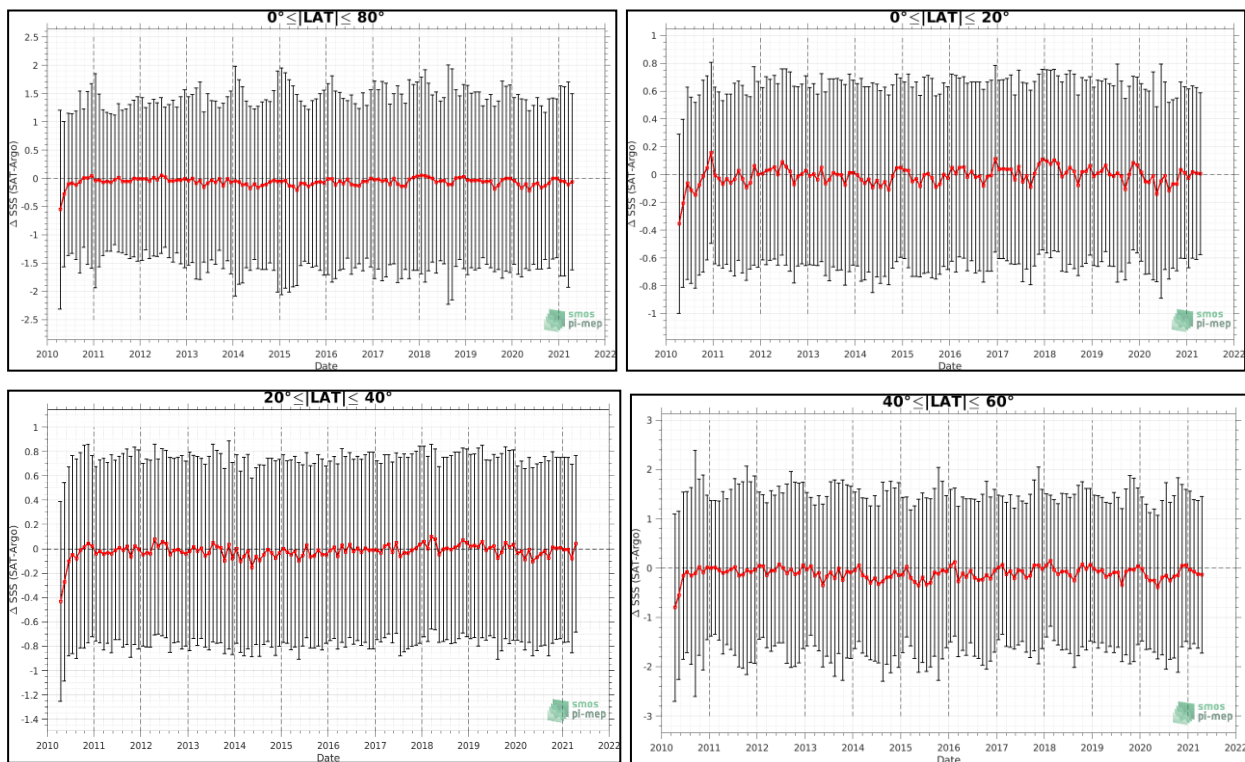


Figure 53: Monthly median (red curves) of Δ SSS (Satellite - Argo) and ± 1 Std (black vertical thick bars) as function of time for all the collected Pi-MEP match-up pairs estimated over the Global Ocean Pi-MEP region and for the full satellite product period are shown for different latitude bands: (a) 80°S-80°N, (b) 20°S-20°N, (c) 40°S-20°S and 20°N-40°N and (d) 60°S-40°S and 40°N-60°N.

While the std of Δ SSS (L2v700 - Argo) strongly varies from one latitudinal band to the next, the mean bias with respect to Argo is around 0 and stable in time in all the bands.

2.3.4 Δ SSS (L2v700 - Argo) sorted as function of geophysical parameters

In Figure 54, we classify the match-up differences Δ SSS (Satellite L2v700 - in situ) between SMOS SSS L2 v700 (ESA) and Argo SSS as function of the geophysical conditions at match-up points. The median and std of Δ SSS (Satellite - Argo) is thus evaluated as function of the:

- In situ SSS values per bins of width 0.2,
- In situ SST values per bins of width 1°C,
- ASCAT daily wind values per bins of width 1 m/s,



- CMORPH 3-hourly rain rates per bins of width 1 mm/h,
- Distance to coasts per bins of width 50 km,
- In situ measurement depth (if relevant).

As found:

- L2 v700 is unbiased with Argo SSS for SSS > 31 pss. For fresher Argo SSS, an increasing negative bias appears with increased Argo SSS freshening. This was not observed with v662.
- L2v700 is unbiased with Argo SST for SST > 15°C. Below 15°C, an increasing fresh bias is observed as SST decreases, reaching -2 pss (SMOS fresher than Argo) at SST=-2°C. There is a net change in the bias pattern with respect v662 in the lowest SST.
- L2v700-Argo SSS bias as a function of wind speed is very similar than with L2v662-Argo SSS but a bit reduced in the highest winds (at 20 m/s, it was ~-1 pss with v662 and it is now ~-0.6 pss with v700).
- Biases as a function for rain-rate and with respect distance to coasts are almost unchanged from v662 to v700.

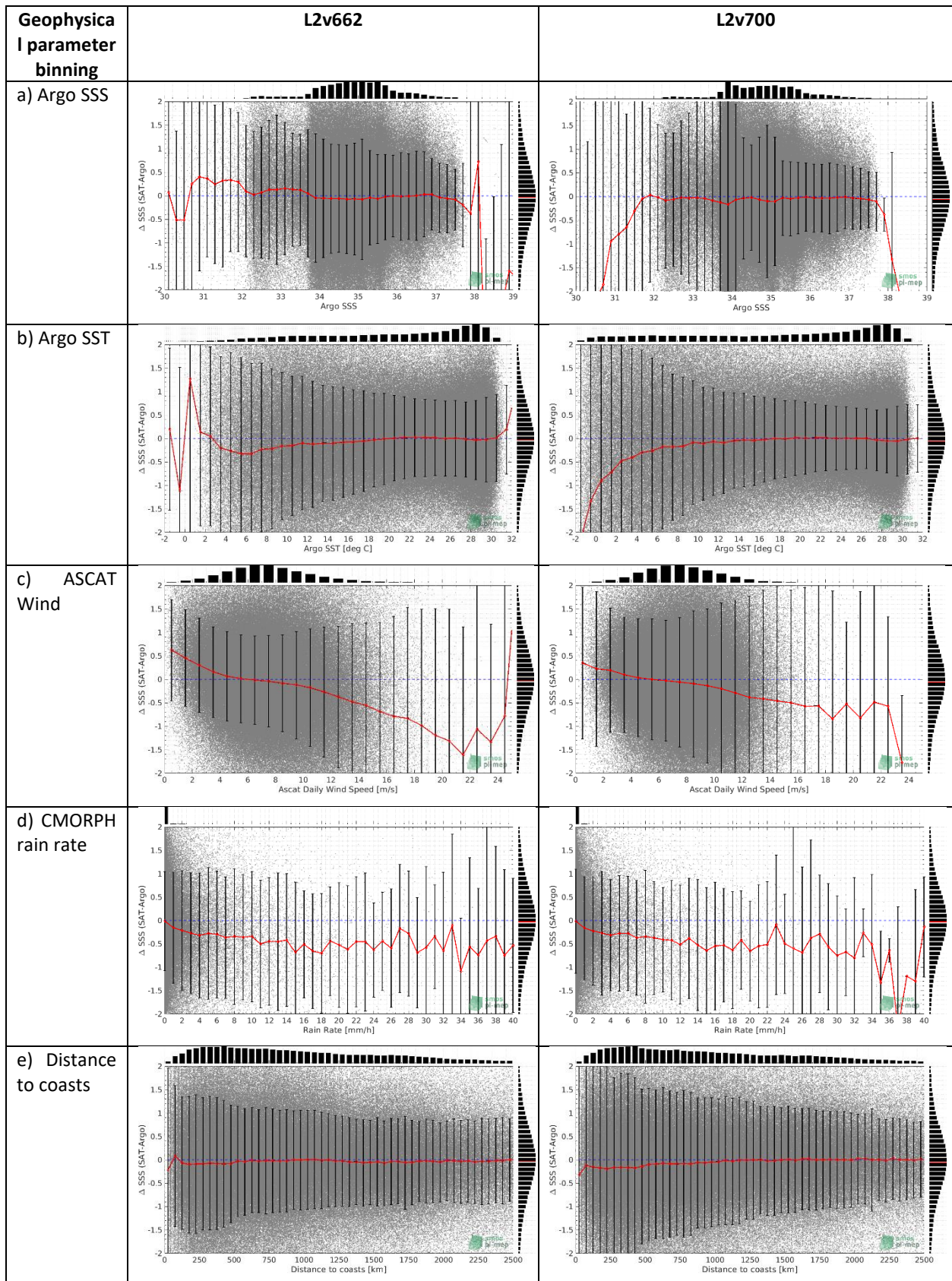


Figure 54: Δ SSS (Satellite - Argo) sorted as function of Argo SSS values a), Argo SST b), ASCAT Wind speed c), CMORPH rain rate d) and distance to coast e). In all plots the median and Std of Δ SSS for each bin is indicated by the red curves and black vertical thick bars (± 1 Std). Left column is for v662. Right column is for v700.

3 Assessment at TB level

3.1 Geophysical Model Function vs SMOS TBs

Despite improvements in the Level-1 processing and in the ocean forward model, biases between measurements and the model remain and they exhibit clear seasonal and latitudinal patterns that are quite consistent over the years. In what follows the measured and modelled first Stokes parameter will be compared in terms of the differences averaged over the alias-free and extended alias-free portions of the field of view. The ocean model used here is close to that used by the L2OS Processor. The main difference is that here the Klein and Swift (1977) rather than the Boutin-Vergely (2020) dielectric model is used to compute the specular emission. The choice of dielectric model may have a small impact on the Hovmöller plots shown here.

3.2 Hovmöller plots

Figure 55 shows the two portions of the field of view used to compute the Hovmöller plots that follow. Both the alias-free (AF-FoV, left) and extended alias-free (EAF FoV, right) domains exclude a set of boundary pixels within 0.044 director cosine units of the boundaries of these domains.

Figure 56 shows the time-latitude bias (SMOS-model) in the first Stokes parameter divided by two ($(T_x+T_y)/2$) over most of the mission (2010-March 2020). There is an overall positive bias in both the AF and EAF FoV averages, with an apparent season cycle with a peak around October in descending passes. Overall, the amplitude of the bias is on the order of 0.5 to 2 kelvin depending on the time of year, and the amplitude of the seasonal cycle does not exhibit a clear variation with the slow interannual solar flux variation shown in the section on sun glint.

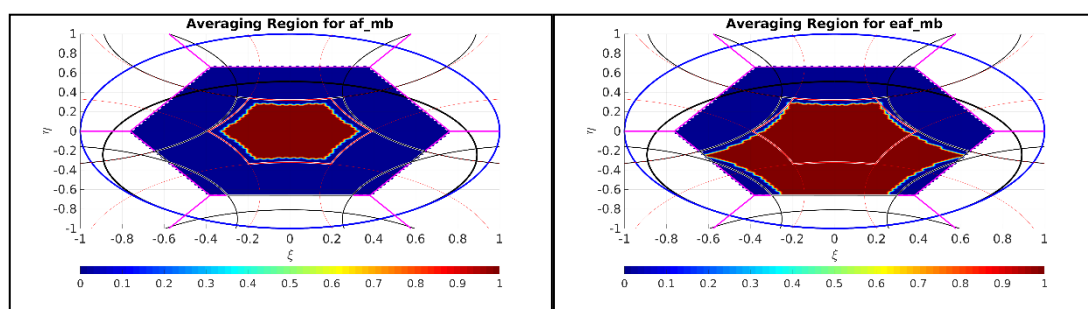


Figure 55: Definition of region of the unit circle used to produce the Hovmöller plots (in red). Left: AF-FoV; Right: EAF-FoV.

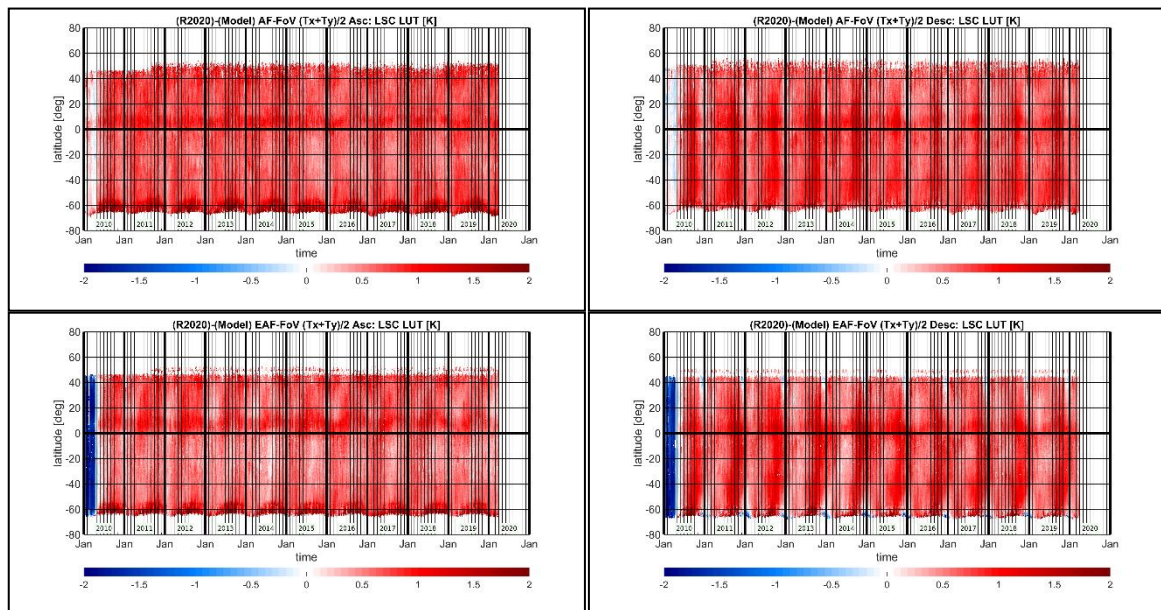


Figure 56: Hovmöller plots showing the time-latitude evolution of the bias in $(Tx+Ty)/2$ for the alias-free field of view (AF-FoV, top panels) and extended alias-free field of view (EAF-FoV, bottom panels) defined in the previous figure. Left: ascending passes; right: descending passes. No average bias has been removed in these plots. Units are kelvin.

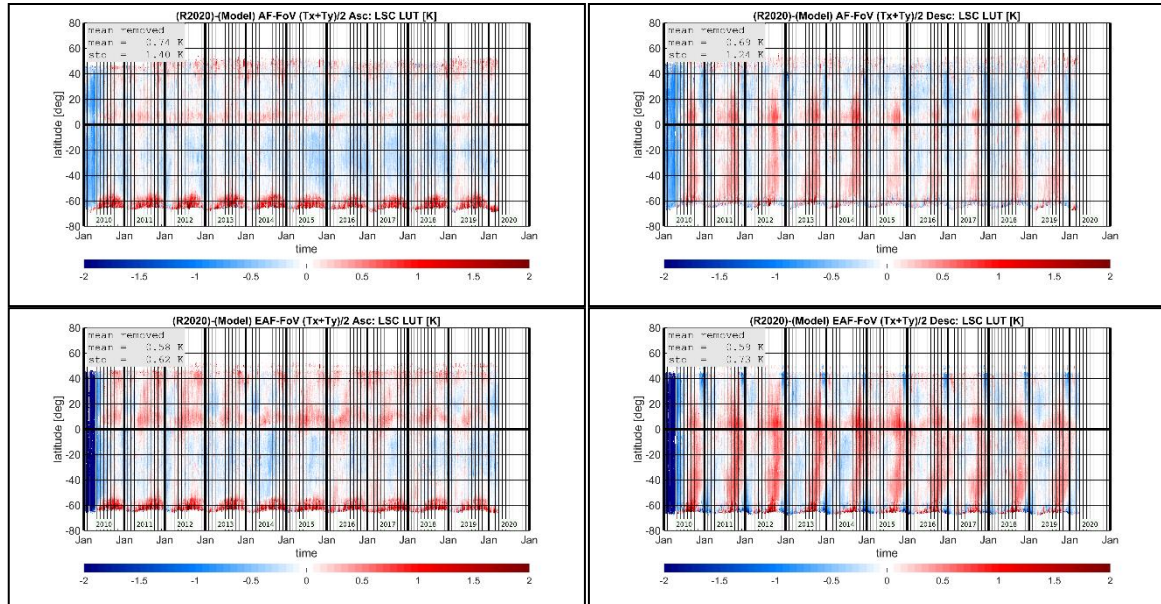


Figure 57: Same as the previous figure except that in each plot the average has been removed to better reveal the seasonal and latitudinal variations.

Seasonal and latitudinal variations are more clearly seen in Figure 57, in which the average biases over each panel in Figure 56 have been removed. The seasonal variation is most clearly visible in descending passes for both the AF and EAF FoV, in which there is a distinct peak in the (SMOS-model) differences south of about 10°N in the September-November period of each year. This seasonal cycle is even more clearly seen in Figure 58, in which the top panels show the descending-ascending difference. The bottom panels in this figure show the celestial sky glint for descending passes. For both portions of the field of view considered here, the seasonal peak in the model sky glint is prominent in both hemispheres but the strongest part of the cycle does not extend to 60°S latitude. This is in contrast with the (SMOS-model) differences, which are most prominent in the southern hemisphere and extend to 60°S in descending passes.

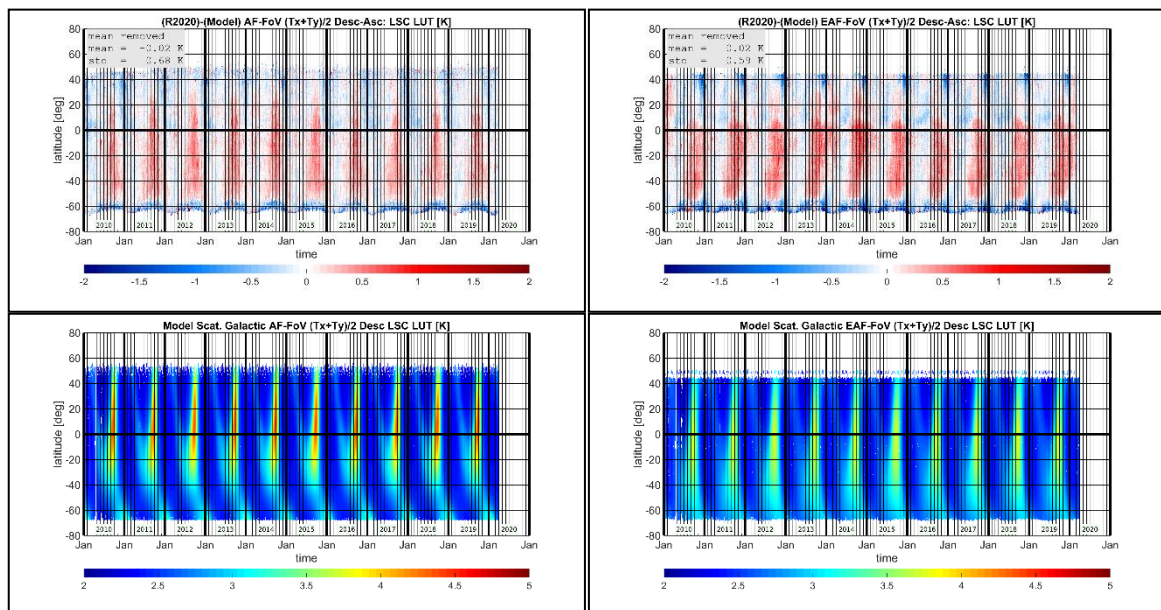


Figure 58: Top row: Hovmöller plots showing the difference between ascending and descending pass bias in $(Tx+Ty)/2$. Bottom row: Celestial sky glint for descending passes for the alias-free (left) and extended alias-free (right) fields of view. Units are kelvin.

4 Ascending/descending Differences

4.1 Latitudinal drift

4.1.1 Results from ISAS

Using comparisons done along the validation protocol procedure (see section 2.1), we have looked at latitudinal differences between SMOS and ISAS salinities. This has been done for ascending and descending orbits separately, considering only SSS_uncorr further than 1000km from land (similar signatures are expected with SSS_corr).

On ascending orbits (Figure 59), v700 SSS is lower than v662 SSS almost everywhere. Negative biases in boreal summer in the north (~up to 40N) are more negative in v700 than in v662. We observe interannual variation of the biases, e.g., more positive in the northern hemisphere in 2012-2014 and in the southern hemisphere in 2012-2014, possibly related to strong sun activity period. We observe much more negative biases close to sea ice with v700, due to ice-sea contamination which was partially compensated in v662 by dielectric constant positive biases in cold waters.

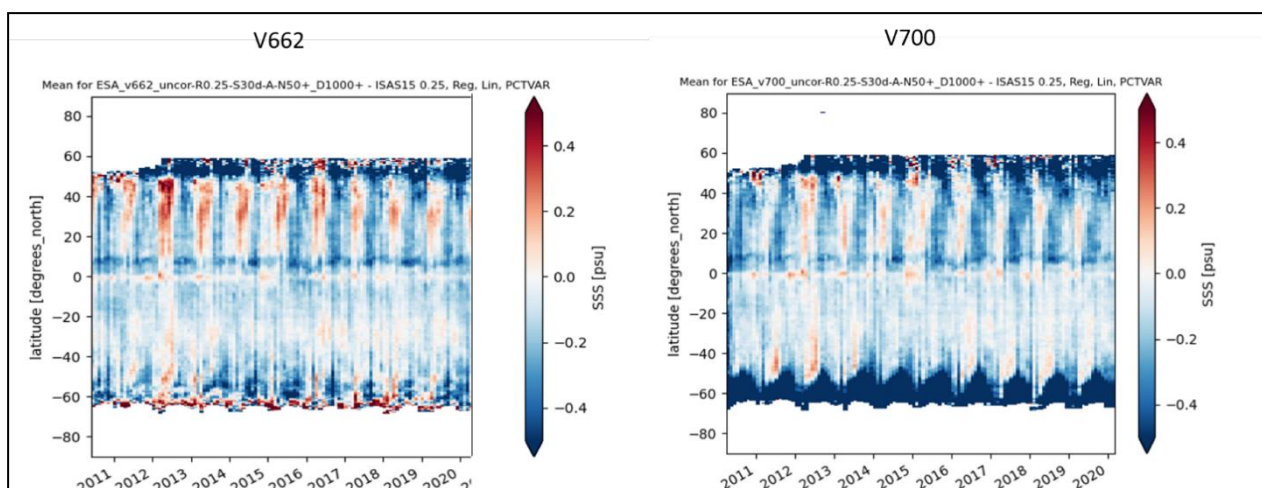


Figure 59: SMOS SSS minus ISAS SSS further than 1000km from coast. Ascending orbits. Only SMOS pixels with more than 50 measurements and only ISAS SSS with PCTVAR<80% have been retained. Left v662, right v700.

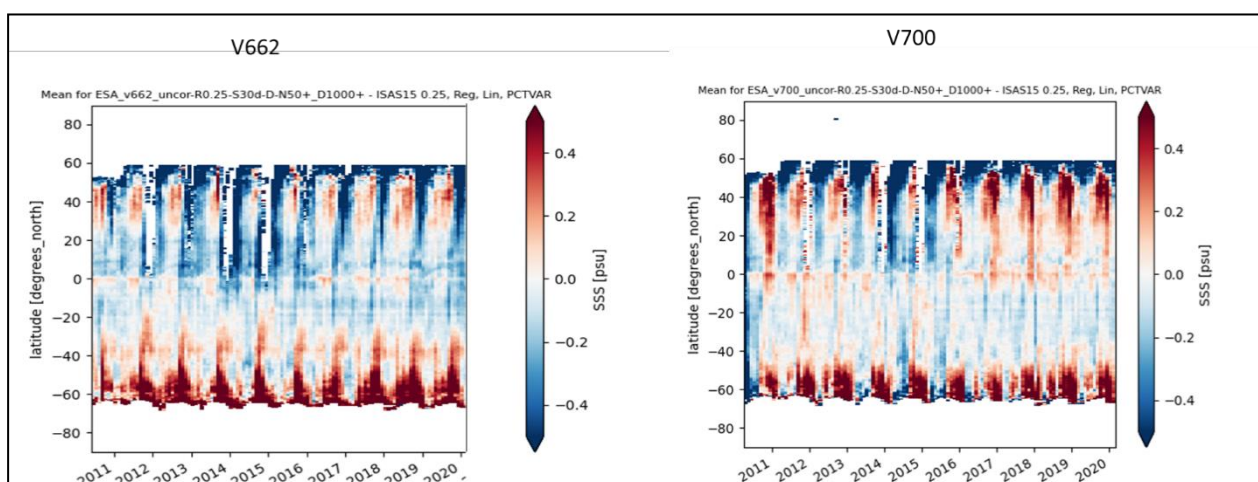


Figure 60: SMOS SSS minus ISAS SSS further than 1000km from coast. Descending orbits. Only SMOS pixels with more than 50 measurements and only ISAS SSS with PCTVAR<80% have been retained. Left v662, right v700.

On descending orbits (Figure 60), we observe a net improvement in the southern hemisphere north of 50°S, partly linked to the dielectric constant parametrization correction, but still seasonal and interannual variation of the biases in the north. Positive biases are observed in the northern and in the southern high latitudes for ~Sept-Feb, in phase in N and S hemisphere, so unlikely a signature of an ocean process.

We now look at the standard deviation of monthly differences as a function of latitude. This metric describes the stability of the biases along the various longitudes.

On ascending orbits (Figure 61), std difference is reduced in the tropics and mid latitudes but increased at high latitudes due to ice-sea contamination which varies with longitudes according to the location of the ice edge.

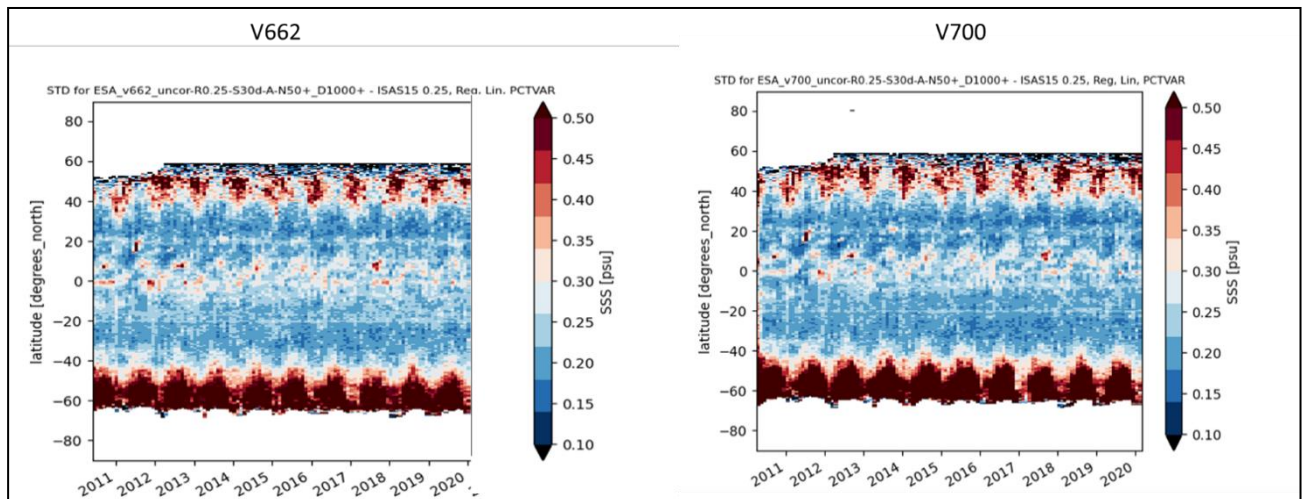


Figure 61: Standard deviation of SMOS SSS minus ISAS SSS further than 1000km from coast. Ascending orbits. Only SMOS pixels with more than 50 measurements and only ISAS SSS with PCTVAR<80% have been retained. Left v662, right v700.

On descending orbits (Figure 62), std difference is reduced in mid latitudes. It seems more scattered in the first half of the mission.

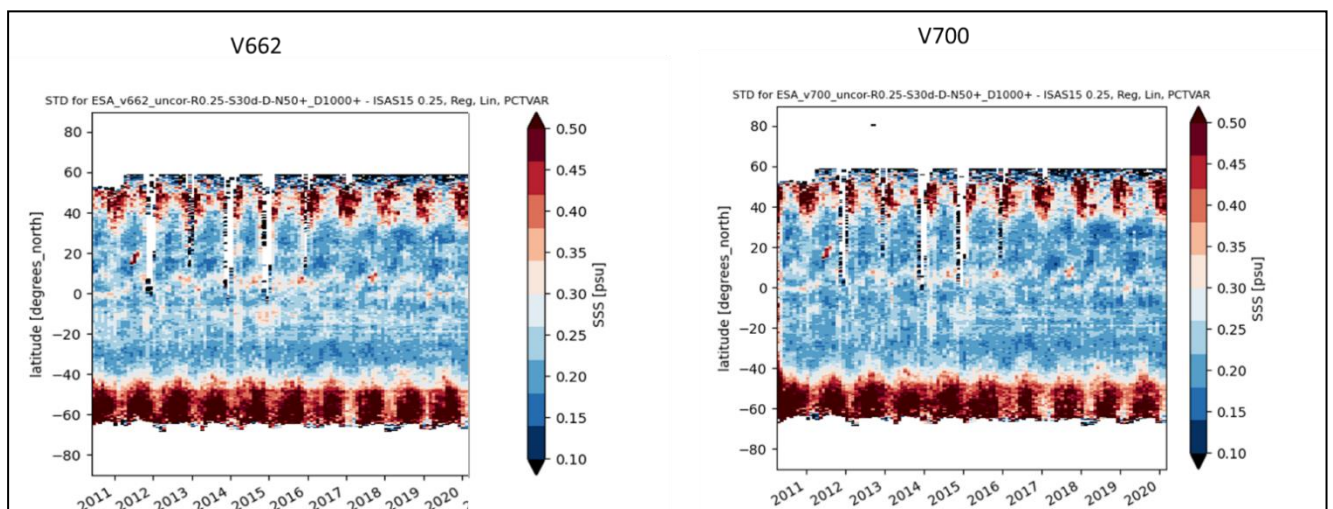


Figure 62: Standard deviation of SMOS SSS minus ISAS SSS further than 1000km from coast. Descending orbits. Only SMOS pixels with more than 50 measurements and only ISAS SSS with PCTVAR<80% have been retained. Left v662, right v700.

In summary:

- Latitudinal seasonal biases have changed between v662 and v700:
 - Ascending orbits:
 - Lower contrast between biases at mid latitude South and North but biases more negative in boreal summer.
 - Ice contamination in the South.
 - Descending orbits:
 - Positive biases have reduced in the South but have increased in the North.

4.1.2 Results from Pi-MEP: L2OSv700/V662 biases versus Argo as a function of Latitude for Ascending + Descending

Zonally-averaged latitudinal mean Δ SSS (L2v700 LSC corrected –Argo) is significantly reduced compared to Δ SSS (L2v662 LSC corrected –Argo) in the band 50°S-40°N (see Figure 63). This is true also (but to a less extent) for un-corrected SSS. The bias Δ SSS (L2v700 LSC corrected –Argo) is strongly increased North of 60°N and south of 50°S.

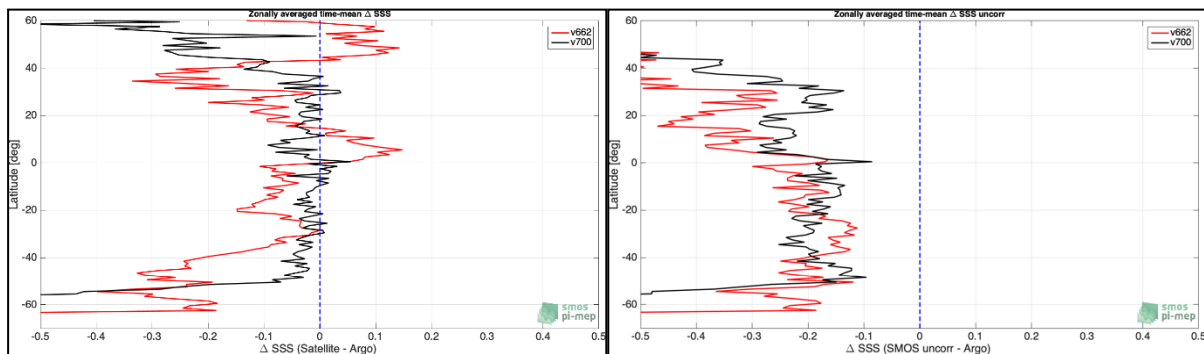


Figure 63 : Zonal mean of Δ SSS (SMOS - Argo) for all the collected Pi-MEP match-up pairs estimated 2010-2021. SMOS V662 is in red and v700 in Black using SSS corrected (left) and uncorrected (right).

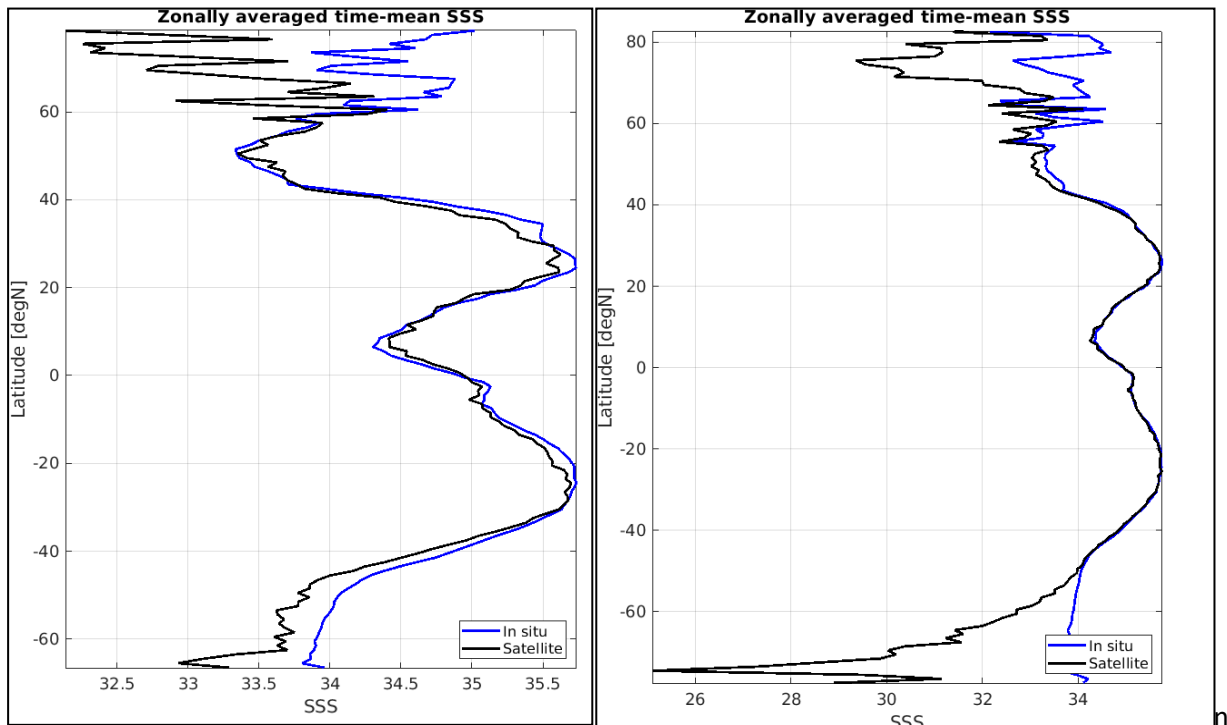


Figure 64: Left panel: Zonal mean SSS from SMOS SSS L2 v662 LSC corrected (black) and from Argo (blue). Right panel: same but for L2 v700.

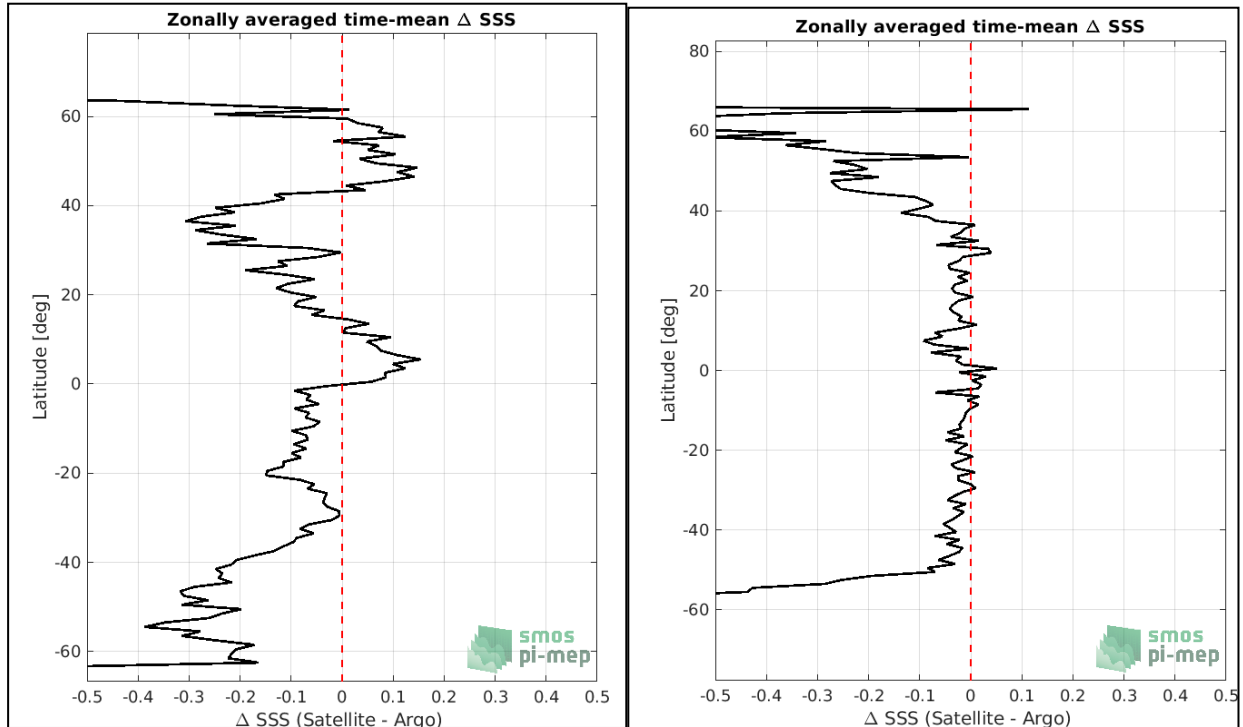


Figure 65: Left panel: Zonal mean of the difference Δ SSS between SMOS SSS L2 v662 LSC corrected and Argo (blue). Right panel: same but for L2 v700.

4.1.3 L2OSv700/V662 biases versus Argo as a function of Latitude for Ascending

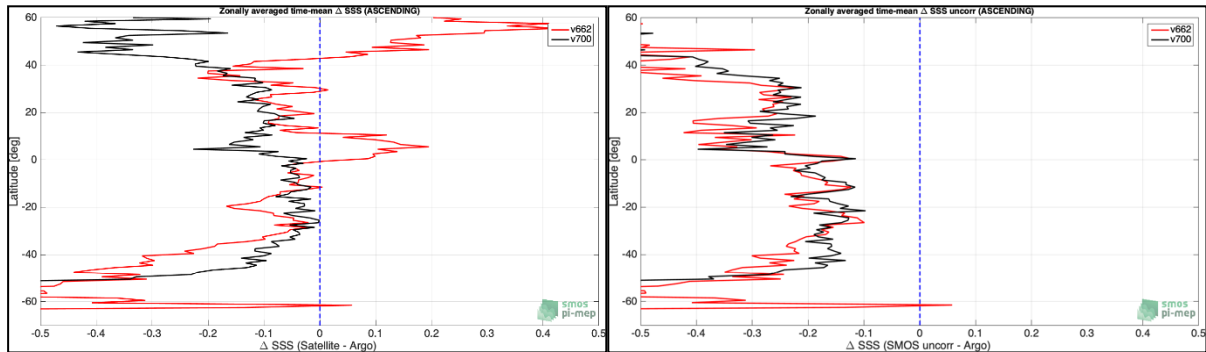


Figure 66 : Zonal mean of ΔSSS (SMOS - Argo) for all the collected Pi-MEP match-up pairs estimated 2010-2021. SMOS V662 is in red and v700 in Black using Ascending SSS corrected (left) and uncorrected (right).

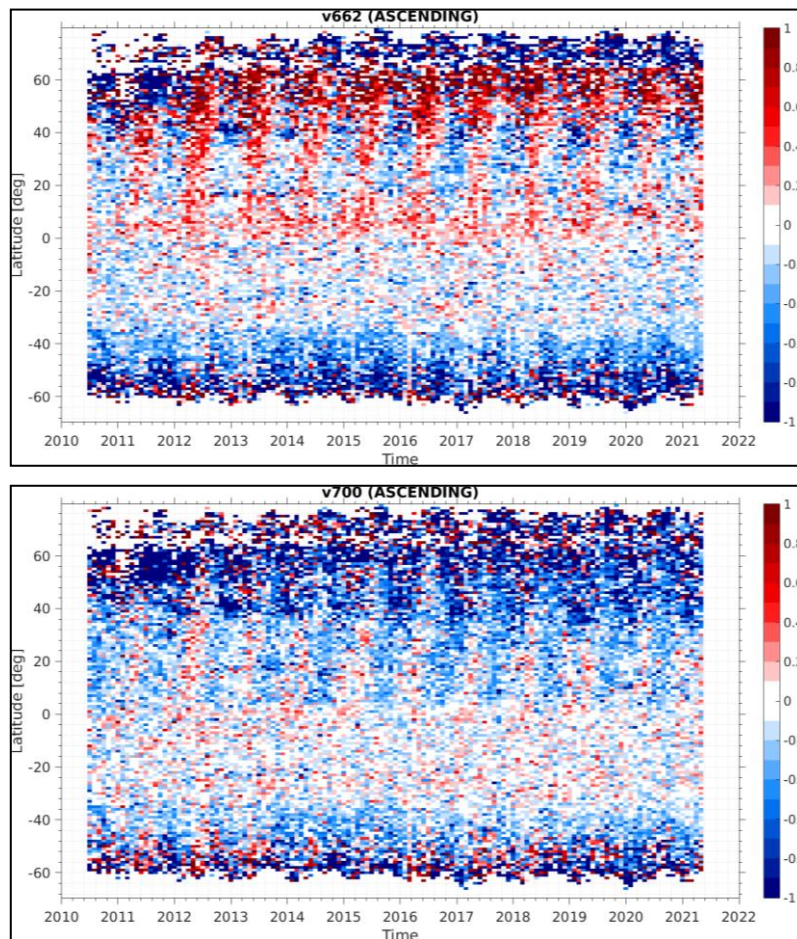


Figure 67: Latitude-time Hovmöller diagram of the difference between SMOS and Argo SSS for Ascending passes v662 (Top) and v700 (Bottom)

4.1.4 L2OSv700/V662 biases versus Argo as a function of Latitude for Descending

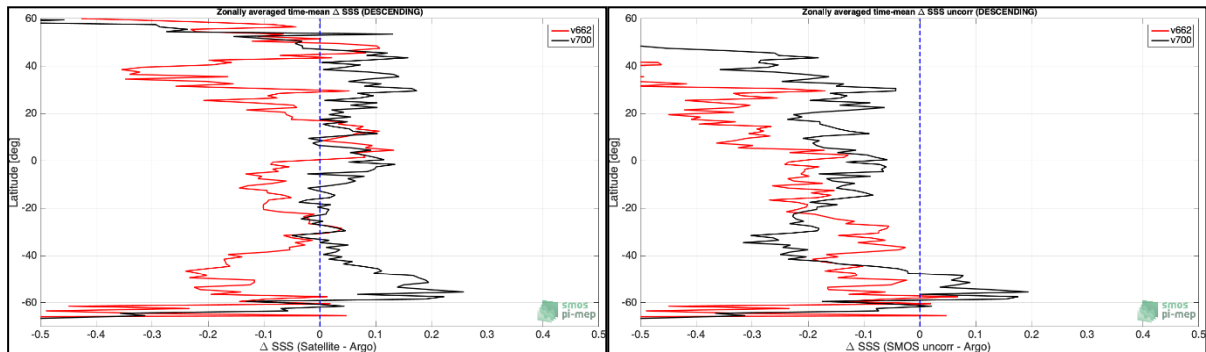


Figure 68 : Zonal mean of Δ SSS (SMOS - Argo) for all the collected Pi-MEP match-up pairs estimated 2010-2021. SMOS V662 is in red and v700 in Black using Descending SSS corrected (left) and uncorrected (right).

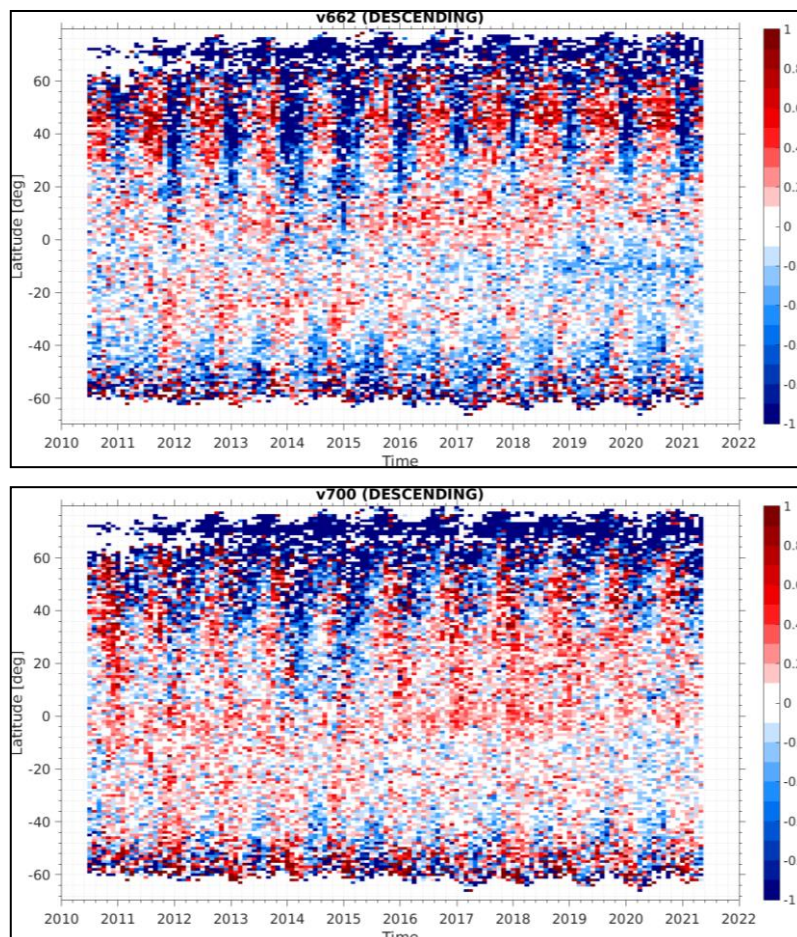


Figure 69: Latitude-time Hovmöller diagram of the difference between SMOS and Argo SSS for Descending passes v662 (Top) and v700 (Bottom)

4.1.5 L3 (from v700/V662) biases versus Argo as a function of Latitude for Ascending + Descending

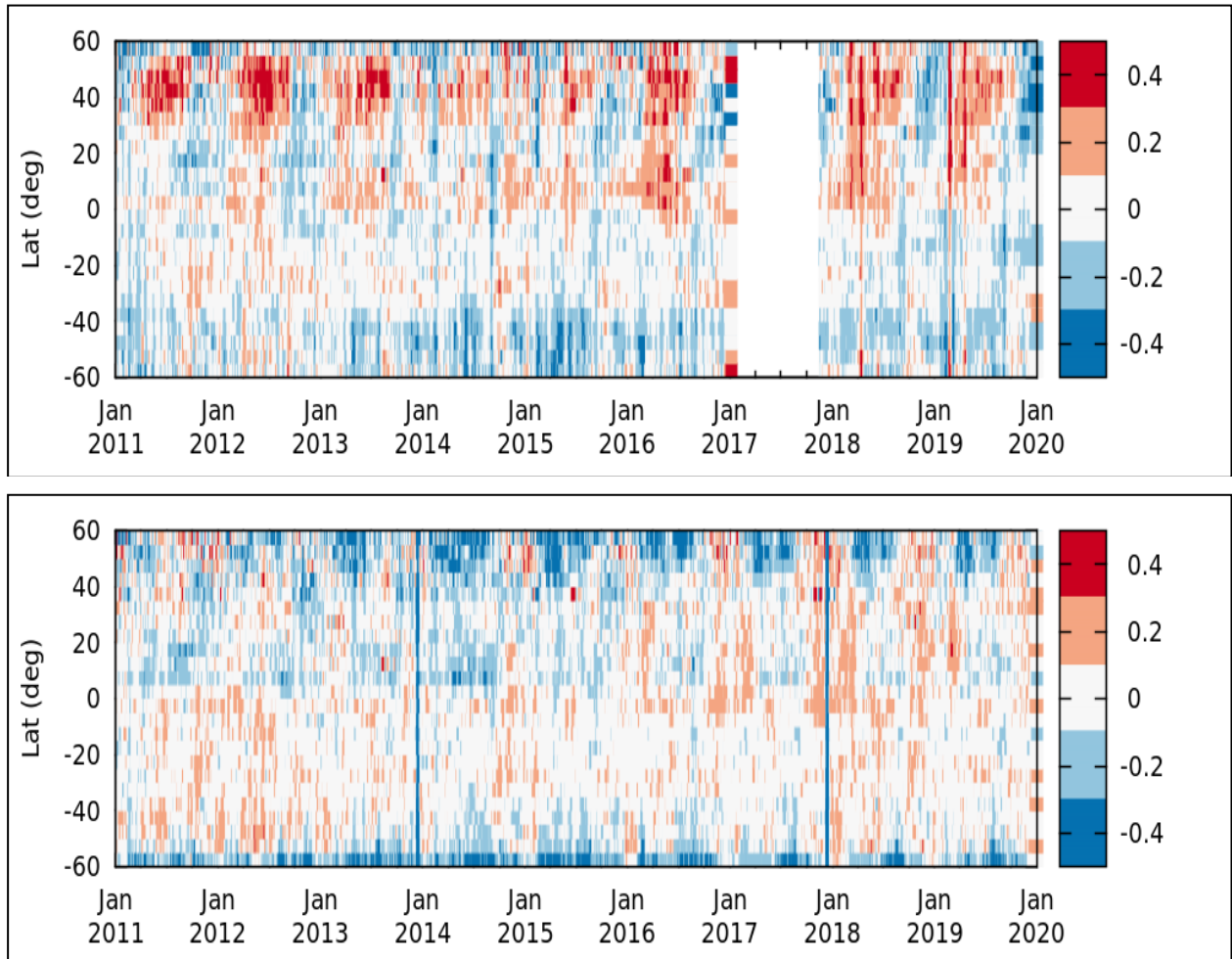


Figure 70: Latitudinal and seasonal biases: ASC+DES. Top is v662. Bottom is v700.

Northern Hemisphere: Positive and seasonal biases in v662 become negative in v700.

Southern Ocean: More negative biases in v700.

5 Land/sea, Ice/sea, and foreign sources of error

5.1 Land/sea contamination assessment

Several analyses have been conducted by ESLs to assess the L2OS data quality changes as a function of the distance to coasts. These include:

- 1) Forward model vs SMOS Tb Data inter-comparisons.
- 2) Analyses of the L2OS SSS/in situ matchups with Argo and TSG data (PI-MEP).
- 3) Validation protocol Results and L3 validation with Argo.

We detail those results in the following sections and provide a summary in a last section.

5.1.1 Forward model vs SMOS Tbs intercomparison

In these first analyses, we compared one month (July 2016) of SMOS L1 Tbs collected at each grid point in the full EAF-FOV with the L2OS forward model prediction using either SMAP or ISAS SSS as a reference. We then mapped the standard deviation of $(Tx_{smos} - Tx_{model})$ and $(Ty_{smos} - Ty_{model})$ for all differences at each grid point on the map. Note that we use either RSS weekly SMAP SSS or ISAS monthly maps as a reference to evaluate the forward model.

5.1.1.1 LSC Uncorrected Ascending passes

To illustrate the impact of the land-sea contamination correction on the reprocessed L2OS, the Figure 71 (next page) shows, for LSC uncorrected ascending passes dTx and dTy biases, the standard deviations of individual reconstructed brightness temperatures over July 2016 as a function of dwell line location on earth as well as the corresponding biases in retrieved SSS (simple linearized method) and dwell line averaged brightness temperature first Stokes parameter divided by two. Note that the reference SSS is obtained from the RSS weekly SMAP SSS.

As found, there are clear increase of the standard deviation of the differences between the model and SMOS data for both Tx and Ty in a band extending ~ 500 kms from coastlines ($> 2K$). For SSS uncorrected, this translates into a strongly underestimated (by 1-4 pss) SSS in this near coastal spatial domain with respect SMAP data. The underestimation is higher at high latitudes.

5.1.1.2 LSC corrected Ascending passes

The following Figure 72 shows the impact of the empirical LSC correction. The biases in both the retrieved SSS and dwell-line averaged first Stokes parameter are significantly reduced compared with the uncorrected results. Moreover, the standard deviations of the individual Tx and Ty brightness temperatures at any given position on earth are significantly reduced in the vicinity of the coastlines. As in the first figure the reference SSS is the RSS weekly SMAP SSS.

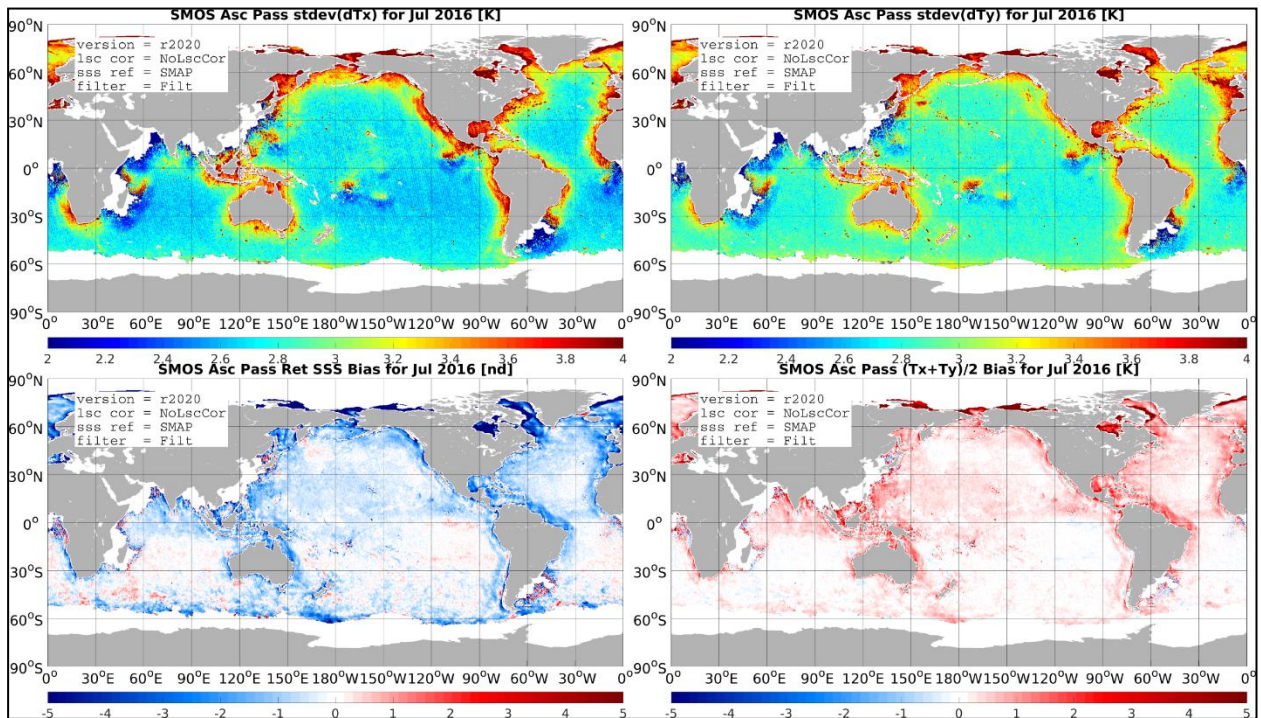


Figure 71: **LSC uncorrected ascending passes**, the Standard deviations of the differences in individual reconstructed brightness temperatures between forward model (forced using **RSS SMAP weekly SSS**) and SMOS Tbs over July 2016 as a function of dwell line location on earth. (top left) Std(dTx) (top right) Std(dTy). (Bottom Left) Corresponding biases in retrieved SSS (simple linearized method) and (bottom right) dwell line averaged brightness temperature first Stokes parameter divided by two.

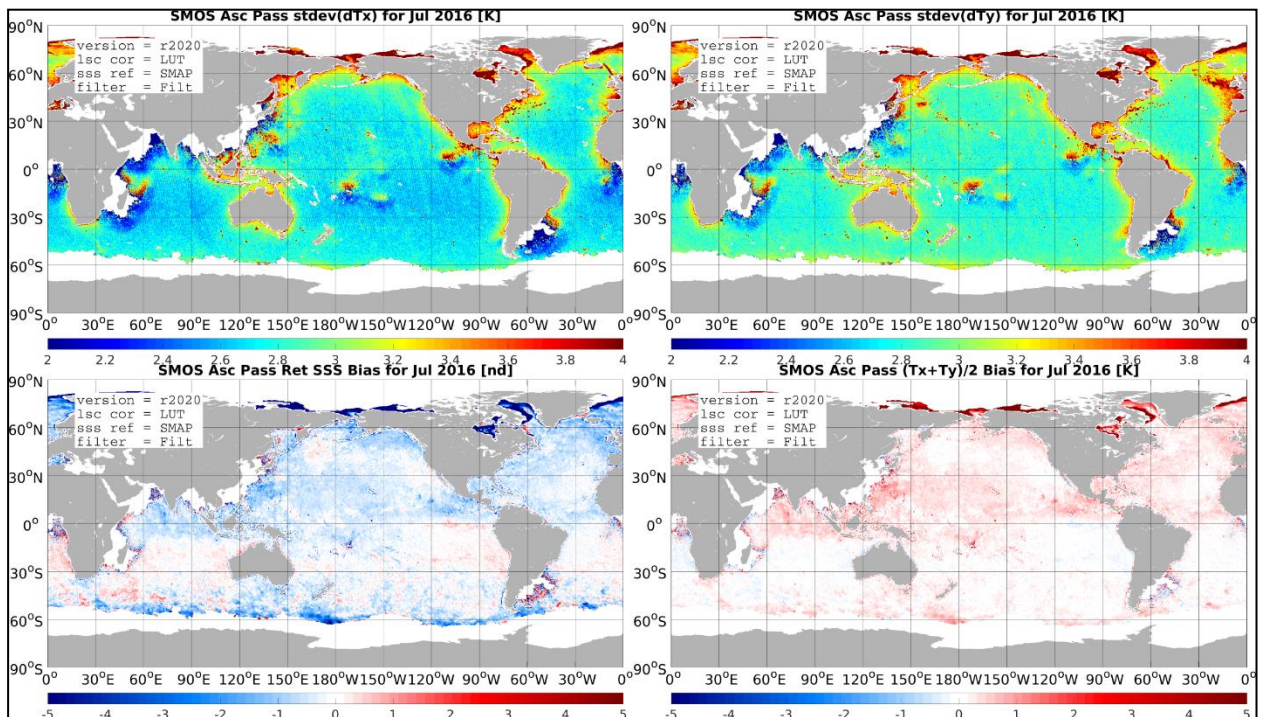


Figure 72: **LSC corrected Ascending passes**, the Standard deviations of the differences in individual reconstructed brightness temperatures between forward model (forced using **RSS SMAP weekly SSS**) and SMOS Tbs over July 2016 as a function of dwell line location on earth. (top left) Std(dTx) (top right) Std(dTy). (Bottom Left) Corresponding biases in retrieved SSS (simple linearized method) and (bottom right) dwell line averaged brightness temperature first Stokes parameter divided by two.

5.1.1.3 Impact of the reference SSS on Ascending passes

To see the impact of the use of SMAP SSS as opposed to ISAS SSS as the reference, the following figure shows the same fields as the previous figure except with ISAS as the reference SSS. The biases and standard deviations are similar except near river plumes where biases with respect to ISAS tend to be larger than with SMAP as the reference (as expected).

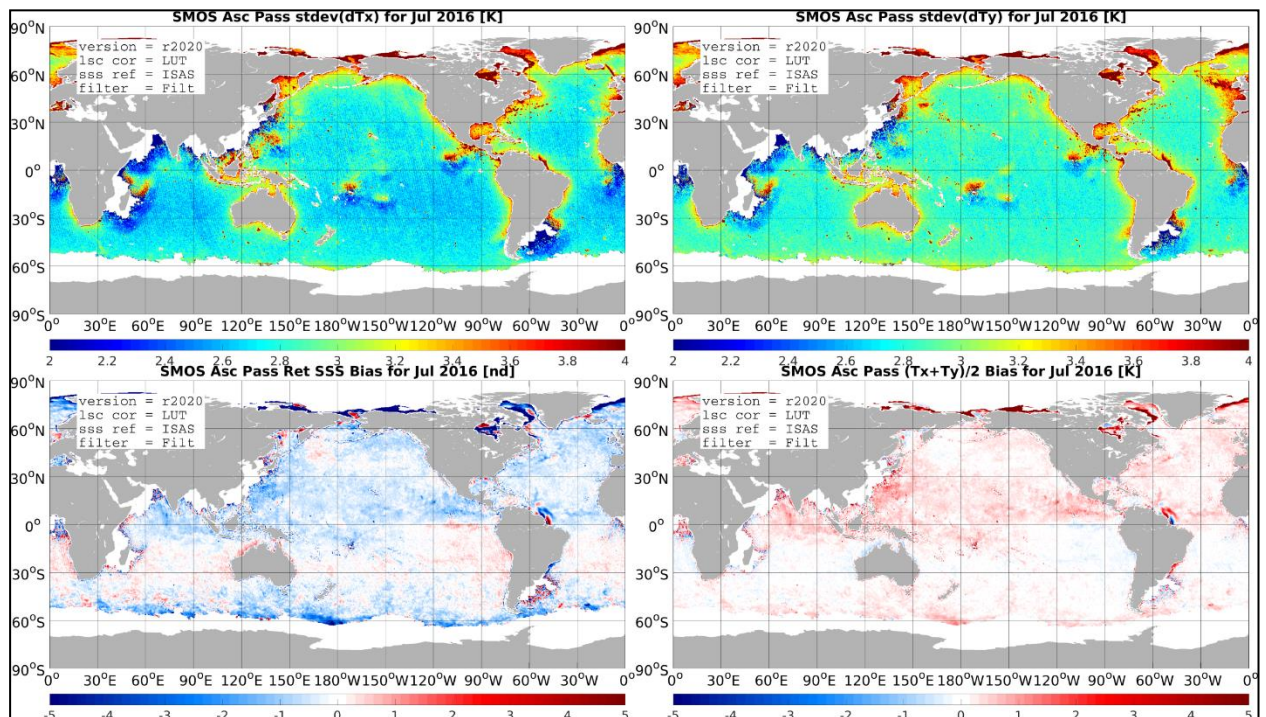


Figure 73: LSC corrected Ascending passes, the Standard deviations of the differences in individual reconstructed brightness temperatures between forward model (forced using ISAS weekly SSS) and SMOS Tbs over July 2016 as a function of dwell line location on earth. (top left) Std(dTx) (top right) Std(dTy). (Bottom Left) Corresponding biases in retrieved SSS (simple linearized method) and (bottom right) dwell line averaged brightness temperature first Stokes parameter divided by two.

5.1.1.4 LSC uncorrected and corrected Descending passes

Analogous figures for descending passes show similar results, although the LSC bias patterns differ from those for ascending passes. Figure 74 is the same as Figure 71 except for descending passes. Note that the continental 'shadow' exhibits a different pattern than for ascending passes.

For corrected salinities, the bias and std are significantly reduced also in descending passes except north of 60°N with a significant over-freshening of SMOS SSS vs SMAP SSS and a smaller amplitude but detectable bias showing successive negative and positive oscillations from 30°S to 60°S.

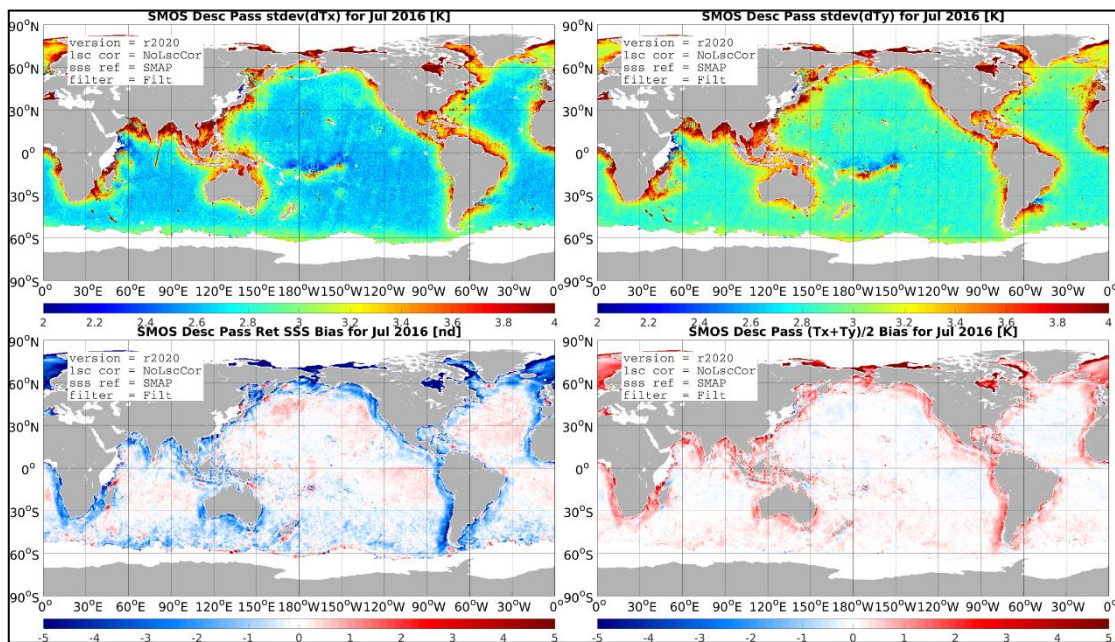


Figure 74: LSC uncorrected descending passes, the Standard deviations of the differences in individual reconstructed brightness temperatures between forward model (forced using RSS SMAP weekly SSS) and SMOS Tbs over July 2016 as a function of dwell line location on earth. (top left) Std(dTx) (top right) Std(dTy). (Bottom Left) Corresponding biases in retrieved SSS (simple linearized method) and (bottom right) dwell line averaged brightness temperature first Stokes parameter divided by two.

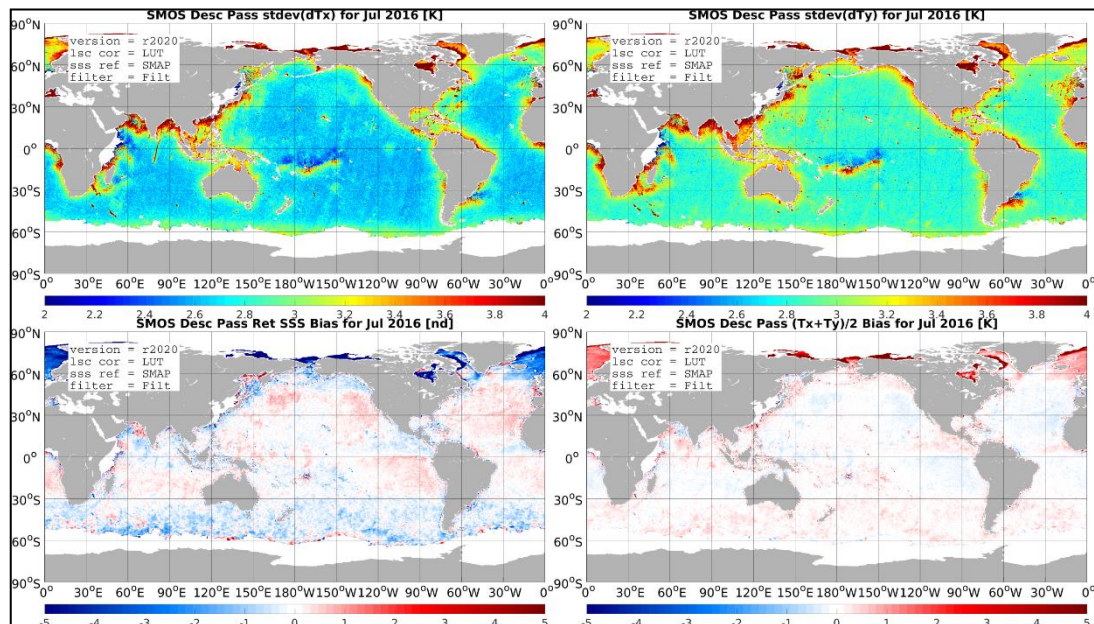


Figure 75 LSC corrected descending passes, the Standard deviations of the differences in individual reconstructed brightness temperatures between forward model (forced using RSS SMAP weekly SSS) and SMOS Tbs over July 2016 as a function of dwell line location on earth. (top left) Std(dTx) (top right) Std(dTy). (Bottom Left) Corresponding biases in retrieved SSS (simple linearized method) and (bottom right) dwell line averaged brightness temperature first Stokes parameter divided by two.

5.1.1.5 Impact of the reference SSS on Descending passes

To see the impact of the use of SMAP SSS as opposed to ISAS SSS as the reference, Figure 76 shows the same fields as the previous figure except with ISAS as the reference SSS. The biases and standard deviations are similar except near river plumes where biases with respect to ISAS tend to be larger than with SMAP as the reference (as expected).

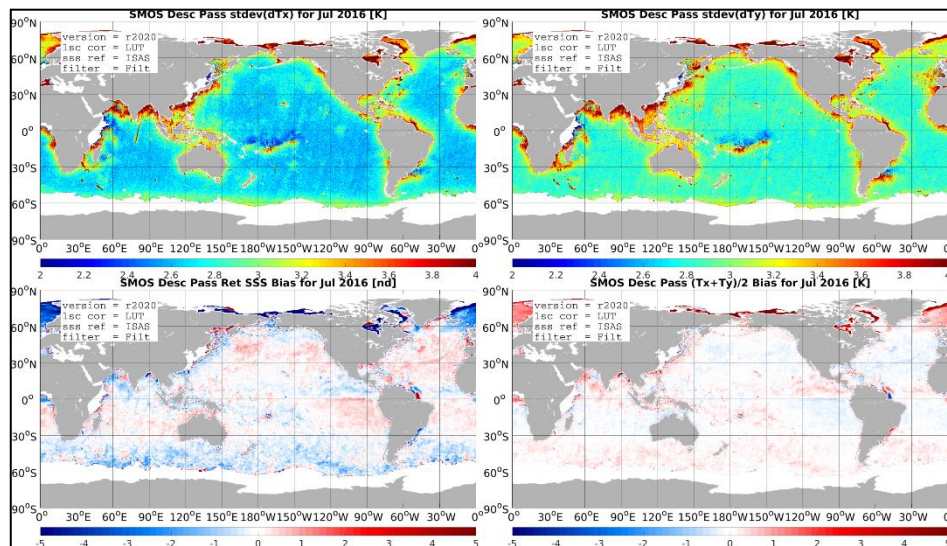


Figure 76: LSC corrected Descending passes, the Standard deviations of the differences in individual reconstructed brightness temperatures between forward model (forced using ISAS monthly SSS) and SMOS Tbs over July 2016 as a function of dwell line location on earth. (top left) Std(dTx) (top right) Std(dTy). (Bottom Left) Corresponding biases in retrieved SSS (simple linearized method) and (bottom right) dwell line averaged brightness temperature first Stokes parameter divided by two.

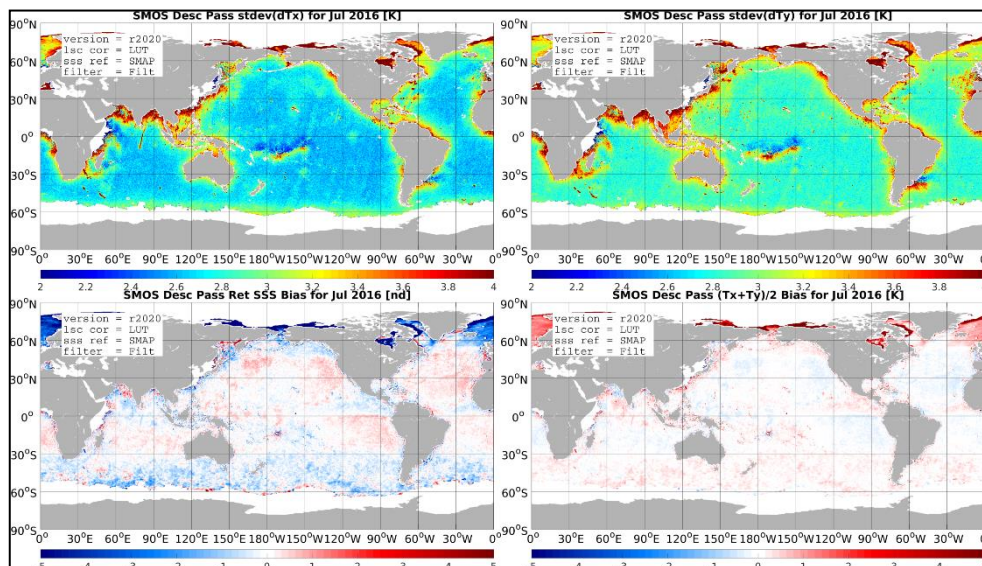


Figure 77 : LSC corrected Descending passes, the Standard deviations of the differences in individual reconstructed brightness temperatures between forward model (forced using RSS SMAP weekly SSS) and SMOS Tbs over July 2016 as a function of dwell line location on earth. (top left) Std(dTx) (top right) Std(dTy). (Bottom Left) Corresponding biases in retrieved SSS (simple linearized method) and (bottom right) dwell line averaged brightness temperature first Stokes parameter divided by two.

5.1.1.6 Impact of the LSC on the Ascending-Descending passes differences

The figure below shows the uncorrected difference between ascending and descending pass biases and brightness temperature standard deviations. The differing ascending and descending pass bias patterns appear as distinct shadows in both the retrieved SSS and first Stokes parameter bias maps. By contrast, the difference maps for the standard deviations show only very weak shadows, indicating that the increased Tb standard deviations in coastal areas exhibit only weak dependence on pass direction.

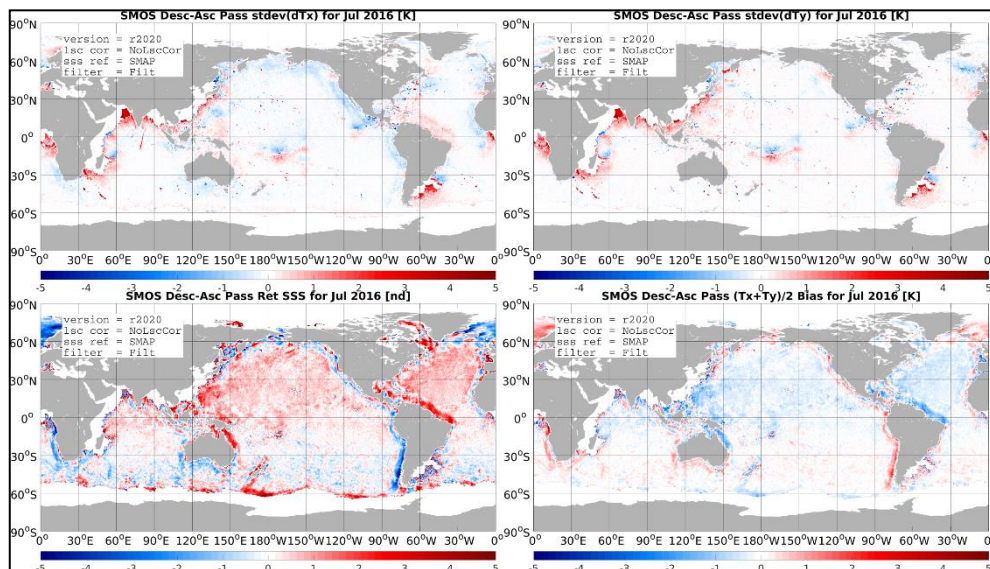


Figure 78: The **uncorrected difference** between ascending and descending pass biases (top left) and brightness temperature standard deviations (top right). Retrieved SSS difference between ascending and descending passes (bottom left) and First Stokes bias (bottom right). Forward model is using RSS SMAP.

The corresponding LUT-corrected maps (Figure 79) show virtually no shadows, suggesting that the LSC correction effectively reduces both the biases and Tb standard deviations.

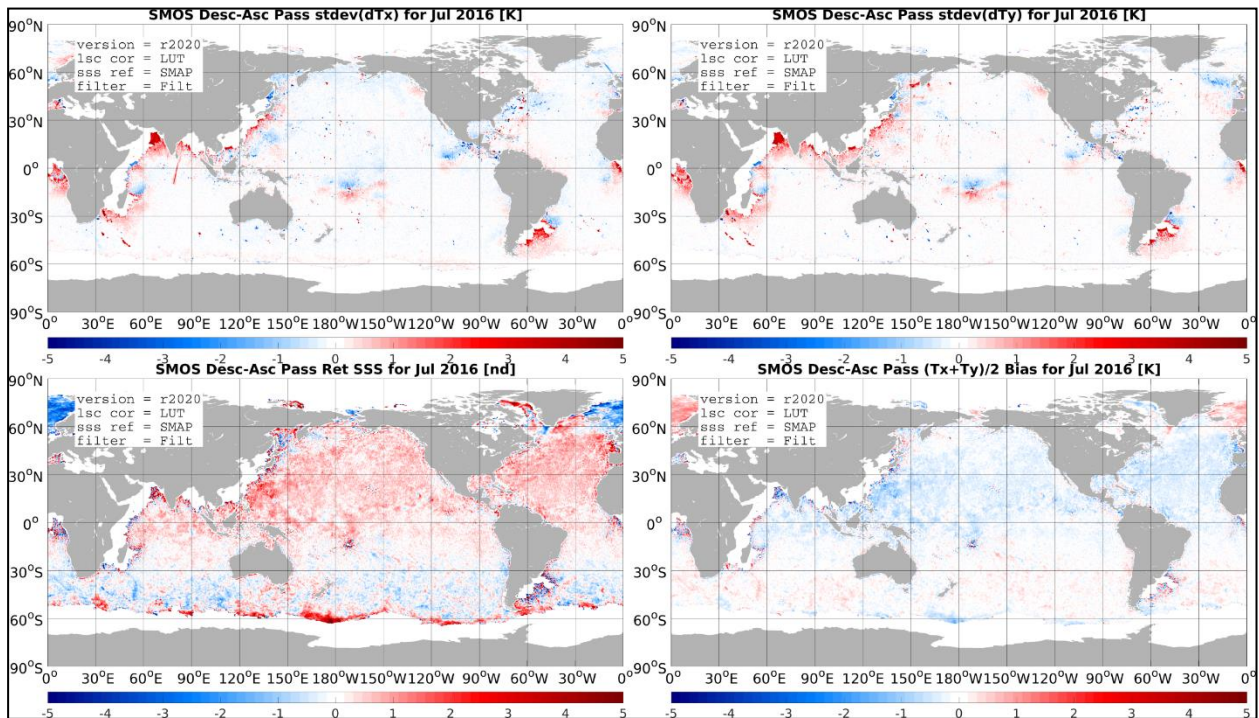


Figure 79: The LSC corrected difference between ascending and descending pass biases (top left) and brightness temperature standard deviations (top right). Retrieved SSS difference between ascending and descending L2OS passes (bottom left) and First Stokes bias (bottom right). Forward model is using RSS SMAP.

5.1.1.7 Summary of Forward model/SMOS Tbs comparison

1. For SSS uncorrected and both passes, there are clear increase of the standard deviation of the differences between the model and SMOS Tb data for both Tx and Ty in a band extending ~500 kms from coastlines (> 2K). Linearized SSS retrievals exhibit a strongly underestimated (by 1-4 pss) SSS near coasts with respect SMAP data. The underestimation is significantly higher at high latitudes.
2. Retrieved SSS in both ascending and descending passes exhibit biases and dell-line averaged first Stokes parameter that are significantly reduced with LSC correction compared with the uncorrected results. Moreover, the standard deviations of the individual Tx and Ty brightness temperatures at any given position on earth are significantly reduced in the vicinity of the coastlines. This is true except north of 60°N with a significant over-freshening of linearized SMOS SSS vs SMAP SSS. In descending passes, there is a smaller amplitude but clearly detectable bias showing successive negative and positive oscillations from 30°S to 60°S.
3. Impact of the use of SMAP SSS as opposed to ISAS SSS as the reference to evaluate the forward model has been assessed: SMOS Tb biases and standard deviations are similar except near river plumes where biases with respect to ISAS tend to be larger than with SMAP used as the reference (as expected).
4. The uncorrected difference between ascending and descending pass biases exhibits distinct coastal shadows in both the retrieved SSS and first Stokes parameter bias maps. By contrast, the difference maps for the standard deviations show only very week shadows, indicating that the increased Tb standard deviations in coastal areas exhibit only weak dependence on pass direction.
5. The LUT-corrected maps of ascending minus descending dTb and SSS show virtually no shadows, suggesting that the LSC correction effectively reduces both the biases and Tb standard deviations.

5.1.2 Pi-Mep SMOS L2 vs in-situ matchup analyses

In this section, we analyse the impact of the LSC through L2OS versus in situ validation. Both L2 SSS data from v662 and v700 processors were co-located with Argo and other in situ SSS data by the PI-MEP platform. The results as a function of distance to coasts are described hereafter. Note that the L2OS Flags used before MDB files generation are defined as follows: we only selected data in the MDB files if the following conditions or flags are met:

- Dg_affov>130
- Control flag set: CTRL ECMWF
- Control flag clear: CTRL NUM MEAS MIN, CTRL NUM MEAS LOW, CTRL MANY OUTLIERS, CTRL SUNGLINT, CTRL MOONGLINT, CTRL REACH MAXITER, CTRL MARQ, CTRL CH2 P, CTRL SUSPECT RFI
- Science flag set: SC LOW WIND, SC LAND SEA COAST1
- Science flag clear: SC ICE, SC SUSPECT ICE

5.1.2.1 L2/Argo match-up Results at Global scale

In Figure 81 (next page), we illustrate the evolution of the L2OS SSS mean biases and RMS differences for both SSS_uncor and SSS_corr with respect to ARGO SSS at co-localized matchups. The differences at match-up points have been binned averaged at global scale as a function of the distance to coasts (x-axis).

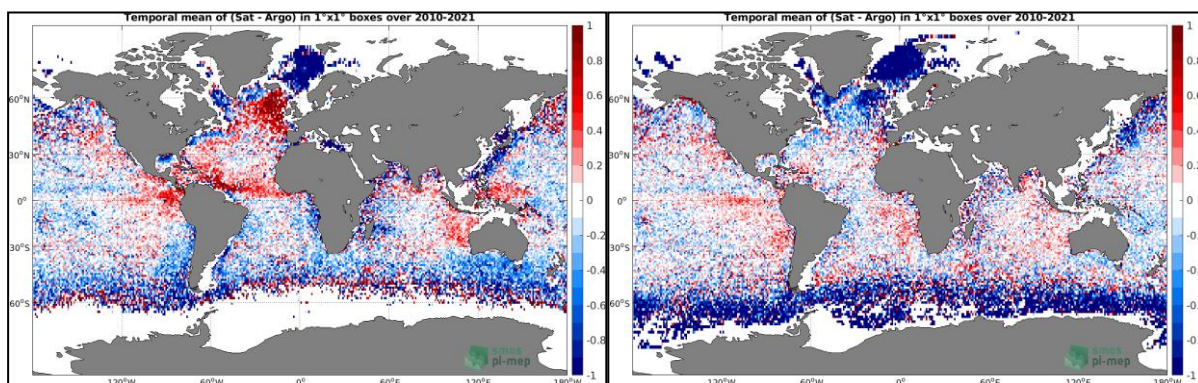


Figure 80 : Temporal mean of the SSS difference (SMOS – Argo) in spatial bins of 1 degree over 2010-2021 for v662 (left) and v700 (right).

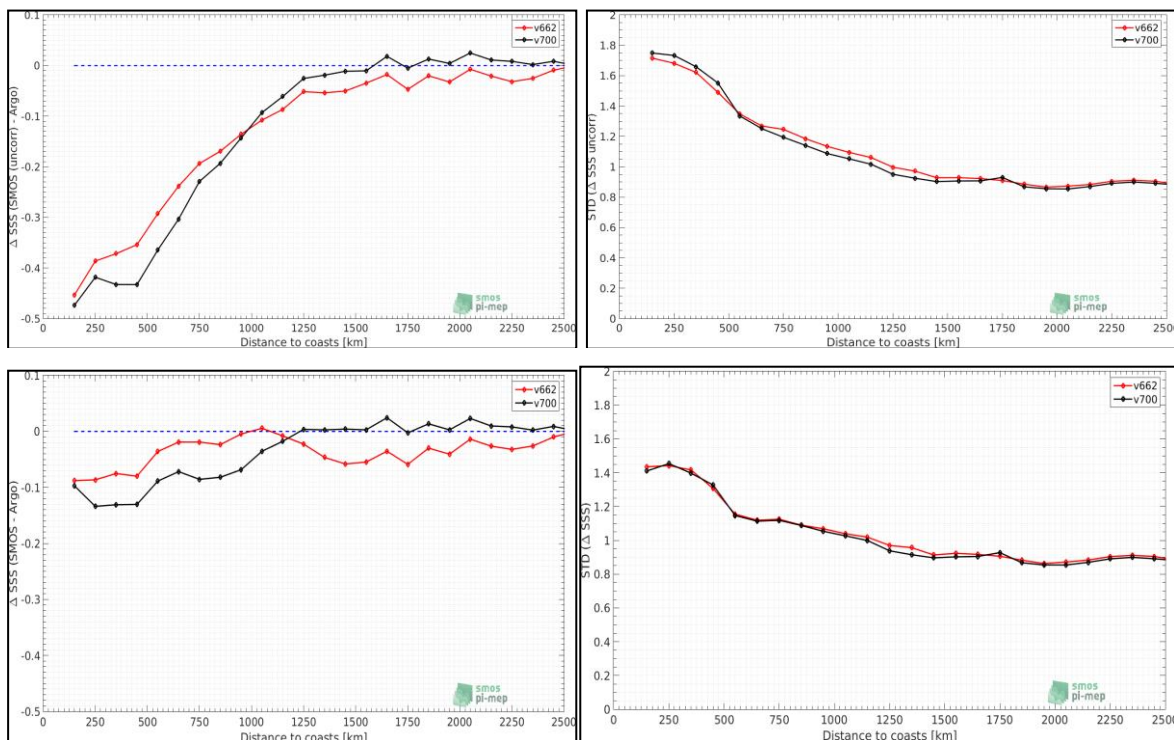


Figure 81: Mean (left) and STD (right) differences between SMOS L2 (v662 in red; v700 in black) and Argo as a function of the distance to coasts (x-axis) at global scale. Top and bottom plots are for SSS_uncorr and SSS_corr, respectively. Statistics are derived at global scale.

As found at global scale:

- 1) The LSC corrected SSS always performs better (both in terms of biases and STD) respect to Argo SSS than uncorrected SSS whatever the processor versions. For example, at 250 kms from nearest coasts, the bias and STD for v700 are ~ -0.4 pss and ~ 1.8 pss for uncorrected SSS, respectively, while they are ~ -0.1 pss and 1.4 pss for corrected SSS.
- 2) The biases for both corrected and uncorrected SSS are slightly (~ 0.05) reduced with v700 compared to v662 for distances to coasts > 1000 kms.
- 3) The SSS biases for both corrected and uncorrected are slightly degraded (several $O(0.01)$ pss) for distances to coasts < 1000 kms.
- 4) The STD(SMOS L2-Argo) as a function of distance to coasts remains almost unchanged at global scale from v700 to v662.

5.1.2.2 L2/TSG match-up at global scale

Colocalized L2OS/TSG SSS show no change of bias regarding distance to coasts for uncorrected SSS from v662 to v700. For corrected SSS, the bias is significantly reduced with respect to uncorrected SSS, but it changes sign from v700 to v662, being not reduced from one processor version to the next. The std is nevertheless reduced (by up to ~ 0.5 pss) with v700 if distance to coast < 600 kms for both corrected and uncorrected SSS.

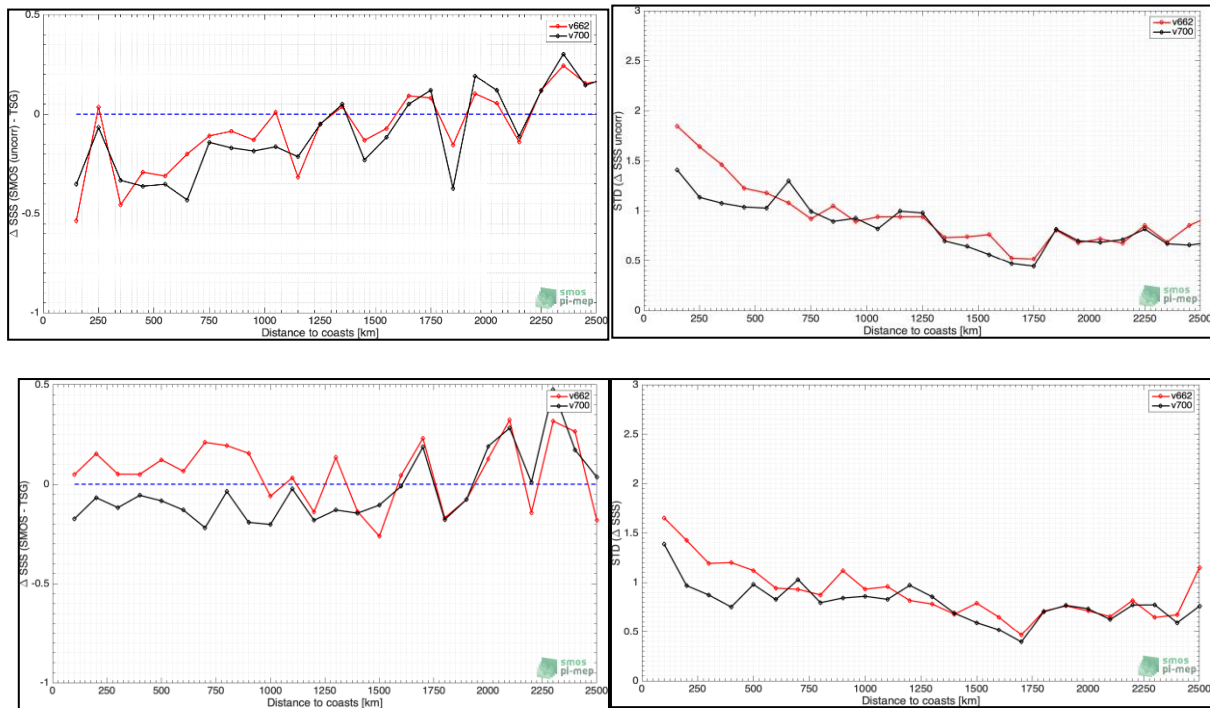


Figure 82: Mean (left) and STD (right) differences between SMOS L2 (v662 in red; v700 in black) and TSG SSS as a function of the distance to coasts (x-axis) at global scale. Top and bottom plots are for SSS_uncor and SSS_corr, respectively. Statistics are derived at **global scale**.

5.1.2.3 L2/Argo match-up Results in the mid-latitudes (45°S-45°N)

As found (Figure 83), the new processor's SSS exhibits much less mean bias and std differences wrt to Argo as a function of distance to coasts in the mid-latitudes compared to v662. For corrected SSS in the mid-latitude, the L2V700 is almost unbiased (bias < 0.05pss) with regard to Argo data as function of the distance to nearest coasts. Uncorrected SSS shows very similar mean bias as a function of distance to coasts from v622 to v700.

LSC corrected v700 exhibits a significantly reduced (by up to ~0.4 pss at 150 kms) std which become stable ~0.8 pss as a function of the distance to coasts while it was increasing with v662 as the distance to coasts diminishes. Note that the Std is reduced up to 2000 kms for both corrected and uncorrected SSS.

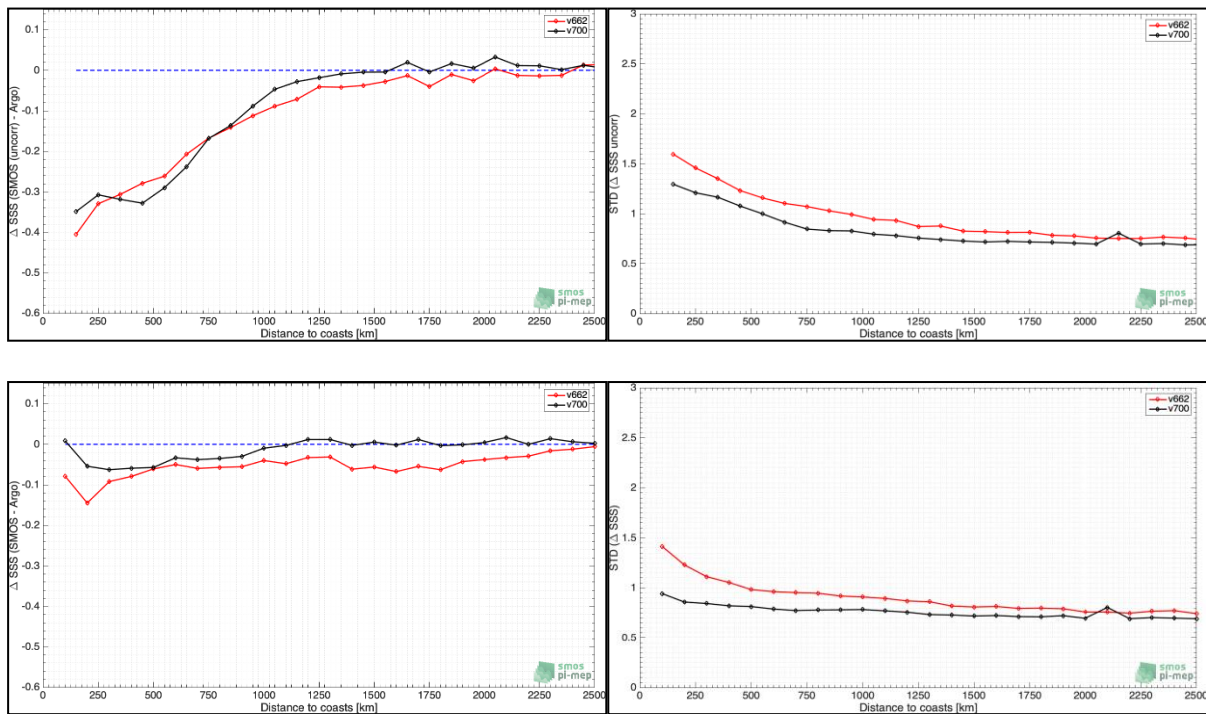


Figure 83: Mean (left) and STD (right) differences between SMOS L2 (v662 in red; v700 in black) and Argo as a function of the distance to coasts (x-axis) at global scale. Top and bottom plots are for SSS_uncor and SSS_corr, respectively. Statistics are derived from matchups collected only in the **mid-latitude (45°S-45°N) band**.

5.1.2.4 L2/TSG match-up Results in the mid-latitudes (45°S-45°N)

As found (Figure 84), the new processor's SSS exhibits much less mean bias and std differences regarding to TSG as a function of distance to coasts in the mid-latitudes compared to v662 for the LSC corrected versions. For corrected SSS in the mid-latitude, the L2V700 is almost unbiased regarding to TSG data as function of the distance to nearest coasts < 1000 kms. Uncorrected SSS shows very similar mean bias as a function of distance to coasts from v662 to v700.

LSC corrected v700 exhibits a significantly reduced (by up to ~0.5 pss at 150 kms) std which becomes stable ~0.7-0.8 pss as a function of the distance to coasts while it was increasing with v662 as the distance to coasts diminishes. Note that the Std is reduced up to 1500 kms for corrected SSS.

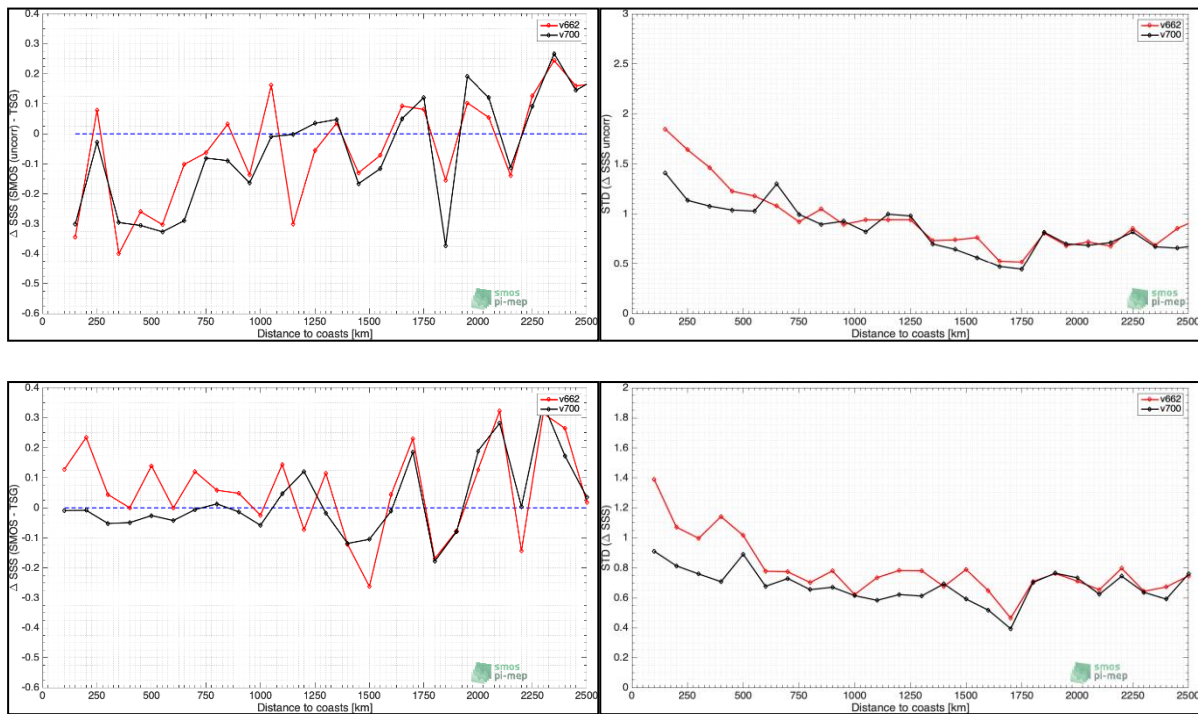


Figure 84: Mean (left) and STD (right) differences between SMOS L2 (v662 in red; v700 in black) and TSG SSS as a function of the distance to coasts (x-axis) at global scale. Top and bottom plots are for SSS_uncor and SSS_corr, respectively. Statistics are derived in the mid-latitudes (45°S-45°N).

5.1.2.5 L2/Argo match-up Results in the tropics (23°S-23°N)

Results observed with Argo in the mid-latitudes are still found in the tropics.

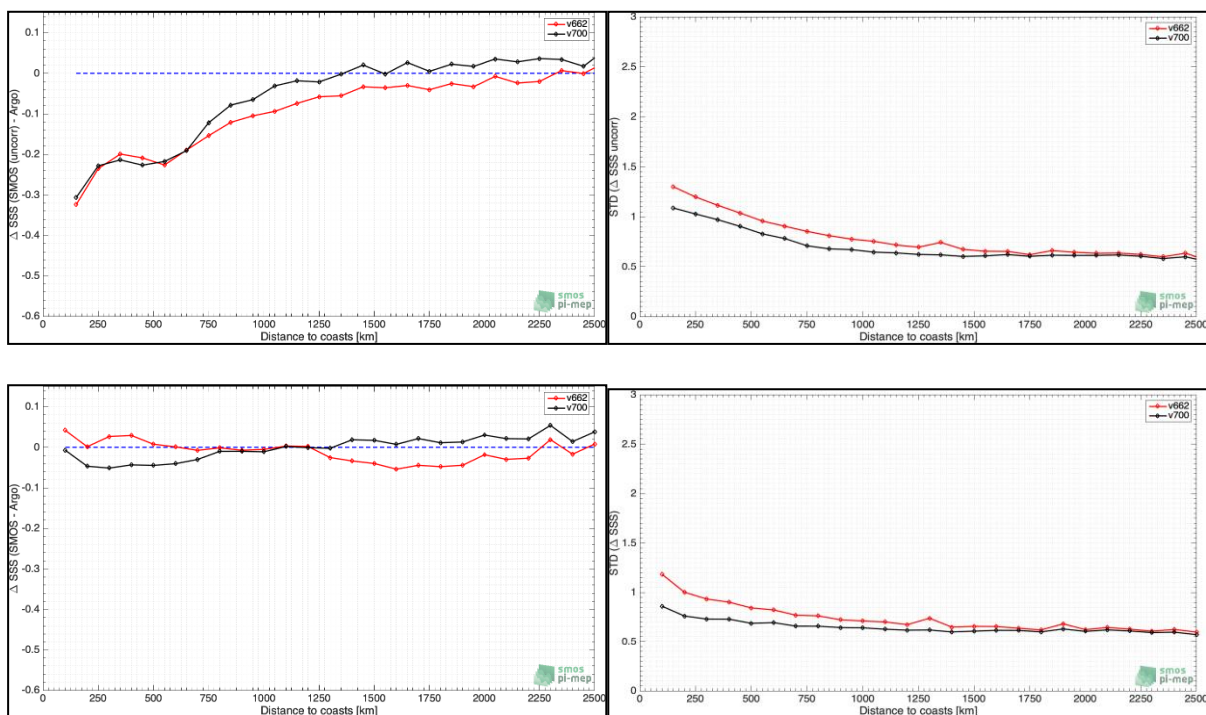


Figure 85: Mean (left) and RMS (right) differences between SMOS L2 (v662 in red; v700 in black) and Argo as a function of the distance to coasts (x-axis) at global scale. Top and bottom plots are for SSS_uncor and SSS_corr, respectively. Statistics are derived from matchups collected only in the Tropics (23°S-23°N) band.

5.1.2.6 L2/Argo match-up Results North of 45°N

North of 45°N, if the distance to coast is less than ~600 kms, both the L2v700 bias and std are degraded with respect v662. The LSC correction is not improving the bias and std vs Argo. The degradation is observed in both Corrected and non-corrected SSS.

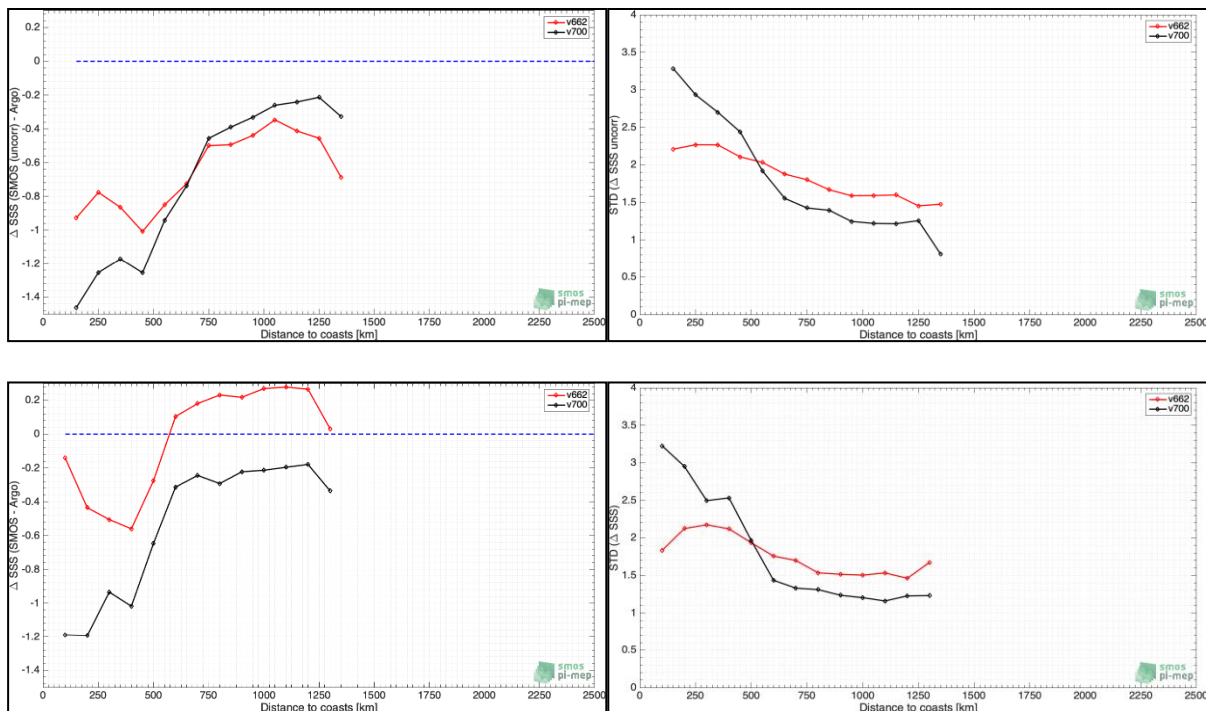


Figure 86: Mean (left) and RMS (right) differences between SMOS L2 (v662 in red; v700 in black) and Argo as a function of the distance to coasts (x-axis) at global scale. Top and bottom plots are for SSS_uncor and SSS_corr, respectively. Statistics are derived from matchups collected only North of 45°N.

5.1.2.7 L2/Argo match-up Results South of 45°S

South of 45°S, if the distance to coast is less than ~2000 kms, both the L2v700 bias and std are significantly degraded with respect v662. The LSC correction is not improving the bias and std regarding Argo. The degradation is observed in both Corrected and non-corrected SSS.

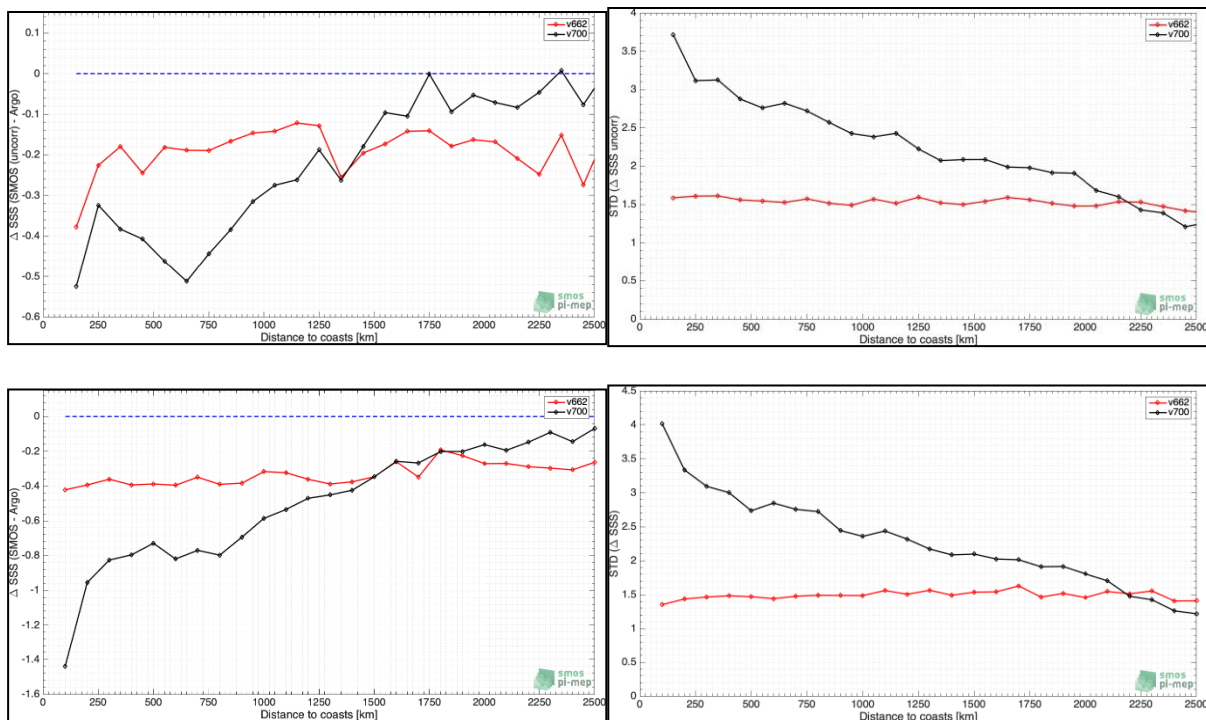
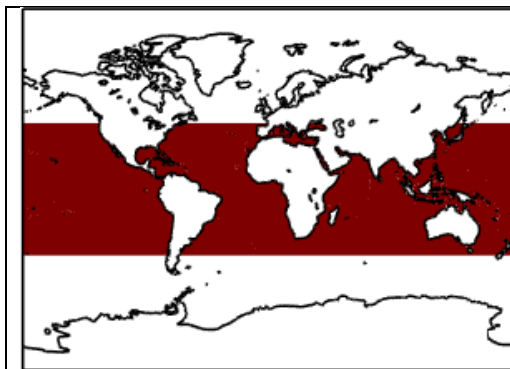


Figure 87: Mean (left) and RMS (right) differences between SMOS L2 (v662 in red; v700 in black) and Argo as a function of the distance to coasts (x-axis) at global scale. Top and bottom plots are for SSS_uncor and SSS_corr, respectively. Statistics are derived from matchups collected only **South of 45°S**.

5.1.2.8 L2/Argo match-up Results for each PI-MEP region

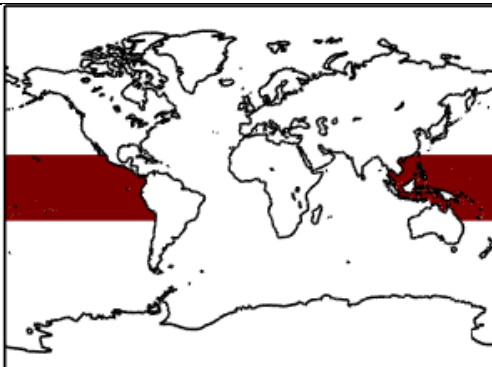
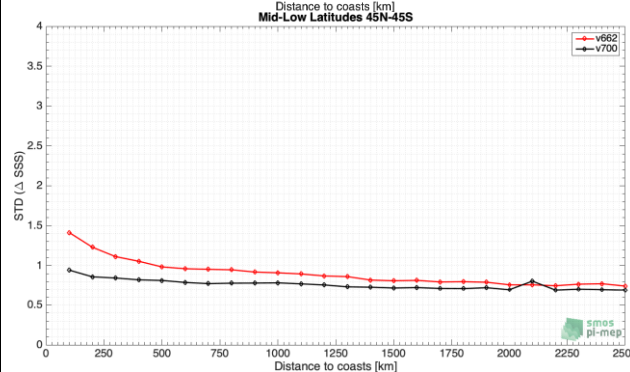
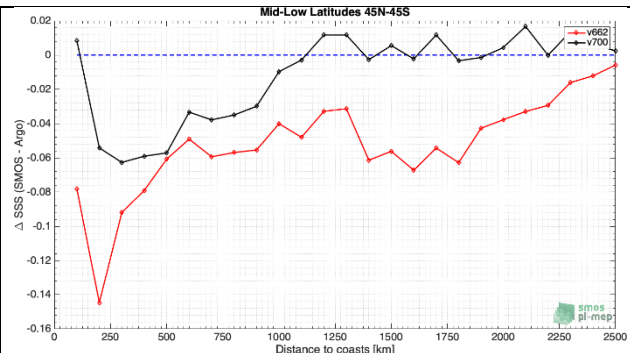
In addition, we analysed the statistics of the differences between SMOS L2v662/L2 v700 and Argo SSS at match-up pairs within the PI-MEP Validation regions (see Pi-MREP website for the definitions):

On the following table of plots, the mask of the region (left panels) and (right panel) the median (top) and the std (bottom) of the SSS difference between SMOS LSC corrected data and Argo data as a function of distance to coasts are provided for each region and each processor version (L2v662 (red) versus L2v700 (black)).



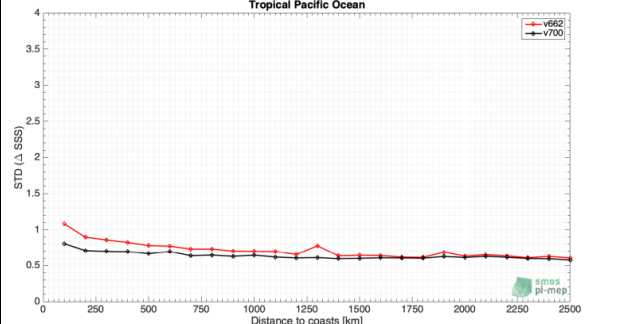
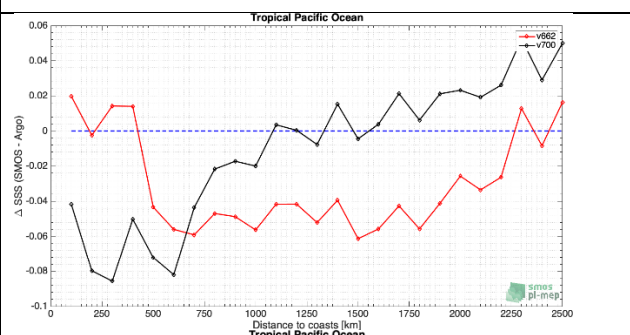
Mid-latitudes: 45°S-45°N

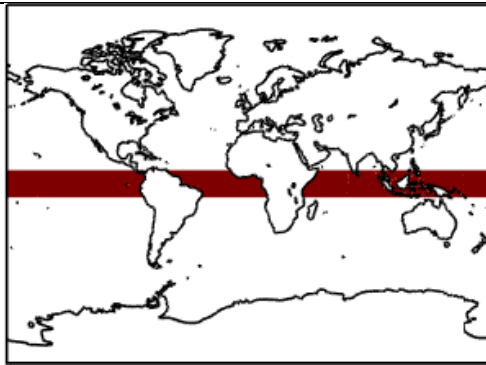
- Bias of v700 wrt to Argo is slightly reduced for all distance to coasts
- STD is reduced for v700 for all distance to coasts up to ~0.5 ps at 100 kms



Tropical bands: 23°S-23°N

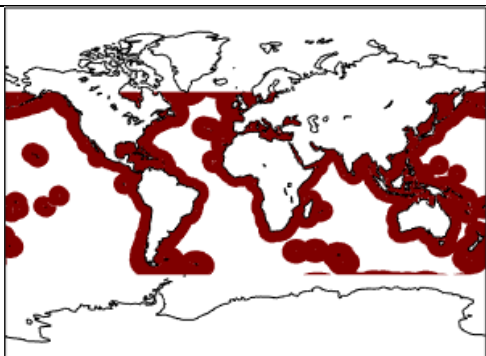
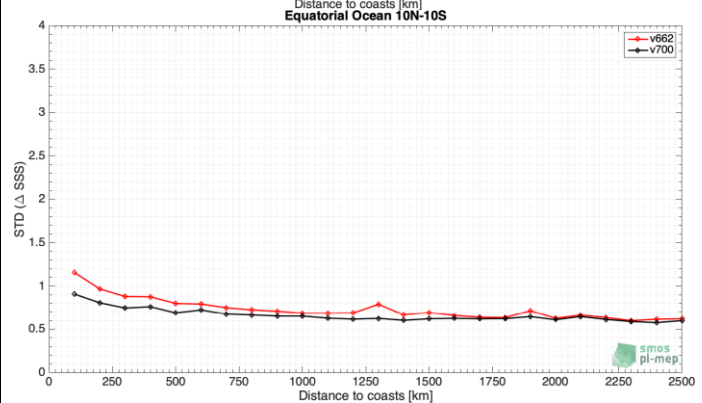
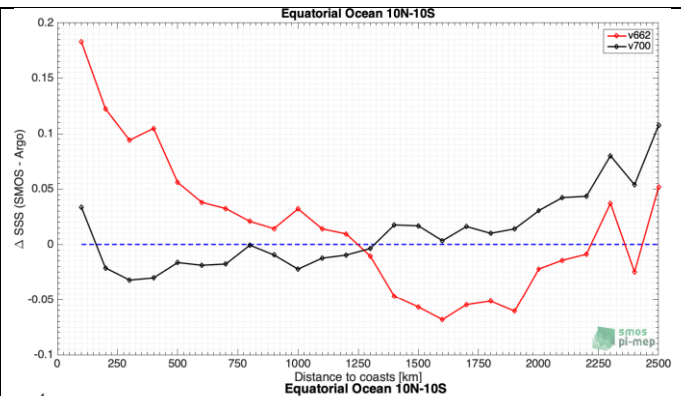
- Bias of v700 wrt to Argo is slightly higher for distance to coasts < 600 km but reduced for greater distance to coasts
- STD is reduced for v700 for all distance to coasts up to ~0.5 ps at 100 kms





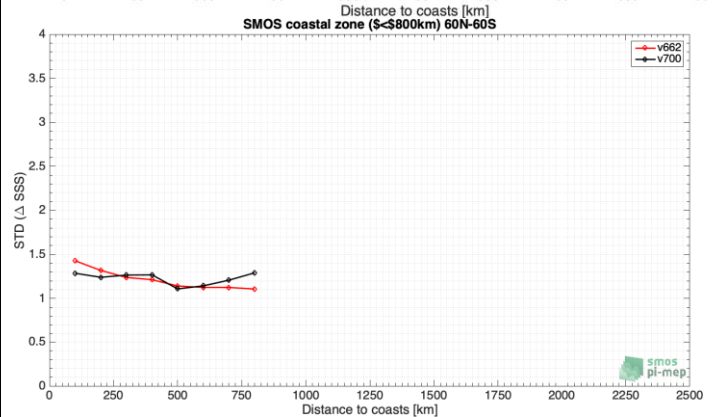
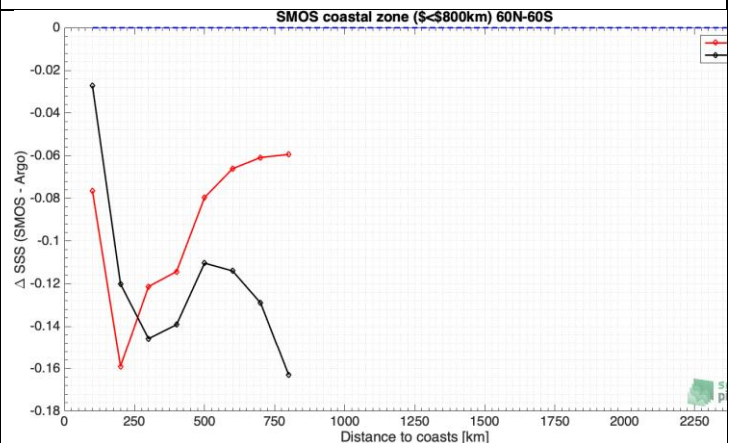
Equatorial band: 10°S-10°N

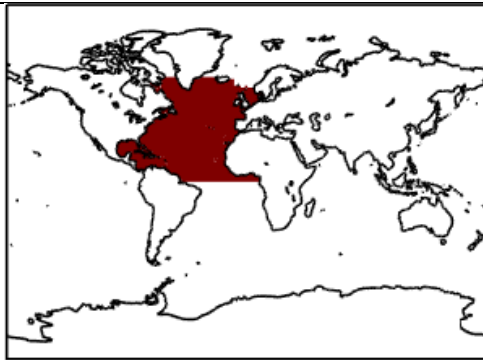
- Bias of v700 wrt to Argo is significantly reduced
- STD is reduced for v700 for all distance to coasts up to ~0.2 pss at 100 kms



SMOS coastal zone (<800km) 60°S-60°N

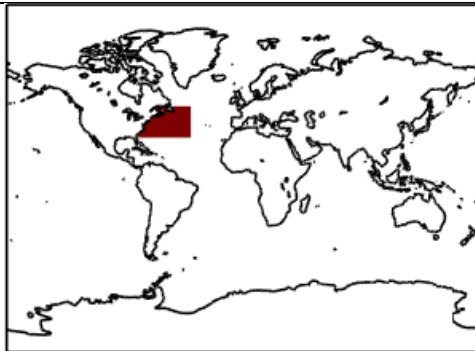
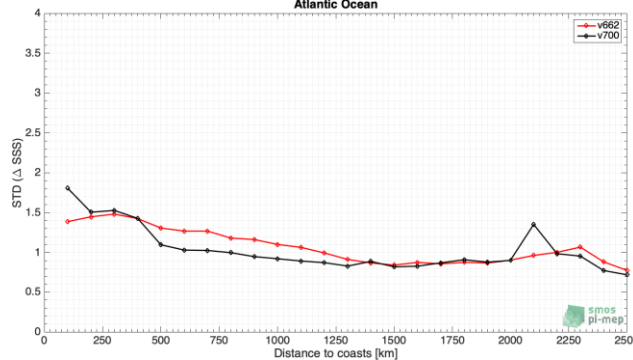
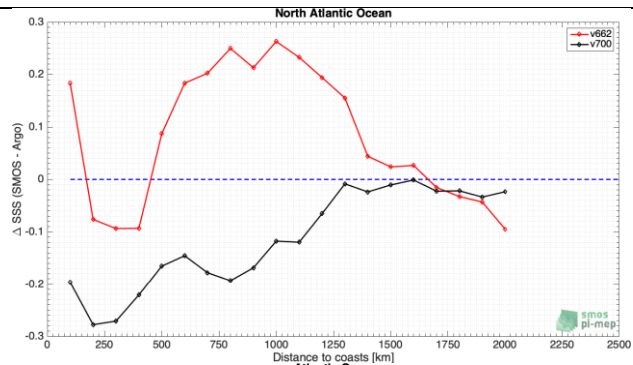
- Bias of v700 wrt to Argo is slightly reduced, for distances to coasts < 250 km, but slightly increased when d > 500 kms
- STD is slightly reduced for v700 for distances to coasts < 250 km, slightly degraded when > 600 kms





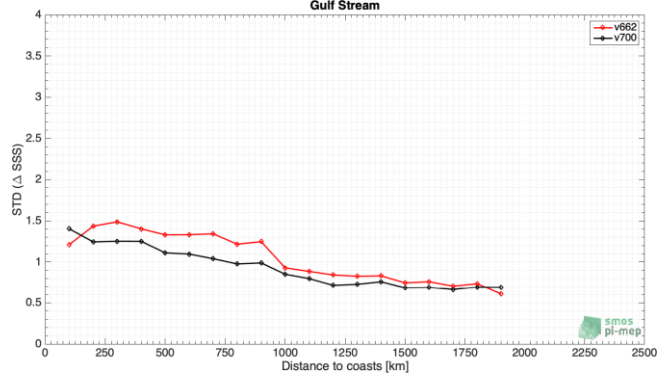
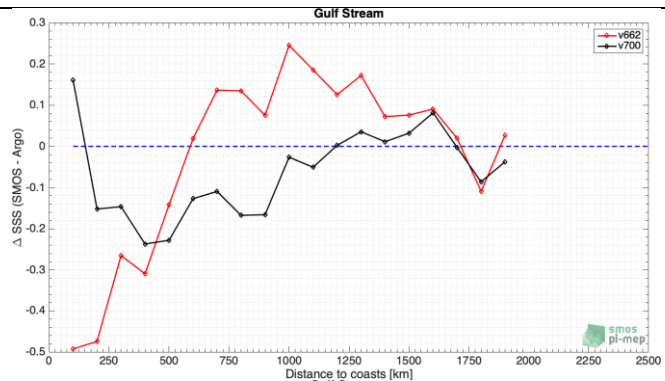
North Atlantic:

- **Bias** of v700 wrt to Argo is **increased** in amplitude when distance to coast < **500 kms** and changed sign (now L2OS is too fresh)
- **STD** is similar for v700 & v662 when d2coast < 500 km, reduced for v700 when d2coast > 500 km



Gulf Stream region:

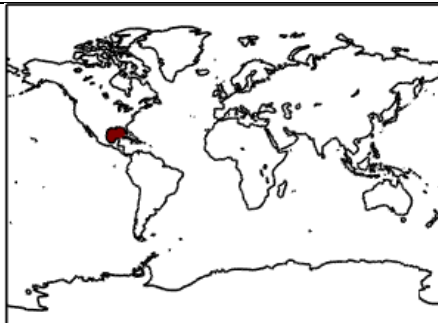
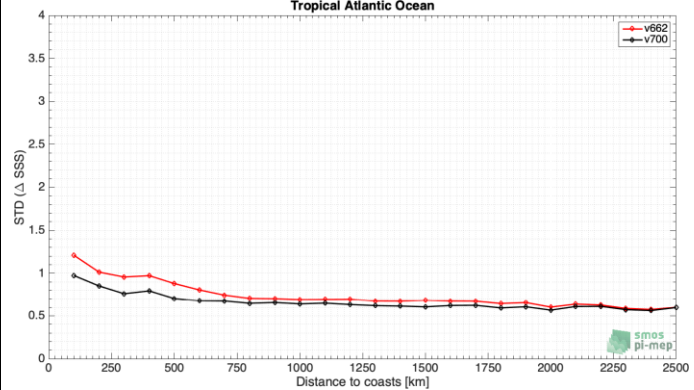
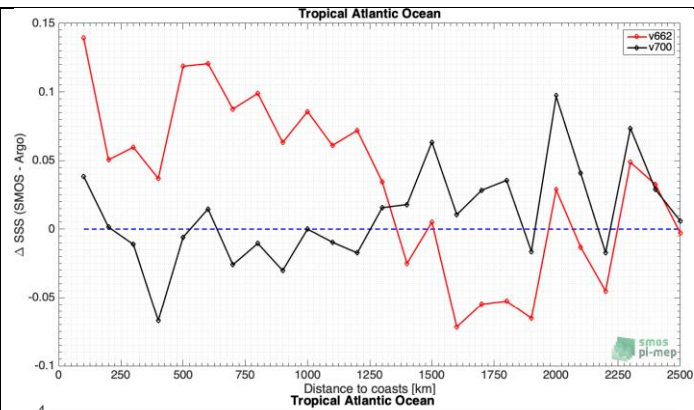
- **Overall Bias reduction with v700** wrt to Argo, particularly when distance to coast < **500 kms (decrease by 0.4 pss at 100 kms)**
- **STD is reduced** (by 0.1-0.2 pss) for all distances to coast > 200 kms)





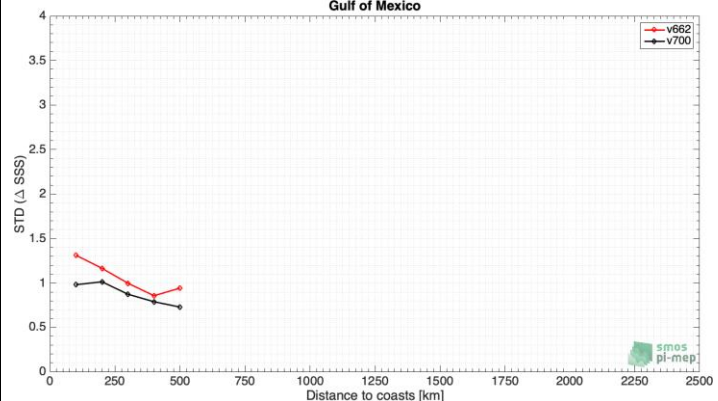
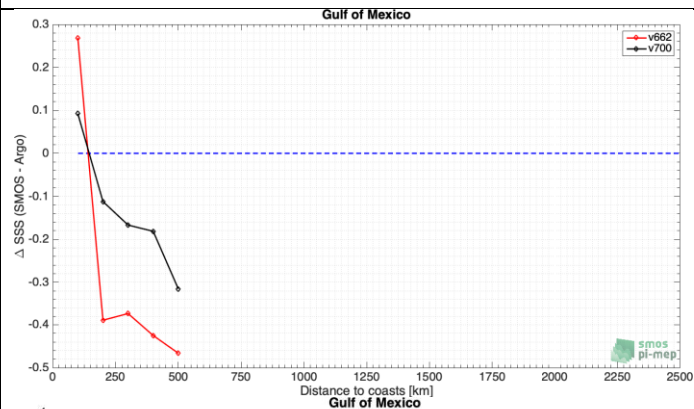
Tropical Atlantic:

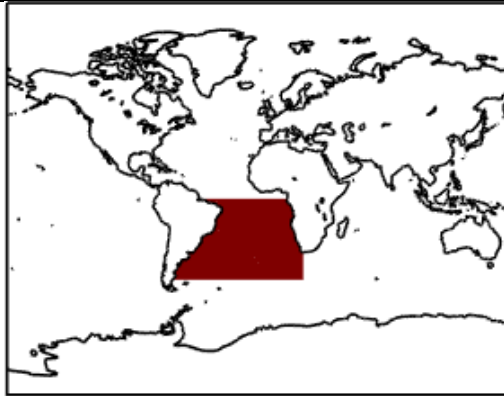
- Bias of v700 wrt to Argo is significantly reduced
- STD is improved for all distance to coasts



Gulf of Mexico

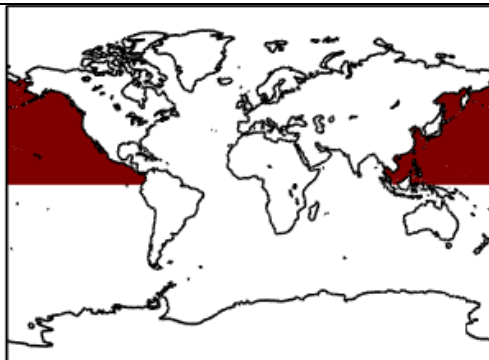
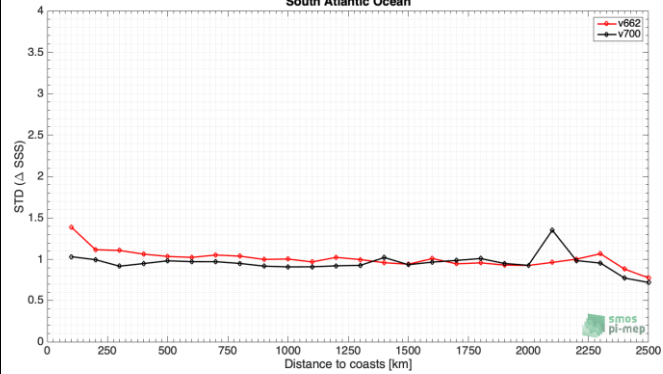
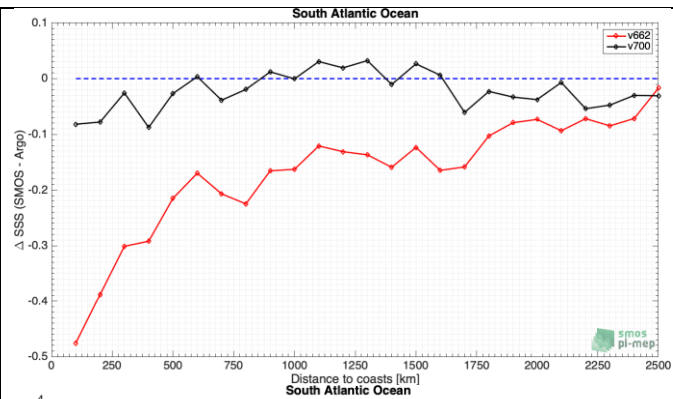
- Bias of v700 wrt to Argo is significantly reduced
- STD is reduced for all distances to coast (by up to ~0.3 pss at 100 kms)





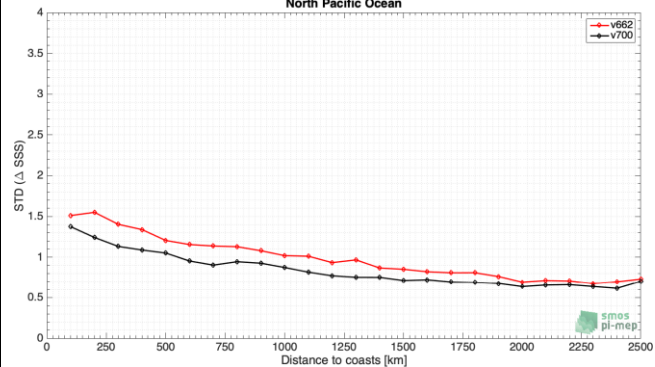
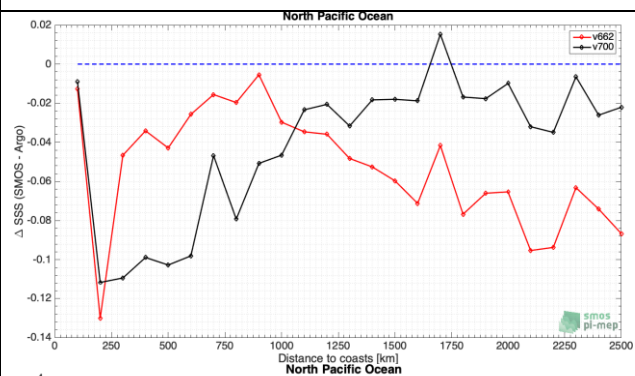
South Atlantic:

- Bias of v700 wrt to Argo is significantly reduced (by up to 0.45 pss at 150 kms from coasts) for all distance to coasts
- STD is slightly reduced for v700 & v662 when d2coast < 500 km, reduced for v700 when d2coast > 500 km



North Pacific:

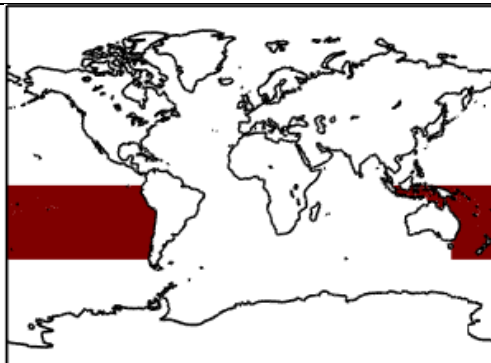
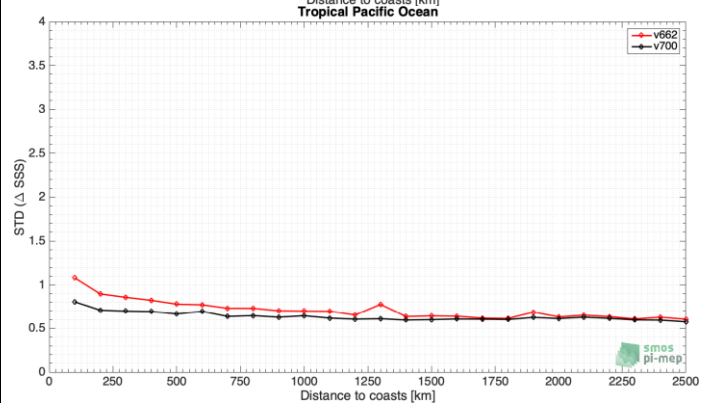
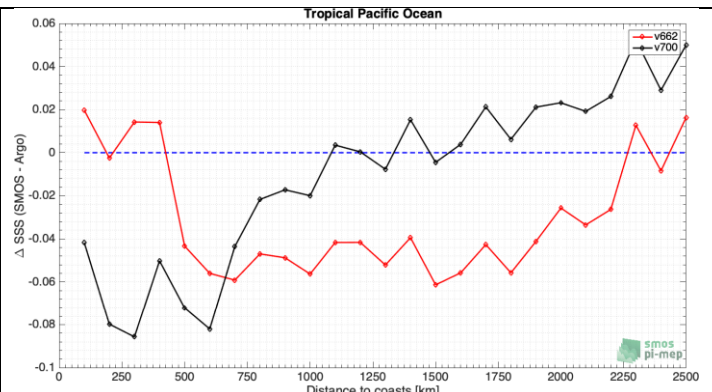
- Bias of v700 wrt to Argo is reduced for distance to coasts > 1000 kms but increased for d2coasts < 1000km
- STD is slightly reduced for v700 for all distance to coasts





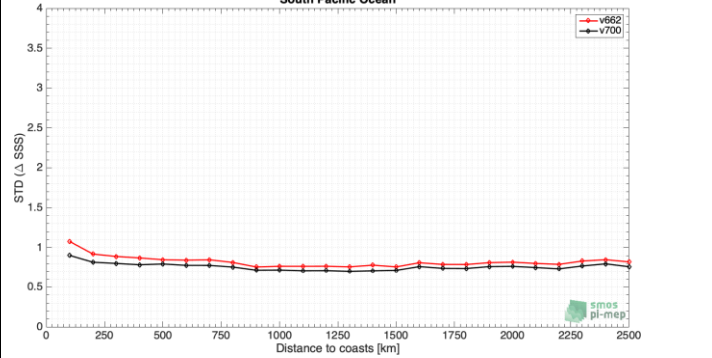
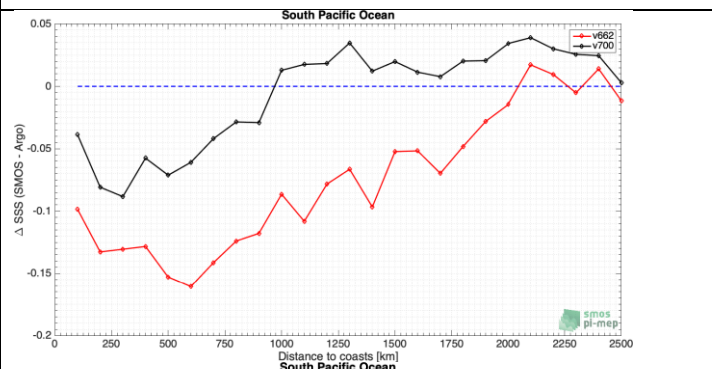
Tropical Pacific:

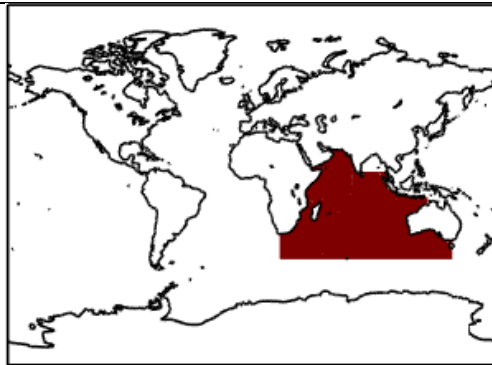
- Bias of v700 wrt to Argo is reduced for distance to coasts > 600 kms but increased for d2coasts < 600km
- STD is slightly reduced for v700 for all distance to coasts



South Pacific:

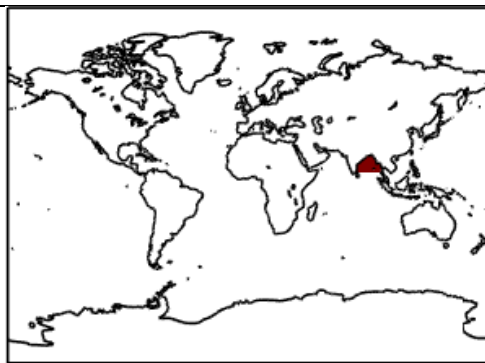
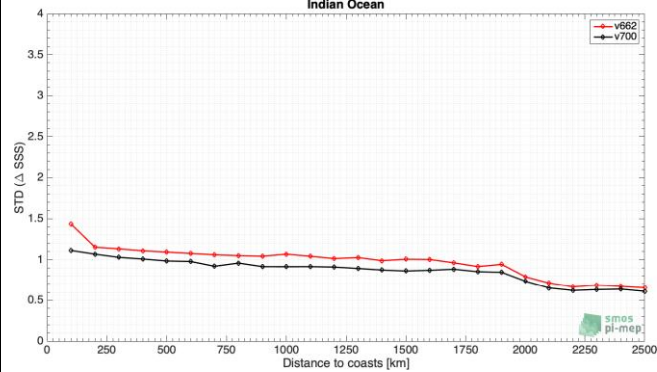
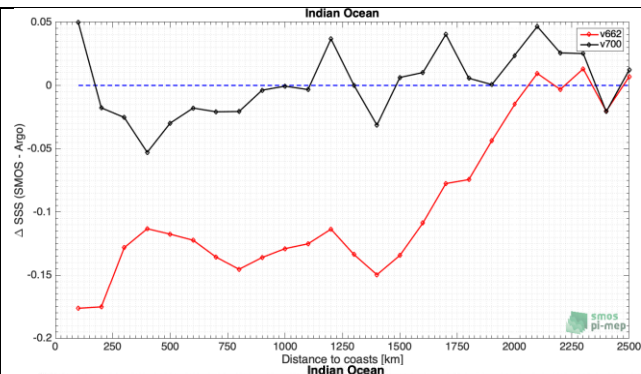
- Bias of v700 wrt to Argo is reduced for all distance to coasts
- STD is slightly reduced for v700 for all distance to coasts





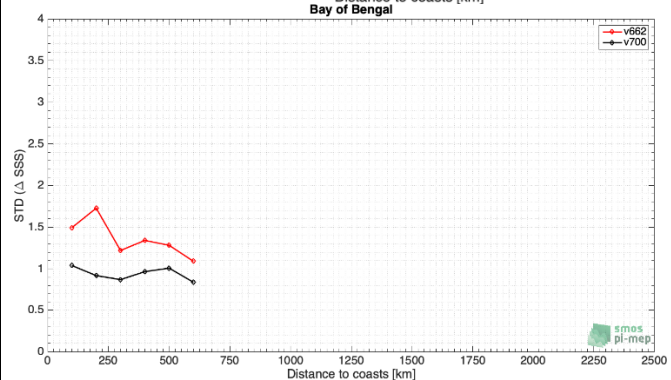
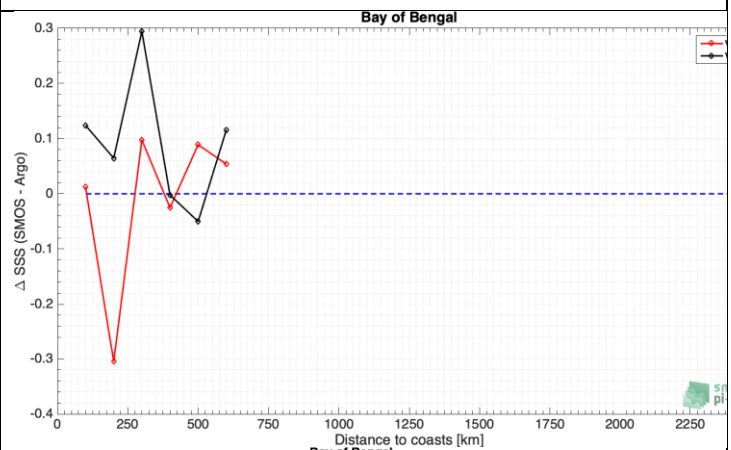
Indian Ocean:

- Bias of v700 wrt to Argo is reduced (by ~0.1 pss) for all distances to coasts
- STD is slightly reduced for v700 for all distance to coasts



Bay of Bengal:

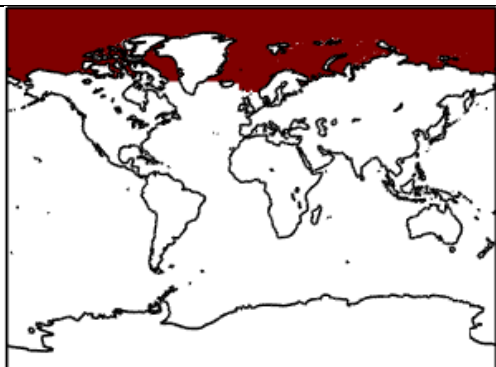
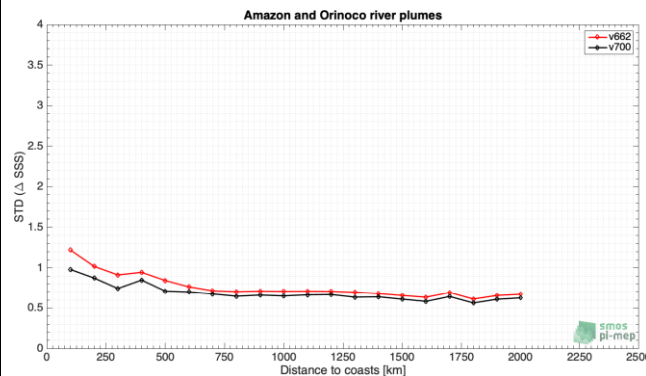
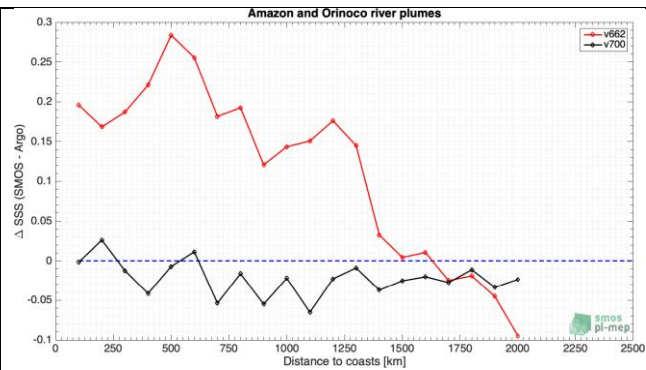
- Bias of v700 wrt to Argo has similar amplitude than with v662 but sign is changed
- STD is reduced by 0.2-0.5 pss for v700 for all distance to coasts





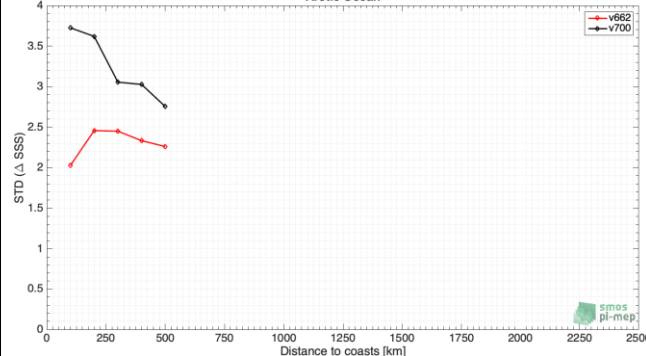
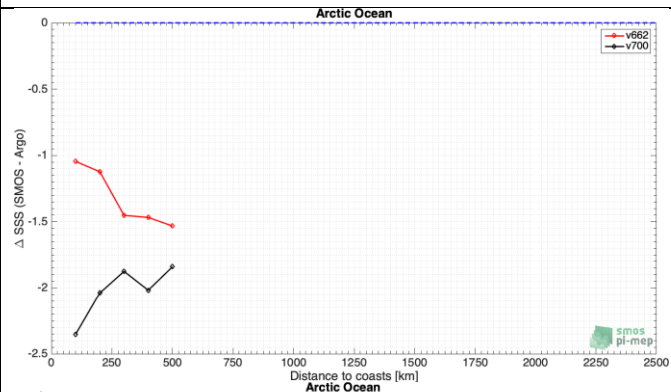
Amazon and Orinoco river plume:

- v700 wrt to Argo is almost **unbiased** wrt distance to coasts
- **STD is reduced by up to 0.2 pss** for v700 for all distance to coasts



Arctic:

- Bias of v700 wrt to Argo is **strongly increased** (by up to 1.5 pss at 100 kms)
- **STD is strongly increased (by 0.5 to 1.5 pss)** for v700 for all distance to coasts



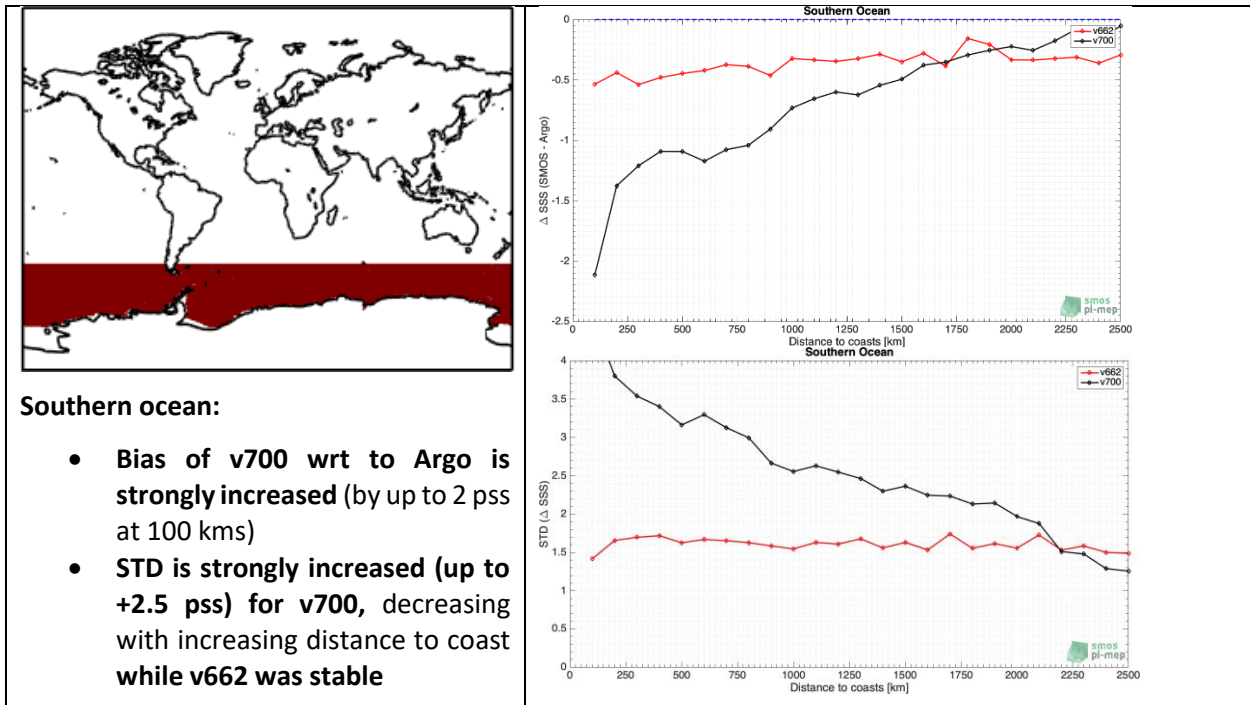


Figure 88: The mask of the region (left panels) and (right panel) the median (top) and the std (bottom) of the SSS difference between SMOS LSC corrected data and Argo data as a function of distance to coasts are provided for each region and each processor version (L2v662 (red) versus L2V700 (black)).

As summarized, the regions above show three major types of statistics with respect the distance to coasts:

- A) **Significantly degraded** (both in terms of bias and std) of the SMOS L2v700 quality regarding Argo as a function of distance to coast in
 - 1) the Arctic Ocean, and,
 - 2) the Southern Ocean
- B) **Significantly improved** (both in terms of bias and std) SMOS L2v700 quality regarding Argo as a function of distance to coast in:
 - 1) All mid latitudes (45°S-45°N)
 - 2) All equatorial latitudes (10°S-10°N)
 - 3) Tropical Atlantic
 - 4) South Atlantic and Pacific
 - 5) Indian Ocean
 - 6) Gulf of Mexico
 - 7) Gulf stream
 - 8) Amazon and Orinoco River plumes
- C) **Slightly improved** (std reduced but bias is increased) or unchanged SMOS L2v700 quality regarding Argo as a function of distance to coast in:
 1. North Pacific
 2. North Atlantic
 3. Tropical bands
 4. Tropical Pacific

5.1.3 Validation protocol analyses and L3 validation with Argo

5.1.3.1 Validation protocol for LSC corrected L2 SSS Ascending+Descending

For these analyses, we compared SMOS ESA v700 and v662 vs ISAS (gridded ARGO fields) using the validation protocol (filtered simple monthly temporal average of the L2 and comparison to ISAS monthly fields). The focus is first on the LSC corrected fields for SSS1, merged Ascending and descending passes and Dcoast < 1000 km. We show only the more robust statistics (in terms of median and Median Absolute Deviation which minimize outliers impacts).

Global : Asc+Desc

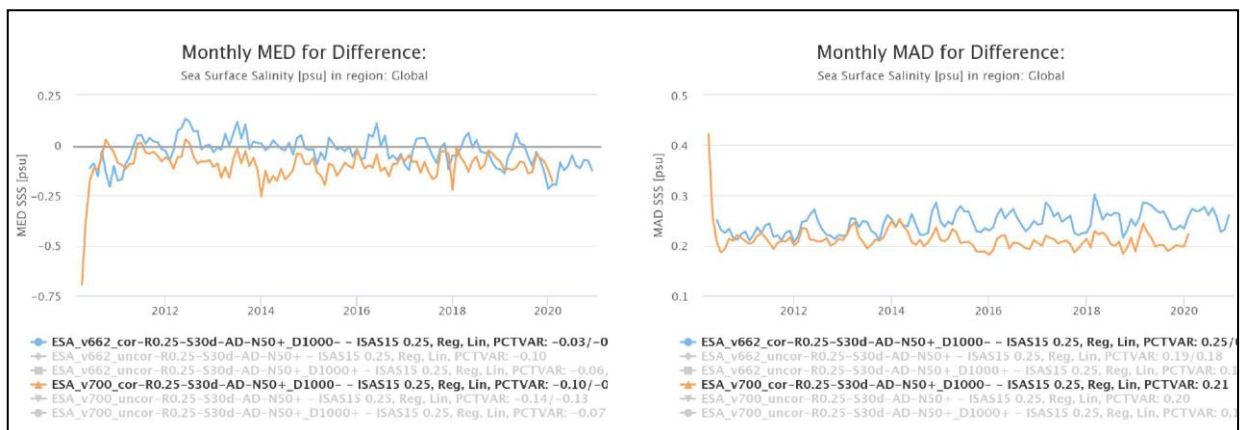


Figure 89: Monthly MEDIAN (left) and MAD (right) difference between SMOS L2-averaged v662 (blue) or v700 (orange) with ISAS. **Global Scale. Asc+Desc.**

- Global Median difference is slightly larger in v700 (-0.10 pss) than in v662 (-0.03 pss); no sign change in v700.
- Global MAD is smaller in v700 and is more stable after 2015.

Mid-latitudes 45°S-45°N

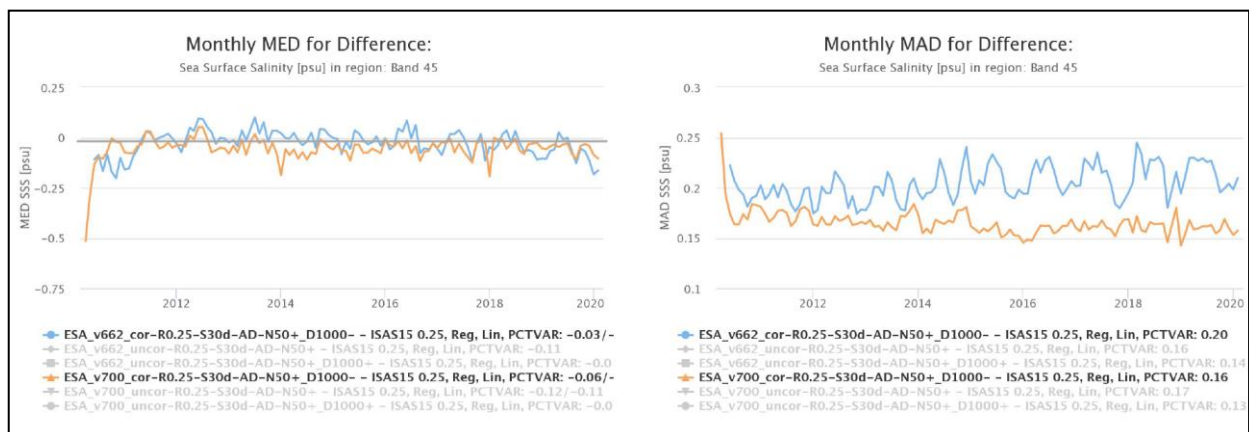


Figure 90: Monthly MEDIAN (left) and MAD (right) difference between SMOS L2-averaged v662 (blue) or v700 (orange) with ISAS. **Mid-latitudes. Asc+Desc.**

- Global Median difference (~ 0) is similar in v700 and v662.
- Global MAD is smaller by ~ 0.05 pss in v700 and is more temporally stable after 2015.

Tropical band 30°S-30°N

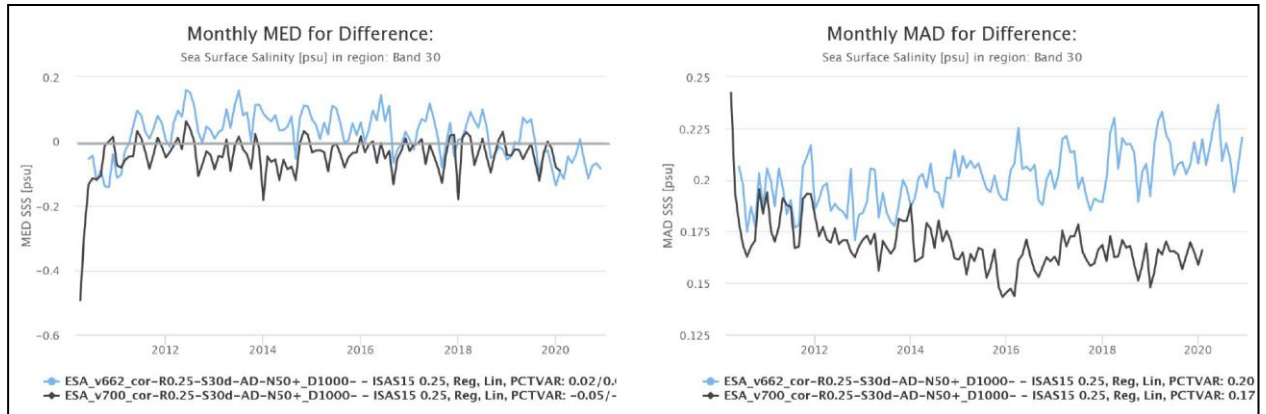


Figure 91: Monthly MEDIAN (left) and MAD (right) difference between SMOS L2-averaged v662 (blue) or v700 (black) with ISAS. **Tropical-latitudes (30°S-30°N)**. Asc+Desc.

- Similar median bias magnitude, but positive in 662 while slightly negative in v700; more stable in v700.
- MAD pattern is like the 45°N-45°S band: there is a clear reduction in amplitude and temporal variability with 700.

Southern Ocean 80°S-60°S

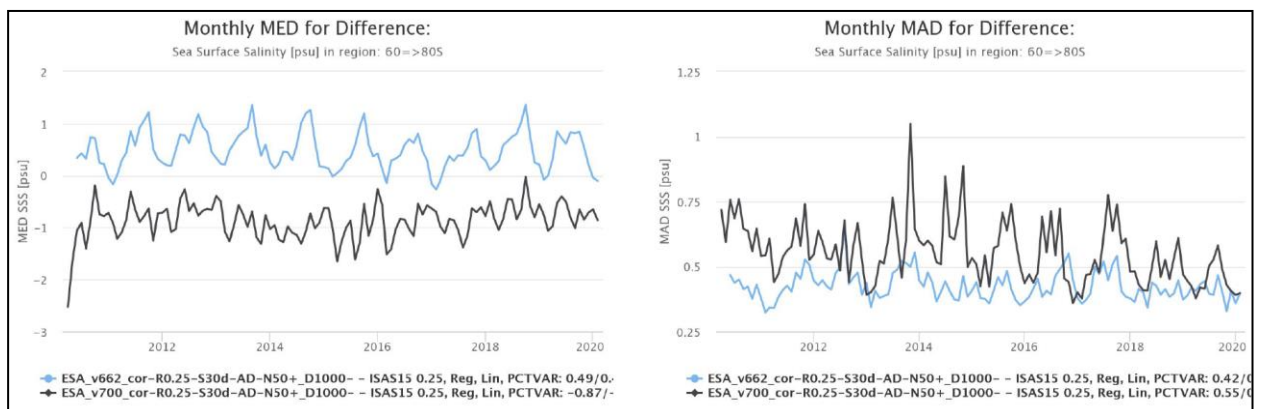


Figure 92: Monthly MEDIAN (left) and MAD (right) difference between SMOS L2-averaged v662 (blue) or v700 (black) with ISAS. **Southern Ocean (80°S-60°S)**. Asc+Desc.

Along Antarctic, v700 SSS show considerably higher bias (by 0.5pss) and MAD (by +0.2-0.3pss) than v662.

Northern Ocean 60°N-80°N

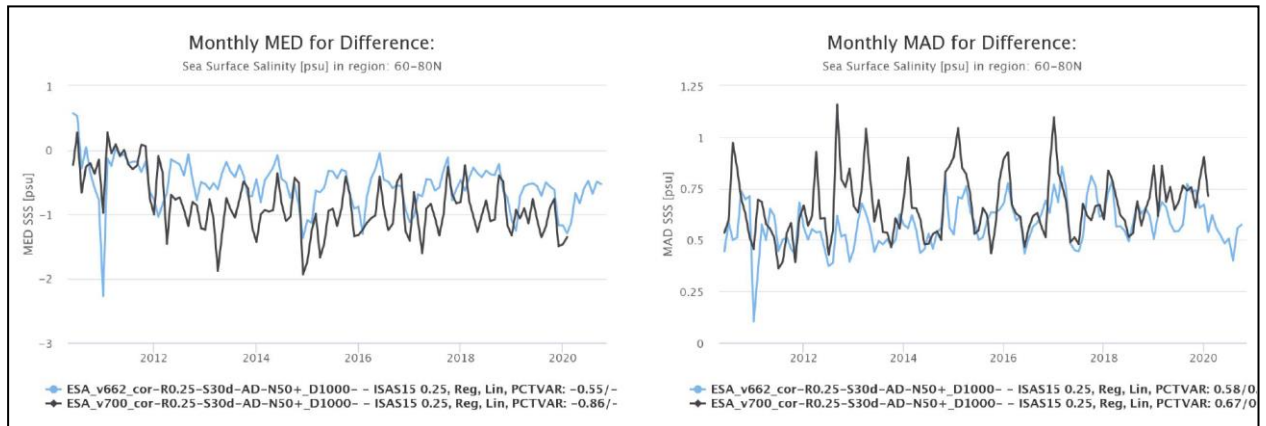


Figure 93: Monthly MEDIAN (left) and MAD (right) difference between SMOS L2-averaged v662 (blue) or v700 (black) with ISAS. Northern Ocean (60°N-80°N). Asc+Desc.

At high northern latitudes, v700 SSS show slightly higher fresh bias and increased MAD variability than v662.

5.1.3.2 Validation protocol for LSC uncorrected L2 SSS- Global Scale

The coastal-effects-uncorrected SSS shows worse performance for v700 (vs ISAS) than v662 in the "coastal" (1000 km) areas of the mid-latitudes: bias is increased by 0.1-0.2 pss. MAD is slightly increased.

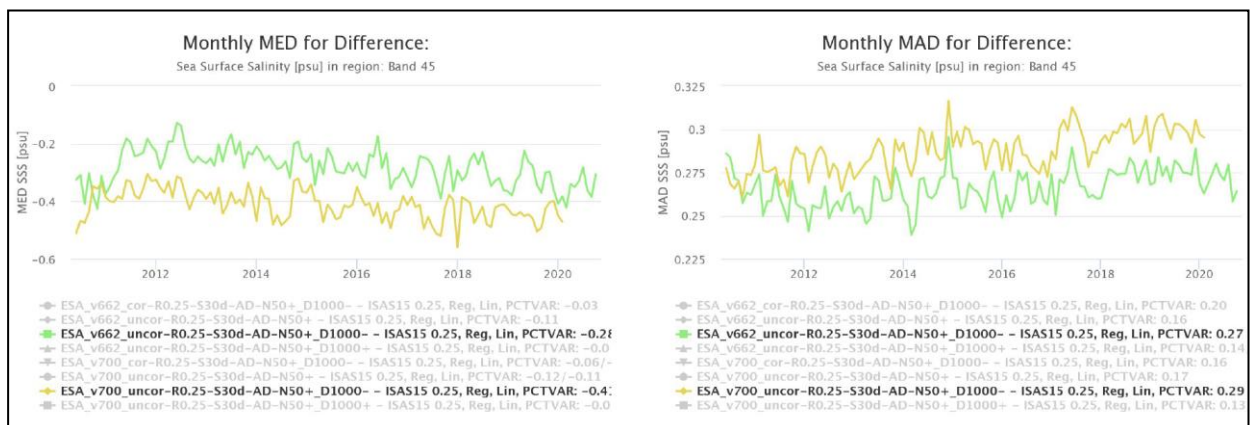


Figure 94: Monthly MEDIAN (left) and MAD (right) difference between SMOS L2-averaged v662 (green) or v700 (yellow) with ISAS. Mid-latitudes (45°S-45°N). Asc+Desc. SMOS L2 SSS is LSC Uncorrected

5.1.3.3 Validation protocol for LSC corrected L2 SSS separating Ascending & Descending passes

For these analyses, we compared SMOS ESA v700 and v662 vs ISAS (gridded ARGO fields) using the validation protocol (filtered simple monthly temporal average of the L2 and comparison to ISAS monthly fields). The focus is now on the LSC corrected fields for SSS1, separating Ascending and descending passes and Dcoast < 1000 km. We show only the more robust statistics (in terms of median and Median Absolute Deviation which minimize outliers impacts).

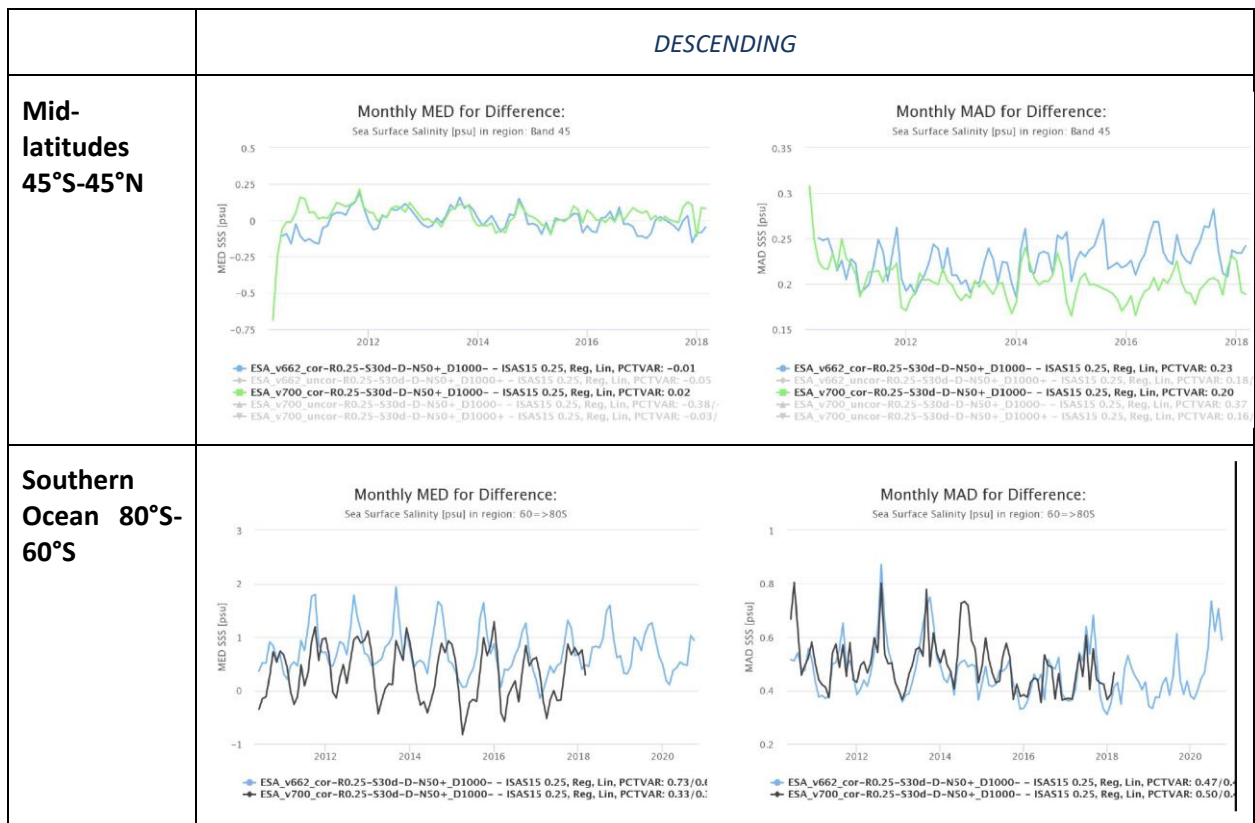
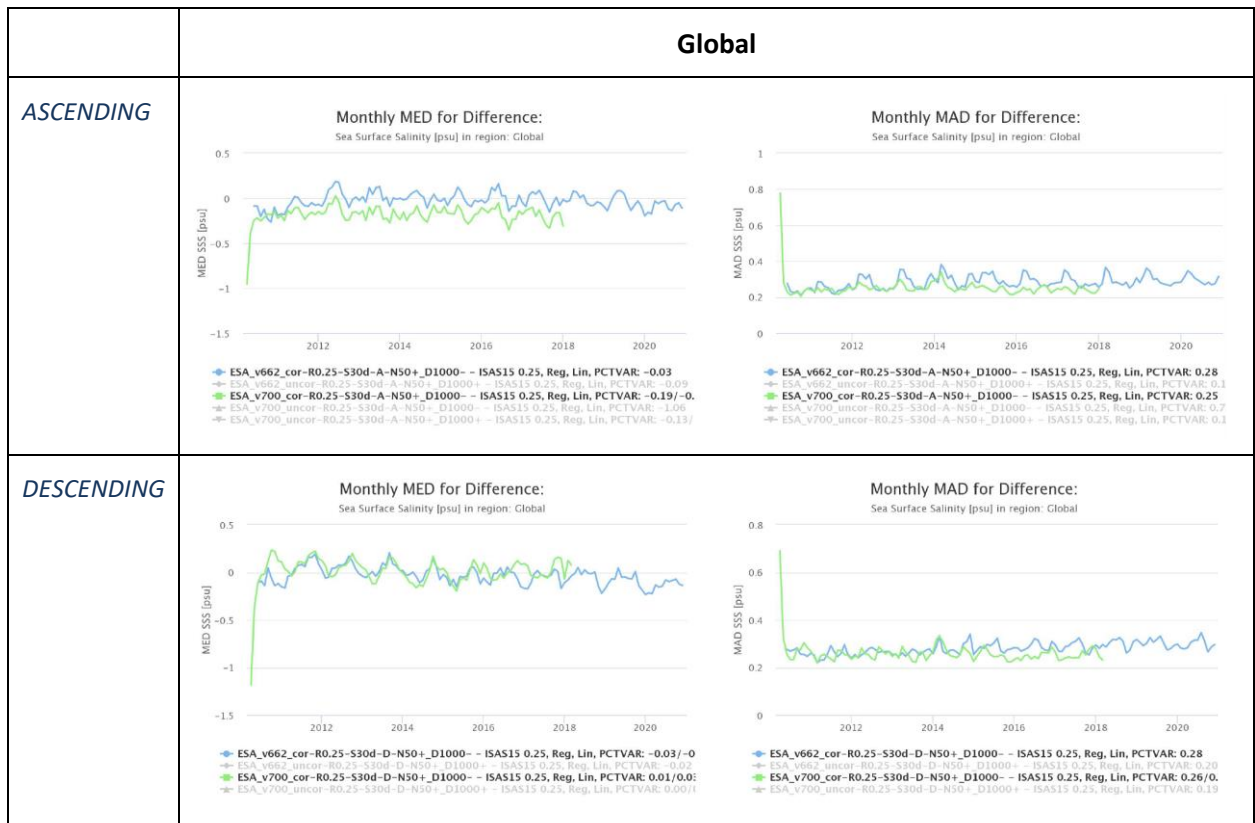


**SMOS ESL for SMOS Level 1 and Level 2
over Land, Ocean, and Ice
- L2OS 3rd Mission Reprocessing Report -**

Ref.: ARG-003-081

Date: 16.07.2021

Page: 107



5.1.3.4 Conclusions of the Validation protocol analyses in the coastal domain

1. Global performance in the "coastal" areas (Dcoast < 1000 km) for the coastal-corrected products is only slightly improved in terms of the MAD(Diff) metrics in the v700 version but is degraded in terms of std (not shown here).
2. Excluding the high latitudes, the bias becomes more stable, and the variability smaller in the v700 version.
3. The stronger bias and increased variability are coming from the high latitudes, probably due to ice areas and zones of ice/water contrast.
4. The mean bias increase comes from the Ascending orbits, and the variability increase is stronger for the Ascending orbits.
5. For coastal-uncorrected products, the v662 shows considerably smaller bias and its variability at Dcoast < 1000 km, compared to v700.

5.1.3.5 L3 validation with ARGO

Nine years of data **2011-2019** have been analyzed for:

- v700: First 10 days in 2014 and 2018 have not been updated (spurious)
- v662: 2017 is missing in BEC reprocessing.

Quality assessment has been conducted for the SSS1 field (**land-sea corrected**) using analysis of SMOS data averaged over 9-day for:

- **ASC (A), DES (D) and ASC+DES (B)**

The following Filters have been applied to the L2OS:

Geophysical filters	Retrieval filters	Geometrical filters
> 50% of meas with ice rain rate > 0.01 mm/h > 20% of meas outliers >10% of meas sunglint / moonglint < 30 valid mea WS > 12 m/s > 33% of meas RFI outlier	Error in iterative scheme SSS>42 SSS<0 Theoretical SSS uncertainty > 5 Chi2_P > 95 % or Chi2_P<5% Num iterations > = 20 Increment in iterative scheme > 100 Nmeas < 16	+/- 360 km from the satellite track

Comparison with Argo measurements:

The 9-day SMOS SSS fields have been compared with the Argo uppermost salinity available during these 9 days in the SMOS cell.

- Argo quality control:
 - Depth in [10 m: 0.5 m]
 - BioArgo and those included in the grey list are discarded.
 - Anomalies (Argo-WOA2013) larger than 10°C or 5 psu discarded.
 - Only considered Argo buoys with T in [-2.5°C: 40°C] and S in [2: 41] psu

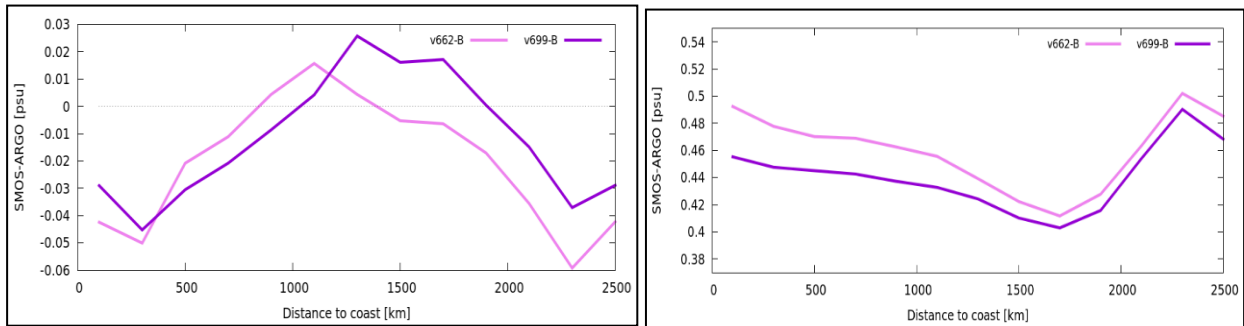


Figure 95: Mean bias (left) and STD (right) between SMOS L3 9-days average and Argo as a function of distance to coasts (v662 pink; v700 purple).

At level 3 and global scale, the corrected data exhibit very similar performances from v662 to v700 in terms of bias and reduced STD for all distances to coasts (up to ~ -0.05 at 150 kms).

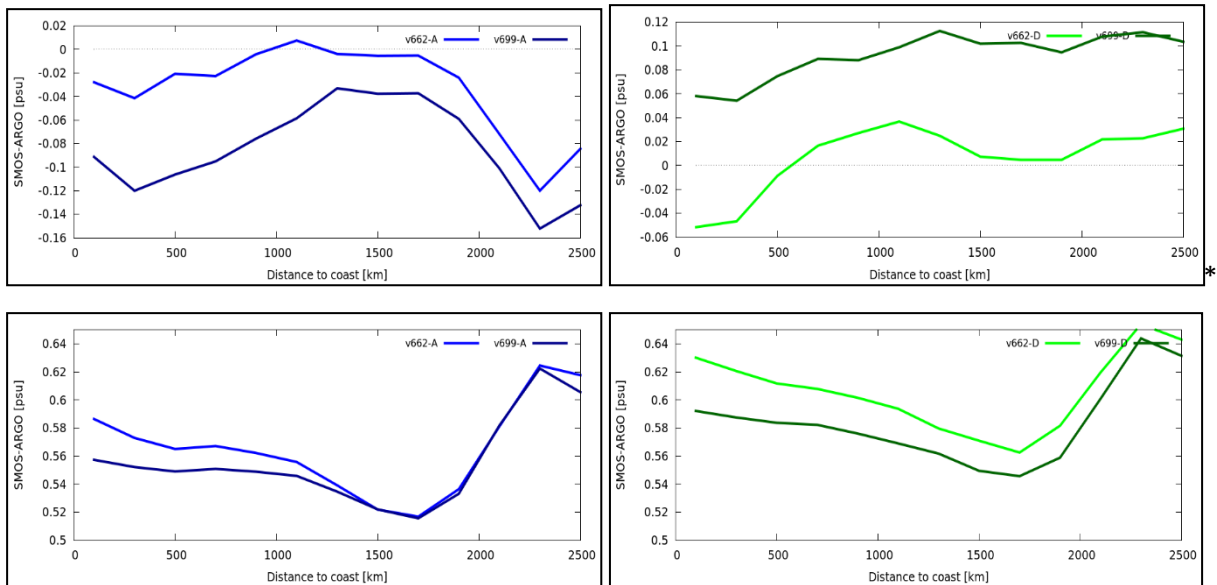


Figure 96: Mean bias (top) and Standard deviation (bottom) between SMOS L3 9-days average and Argo as a function of distance to coasts for ascending passes (left, v662 blue; v700 dark blue) and descending passes (right, v662 green; v700 dark green).

- Predominant negative biases in ascending passes for v700.
- Predominant positive biases in descending passes for v700.
- In v662 positive and negative biases are compensated leading to a better performance than in v700.
- STD respect to ARGO is systematically reduced with v700, the closer to the coast the better.

5.1.4 LSC assessment summary

Several analyses have been conducted by various ESLs to assess the L2OS data quality changes as a function of the distance to coasts. These include:

- Forward model vs SMOS Tb Data intercomparisons.

- Analyses of the L2OS SSS/in situ matchups with Argo and TSG data (PI-MEP).
 - Validation protocol Results and L3 validation with Argo.
1. For SSS uncorrected and both passes, there are clear increase of the standard deviation of the differences between the model and SMOS data for both Tx and Ty in a band extending ~500 kms from coastlines (> 2K). Linearized SSS retrievals exhibit a strongly underestimated (by 1-4 pss) SSS near coasts with respect SMAP data. The underestimation is significantly higher at high latitudes.
 2. For coastal-uncorrected SSS products, the v662 shows considerably smaller bias and its variability at Dcoast < 1000 km, compared to v700.
 3. Retrieved SSS in both ascending and descending passes exhibit biases and dwell-line averaged first Stokes parameter that are significantly reduced with LSC correction compared with the uncorrected results. Moreover, the standard deviations of the individual Tx and Ty brightness temperatures at any given position on Earth are significantly reduced in the vicinity of the coastlines. This is true **except north of 60°N with a significant over-freshening of linearized SMOS SSS vs SMAP SSS**. In descending passes, there is a smaller amplitude but clearly detectable bias showing successive negative and positive oscillations from 30°S to 60°S.
 4. **Impact of the use of SMAP SSS as opposed to ISAS SSS** as the reference to evaluate the forward model has been assessed: **SMOS Tb biases and standard deviations are similar except near river plumes** where biases with respect to ISAS tend to be larger than with SMAP used as the reference (as expected).
 5. The **uncorrected difference between ascending and descending pass biases** exhibits distinct coastal shadows in both the retrieved SSS and first Stokes parameter bias maps. **By contrast**, the difference maps **for the standard deviations** show only very week shadows, indicating that **the increased Tb standard deviations in coastal areas exhibit only weak dependence on pass direction**.
 6. **We found a Significantly degraded** (both in terms of bias and std) SMOS L2v700 quality wrt in situ data (Argo, TSG pointwise co-localization or using ISAS and validation protocol) as a function of distance to coasts in
 - 1) the Arctic Ocean, and,
 - 2) the Southern Ocean
 7. **We found Significantly improved** (both in terms of bias and std) SMOS L2v700 quality wrt in situ data (Argo, TSG pointwise co-localization or using ISAS and validation protocol) as a function of distance to coasts in:
 - 1) All mid latitudes (45°S-45°N)
 - 2) All equatorial latitudes (10°S-10°N)
 - 3) Tropical Atlantic
 - 4) South Atlantic and Pacific
 - 5) Indian Ocean
 - 6) Gulf of Mexico
 - 7) Gulf stream
 - 8) Amazon and Orinoco River plumes
 8. **Slightly improved** (std reduced but bias is increased) or unchanged SMOS L2v700 quality wrt Argo as a function of distance to coast in:
 1. North Pacific
 2. North Atlantic



3. Tropical bands
4. Tropical Pacific
9. **The mean bias increase for corrected SSS at global scale comes mostly from the Ascending orbits at high latitudes, and the variability increase is stronger for the Ascending orbits.**

5.2 Ice/sea contamination assessment

To assess ice-sea contamination, the validation protocol (see section 2.1) has been applied to ISAS maps in the Southern Ocean without applying a criterion on PCTVAR, in order not to discard regions in the vicinity to ice.

On ascending orbits (Figure 97, left), we clearly see the contamination by ice extending up to about 10° from the ice edge with a magnitude like land-sea contamination for specific geometries.

On descending orbits (Figure 97, right), positive biases north of 70°S are systematically reduced, negative differences appear south of 70°S.

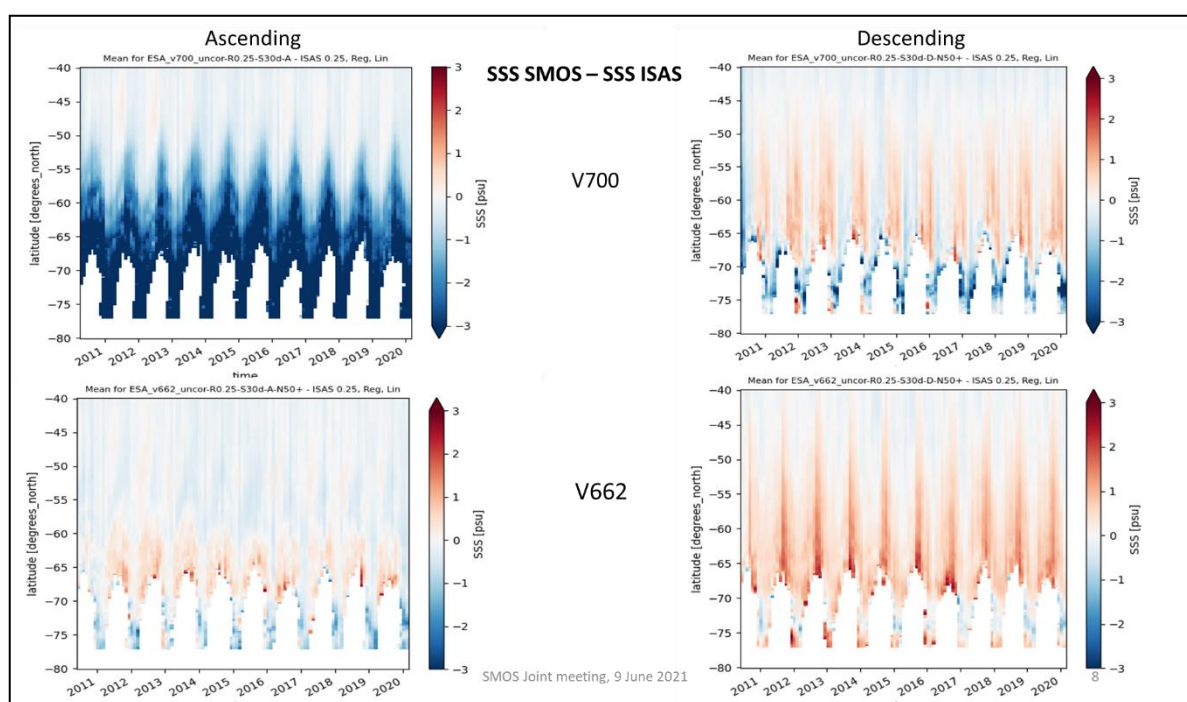


Figure 97: SMOS SSS minus ISAS SSS. Left: Ascending orbits, right: Descending orbits. Only SMOS pixels with more than 50 measurements have been retained. Top v700, bottom: v662.

To better understand the origin of the increased differences, we have looked at the differences as a function to the distance to the ice edge. Ice edge varies much in longitude and hence it is quite difficult to diagnose the origin of the biases when looking only at longitudinal averages as on Figure 97. To disentangle effects of L1 changes and of L2 dielectric constant model change, the 2016 year has been processed with a pre-release version of L1 v7 (Sce 8c) and KS dielectric constant model in L2OS (Figure 98). The ice contamination appears to be more negative on ascending orbits, slightly more positive on descending orbits related to L1 changes. As will be shown in section 7.1, the change of dielectric constant model leads to slightly more negative biases on ascending orbits but also to biases closer to 0 on descending orbits.

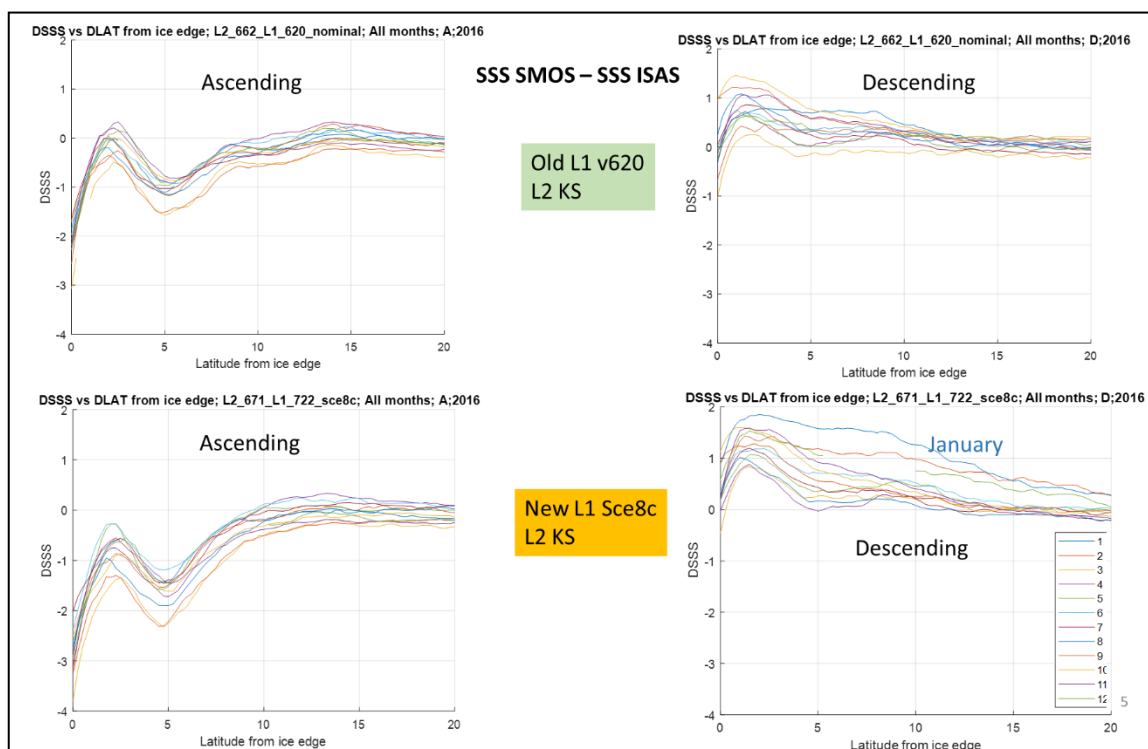


Figure 98: SMOS SSS minus ISAS SSS as a function to the distance from the ice edge in the Southern Ocean. Each colour line corresponds to a different month. Left: Ascending orbits, right: Descending orbits. Top v62, bottom: L1 Sce 8c processed with KS dielectric constant model.

5.3 Sun glint

Since the beginning of the SMOS mission the solar flux has passed through a maximum, which occurred in the 2014-2015 period, during which the sun brightness temperature at L-band reached nearly 300,000K. Superimposed on the long time-scale evolution is a strong quasi-monthly Carrington cycle. Solar flux variation on this timescale is strongest in the period of maximum solar flux and reaches nearly 50,000K. Smaller variations occur on smaller (even sub-orbital) time scales. Quiet sun conditions have prevailed since the beginning of 2017.

For this reprocessing, the choice was made to use a daily reference solar flux produced by RedLab/SERCO. This reference time series is based upon carefully intercalibrated radioastronomy measurements made at several frequencies. Figure 99 shows this daily solar flux.

A compact way to see where sun glint is expected to impact the brightness temperatures is to compute the average sun glint over the extended alias-free field of view and to plot the result as a function of time of year and latitude. The result for 2016 is shown in Figure 100, where it is seen that sun glint is strongest for descending passes between November and February south of about 30°S. During this period ascending passes are also affected by the glint but with a much lower amplitude (lower by an order of magnitude).

To see the potential impact on retrieved salinity (if measurement affected by sun glint were not filtered), it is instructive to plot the dwell line averaged difference between measured and modelled first Stokes parameter without any sun glint filtering. Figure 101 shows these differences for 29 Jan 2012 (for which the daily reference sun Tb is 166680K) and 19 Dec 2014 (for which the daily reference sun Tb is 281722K). These two dates are chosen because they correspond to low and high solar fluxes. The left panels show the difference $(T_x + T_y)/2$ without sun glint included in the forward model. The sun glint appears as a prominent band of high bias on the western side of the descending passes, south of about 30°S. As expected, the glint is significantly more prominent in the 2014 high flux case than in the 2012 low

flux case, with SMOS-model differences exceeding 10 K in $(T_x+T_y)/2$. Considering the sensitivity of retrieved SSS to the first Stokes parameter, this would correspond to a negative retrieved SSS bias exceeding 20 pss in magnitude. The right panels show the corresponding differences with the sun glint included in the forward model, computed using the Kirchhoff scattering model, ECMWF 10 m wind speed, and the SERCO/RedLab daily reference solar flux multiplied by a scale factor of about 0.91. Evidently, the sun glint model can represent the measured glint quite well, although it is not clear if the model accuracy is sufficient to be able to reliably retrieve SSS where the glint is strong. For this reason, the L2OS processor flags grid points strongly affected by sun glint.

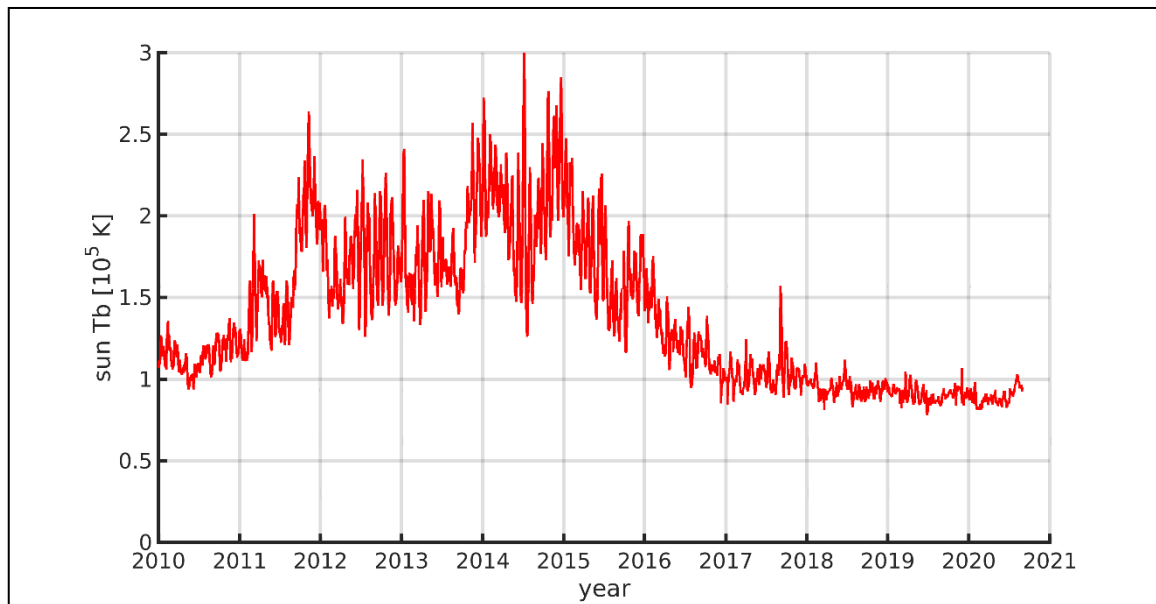


Figure 99: Time series of daily unpolarized solar flux (units of 10^5 K) obtained by rescaling the SERCO daily reference solar flux by a factor of 0.9196.

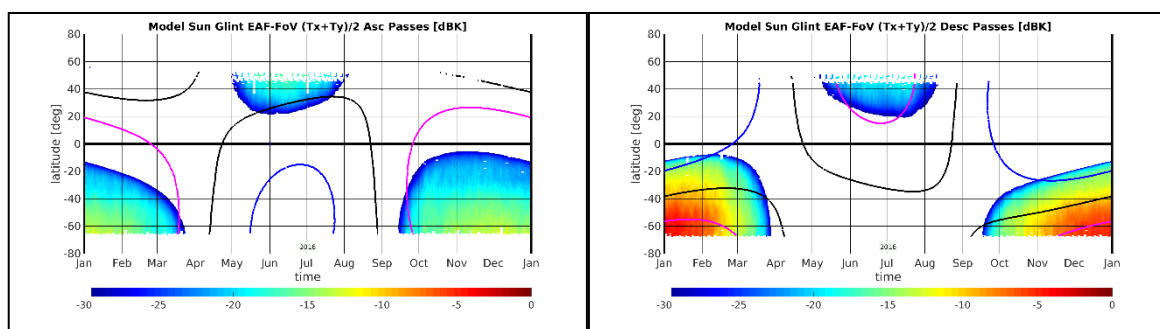


Figure 100: Extended alias-free field of view averaged sun glint $(T_x+T_y)/2$ as a function of time in 2016 and latitude. Units are dBK since the signal level is extremely small. Left: ascending passes; Right: descending passes.

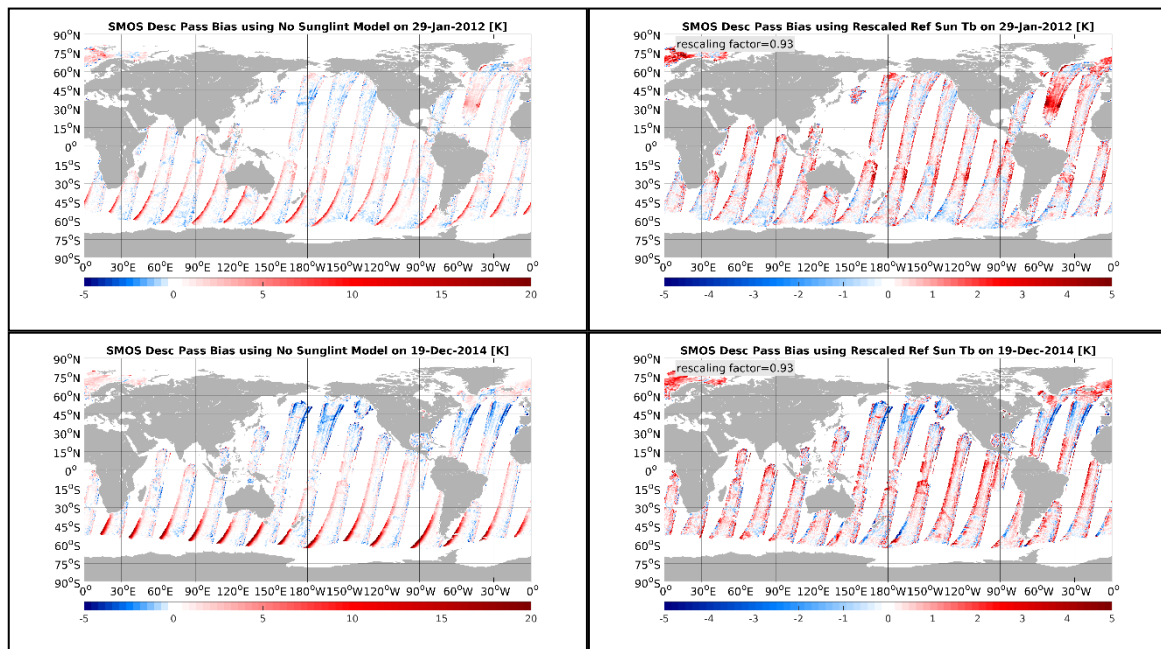


Figure 101: Examples of the impact of sun glint on dwell-line averaged difference between MIRAS and forward model first Stokes parameter divided by two $(T_x+T_y)/2$ (using brightness temperatures in the extended alias-free field of view). Units are kelvin. Top panels: 29 January 2012 without (left) and with right) sun glint included in the forward model. Sun glint is computed using the rescaled SERCO daily reference solar flux.

6 Ocean Target Transformation Trends

Analysis of the measured L1c ($TbL1c$) and modelled L2OS brightness temperature ($Tbmodel$) values during commissioning phase showed that the L2OS forward model brightness temperature values do not match those from the L1c input. The differences appeared to be systematic in the cosine coordinates antenna frame in areas far from land. A correction for this systematic error was needed, so the SMOS L1c Tb can be used to retrieve salinity.

The correction consists of the reconstruction of the systematic bias pattern by using differences in Tb values far from land, and then using that to correct the measured Tb values globally. This is called the Ocean Target Transformation (OTT). The differences in Tb values, denoted ΔTb are obtained by $\Delta(\xi,\eta)=TbL1c(\xi,\eta)-Tbmodel(\xi,\eta)$ according to the (ξ,η) position in the antenna frame.

The dynamic of the $\Delta(\xi,\eta)$ can be used as an indicator of the L1 calibration efficiency. This dynamic can be investigated spatially in the (ξ, η) plane by calculating the standard deviation of ΔTb (ξ, η) and temporally by monitoring the variations of the mean of ΔTb (ξ, η) as a function of time.

A systematic comparison between versions v662 and v700 is proposed below. The products used for this validation are the SM_REPR_AUX_OTT1F files available on request from the DPGS. They are made up of ΔTb (ξ, η) calculated for the polarizations (TX, TY, St3, St4), ascending and descending orbits separately. Statistics are calculated excluding the portion of the FOV affected by the sun point.

Figure 102 shows that on average the ascending OTTs are closer to 0 in v700 than in v662. Unexpected behaviour is observed for the Y polarization which changes trend from 2015 to stabilize again afterwards. For this polarization, v662 is more stable in terms of median value. The amplitude of the seasonal fluctuations is slightly lower in the new version. The st3 follows the same modulation in both versions.

The behaviour of top-down OTTs is similar with a more marked seasonal dynamic (Figure 103).

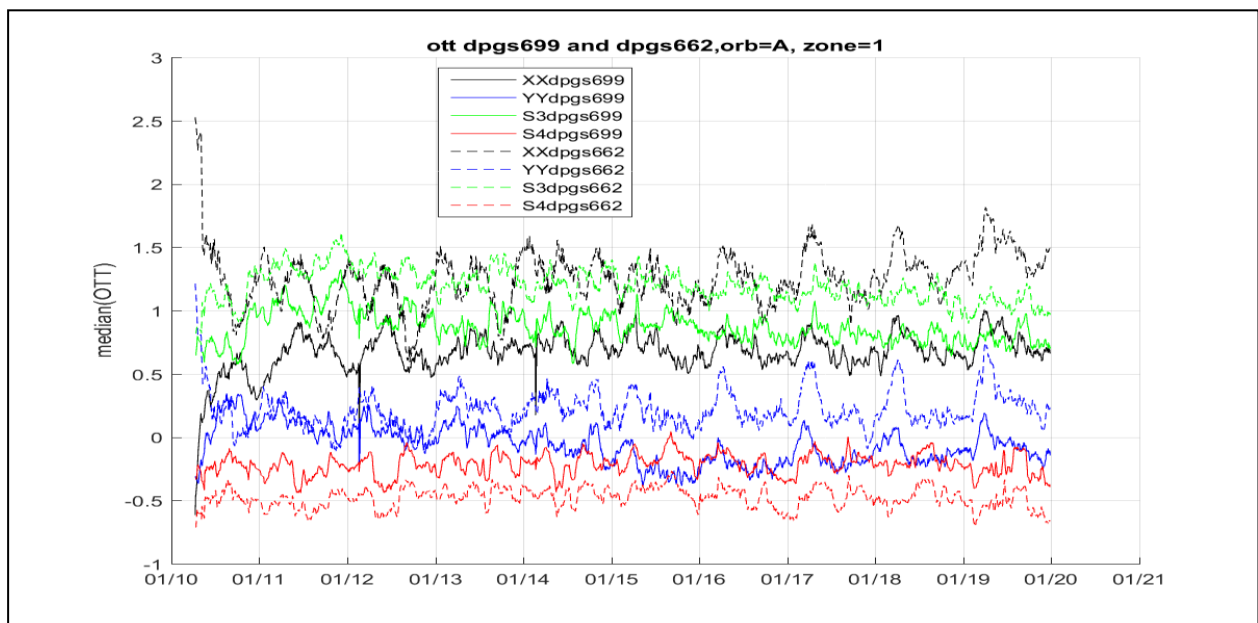


Figure 102: Median of the OTT according to the time for the four polarizations (TX, TY, St3, St4) in black, blue, green, and red, respectively. Full lines correspond to v700, dashed lines to v662. Ascending orbits.

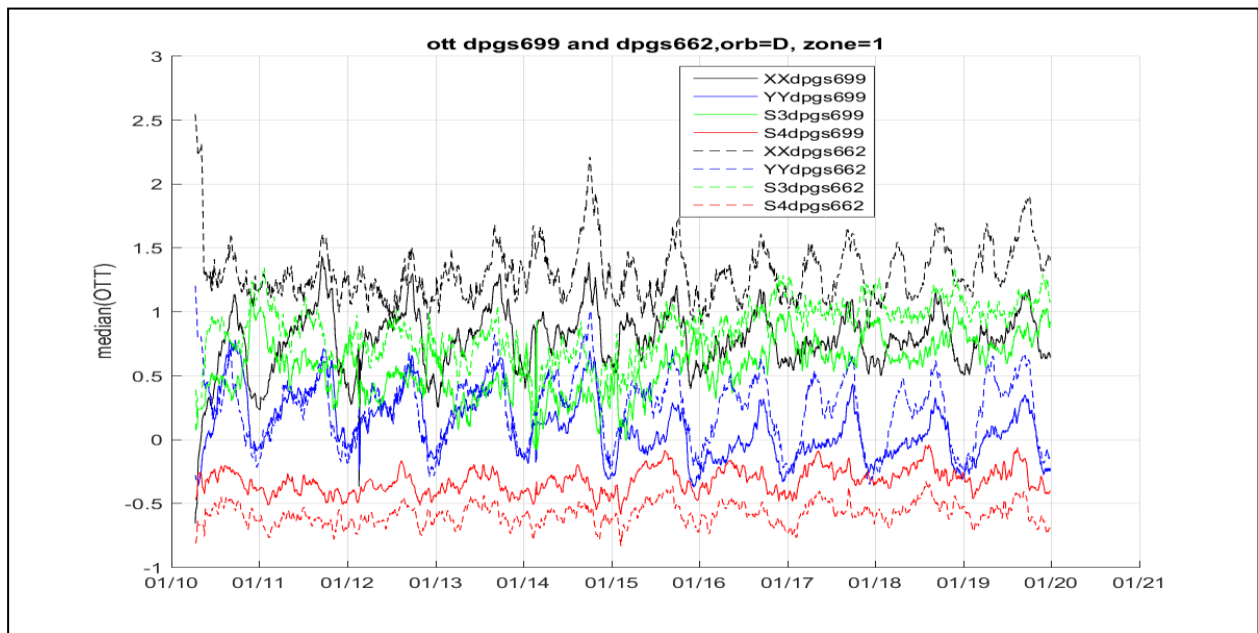


Figure 103: Median of the OTT according to the time for the four polarizations (TX, TY, St3, St4) in black, blue, green, and red, respectively. Full lines correspond to v700, dashed lines to v662. Descending orbits.

Regarding the standard deviation of $\Delta T_b(\xi, \eta)$ (Figure 104), it is lower in the v700 except for the X polarization. The variations of the median of the OTT Y (Figure 102) are to be compared with the decrease in the standard deviation from 2015. The decrease with time of OTT Y standard deviation is accompanied by an increase of OTT St3 standard deviation for both versions and this in a way more marked in descending orbits. The origin of these trends is not currently fully understood. The St4 is much more homogeneous on the FOV in v700.

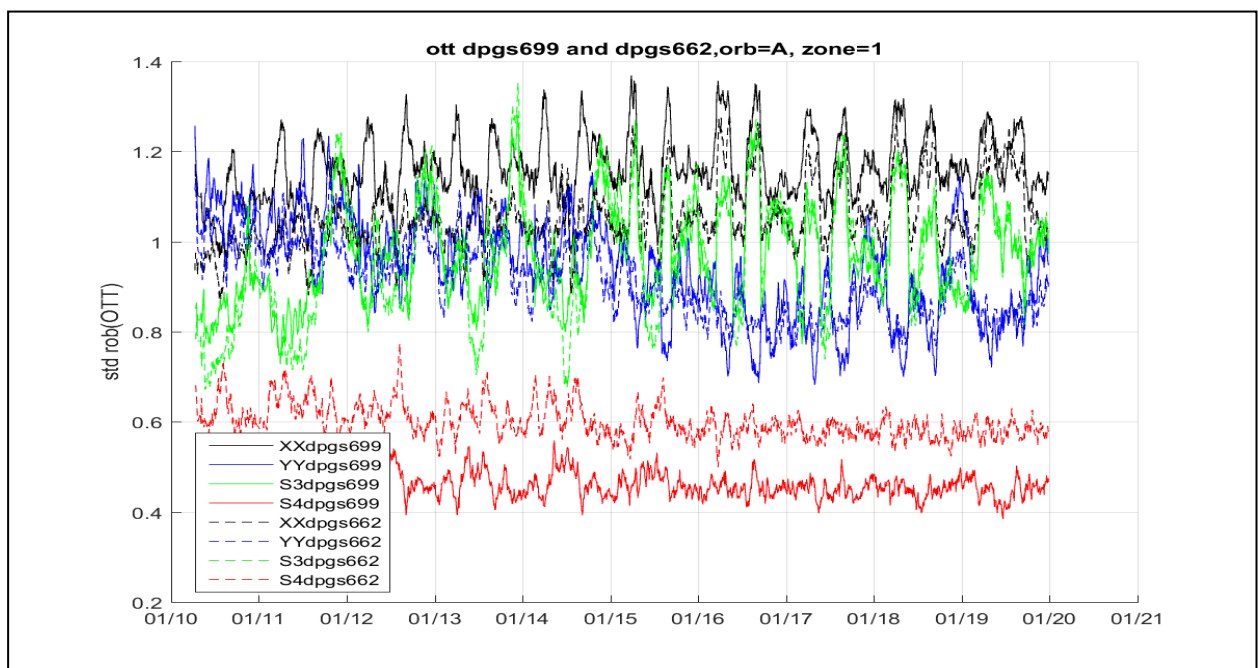


Figure 104: Standard deviation of the OTT according to the time for the four polarizations (TX, TY, St3, St4) in black, blue, green, and red, respectively. Full lines correspond to v700, dashed lines to v662. Ascending orbits.

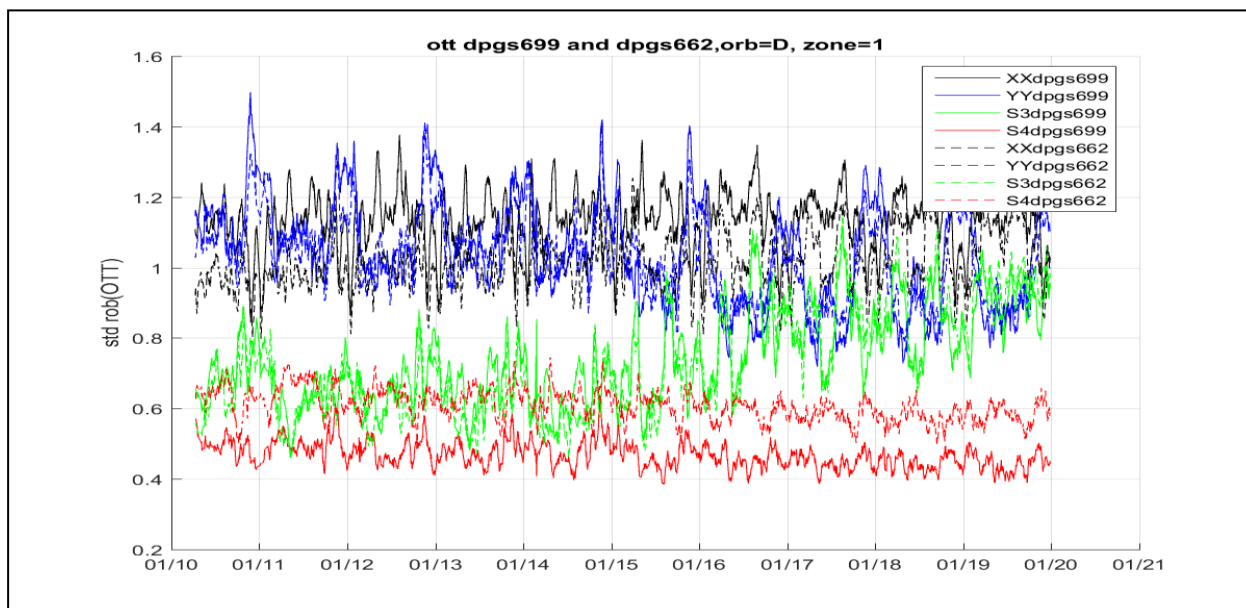


Figure 105: Standard deviation of the OTT according to the time for the four polarizations (TX, TY, St3, St4) in black, blue, green, and red, respectively. Full lines correspond to v700, dashed lines to v662. Descending orbits.

To diagnose the dynamics of $\Delta T^b(\xi, \eta)$ in the (ξ, η) plane, Figure 106 shows the annual anomalies of OTT TX (after the withdrawal of the global average) over the period [2011- 2019]. The v700 appears to be more stable over time, with a reduction in dynamics at the start of the period [2011-2013].

For TY polarization (Figure 107), negative anomalies at the start of the period for version v662 become positive for version v700.

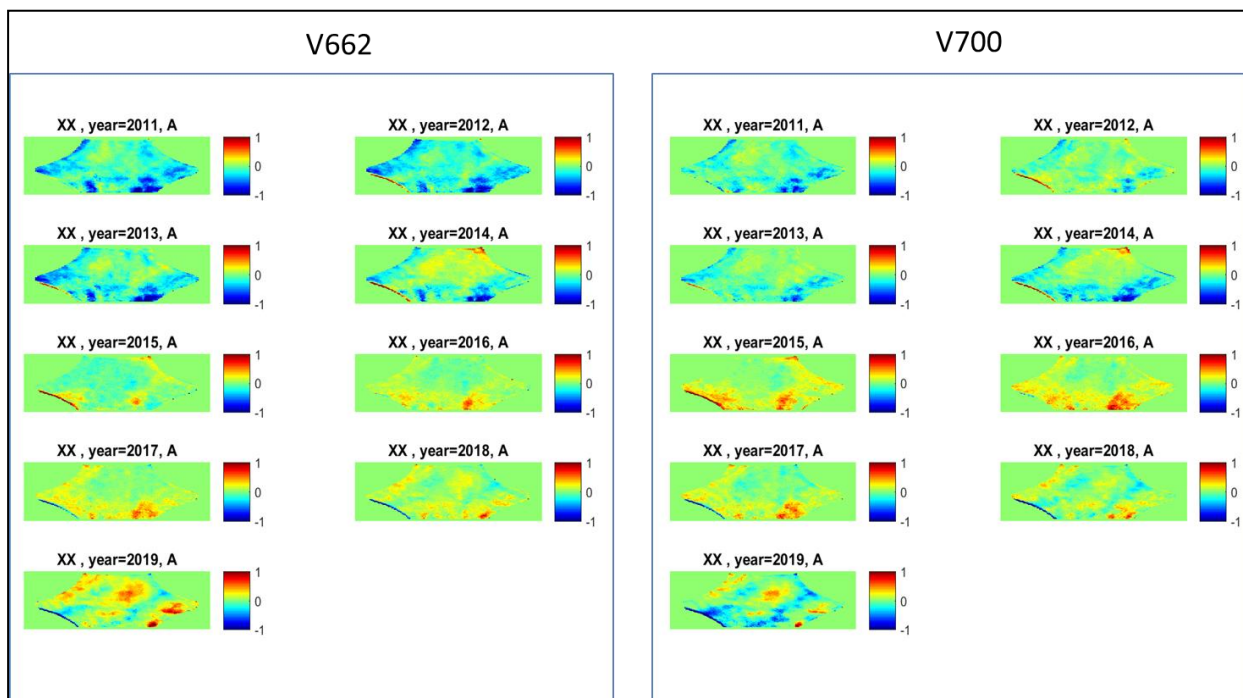


Figure 106: OTT anomalies over 2011-2019, X polarization, ascending orbits. Left panel shows v662 OTTs, right panel, v700 OTTs.

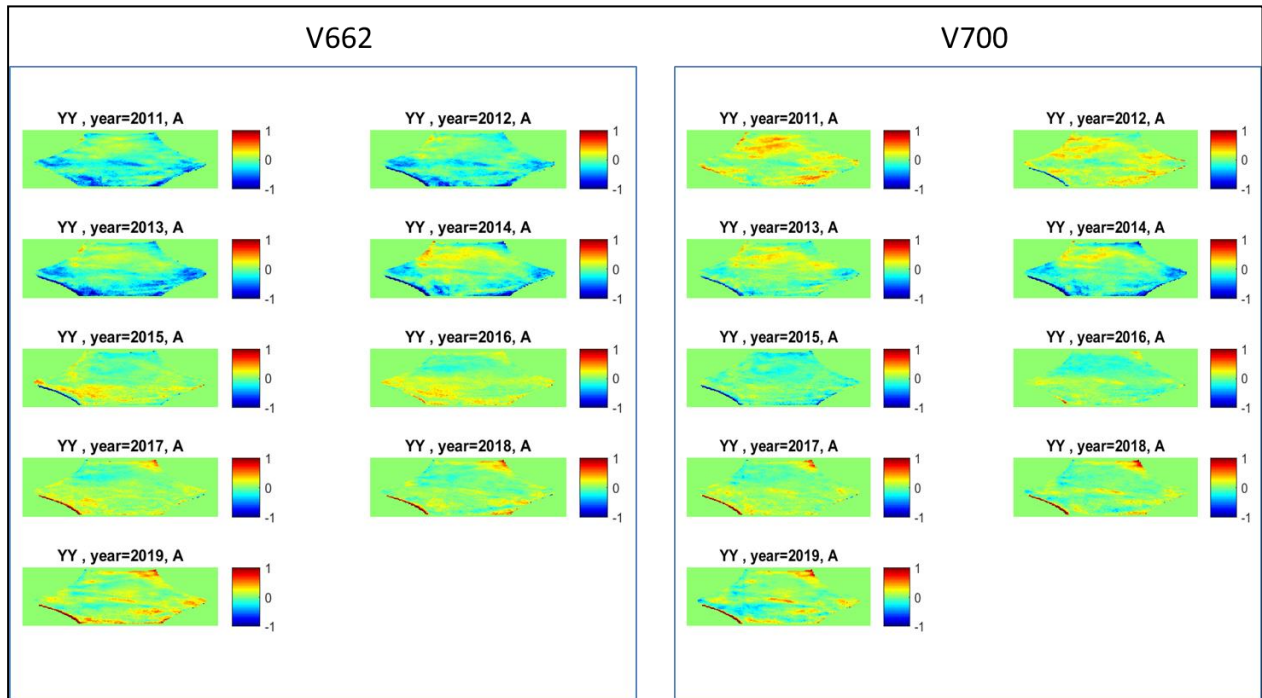


Figure 107: OTT anomalies over 2011-2019, Y polarization, ascending orbits. Left panel shows v662 OTTs, right panel, v700 OTTs.

The OTTs v700 are generally more homogeneous than the OTT v662. There was therefore a significant impact of the new calibrations proposed in the new L1 v724 on the stability of the reconstruction of TBs on the FOV.

7 Dielectric constant and Cardioid models

7.1 Impact of new dielectric constant model

The impact of the new dielectric constant model is expected to be a large decrease of SSS (up to -1ps) in the cold water and a slight increase in warm waters (<0.1) (Boutin et al. 2020).

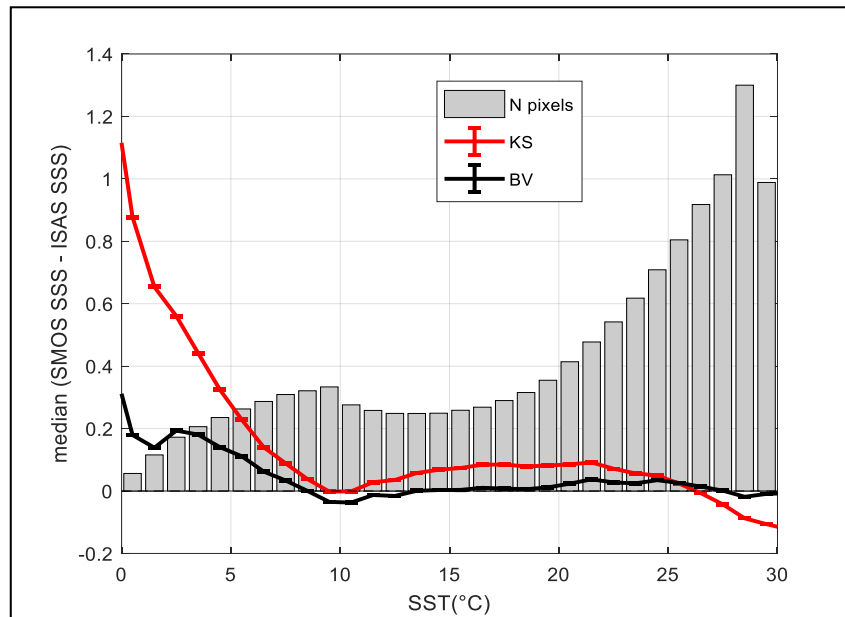


Figure 108: Expected change in SSS (red curve minus black curve) due to dielectric constant model change (see Boutin et al. 2020 for more details).

An example of the expected change for the month of April 2016 is shown on Figure 109.

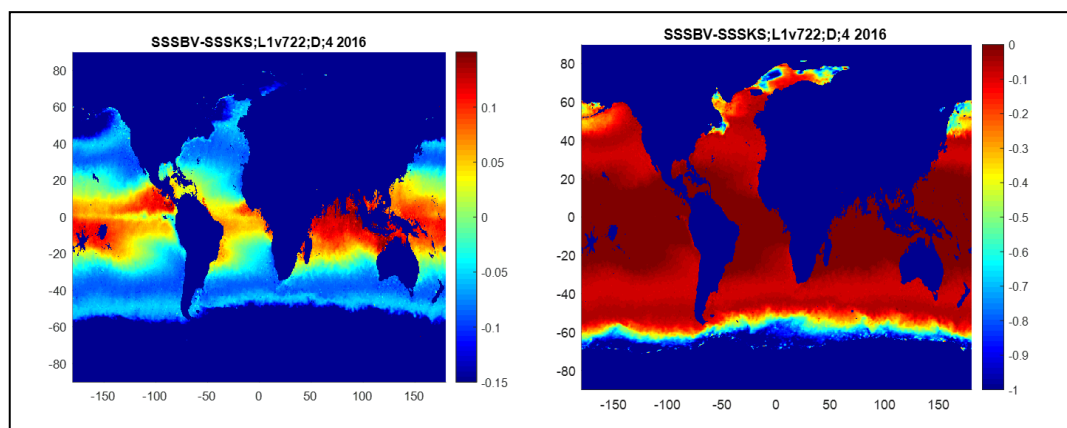


Figure 109: Expected SSS difference due to the change in dielectric constant model (SSS BV – SSS KS) over moderate to warm SST (left), over full SST range (right)

For v700, we observe the tendencies shown in Figure 109, in addition to the changes due to the L1 changes. At mid latitude, the change is relatively small compared to the noise in SMOS SSS, so it is quite

difficult to assess the improvement, but it is likely that the dielectric constant model change contributes to reducing the standard deviation of the SMOS-ISAS differences we saw at mid latitudes (Figure 9).

In cold waters (SST <10°C), in the Southern Ocean, the improvement is clear on both descending and ascending orbits, apart from the 10° band contaminated by the ice edge. This is illustrated on Figure 110, where the SSS biases related to cold SST was very clear on v662 in the southern Atlantic Ocean. With v700, the bias is much reduced in the southern Atlantic Ocean even though, at less than 10° from the ice edge ice-sea contamination leads to negative biases on ascending orbits.

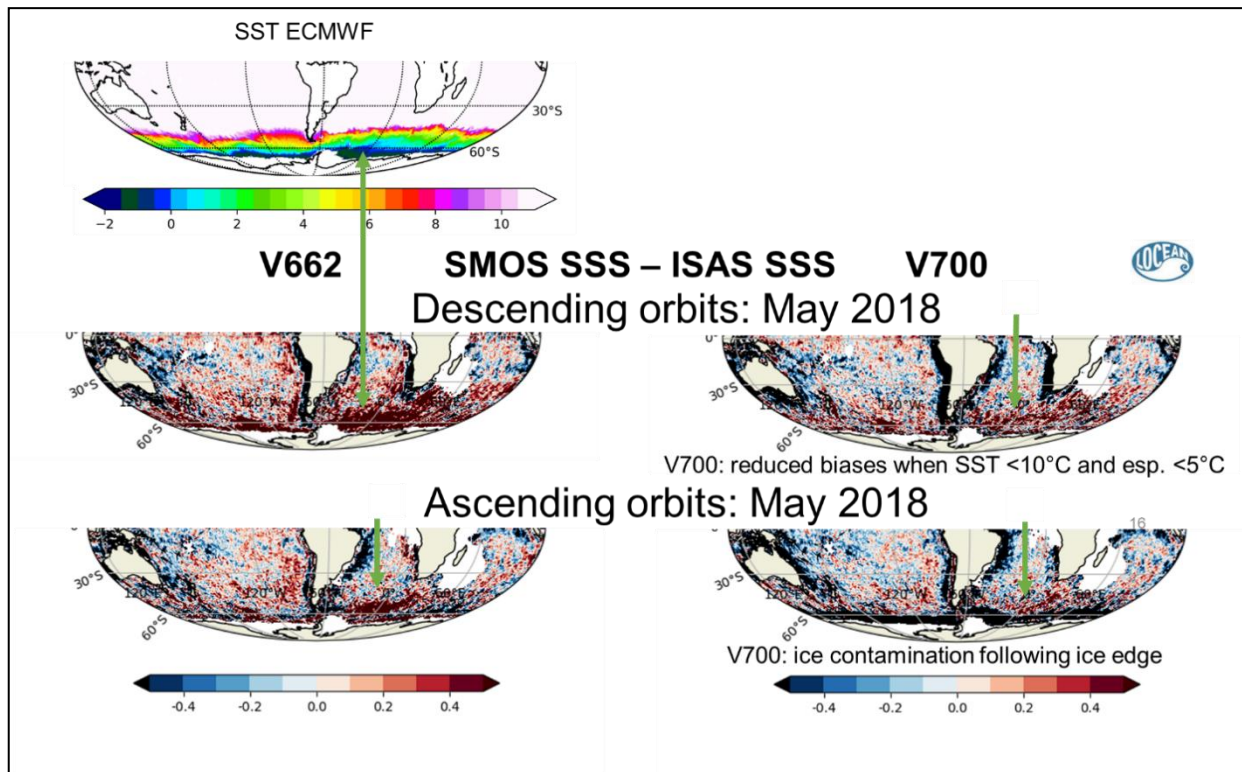


Figure 110: SMOS minus ISAS SSS in the Southern hemisphere in May 2018. Left v662, right: v700. Top: SST, middle: Descending orbits, bottom: ascending orbits.

Close to ice edge, in addition to the L1 changes illustrated in section 5.2, the change of dielectric constant model leads to slightly more negative biases on ascending orbits but also to biases closer to 0 on descending orbits as shown on the processing of the 2016 year with pre-released L1 and KS or BV dielectric constant model (Figure 111, next page).

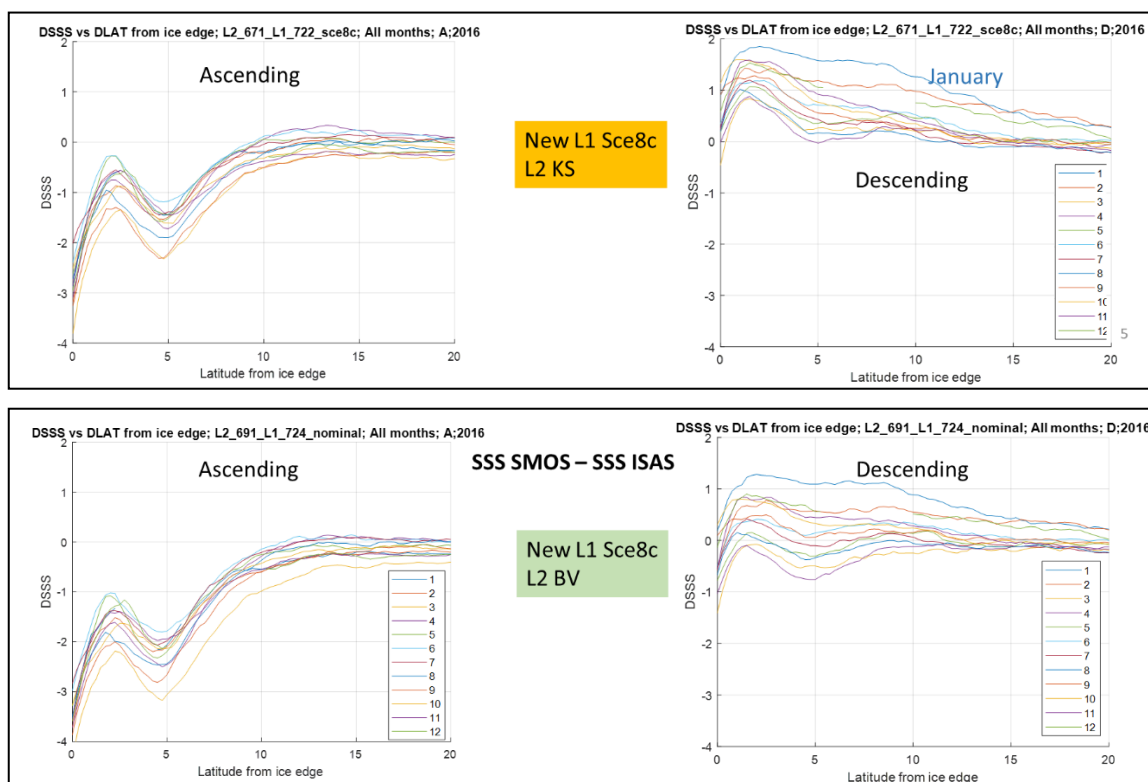


Figure 111: SMOS SSS minus ISAS SSS as a function to the distance from the ice edge in the Southern Ocean. Each colour line corresponds to a different month. Left: Ascending orbits, right: Descending orbits. Top: L1 Sce 8c processed with KS dielectric constant model; bottom: L1 Sce 8c processed with BV dielectric constant model.

7.2 Cardioid model

ESL team has introduced a specific parameter, the so-called Acard, which is a proxy of dielectric constant model and an alternative to the one from Klein&Swift. The Acard parameter is very robust and well adapted for TB processing.

The estimation of Acard is made from the TB corrected from coastal contamination (5.1). The comparison of Acard v662 and v700 therefore shows two effects: the LSC correction and the new L1 reprocessing in full ocean and close to the ice edge (where the LSC correction is not applied).

First, note that the Acard data in descending orbits between October and January must be filtered on the right edge of the FOV (xswath <350km) in the southern hemisphere. This effect is probably linked to solar contamination and the eclipse period. This effect affects both versions.

Figure 112, Figure 113, and Figure 114 show respectively 3 months of the year 2016: May, July, September, ascending orbits. In general, we see that $\text{mean}(\text{Acard v700} - \text{Acard v662})$ is correlated with $\text{mean}(\text{SSS v700} - \text{SSS v662})$. Acard is found to be more robust at low SST than SSS. On the other hand, at high SST, Acard is much more reactive to a change in the TBs (for example Figure 112, in the tropical band). We notice that there is a bias which appears far from the coasts in the northern hemisphere in v700 (v662 is little or no biased). This bias is maximum in July and then decreases in September. This trend is observed over the 10 years of data and is not specific to the year 2016. The marked differences in the equatorial Atlantic correspond, for their part, to an improvement in the LSC correction. Indeed, in v662, the SMOS salinities are too large.

Still in ascending orbits, we notice a large $\text{std}(\text{SSS v700} - \text{SSS v662})$ at high southern latitudes. This strong std could be due to the change of dielectric constant model in the v700. However, we also observe a strong $\text{std}(\text{Acard v700} - \text{Acard v662})$. Knowing that Acard does not directly depend on the dielectric

constant model, we can deduce that the high value of $\text{std}(\text{SSS v700} - \text{SSS v662})$ is not related only to the change of the dielectric constant but also to the L1 processing. In version v662, Acard estimated at low temperatures is too large. Here, we notice that the estimated Acard is lower, which goes in the expected direction.

In descending orbits (Figure 115, Figure 116 and Figure 117), the mid-ocean bias observed in July in ascending orbits does not appear. In addition, the large values of $\text{std}(\text{Acard v700} - \text{Acard v662})$, do not appear at high southern latitudes either. This confirms that there is an increase in the bias of near-ice TBs in ascending orbits in v700.

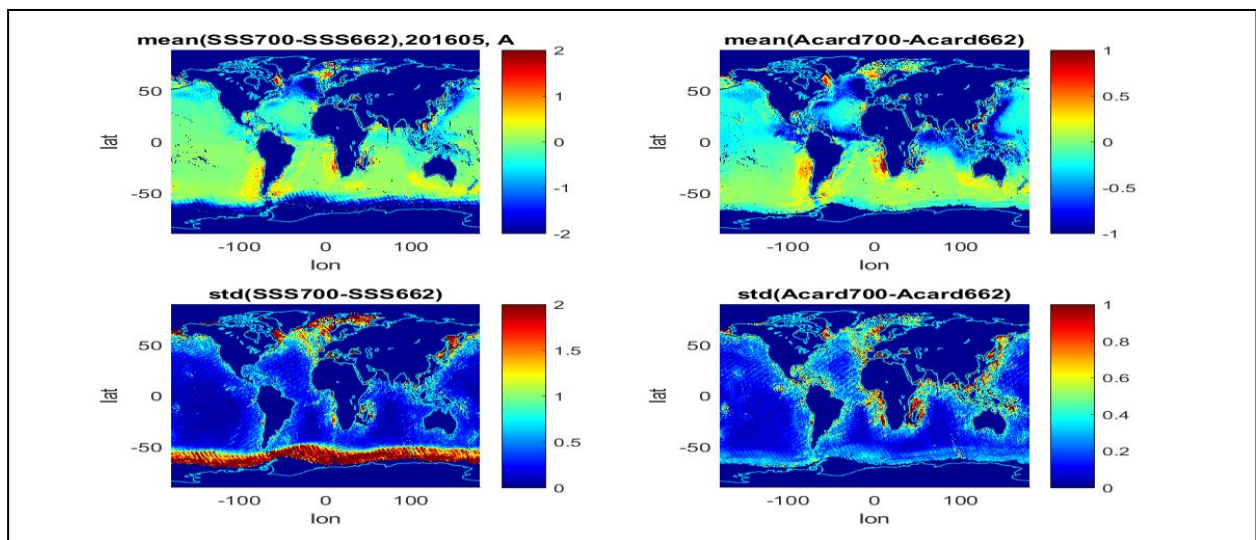


Figure 112: Monthly average of Acard and SSS from v662 and v700, ascending orbits. Top left: $\text{mean}(\text{SSS v700} - \text{SSS v662})$; top right: $\text{mean}(\text{Acard v700} - \text{Acard v662})$; bottom left: $\text{std}(\text{SSS v700} - \text{SSS v662})$; bottom right: $\text{std}(\text{Acard v700} - \text{Acard v662})$. May 2016.

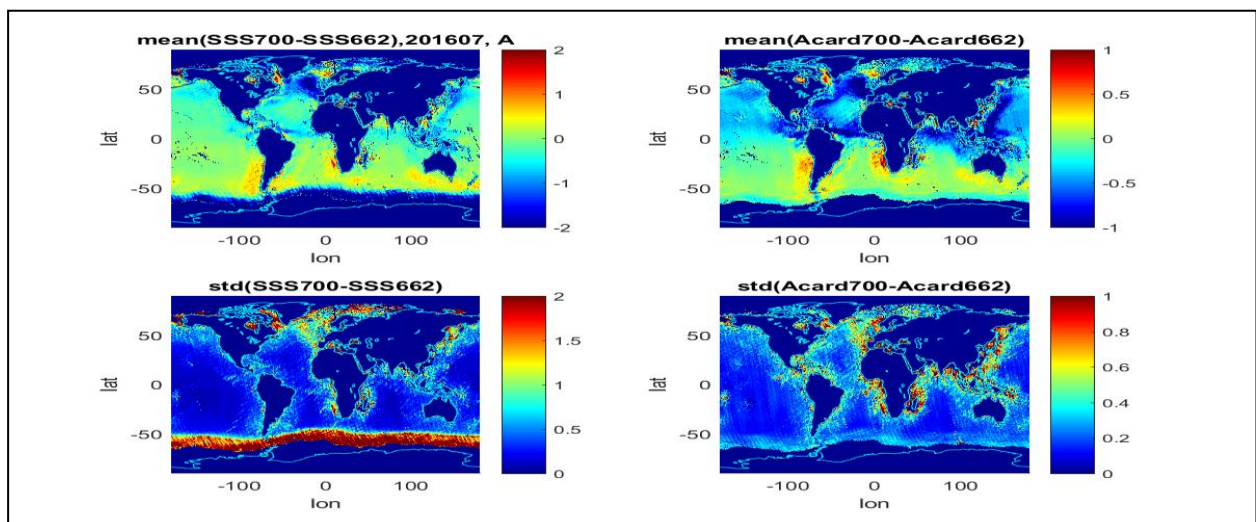


Figure 113: Monthly average of Acard and SSS from v662 and v700, ascending orbits. Top left: $\text{mean}(\text{SSS v700} - \text{SSS v662})$; top right: $\text{mean}(\text{Acard v700} - \text{Acard v662})$; bottom left: $\text{std}(\text{SSS v700} - \text{SSS v662})$; bottom right: $\text{std}(\text{Acard v700} - \text{Acard v662})$. July 2016.

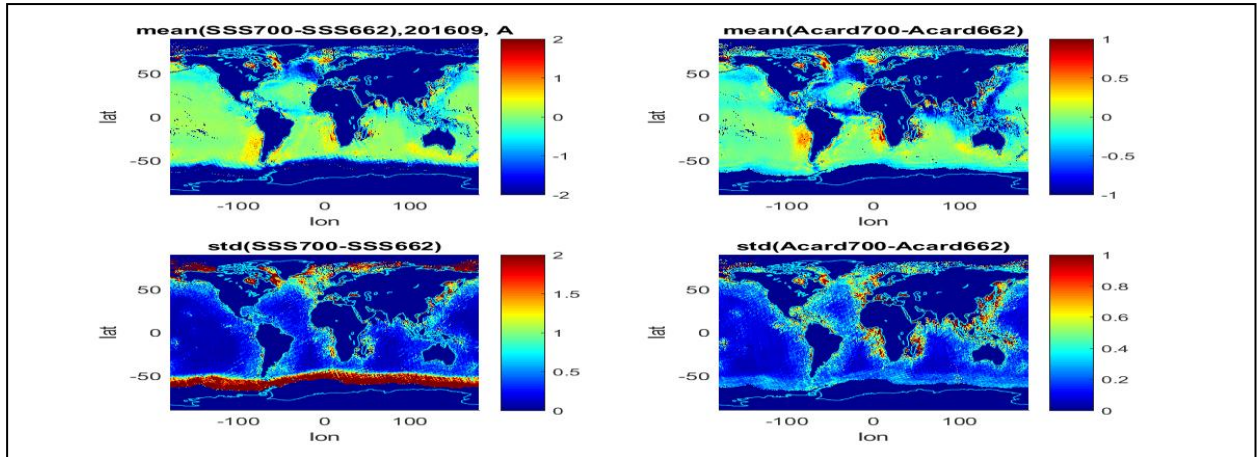


Figure 114: Monthly average of Acard and SSS from v662 and v700, ascending orbits. Top left: $\text{mean}(\text{SSS v700} - \text{SSS v662})$; top right: $\text{mean}(\text{Acard v700} - \text{Acard v662})$; bottom left: $\text{std}(\text{SSS v700} - \text{SSS v662})$; bottom right: $\text{std}(\text{Acard v700} - \text{Acard v662})$. September 2016.

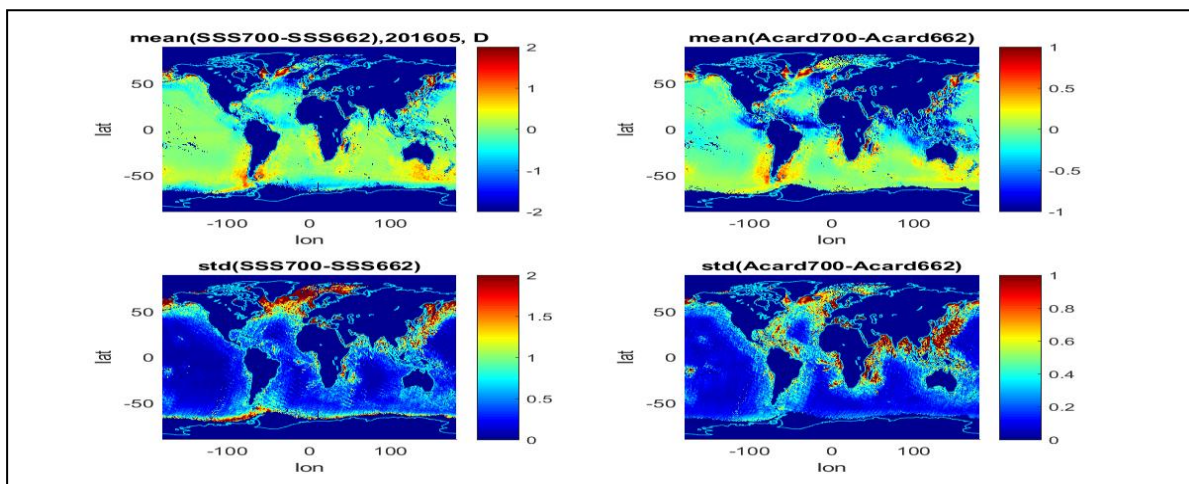


Figure 115: Monthly average of Acard and SSS from v662 and v700, descending orbits. Top left: $\text{mean}(\text{SSS v700} - \text{SSS v662})$; top right: $\text{mean}(\text{Acard v700} - \text{Acard v662})$; bottom left: $\text{std}(\text{SSS v700} - \text{SSS v662})$; bottom right: $\text{std}(\text{Acard v700} - \text{Acard v662})$. May 2016.

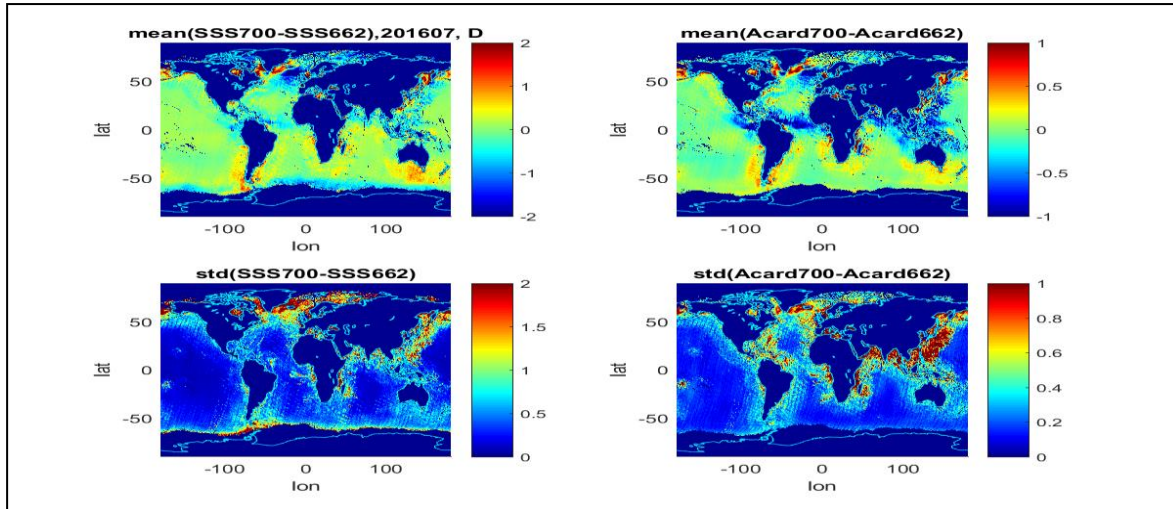


Figure 116: Monthly average of Acard and SSS from v662 and v700, descending orbits. Top left: $\text{mean}(\text{SSS v700} - \text{SSS v662})$; top right: $\text{mean}(\text{Acard v700} - \text{Acard v662})$; bottom left: $\text{std}(\text{SSS v700} - \text{SSS v662})$; bottom right: $\text{std}(\text{Acard v700} - \text{Acard v662})$. July 2016.

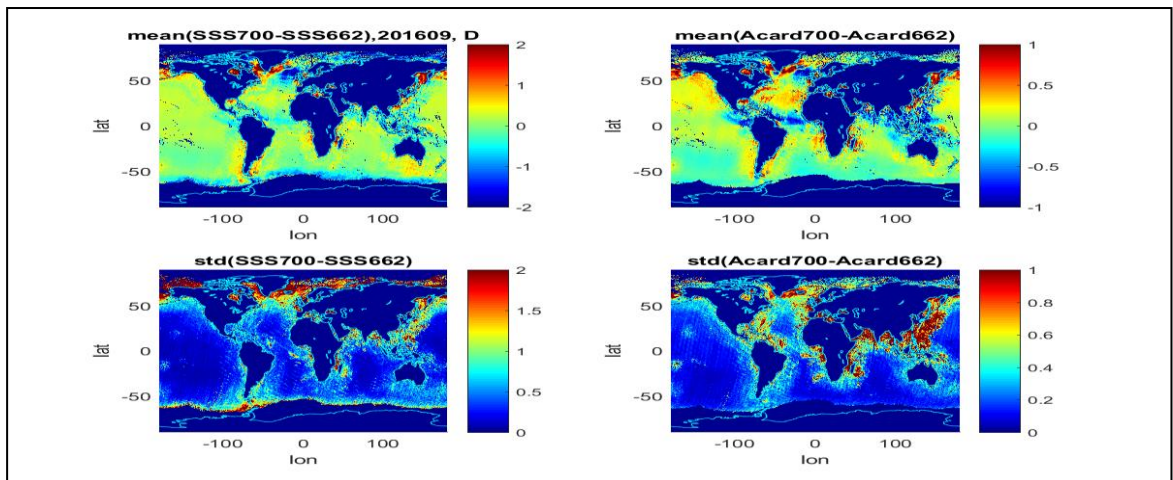


Figure 117: Monthly average of Acard and SSS from v662 and v700, descending orbits. Top left: $\text{mean}(\text{SSS v700} - \text{SSS v662})$; top right: $\text{mean}(\text{Acard v700} - \text{Acard v662})$; bottom left: $\text{std}(\text{SSS v700} - \text{SSS v662})$; bottom right: $\text{std}(\text{Acard v700} - \text{Acard v662})$. September 2016.

References

- [Argo] Argo: Argo float data and metadata from Global Data Assembly Centre (Argo GDAC). SEANOE., <https://doi.org/10.17882/42182>, 2000.
- [Fore.2016]. Fore, A., Yueh, S. H., Tang, W., Stiles, B. W., and Hayashi, A. K.: Combined Active/Passive Retrievals of Ocean Vector Wind and Sea Surface Salinity With SMAP, *IEEE TRANSACTIONS ON GEOSCIENCE AND REMOTE SENSING*, 54, 7396–7404, <https://doi.org/10.1109/TGRS.2016.2601486>, 2016.
- [Gaillard.2016] Gaillard Fabienne, Reynaud Thierry, Thierry Virginie, Kolodziejczyk Nicolas, von Schuckmann Karina (2016). In-situ based reanalysis of the global ocean temperature and salinity with ISAS: variability of the heat content and steric height. *Journal Of Climate*, 29(4), 1305-1323. Publisher's official version : <https://doi.org/10.1175/JCLI-D-15-0028.1> , Open Access version : <https://archimer.ifremer.fr/doc/00309/42030/>.
- [Gonzalez-Gambau.2020] González-Gambau, V., Turiel, A., González-Haro, C., Martínez, J., Olmedo, E., Oliva, R., and Martín-Neira, M.: Triple collocation analysis for two error-correlated datasets: Application to L-band brightness temperature over land, *Remote Sensing*, 12, 3381, 750 <https://doi.org/10.3390/rs12203381>, 2020
- [Gruber.2016] Gruber, A., Su, C., Crow, W. T., Zwieback, Z., Dorigo, W. A., and Wagner, W.: Estimating error cross-correlations in soil moisture data sets using extended collocation analysis, *Journal of Geophysical Research: Atmospheres*, 121, 1208–1219, <https://doi.org/10.1002/2015JD024027>, 2016.
- [Hoareau.2018] Hoareau, N., Portabella, M., Lin, W., Ballabrera-Poy, J., and Turiel, A.: Error Characterization of Sea Surface Salinity Products Using Triple Collocation Analysis, *IEEE Transactions on Geoscience, and Remote Sensing*, 56, 5160–5168, <https://doi.org/10.1109/TGRS.2018.2810442>, 2018.
- [Meissner.2018] Meissner, T., Wentz, F., and Le Vine, D.: The Salinity Retrieval Algorithms for the NASA Aquarius Version 5 and SMAP Version 3 Releases, *Remote Sensing*, 10, <https://doi.org/10.3390/rs10071121>, 2018.
- [Olmedo.2021] Olmedo, E., González-Haro, C., Hoareau, N., Umbert, M., González-Gambau, V., Martínez, J., Gabarró, C. and Turiel, A. Nine years of smos sea surface salinity global maps at the barcelona expert center. *Earth System Science Data*, 13 : 857 –888, 2021
- [Pierdicca.2017].Pierdicca, N., Fascetti, F., Pulvirenti, L., and Crapolicchio, R.: Error characterization of soil moisture satellite products: Retrieving error cross- correlation through extended quadruple collocation, *IEEE Journal of Selected Topics in Applied Earth Observations and Remote Sensing*, 10, 4522–4530, <https://doi.org/10.1109/JSTARS.2017.2714025>, 2017.
- [Yin.2012] Yin, X., J. Boutin, and P. Spurgeon (2012b), First Assessment of SMOS Data Over Open Ocean: Part I: Pacific Ocean, *IEEE Transactions on Geoscience and Remote Sensing*, 50(5), 1648-1661, doi:10.1109/tgrs.2012.2188407.



***SMOS ESL for SMOS Level 1 and Level 2
over Land, Ocean, and Ice
- L2OS 3rd Mission Reprocessing Report -***

Ref.: ARG-003-081

Date: 16.07.2021

Page: 127

End of Document